

Investigation of a Drive Mechanism Modification to Increase Thermodynamic Power
of a Low Temperature Differential Gamma Type Stirling Engine

by

Michael E. Nicol-Seto

A thesis submitted in partial fulfillment of the requirements for the degree of

Master of Science

Department of Mechanical Engineering

University of Alberta

ABSTRACT

This work presents the findings of an investigation into the modification of the drive mechanism of a low temperature differential gamma type Stirling engine with the aim of improving the thermodynamic performance and power production. A drive mechanism was conceptualized that could modify the displacer and piston motion profiles to be more discontinuous by dwelling the pistons at top dead center and bottom dead center during an engine cycle. The discontinuous motion better replicated the ideal Stirling thermodynamic cycle. Motion modification was achieved using interchangeable non-circular gear sets to vary the displacer and piston crankshaft speeds throughout an engine cycle. Preliminary thermodynamic analysis using a simple isothermal model validated the design, and so an engine was retrofit with the novel drive mechanism. Three sets of oval elliptical non-circular gears were tested: a set of round gears of eccentricity $e = 0$ used to replicate a conventional unmodified drive mechanism, and two oval gear sets of eccentricity $e = 1/5$ and $e = 1/3$ that incrementally increased the dwell of the displacer and piston.

A series of steady state experiments were conducted on the modified engine that tested the performance of the motion modifications: displacer dwelling, piston dwelling, and combined dwelling. A supplemental set of trials were run that dwelled the displacer mid-stroke to reduce displacer velocity combined with piston dwelling. All experiments were conducted with a thermal source at 90 °C and a thermal sink at 5 °C.

Results of displacer dwelling experiments simultaneously validated, and went against, the anticipated improvement in performance. Preliminary modeling and reports

in the literature anticipated increased indicated cycle work and power. The findings of this investigation indicated that dwelling the displacer did improve the indicated thermodynamic work of the cycle, but was also detrimental to maximum engine power. The reduction in power was caused by a reduction in engine running speed, which was attributed to the increased maximum displacer speed of the dwelled motion. The trial using the $e = 1/3$ gears reduced maximum power by 27.4%, despite improving improving shaft work by 9.5%. The supplemental trials with reduced maximum displacer speed resulted in increases to engine speed and slight increases to maximum power.

Experiments where the piston was dwelled had neutral or positive outcomes. The indicated work of the cycle was increased as anticipated, but the shaft work was not improved proportionally. The reduced mechanism effectiveness was attributed to additional mechanism friction. Piston dwelling did not reduce engine velocity. The most substantial gain in engine power was observed during the trial with reduced displacer velocity and the $e = 1/5$ gear set dwelling the piston, which improved the maximum power by 4.0%.

The empirical results highlighted a shortcoming of the initially positive thermodynamic modeling results. The model cannot predict engine speed, and so could not anticipate the reduction to engine cyclic rate, despite improvements to the indicated thermodynamic work. The findings of this investigation suggest that improvements to engine running speed and mechanism effectiveness are necessary to realize the thermodynamic gains achieved by the dwelling of the displacer and piston at the tested engine operating conditions.

PREFACE

This thesis is an original work by Michael Nicol-Seto. Aspects of the research presented in chapters 6 have been published in the following conference publications:

M. Nicol-Seto, J. Michaud, S. Middleton, and D. S. Nobes, “*Non-Traditional Drive Mechanism Designs for the Improvement of Heat Transfer in Low Temperature Differential Stirling Engines*”, Proceedings the 18th International Stirling engine Conference, Tainan, Taiwan, Sep. 2018, pp. 353-365

M. Nicol-Seto and D. Nobes, “*Performane Of A Modified Drive Mechanism On A Low Temperature Differential Stirling Engine*”, Progress in Canadian Mechanical Engineering. Volume 4, Jun. 2021.

M. Nicol-Seto and D. Nobes, “*Experimental evaluation of piston motion modification to improve the thermodynamic power output of a low temperature gamma Stirling engine*”, 19th International Stirling Engine Conference, Rome, Sep. 2021

The author has also contributed to conceptual design and solid modeling presented in the following publication. These contributions did not directly contribute to this thesis.

M. Lottmann *et al.*, “*Early Development Of A 100 Watt Low Temperature Difference Stirling Engine*”, Progress in Canadian Mechanical Engineering. Volume 4, Jun. 2021.

ACKNOWLEDGEMENTS

The author would like to acknowledge the following people for their contributions to the completion of this work:

Dr. David S. Nobes for committed assistance and supervision.

Support and contribution given by members, past and present, of the Stirling engine research group:

Linda Hasanovich

Steven Middleton

Jason Michaud

Calynn Stumpf

Connor Speer

David Miller

Alexander Hunt

Matthias Lottman

as well as the other graduate student members, and co-op students, of the of the broader Nobes research group.

The author would like to acknowledge the loving support of family and and friends who have inspired, counselled, encouraged, and otherwise enhanced this undertaking.

Finally, the author would like to acknowledge the financial support for this project provided by:

Natural Sciences and Engineering Research Council (NSERC) of Canada,

Future Energy Systems (FES)

Alberta Innovates Energy and Environmental Solutions, and

Terrapin Geothermics

TABLE OF CONTENTS

Abstract.....	ii
Preface.....	iv
Acknowledgements.....	v
List of Tables.....	xiv
List of Figures.....	xvii
List of Symbols.....	xxiv
1 Introduction.....	1
1.1 Motivation.....	1
1.2 The Ideal Stirling Thermodynamic Cycle.....	3
1.2.1 Isochoric heat addition: 1 – 2.....	5
1.2.2 Isothermal expansion: 2 – 3.....	5
1.2.3 Isochoric heat rejections: 3 – 4.....	5
1.2.4 Isothermal compression: 4 – 1.....	5
1.2.5 Cycle Indicator Diagram.....	6
1.2.6 Limitations of the Ideal Thermodynamic Cycle.....	8
1.3 The Practical Stirling Engine.....	9
1.3.1 Components of a Gamma Stirling Engine.....	13
1.3.2 The Kinematic Gamma Stirling Engine.....	15
1.3.3 Piston and Displacer Motion and Phasing.....	16
1.3.4 Compression Ratio of LTD Stirling Engines.....	19
1.3.5 Buffer Pressure, Efficacious and Forced Work.....	20
1.3.6 Shaft Work and Shaft Power.....	22

1.3.7	Mechanism Effectiveness.....	23
1.4	Drive Mechanism Modifications in Pursuit of a More Ideal Thermodynamic Cycle	26
1.5	A Gamma Stirling Engine with Non-Circular Gearing.....	28
1.6	Thesis Objective and Structure.....	30
2	Performance Modeling	32
2.1	Isothermal Model of the Stirling engine.....	32
2.1.1	Model description	32
2.1.2	Model assumptions	33
2.1.3	Model Analysis and Equations	34
2.1.4	Model Implementation	37
2.2	Kinematics of Oval Non-Circular Gears	40
2.2.1	Ellipse Geometry	41
2.2.2	Kinematics of Mating Ellipses.....	43
2.2.3	Design of Oval Non-Circular Centroides	45
2.3	Results of the Isothermal Modeling.....	48
2.3.1	Baseline Conventional Motion Results	48
2.3.2	Displacer Dwelling.....	51
2.3.3	Piston Dwelling.....	55
2.3.4	Combined Displacer and Piston Dwelling.....	59
2.3.5	Triangle Displacer Motion with Dwelled Piston.....	63
2.4	Model Result Discussion and Limitations.....	69
3	Experimental Equipment and Instrumentation.....	70
3.1	The EP1-M LTD Gamma Stirling Engine	70
3.1.1	Engine Body Pressure Shell.....	71

3.1.2	Finned Tube Heat Exchangers & Regenerator.....	72
3.1.3	Elastomer Bellow Piston.....	74
3.1.4	Displacer and Crosshead	77
3.1.5	Drive Mechanism and Engine Brake	79
3.2	Modeling and Manufacture of Oval Gears	84
3.2.1	Modeling the Non-Circular Involute Gears	84
3.2.2	Manufacturing and Final Fitting of Gears	90
3.3	Working Space Volumes of the EP1-M.....	93
3.4	Operation and Support System.....	95
3.5	Engine Instrumentation and Data Acquisition	97
3.5.1	Source and Sink Temperature Measurements	98
3.5.2	Working Fluid Temperature	101
3.5.3	Engine and Pressure Measurements	104
3.5.4	Buffer pressure measurement.....	107
3.5.5	Output Shaft and Crankshaft Rotary Position.....	107
3.5.6	Output Torque	109
3.6	Data Acquisition System Details	110
3.6.1	Data Collection Rates.....	112
4	Experimental Procedures and Preliminary Testing.....	115
4.1	Preliminary Engine Testing	115
4.1.1	Source and Sink Temperature and Piston Stroke Optimization	116
4.1.2	Manufacture and Break-in of 3D Printed Non-Circular Gears	117
4.2	Engine Transient Testing	118
4.3	Bellow Volume Variation Calibration and Measurement	120
4.3.1	Volume Variation Calibration Experimental Setup.....	120

4.3.2	Volume Variation Experimental Procedure.....	122
4.3.3	Volume Variation Image Processing	123
4.3.4	Volume Variation Results	127
4.4	Testing Sequence	129
4.5	Steady State Engine Trial Procedures	131
4.5.1	Engine Start and Warm-up Procedure	131
4.5.2	Steady State Trials	133
5	Data Processing	135
5.1	Calculation of Uncertainties	135
5.2	Data Processing Methodology	137
5.2.1	Determination of Angular Positions	137
5.2.2	Thermocouple and RTD Data Alignment.....	139
5.2.3	Data Cropping to Complete Cycles	140
5.2.4	Determination of DP and PP Crankshaft Position	140
5.2.5	Determination of Engine Volume.....	141
5.2.6	Data Conversion.....	141
5.2.7	Data Organization and Averaging	142
5.3	Calculated Parameters	143
5.3.1	Calculation of Engine Speed	143
5.3.2	Calculation of Shaft Work and Shaft Power	144
5.3.3	Indicator Diagram Work Components	144
5.3.4	Estimation of Mechanism Effectiveness	145
5.3.5	Calculation of Heat Transfer rates and Engine Efficiency	146
5.3.6	Engine Efficiency and Global Losses	148
5.3.7	Recalculation of Isothermal Modeling Results.....	149

6	Evaluation Engine Performance	150
6.1	Result Plots Generation and Format.....	151
6.1.1	Test Group Trial Comparisons	151
6.1.2	Test Group Power and Torque Curves.....	154
6.1.3	Maximum Power Data Sets Results	155
6.1.4	Test Group Work Curves.....	158
6.2	Baseline Motion: Test Group 01.....	160
6.2.1	Indicator Diagram for Baseline Test	161
6.2.2	Indicator Diagram Trends for Baseline Test Group 01	162
6.3	Displacer Dwelling: Test Groups 02 and 10	165
6.3.1	Displacer Dwelling: Torque and Power Curves	166
6.3.2	Displacer Dwelling: Maximum Power Indicator Diagrams	167
6.3.3	Indicator Diagram Trends over Trials of the Displacer Dwelling Test Groups	169
6.3.4	Dwelled Displacer Conclusions	171
6.4	Piston Dwelling: Test Groups 06 and 07	172
6.4.1	Piston Dwelling: Torque and Power Curves	173
6.4.2	Piston Dwelling: Maximum Power Indicator Diagrams	174
6.4.3	Indicator Diagram Trends Over Trials of the Piston Dwelling Test Groups	177
6.4.4	Piston Dwelling Conclusions	179
6.5	Combined Displacer and Piston Dwelling: Test Groups 05 and 09.....	180
6.5.1	Combined Dwelling: Torque and Power Curves.....	181
6.5.2	Combine Dwelling: Maximum Power Indicator Diagrams	182
6.5.3	Indicator Diagram Trends Over Trials of the Combined Dwelling Test Groups	185

6.5.4	Combined Dwelling Conclusions	186
6.6	Triangle Displacer and Piston Dwelling: Test Groups 03, 04, and 08	187
6.6.1	Triangular Displacer Motion and Dwelled Piston: Torque and Power Curves	188
6.6.2	Triangular Displacer Motion and Dwelled Piston: Maximum Power Indicator Diagrams	190
6.6.3	Indicator Diagram Trends over Trials of the Triangular Displacer Motion and Dwelled Piston Test Groups	193
6.6.4	Triangular Displacer Motion and Dwelled Piston Conclusions	197
7	Evaluation of the Isothermal Model	198
7.1	Baseline Test Group 01	198
7.2	Piston Dwelling Test Group 07	203
7.3	Combined Dwelling Test Group 09	206
7.4	Discussion of the Utility of the Isothermal Model	209
8	Conclusions	210
	References	214
A	Uncertainty Equations	219
A.1	Random Uncertainty	220
A.2	Systematic Uncertainty	221
	Combined Standard Uncertainty for Measured Variables	222
A.3	Propagation of Uncertainty	222
B	Uncertainties and Calibrations of Measured Variables	224
B.1	Pump Calibration and Uncertainty	225
B.1.1	Calibration Details: 2020-12-10	225
B.2	RTD	227
B.2.1	Instrument Calibration: 2020-11-03	228

B.3	Thermocouple.....	229
B.3.1	Instrument Calibration: 2020-11-03.....	231
B.4	Piezoelectric Pressure Sensor.....	232
B.4.1	Instrument calibration.....	233
B.5	Diaphragm Pressure Transducer.....	235
B.5.1	Calibration: 2019-10-16.....	236
B.6	Output Shaft and Crankshaft Rotary Position.....	239
B.6.1	Gear backlash calibration.....	239
B.7	Torque Transducer.....	241
B.7.1	Calibration Details.....	241
B.8	Atmospheric Pressure.....	243
B.8.1	Calibration: 2020-08-17.....	243
C	Uncertainties of Calculated Variables.....	248
C.1	Engine Speed.....	249
C.2	Shaft work and Shaft Power.....	250
C.3	Indicated work.....	251
C.4	Mechanism Effectiveness Uncertainty.....	252
C.5	Heat Transfer Rates.....	254
C.6	Engine Efficiency and Global Losses Uncertainty.....	256
D	Data Collection Plan and Log.....	258
E	Data Processing Code.....	282
E.1	Isothermal Model Script.....	283
E.2	Oval Elliptical Gear Transmission and Derivative Function Script.....	289
E.3	Data Processing Script.....	292
E.4	Engine Volume Table Lookup Script.....	318

E.5	Encoder Position Array Generation Sub Function	321
E.6	Volume Variation Imagine Processing Script.....	325
F	Drawing Package	333

LIST OF TABLES

Table 2.1 –Preliminary isothermal modeling parameters for analysis of the EP1-M	39
Table 2.2 – Baseline isothermal modeling results	51
Table 2.3 – Displacer dwelling modeling results	54
Table 2.4 – Piston dwelling modeling results	58
Table 2.5 – Combined displacer and piston dwelling modeling results	62
Table 2.6 – Triangle displacer and dwelled piston modeling results	68
Table 3.1 – Heat exchanger properties	74
Table 3.2 – Regenerator properties.....	74
Table 3.3 – Piston properties	76
Table 3.4 – Displacer properties	77
Table 3.5 – Flywheel properties	82
Table 3.6 – Gear properties	89
Table 3.7 – Gear printing settings	91
Table 3.8 – EP1-M working fluid volume spaces.....	94
Table 3.9 – Heating and cooling loop specifications	96
Table 3.10 – Calibrated thermal fluid delivery rates for the hot source and the cold sink loops	96
Table 3.11 – Directly recorded engine parameters	97
Table 3.12 – RTD Sensor specifications	99
Table 3.13 – Processing and calibration data for RTDs	100
Table 3.14 – Thermocouple sensor specifications	102
Table 3.15 – Processing and calibration data for thermocouples.....	103
Table 3.16 – Pressure sensors specifications.....	104
Table 3.17 – Processing and calibration data for engine pressure sensors	106
Table 3.18 – Atmospheric pressure measurement device properties	107
Table 3.19 – Processing and calibration data for atmospheric pressure sensor	107
Table 3.20 – Crankshaft position measurement device properties.....	108
Table 3.21 – Engine output torque measurement device properties	109

Table 3.22 – Processing and calibration data for torque sensor	109
Table 3.23 – DAQ data collection properties	114
Table 4.1 – Test group trial sequence	129
Table 5.1 – Calculated engine parameters.....	143
Table 5.2 – Heat transfer variables and uncertainties	147
Table 6.1 – General experimental controlled variables for all test groups	150
Table 6.2 – Test conditions of baseline motion test group 01	160
Table 6.3 – Test group 01 maximum power data set values	162
Table 6.4 – Test conditions of displacer dwelling motion test group 02	165
Table 6.5 – Test conditions of displacer dwelling motion test group 10	165
Table 6.6 – Test group 02 maximum power data set values	168
Table 6.7 – Test group 10 maximum power data set values	169
Table 6.8 – Test conditions of piston dwelling motion test group 06	172
Table 6.9 – Test conditions of piston dwelling motion test group 07	172
Table 6.10 – Test group 06 maximum power data set values	176
Table 6.11 – Test group 07 maximum power data set values	176
Table 6.12 – Test conditions of combined displacer and piston dwelling motion test group 05.....	180
Table 6.13 – Test conditions of combined displacer and piston dwelling motion test group 09.....	180
Table 6.14 – Test group 05 maximum power data set values	184
Table 6.15 – Test group 09 maximum power data set values	184
Table 6.16 – Test conditions of combined displacer and piston dwelling motion test group 03.....	187
Table 6.17 – Test conditions of combined displacer and piston dwelling motion test group 04.....	187
Table 6.18 – Test conditions of combined displacer and piston dwelling motion test group 08.....	188
Table 6.19 – Test group 03 maximum power data set values	191
Table 6.20 – Test group 04 maximum power data set values	192
Table 6.21 – Test group 08 maximum power data set values	192

Table 7.1 – Changed isothermal model variables from results of test group 01	198
Table 7.2 – Test group 01 maximum power data set and updated model results	201
Table 7.3 – Changed isothermal model variables from results of test group 07	203
Table 7.4 – Test group 07 maximum power data set and updated model results	205
Table 7.5 – Changed isothermal model variables from results of test group 09	206
Table 7.6 – Test group 09 maximum power data set and updated model results	208

LIST OF FIGURES

Figure 1.1 – Simple schematic of the four thermodynamic processes that make up the ideal Stirling cycle comprised of: (a) isochoric heat addition, (b) isothermal expansion, (c) isochoric heat rejection, (d) and isothermal compression	4
Figure 1.2 – Thermodynamic processes of the Stirling cycle plotted on engine pressure-volume axis (clockwise from top left): (a) isochoric heat addition, (b) isothermal expansion, (c) isochoric heat rejection, (d) and isothermal compression	6
Figure 1.3 – Indicator diagram of an ideal Stirling cycle heat engine	8
Figure 1.4 – Simple schematic of an alpha type Stirling engine undergoing the ideal Stirling cycle (clockwise from top left): (a) isochoric heat addition, (b) isothermal expansion, (c) isochoric heat rejection, (d) and isothermal compression	10
Figure 1.5 – Simple schematic of a gamma Stirling engine undergoing the ideal Stirling cycle (clockwise from top left): (a) isochoric heat addition, (b) isothermal expansion, (c) isochoric heat rejection, (d) and isothermal compression	11
Figure 1.6 – Schematic of a gamma type Stirling engine incorporating additional engine components	13
Figure 1.7 – Partial section view of a simplified kinematic gamma type Stirling engine	16
Figure 1.8 – Displacement of gamma engine pistons (a) an ideal Stirling cycle and (b) the kinematic Stirling engine with harmonic slider-crank piston motion	17
Figure 1.9 – Comparison of the P-V indicator diagrams of an ideal Stirling cycle machine and the practical kinematic Stirling cycle machine.....	18
Figure 1.10 – Pressure volume indicator diagram showing (a) efficacious and forced work of expansion and (b) the efficacious and forced work of compression	21
Figure 1.11 – Indicator diagram depicting the components of indicated work and forced work	22
Figure 1.12 – Schematic of a gamma engine showing the energy flows through components of the engine drive mechanism (adapted from Senft [29])	24
Figure 1.13 – Conceptual embodiment of a gamma Stirling engine with a drive mechanism using non-circular gears.....	29

Figure 2.1 – Graphical representation of the isothermal model for a gamma Stirling engine showing the (a) working space volumes and (b) the prescribed temperature profile of the spaces	33
Figure 2.2 – Elliptical centrodes showing (a) basic geometry elements and (b) a mating pair of identical elliptical centrodes (modified from Litvin [51])	41
Figure 2.3 – Modified elliptical centrodes forming a mating pair (modified from Litvin [51]).....	44
Figure 2.4 – Derivative function results for the investigated oval non-circular centrode pairs	46
Figure 2.5 – Polar plot of the modified oval elliptical centrodes.....	47
Figure 2.6 – Model no. 1 baseline isothermal (a) indicator diagram and (b) pressure and volume curves	50
Figure 2.7 – Model no. 2: dwelled displacer $e = 1/5$ isothermal (a) indicator diagram and (b) pressure and volume curves.....	52
Figure 2.8 – Model no. 3: dwelled displacer $e = 1/3$ isothermal (a) indicator diagram and (b) pressure and volume curves.....	53
Figure 2.9 – Model no. 4: dwelled piston $e = 1/5$ isothermal (a) indicator diagram and (b) pressure and volume curves.....	56
Figure 2.10 – Model no. 5: dwelled piston $e = 1/3$ isothermal (a) indicator diagram and (b) pressure and volume curves.....	57
Figure 2.11 – Model no. 6: combined dwelled piston $e = 1/5$ and displacer $e = 1/5$ isothermal (a) indicator diagram and (b) pressure and volume curves	60
Figure 2.12 – Model no. 7: combined dwelled piston $e = 1/3$ and displacer $e = 1/3$ isothermal (a) indicator diagram and (b) pressure and volume curves	61
Figure 2.13 – Displacement profile of engine pistons for a displacer crankshaft phased $e = 1/5$ centrode and a conventional $e = 0$ centrode piston crankshaft	63
Figure 2.14 – Model no. 8: triangle displacer $e = 1/5$ and conventional piston $e = 0$ isothermal (a) indicator diagram and (b) pressure and volume curves	65
Figure 2.15 – Model no. 9: triangle displacer $e = 1/5$ and conventional piston $e = 1/5$ isothermal (a) indicator diagram and (b) pressure and volume curves	66

Figure 2.16 – Model no. 9: triangle displacer $e = 1/5$ and conventional piston $e = 1/3$ isothermal (a) indicator diagram and (b) pressure and volume curves	67
Figure 3.1 – Annotated partial section view of the EP1-M low temperature Stirling engine identifying key components	71
Figure 3.2 – Section view of the EP1-M engine body.....	72
Figure 3.3 – Annotated view of the EP1-M heat exchangers and regenerator stack.....	73
Figure 3.4 – Solid model of 3D printed regenerator section annotated with flow channel dimensions.....	74
Figure 3.5 – Partial section view of the solid model of the EP1-M elastomeric piston bellow and internal structures	75
Figure 3.6 – Piston crosshead, connecting rods, and piston crankshaft.....	76
Figure 3.7 – Partial section view of the displacer solid model	78
Figure 3.8 – Displacer crosshead, connecting rods, and piston crankshaft.....	79
Figure 3.9 – Profile view of the EP1-M engine drive mechanism and instrumentation output.....	80
Figure 3.10 – Explode view of the engine crankshaft mounting plate used for swapping out the crank shaft gear sets.(mounting plate shown transparent for clarity)	81
Figure 3.11 – Annotated view of flywheel and rotary encoder.....	82
Figure 3.12 – Annotated view of instrument plate and friction brake assembly.....	83
Figure 3.13 – Pressure angle plot for the complete rotation of a driving gear for the modified oval centrode pairs investigated	86
Figure 3.14 – Modified oval elliptical centrode of eccentricity $e = 1/3$ showing the minimum radius of curvature as determined from SOLIDWORKS	87
Figure 3.15 – Annotated view of Gearotic 3.06 user interface modeling a toothed oval $e = 1/3$ gear pair	89
Figure 3.16– Solid model of the $e = 15$ eccentric gear pair for the displacer crank.....	90
Figure 3.17 – Internal structure of the printed gears from a failed print.....	91
Figure 3.18 – Assortment of the final printed gears of (a) $e = 0$ centrode, (b) $e = 1/5$ centrode, and (c) $e = 1/3$ centrode.....	92
Figure 3.19 – Section view of EP1-M with colour coded working space volume areas .	93
Figure 3.20 – Schematic of engine instrumentation and data acquisition system	98

Figure 3.21 – Section view of RTD measurement location on EP1-M heat exchanger manifold	99
Figure 3.22 – Plot of RTD1 calibration curve and linear calibration constant	100
Figure 3.23 – Section view engine body showing the location of the expansion space thermocouple T0 and compression space thermocouple T1.....	101
Figure 3.24 – Plot of T0 calibration curve and linear calibration constant	103
Figure 3.25 – Section view engine body showing the location of the working fluid pressure sensors	104
Figure 3.26 – Plot of DP15 manometer calibration and linear calibration constant	106
Figure 3.27 – User interface of LabWindows CVI data capture program with annotations	111
Figure 3.28 – Sample of the first few rows of the acquired *.log file for the multi function I/O device.....	112
Figure 4.1 – Early 3D printed oval gear showing straight profile design and a detail view of the flared edge resulting from printing over extrusion	117
Figure 4.2 – Instantaneous engine speed recorded for a step change in engine loading	119
Figure 4.3 – Volume variation calibration trial setup showing the camera and EP1-M with the bellow profile as captured by the imaging camera	121
Figure 4.4 – Annotated section view of EP1-M piston with target arm and relevant dimensions.....	122
Figure 4.5 – Unprocessed pixel space calibration image from volume variation calibration.....	123
Figure 4.6 – Comparison of a (a) raw captured image and the (b) initial processed image with highly defined edges	124
Figure 4.7 – Annotated view of (a) cropping lines used on bellow image and (b) the cropped image of the bellow radii	125
Figure 4.8 – Fully processed (average, cropped, and inverted) pixel space radial profile of bellow (red bounding box added to establish full image size)	126
Figure 4.9 – Fitted curve of bellow external volume at each rotary encoder position for the volume variation calibration trial	128

Figure 5.1 – Visualization of rotary encoder discretizing and signal averaging scheme	138
Figure 5.2 – Visualization of thermocouple data to voltage data alignment and averaging scheme	140
Figure 6.1 – Test group 01 torque curves across trials	152
Figure 6.2 – Test group 01 power curves across trials.....	152
Figure 6.3 – Comparative torque curves for displacer dwelling test groups 02 and 10	154
Figure 6.4 – Comparative power curves for displacer dwelling test groups 02 and 10	155
Figure 6.5 – Example maximum power data set P-V indicator diagram.....	157
Figure 6.6 – Example maximum power data set Pressure and Volume curves plotted for a full engine cycle	157
Figure 6.7 – Example diagram of trends for indicator work components and mechanism effectiveness for trial	159
Figure 6.8 – Test group 01 maximum power data set P-V indicator diagram.....	161
Figure 6.9 – Test group 01 trial trends for indicator diagram work components and mechanism effectiveness.....	163
Figure 6.10 – Comparison of P-V indicator diagrams over the range of shaft work output for test group 01 maximum power trial.....	163
Figure 6.11 – Comparative torque curves for displacer dwelling test groups 02 and 10 and the baseline.....	166
Figure 6.12 – Comparative power curves for displacer dwelling test groups 02 and 10 and the baseline.....	167
Figure 6.13 – Maximum power data set P-V indicator diagrams for test group 02 and 10 compared to the baseline indicator diagram	168
Figure 6.14 – Test group 02 trends for indicator diagram work components and mechanism effectiveness.....	170
Figure 6.15 – Test group 10 trends for indicator diagram work components and mechanism effectiveness.....	170
Figure 6.16 – Comparative torque curves for piston dwelling test groups 06 and 07 and the baseline.....	173

Figure 6.17 – Comparative power curves for piston dwelling test groups 06 and 07 and the baseline.....	174
Figure 6.18 – Maximum power data set P-V indicator diagrams for test group 06 and 07 compared to the baseline indicator diagram	175
Figure 6.19 – Test group 06 trends for indicator diagram work components and mechanism effectiveness.....	177
Figure 6.20 – Test group 07 trends for indicator diagram work components and mechanism effectiveness.....	178
Figure 6.21 – Comparative torque curves for combined displacer and piston dwelling test groups 05 and 09 and the baseline	181
Figure 6.22 – Comparative power curves for combined displacer and piston dwelling test groups 05 and 09 and the baseline	182
Figure 6.23 – Maximum power data set P-V indicator diagrams for test group 05 and 09 compared to the baseline indicator diagram	183
Figure 6.24 – Test group 05 trends for indicator diagram work components and mechanism effectiveness.....	185
Figure 6.25 – Test group 09 trends for indicator diagram work components and mechanism effectiveness.....	186
Figure 6.26 – Comparative torque curves for triangular displacer motion and piston dwelling test groups 03, 04, 08, and the baseline	189
Figure 6.27 – Comparative power curves for triangular displacer motion and piston dwelling test groups 03, 04, 08, and the baseline	189
Figure 6.28 – Maximum power data set P-V indicator diagrams for test group 03, 04, and 08 compared to the baseline indicator diagram	190
Figure 6.29 – Test group 03 trends for indicator diagram work components and mechanism effectiveness.....	194
Figure 6.30 – Test group 04 trends for indicator diagram work components and mechanism effectiveness.....	194
Figure 6.31 – Test group 08 trends for indicator diagram work components and mechanism effectiveness.....	195

Figure 6.32 – Minimum shaft work data set P-V indicator diagrams for test group 03, 04, and 08 compared to the baseline indicator diagram	196
Figure 6.33 – Maximum shaft work data set P-V indicator diagrams for test group 03, 04, and 08 compared to the baseline indicator diagram.....	196
Figure 7.1 – Maximum power data set P-V indicator diagrams of experimental results and updated model for test group 01	199
Figure 7.2 – Maximum power data set P-V indicator diagrams of experimental results and updated model for test group 01	200
Figure 7.3 – Average instantaneous working space temperatures of the maximum power data set of test group 01.....	202
Figure 7.4 – Maximum power data set P-V indicator diagrams of experimental results and updated model for test group 07	204
Figure 7.5 – Maximum power data set P-V indicator diagrams of experimental results and updated model for test group 07	205
Figure 7.6 – Maximum power data set P-V indicator diagrams of experimental results and updated model for test group 09	207
Figure 7.7 – Maximum power data set P-V indicator diagrams of experimental results and updated model for test group 09	208

LIST OF SYMBOLS

Latin Alphabet Symbols and Abreviations

Variable	Description	Unit
A	Area	m^2
a	Ellipse major axis	-
B_x	elemental systematic / bias uncertainties of measurement x	various
b	Ellipse minor axis	-
BDC	Bottom dead center	
c	Foci distance	-
c_p	Specific heat capacity	$J/kg \cdot K$
ct	Centrode curve	-
CR	Compression ratio	-
d	Diameter	mm, in
E	Mechanism effectiveness	-
e	Ellipse eccentricity	-
FFF	Fused filament fabrication	-
f	Frequency	Hz
g	Gravity	m/s^2
h	Height	mm or m
I	Contact ratio	-
J	Contact point between gears	-
k_{21}	Derivative function for mating centrodes 2 and 1	-
L	Gear center to center distance	in
l	Length	mm or m
LTD	Low temperature differential	-
M	Measurement signal value	V
m	Mass	g or kg
N	Tooth number	-
n	Number of samples / sources	-
P	Pressure	Pa

p_d	Diametral pitch	in^{-1}
p_s	Shaft power	W
Q	Heat transfer or energy flow	J
R_x	Precision / random uncertainty of calculated mean x	various
r	Radius	mm, in
S_x	Standard deviation of mean x	various
T	Temperature	$^{\circ}\text{C}$ or K
t	Time	s
TDC	Top dead center	-
$t_{\frac{\alpha}{2}, \nu}$	Student's two tail t-score of a normally distributed sample with a confidence interval of $1-\alpha$ and ν degrees of freedom	-
u	Uncertainty	various
V	Volume	m^3 or L
W	Work	J
w	Elliptical gear modification factor	-
x	Generic variable	-
y	Generic variable	-

Greek Alphabet Variables

Variable	Description	Unit
α	Phase angle	$^{\circ}$ or rad
θ	Angles	$^{\circ}$ or rad
η	Efficiency	-
τ	Torque	N·m
φ_n	Polar angle relative to centrode origin	$^{\circ}$ or rad
φ_c	Rack cutter angle	$^{\circ}$ or rad
φ_{pa}	Pressure angle	$^{\circ}$ or rad
φ_t	Centrode tangent angle	$^{\circ}$ or rad
ω	Angular velocity	rad/s, RPM

1 INTRODUCTION

This introduction provides context to this work investigating the performance of modifications to the drive mechanism of an experimental low temperature differential (LTD) gamma type Stirling engine. Relevant background regarding the motivation behind the investigation is provided along with a brief summary of the relevant science of Stirling engines and their method of operation. This includes a review of pertinent literature on the subjects discussed. The final portion of this introduction describes the objective of the investigation and the layout of the remainder of the document.

1.1 Motivation

The Sixth Assessment Report of the Intergovernmental Panel on Climate Change (IPCC) [1] has highlighted the urgent need to limit the cumulative CO₂ equivalent emissions from anthropogenic sources to mitigate harms resulting from global warming. These warnings come amid a backdrop of growing global energy demand, with worldwide electricity demand predicted to rise 4.5% in 2021 [2]. Despite advances in proportions of renewable generation, fossil fuels made up 64% [3] of electricity generation in 2019, and consumption continues to grow to meet new demand [2]. 91% of Alberta's electricity generation is fueled by fossil fuels [4], and the sector accounted for 44.3 MT CO₂ equivalent emissions in 2017, equivalent to 60% of Canada's total emissions from power generation.

Amidst this growing energy demand and concerns regarding generation emissions there has been strong growth in renewable electrical generating capacity, rising globally by 35% in 2020 [2]. Historically, and up to the present day, Stirling engines have been investigated and used as means of producing power from renewable energy sources. Being an externally heated engine technology, Stirling engines have been adapted to produce power from a vast array of zero-emission thermal sources that include: nuclear and radio isotopes [5][6], solar radiation [7][8], biomass [9], geothermal sources [10], and waste heat [11] including cryogenic waste heat [12]. The appeal of Stirling engines as renewable thermal energy conversion machines is their easy adaptation to

distributed generation [13][5], use of a variety of thermal sources, and scalability to small sizes [14] where other heat engine types like organic Rankine cycles become uneconomical [15].

An area of increasing interest for Stirling engines is the development of designs capable of exploiting so-called low temperature differential (LTD) heat sources. [16]. A review by Wang et al. [11] investigated Stirling engines designed to recover low and moderate temperature heat characterized to be low temperature differential engines as operating below 250 °C. The exact threshold for what a low temperature differential in terms of Stirling engines is not defined, but many self described low temperature engines operate below 100 °C [11]. Engines within this range have been explored for development of low-temperature solar applications [17].

The research group that the author is a part of has been focused on research into LTD Stirling engines to produce power from low temperature heat sources. Many such heat sources are abundant in Alberta and include geothermal resources [18][19] and industrial waste heat [16]. The challenge lies in designing LTD Stirling engines that are sufficiently powerful, reliable, and cost effective to economically contribute to zero-emission electricity generation.

1.2 The Ideal Stirling Thermodynamic Cycle

The academic description of the Stirling thermodynamic cycle [20] is a closed loop cycle that has four repeated processes: isochoric heat addition, isothermal expansion, isochoric heat rejection, and isothermal compression. Some characteristics that are typically present in an engine making use of the Stirling cycle [21] are noted below:

- A sealed working space where the volume can change.
- A charge of working fluid contained in working space that can be expanded and compressed.
- An external source of thermal energy that may be transferred to the working fluid through the boundaries of the working space.
- An external thermal sink to which heat may be rejected from the working fluid through the boundaries of the working space.

A simple conceptualization of a Stirling cycle device is shown in Figure 1.1 undergoing the Stirling cycle thermodynamic processes. The conceptualization is a rigid cylinder with a piston forming the working space of the engine and sealing in an ideal gas working fluid. The walls of the cylinder are assumed to be perfectly conducting.

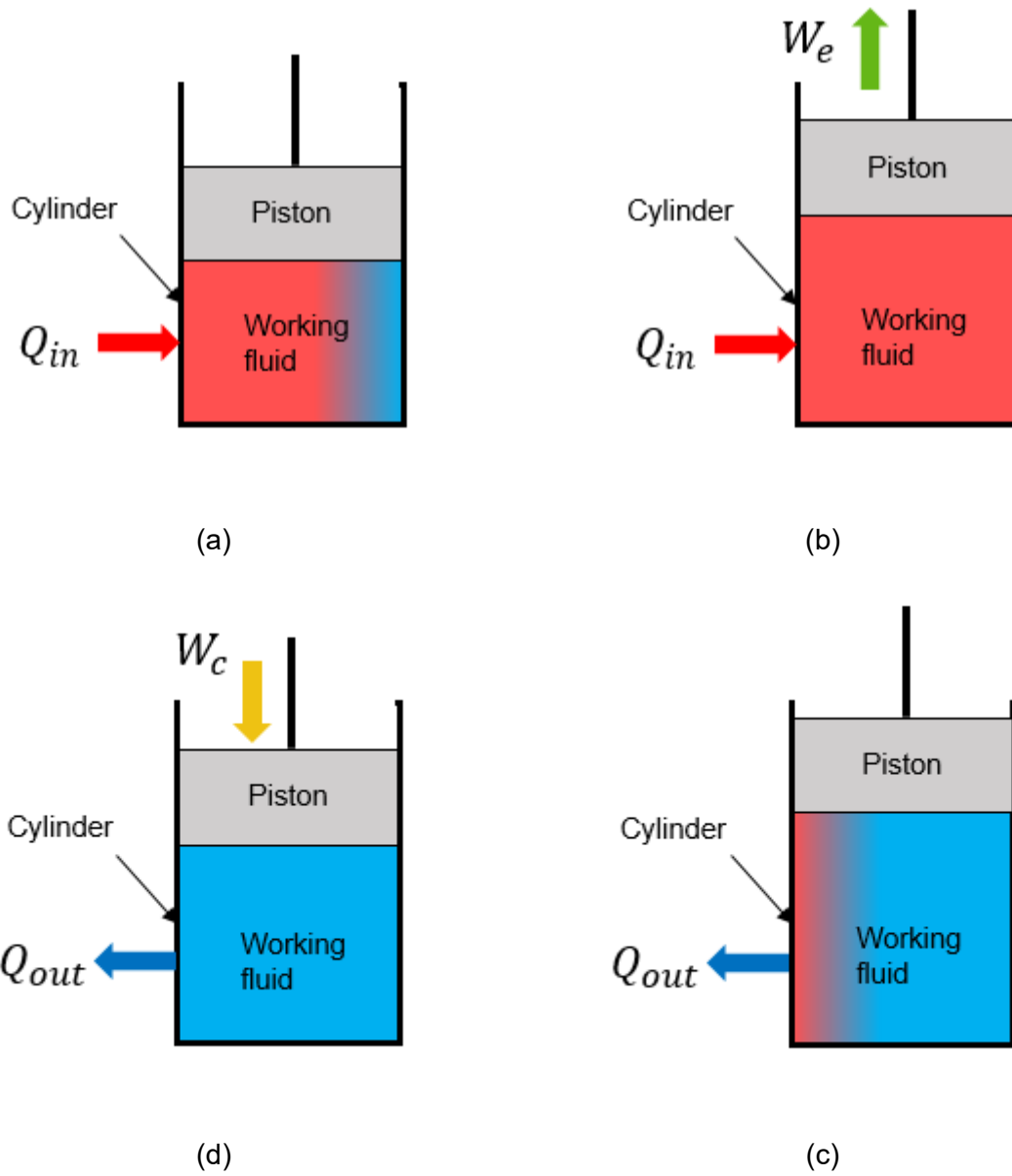


Figure 1.1 – Simple schematic of the four thermodynamic processes that make up the ideal Stirling cycle comprised of: (a) isochoric heat addition, (b) isothermal expansion, (c) isochoric heat rejection, (d) and isothermal compression

1.2.1 Isochoric heat addition: 1 – 2

The engine working space is held at its minimum volume (V_{min}) while heat is transferred to the working fluid through the boundaries of the working space. The working fluid starts the process at the thermal sink temperature (T_{Sink}), and rises to the thermal source temperature (T_{Source}). As the volume of the working fluid is constrained, the pressure of the working fluid increases from P_1 to P_2 as:

$$P_2 = P_1 \cdot \frac{T_{Source}}{T_{Sink}} \quad 1.1$$

1.2.2 Isothermal expansion: 2 – 3

The working space expands from a minimum volume of (V_{min}) to a maximum volume of (V_{max}) while heat is transferred to maintain the working fluid at the thermal source temperature (T_{Source}). The pressure of the working fluid drives the volume change by moving the piston of the working space, and pressure drops from P_2 to P_3 as:

$$P_3 = P_2 \cdot \frac{V_{min}}{V_{max}} \quad 1.2$$

1.2.3 Isochoric heat rejections: 3 – 4

The working space is held at its maximum volume (V_{max}) while heat is rejected from the working fluid through the boundaries of the working space. The working fluid starts the process at the thermal source temperature (T_{Source}), and drops to the thermal sink temperature (T_{Sink}). As the volume of the working fluid is constrained, the pressure of the pressure of working fluid drops from P_3 to P_4 as:

$$P_4 = P_3 \cdot \frac{T_{Sink}}{T_{Source}} \quad 1.3$$

1.2.4 Isothermal compression: 4 – 1

The working space compresses from a maximum volume (V_{max}) to a minimum volume (V_{min}) while heat is removed to maintain the working fluid at the thermal sink temperature (T_{Sink}). Outside work changes the volume of the working space by acting on the piston of the working space, and pressure drops from P_4 to P_1 as:

$$P_1 = P_4 \cdot \frac{V_{max}}{V_{min}} \quad 1.4$$

1.2.5 Cycle Indicator Diagram

Figure 1.2 shows the individual thermodynamic processes of the Stirling cycle plotted on a pressure and volume axis. The areas on the P-V diagram show areas of work done by, and to, the device [22].

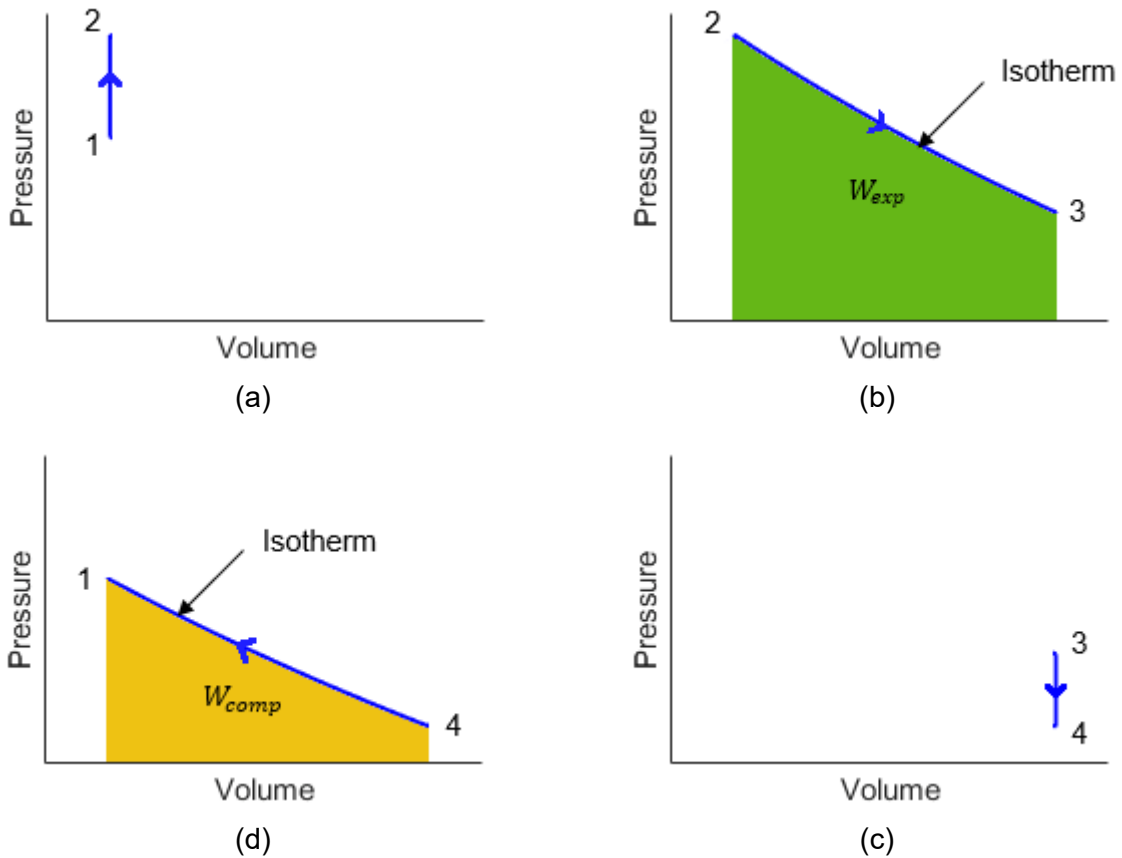


Figure 1.2 – Thermodynamic processes of the Stirling cycle plotted on engine pressure-volume axis (clockwise from top left): (a) isochoric heat addition, (b) isothermal expansion, (c) isochoric heat rejection, (d) and isothermal compression

The expansion work is the work done by the engine working fluid on the engine surroundings during expansion. Graphically, it is described as the area under the upper portion of the curve as shown in Figure 1.2 (b). It is mathematically described by the following:

$$W_{exp} = \int_{V_{min}}^{V_{max}} P_{exp} \cdot dV \quad 1.5$$

where: W_{exp} = absolute expansion work [J]
 V_{max} = maximum engine volume [m³]
 V_{min} = minimum engine volume [m³]
 P_{exp} = engine pressure during expansion [Pa]
 V = engine volume [m³]

The area under the lower section of the curve meanwhile is the compression work, or work done on the engine working fluid by the engine surroundings as shown in Figure 1.2(d). It is described by the following:

$$W_{comp} = \int_{V_{max}}^{V_{min}} P_{comp} \cdot dV \quad 1.6$$

where: W_{comp} = absolute compression work [J]
 V_{min} = Minimum engine volume [m³]
 V_{max} = Maximum engine volume [m³]
 P_{comp} = Engine pressure during expansion [Pa]
 V = Engine volume [m³]

Combining the P-V plots of Figure 1.2 and forming them into a cycle produces the P-V indicator diagram for the engine. The indicated work (W_{ind}) is the area enclosed by the P-V curve, and is thus of net of the expansion work and compression work:

$$W_{ind} = W_{exp} - W_{comp} \quad 1.7$$

This indicated work is the net work delivered by the engine with each cycle, and is shown on the P-V indicator diagram in Figure 1.3.

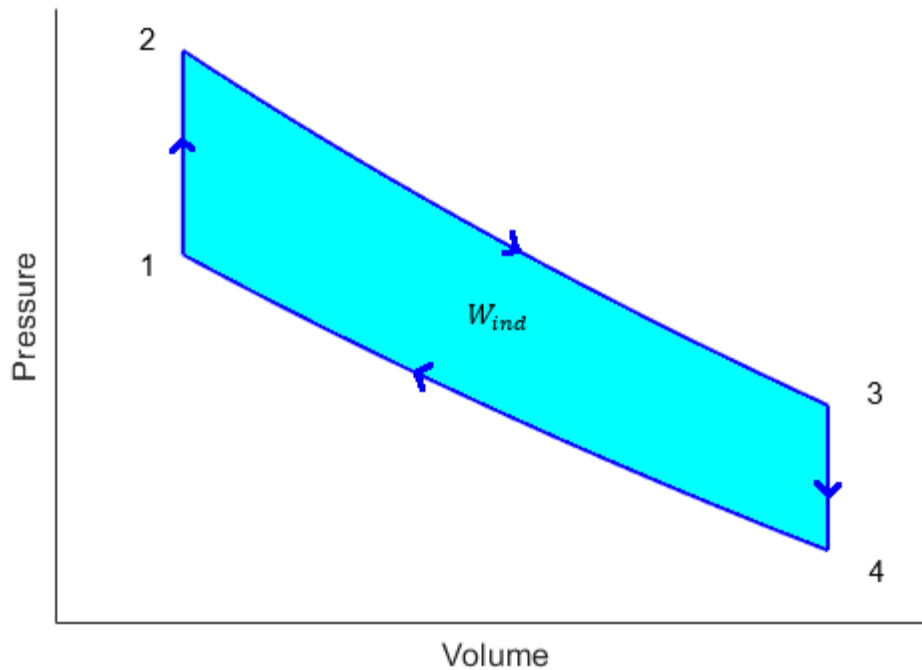


Figure 1.3 – Indicator diagram of an ideal Stirling cycle heat engine

1.2.6 Limitations of the Ideal Thermodynamic Cycle

There are limitations with the academic model of the Stirling engine that would be encountered in a real-world implementation of a device as depicted in Figure 1.1. Any real material from which a rigid pressure containing vessel could be made would not be capable of instantaneous heat transfer. Likewise, the working fluid itself would not be able to conduct heat instantaneously and uniformly unless given sufficient time. Given that power is the product of work multiplied by the frequency of cycles, it is generally in the interest of designers to produce an engine that cycles as fast as possible. As such the volume inside the cylinder is often better described as adiabatic [23] or polytropic [22] when undertaking detailed analysis the engines. However, for the purposes of preliminary analysis, use of the isothermal assumption allows for a quick analysis to explore the many variables of engine development, and later analysis be done with more advanced modeling techniques. Further limitations regarding the practical implementation of the academic cycle are discussed in the following section.

1.3 The Practical Stirling Engine

The single piston and cylinder model used to describe the ideal Stirling cycle in section 0 is suitable for an academic understanding. The assumptions inherent to that model also make it a highly impractical engine. The assumption of an infinitely conducting vessel, with no thermal heat capacity itself, which is able to respond instantly to the heat addition and rejection phases of the cycle is very problematic to design. Also, as was noted in section 1.2.6, the desire to complete as many cycles as possible to produce power requires engine design that permits efficient heat addition and rejection to the working fluid through the boundaries of the engine working space.

Implementations the Stirling cycle separate the heat addition space from the heat rejection space. The simplest implementation conceptually presented by Walker [21] is to add a through bore to the cylinder and add an additional piston on the opposite end of the engine. The working space, bounded by both pistons, is then free to move in the engine as seen in Figure 1.4. Any arrangement of engine where two pistons form two boundaries of the working space is categorized as an alpha type Stirling engine [23]. For the isochoric heat addition process both pistons move in unison, maintaining a constant volume working space, and the working fluid moves from the heat rejection side of the engine to the heat addition side. The piston bounding the engine on the heat addition side expands during the isothermal expansion process. After expansion both pistons again move in unison, transferring the working fluid back to the heat rejection side of the engine. Finally, the fluid is compressed by the compression piston. A static dividing line can be added to the engine working space. The portion of the total working space in which the working fluid has heat added, and is expanded, is called the expansion space. The portion of the total working space in which the working fluid has heat rejected, and is compressed, is called the compression space.

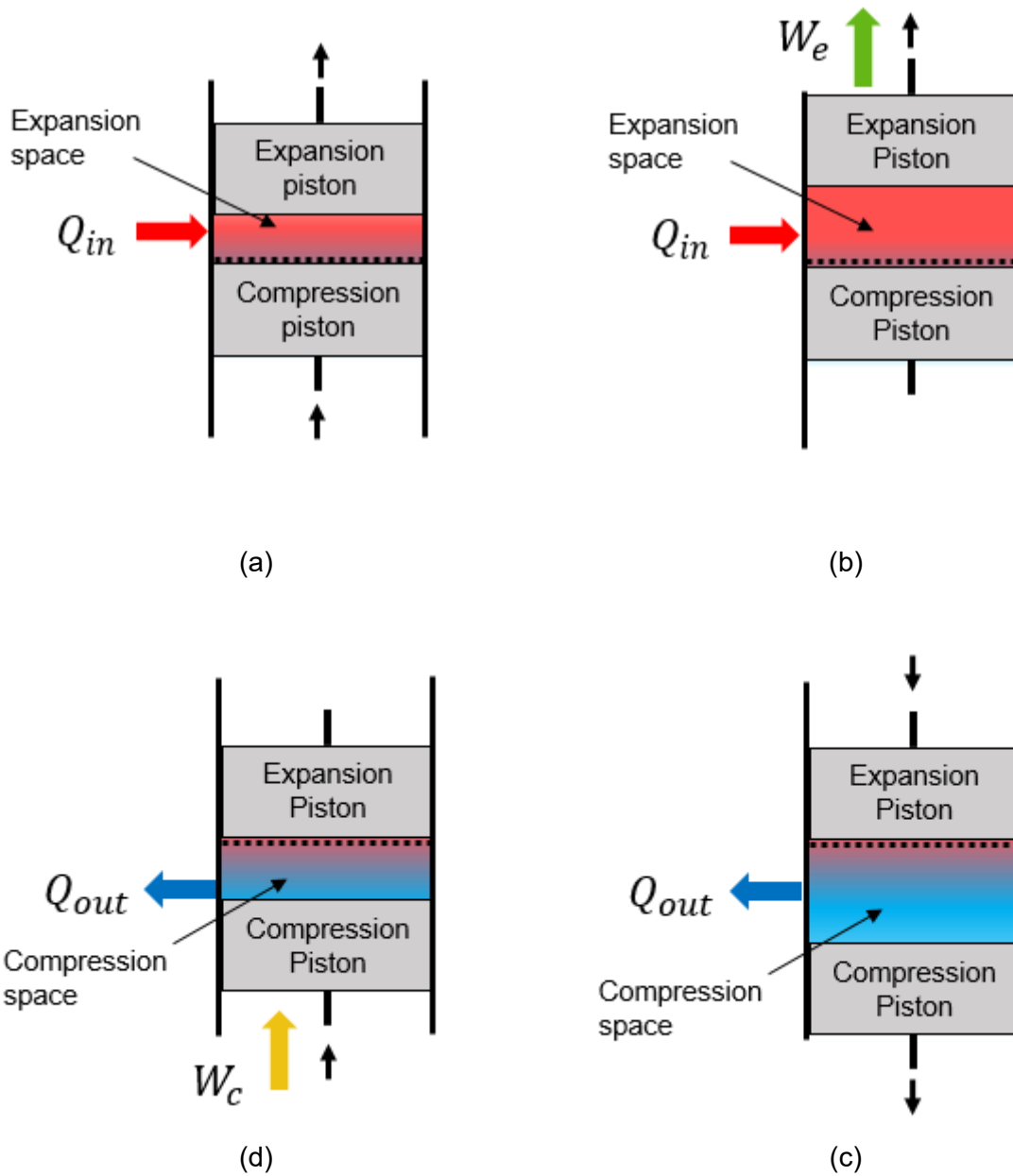


Figure 1.4 – Simple schematic of an alpha type Stirling engine undergoing the ideal Stirling cycle (clockwise from top left): (a) isochoric heat addition, (b) isothermal expansion, (c) isochoric heat rejection, (d) and isothermal compression

The other two principal configurations of Stirling engine are the beta and gamma types. A conceptual gamma type Stirling engine is shown in Figure 1.5 undergoing the thermodynamic processes of the Stirling cycle. In both the gamma and beta type engines the task of moving the working fluid between the expansion space and compression space, and the task of changing the volume of the engine working is split

between two dedicated pistons: the displacer piston and the power piston [23]. Throughout the remainder of this work the displacer piston will be referred to as the displacer, while the power piston will be referred to as the piston. Pistons will refer to both the displacer and the piston together.

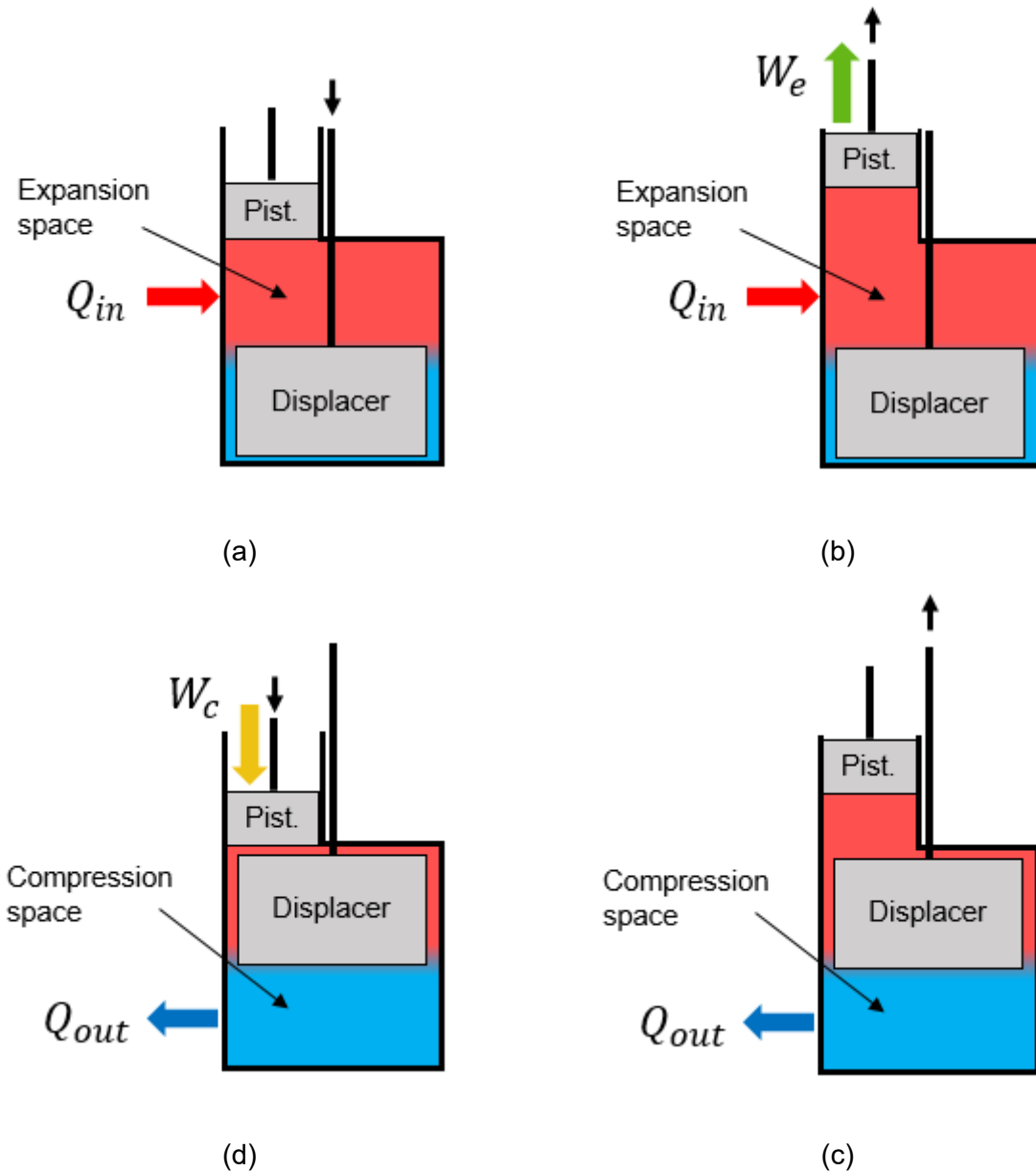


Figure 1.5 – Simple schematic of a gamma Stirling engine undergoing the ideal Stirling cycle (clockwise from top left): (a) isochoric heat addition, (b) isothermal expansion, (c) isochoric heat rejection, (d) and isothermal compression

The displacer is an incompressible structure located within the working space of the engine that moves between the expansion space and the compression space. The working fluid is displaced by the displacer and occupies the working space opposite of the displacer location. The displacer does no work as the volume of the working space is not changed by its motion, with the small exception of the displacer rod if present.

The piston is responsible for changes in the working space volume, doing work on the engine surroundings, or having work done on it. All working spaces of the engine are interconnected and engine pressure change can influence the piston regardless if it is coupled to the expansion or the compression spaces. The piston forms part of the expansion space of the engine modeled in Figure 1.5.

The distinguishing feature between beta and gamma type engines is that for gamma engines, the two pistons exist in separate cylinders that do not overlap. For beta type engines the piston and displacer exist in the same cylinder bore and may overlap displacements [23]. From interpretation of the original patent for the Stirling cycle engine filed by Robert Stirling [24],[25],[26] the first conception of a Stirling engine was a beta type. This investigation concerns an experimental gamma type engine.

1.3.1 Components of a Gamma Stirling Engine

Persons familiar with small demonstration Stirling engines, so-called “coffee-cup” engines [27], will find the layout of the conceptual engine depicted in Figure 1.5 to be familiar. A gamma type engine in the configuration shown in Figure 1.5 is one of the simplest functional embodiments of a physical engine operating by the Stirling cycle.

For larger engines additional components are typically incorporated into designs to improve performance. These additions include:

- Expansion and compression space heat exchangers
- A regenerator
- A mechanism

A schematic of a simplified gamma engine with these additional features is shown in Figure 1.6.

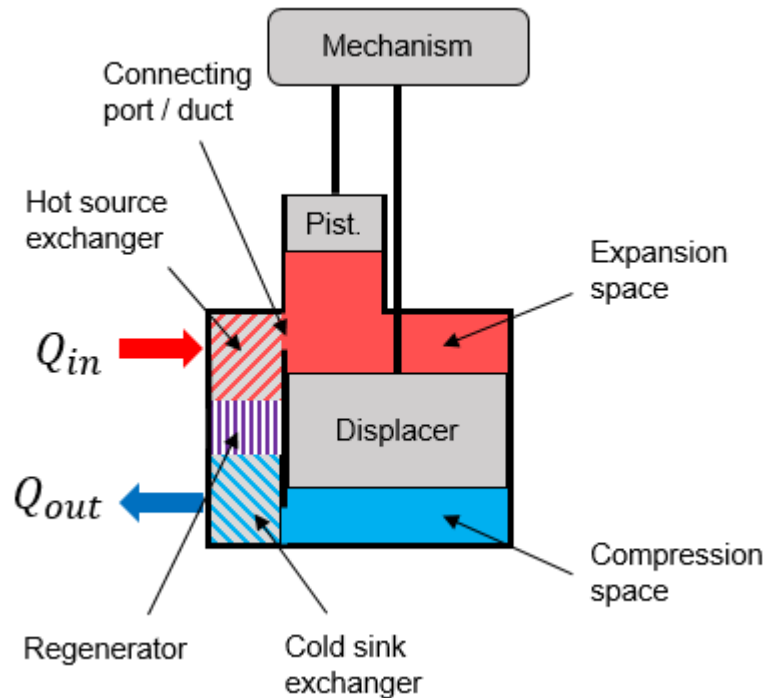


Figure 1.6 – Schematic of a gamma type Stirling engine incorporating additional engine components

1.3.1.1 Heater or Hot Source Exchanger

Heat exchangers of some variety are often incorporated into the working space of the engine with the aim of improving heat transfer to the engine working fluid while moving to, or while inside, the expansion space. As engines grow in size, the surface area of the working space boundaries of the engine do not scale at the same rate as the contained volume of working fluid in the engine. The hot source heat exchanger improves the heat transfer to the working fluid by increasing the heat transfer surface area. External to the engine working space the heater also typically improves heat transfer to the engine from the thermal source. The heat exchanger often resides in the flow path that unites the compression space to the expansion space on either side of the displacer.

1.3.1.2 Cooler or Cold Sink Exchanger

The cold sink heat exchanger improves heat rejection from the engine working fluid to the thermal sink. The exchanger is the counterpart to the hot source exchanger and is located in or is adjacent to the compression space of the engine. The two exchangers may have different sizes or designs depending on the design of the engine and the anticipated thermal sink.

1.3.1.3 Regenerator

The regenerator, also called the economizer [24],[25] in the original Stirling patents is a component that is characteristic of a Stirling engine [22]. It serves the function of a thermal battery that absorbs heat from passing working fluid as it is cycled from the expansion space to the compression space as part of the isochoric heat rejection process. The regenerator then releases the stored heat to the passing working fluid as it cycles back to the expansion space from the compression space during the isochoric heat transfer process. The regenerator is critical to engine efficiency and reduces the heat transfer requirements of the engine heat exchangers. The ideal regenerator has a high heat capacity, high surface area, and low thermal conductivity [28].

1.3.1.4 Mechanism

A mechanism is present to extract the work from the engine and coordinate the engine pistons to carry out the Stirling cycle. The Mechanism has important implications regarding the thermodynamic performance of the engine and is discussed in greater detail in the following section

1.3.2 The Kinematic Gamma Stirling Engine

Engines can be further distinguished by the means by which the engine piston and displacer are controlled and extract work from the engine. This investigation focuses on cyclic kinematic engines [29], also called reciprocating engines, where there is some form of mechanism that constrains the engine pistons and links them together and to the engine output. Other designs of Stirling cycle engines do not employ a traditional mechanism. These include free-piston engines [30][31] where the engine pistons move in sequence under influences of the cycle pressure and harmonics of springs. A hybrid design of kinematic engines and free piston engines is the Ringbom [32] design that has a free piston displacer and a kinematic piston producing rotational engine output. Another variety of the free-piston engines is the liquid piston Fluidyne Stirling engine [33][34] which replaces the displacer with an oscillating column of fluid, and a piston consisting of a free water surface that converts the cycle pressure swings into hydrostatic head. More recently Stirling cycle thermoacoustic engines [35][36] have been developed that use acoustic waves inside the engine to displace the working fluid between the hot and cold ends of the engine. Thermoacoustic engines recover cycle work via small displacement diaphragms acting as a power piston.

In a kinematic gamma type engine the motion of the engine piston and displacer is controlled and coordinated by a mechanical drive mechanism, and this mechanism converts the engine work into the desired output work form. For most engines this is rotational motion of a shaft. The linear motion of the engine piston and displacer is predominantly converted to rotational motion of the output crankshaft via a variety of slider-crank mechanism. A schematic of a kinematic gamma type Stirling engine is shown in Figure 1.7. The engine features a crankshaft driving the engine pistons with a simple slider-crank mechanism. A flywheel is coupled the crankshaft and serves to

smooth the work output of the engine from the intermittent positive work of the piston, and acts as a mechanical battery to provide energy for the compression work segments of the cycle.

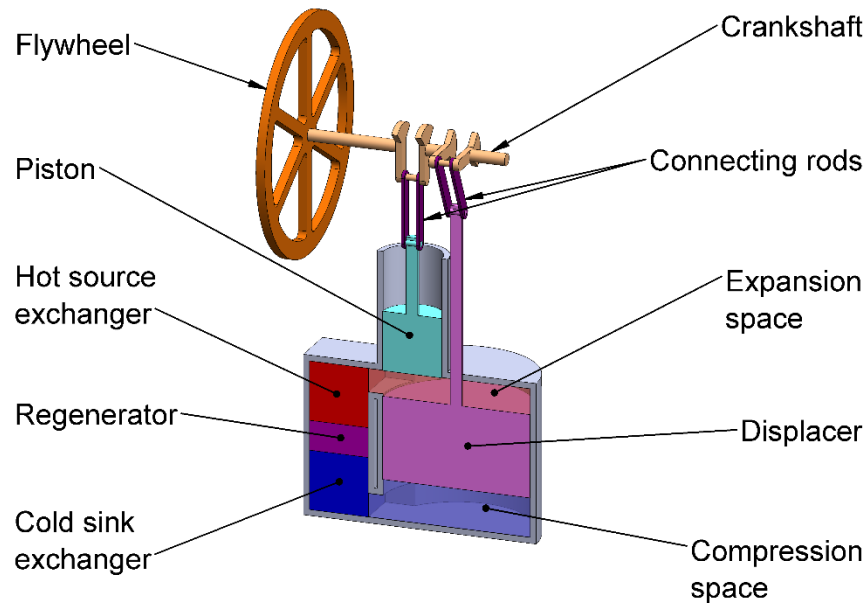
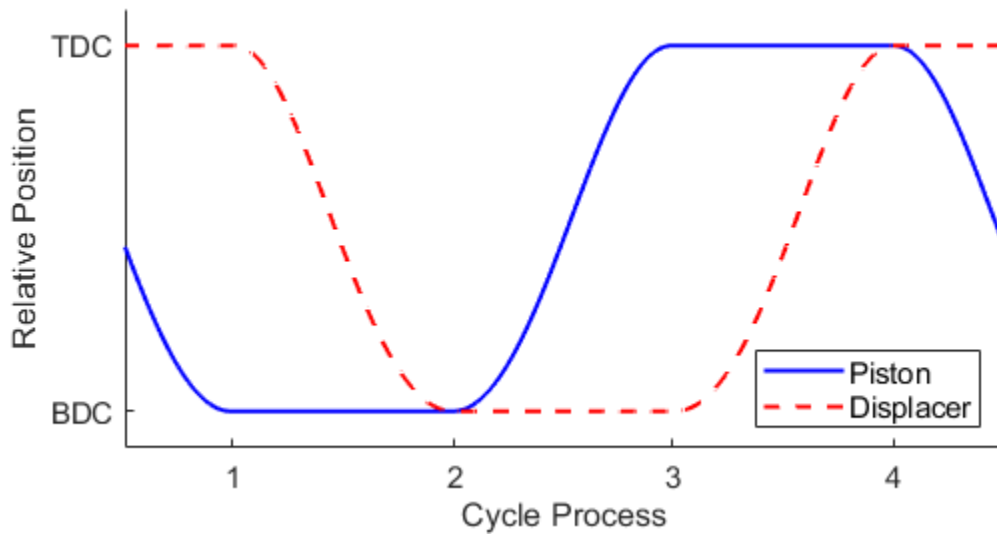


Figure 1.7 – Partial section view of a simplified kinematic gamma type Stirling engine

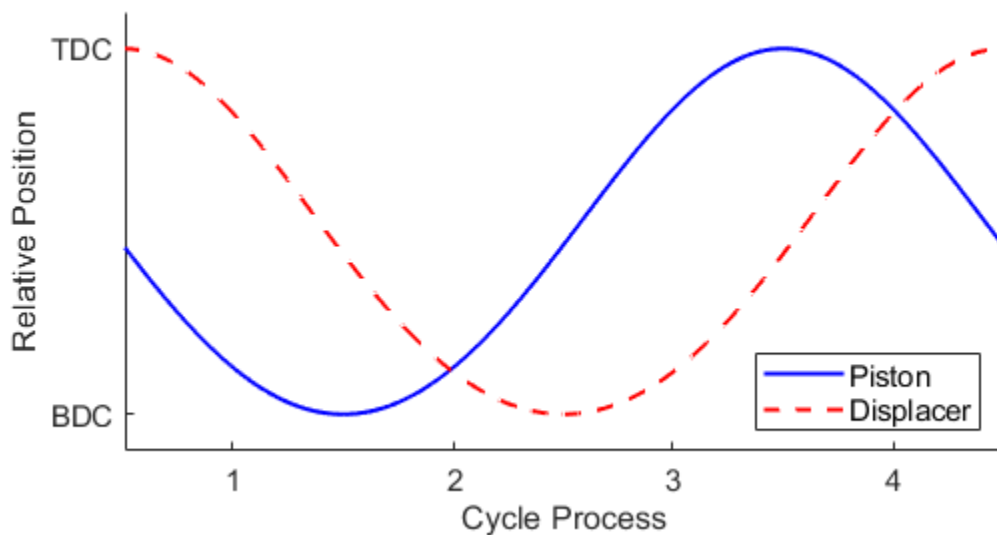
1.3.3 Piston and Displacer Motion and Phasing

Thermodynamic processes of the Stirling cycle in a practical engine are characterized by the controlled movements of the working fluid and volume boundary of the working space. To undertake the ideal Stirling cycle as described in section 0 in a practical gamma engine as configured in Figure 1.6, the movement of the displacer and piston need to occur in sequential steps from as depicted in Figure 1.8 (a). The motion profiles show the displacement of the pistons from their top dead center (TDC) positions to their bottom dead center (BDC) positions. In a kinematic gamma engine, with motion of the piston and displacer constrained by slider-crank mechanisms as depicted in Figure 1.7, the movements of the pistons is continuous. With the appropriate phasing of crank arms the piston and displacer motion profiles will effect the processes of the

Stirling thermodynamics cycle as shown in Figure 1.8 (b). The movements of the piston and displacer are a quarter cycle out of phase with one another, or 90° out of phase in the framework of a 360° rotation of the crankshaft. This phase difference between the displacer and the piston is known as the phase angle (α) of a Stirling engine. For LTD gamma engines, a phase angle of $\alpha \approx 90^\circ$ results in the theoretical maximum indicated work for a cycle [37][38] .



(a)



(b)

Figure 1.8 – Displacement of gamma engine pistons (a) an ideal Stirling cycle and (b) the kinematic Stirling engine with harmonic slider-crank piston motion

When comparing the ideal displacement profiles depicted in Figure 1.8(a) to those of the kinematic engine shown in Figure 1.8(b) it can be observed that the kinematic engine has substantial motion overlap between the displacer and piston. The motion overlap results in overlap of thermodynamic sequences of the Stirling cycle. The result is that the indicator diagram for the practical engine has a much more rounded curve when compared to the ideal cycle with fully discontinuous motion. A comparison between the ideal and the practical cycle indicator diagrams under the same engine conditions is shown in Figure 1.9. The reduced area of the practical cycle represents lost work potential per cycle of the engine that could be achievable under an engine operating with the fully discrete piston motion depicted in Figure 1.8(a).

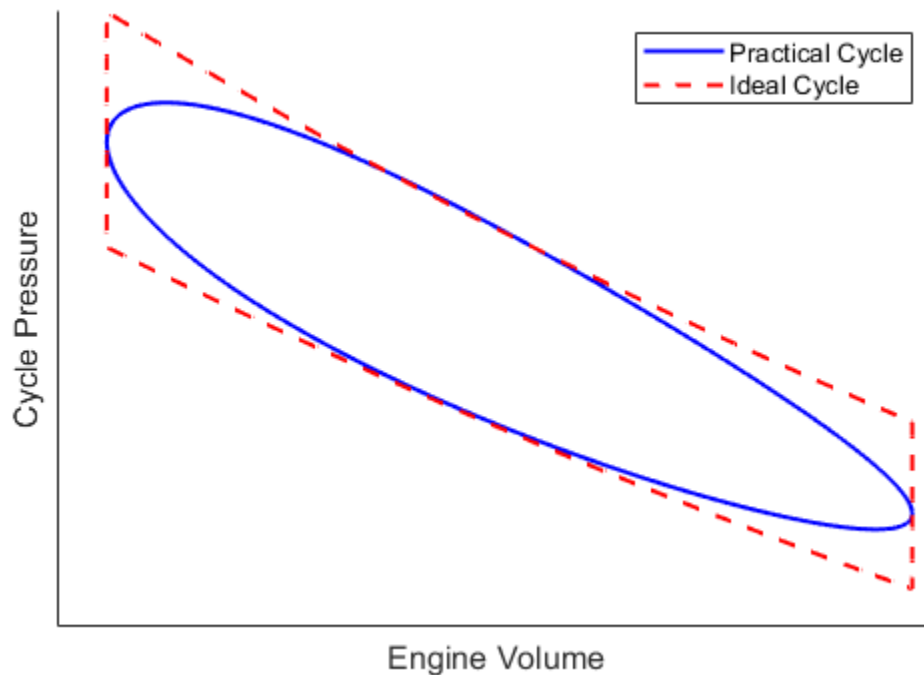


Figure 1.9 – Comparison of the P-V indicator diagrams of an ideal Stirling cycle machine and the practical kinematic Stirling cycle machine

1.3.4 Compression Ratio of LTD Stirling Engines

Most LTD Stirling engines are gamma types [11]. Egas and Clucas [39] note that the gamma configuration has inherent advantages in achieving low engine compression ratios (CR) that are ideal low temperature differential operation. Compression ratio is:

$$CR = \frac{V_{max}}{V_{min}} \quad 1.8$$

where: V_{max} = maximum engine volume [m³]
 V_{min} = minimum engine volume [m³]

This advantage of gamma engines with regards to compression ratio comes from separating the functions of working fluid movement and engine volume variation between the displacer and piston respectively. The separation allows great flexibility in selecting piston diameters and strokes of both pistons independently to optimize compression ratio.

The upper bound of compression ratio for an ideal Stirling cycle machine is described by Egas and Clucas [39] as equivalent to the temperature ratio between the thermal source (T_{Source}) and thermal sink (T_{Sink}):

$$CR_{ideal} = \frac{T_{Source}}{T_{Sink}} \quad 1.9$$

where: T_{Source} = thermal source temperature [K]
 T_{Sink} = thermal sink temperature [K]

Ivo Kolin's [26] empirical work on LTD Stirling engines led to the development of an empirically determined optimum engine compression ratio:

$$CR_{Kolin} = 1 + \frac{T_{Source} - T_{Sink}}{1100} \quad 1.10$$

Prior work by Stumpf [40], working within the same research group as the author, optimized the compression ratio for a LTD gamma engine working between a thermal source of 95 °C and a thermal sink of 2 °C. Stumpf [40] developed an expression for optimum compression ratio between the values of Kolin and that of Egas and Clucas as:

$$CR = 0.624 \frac{T_H}{T_C} + 0.376 \quad 1.11$$

1.3.5 Buffer Pressure, Efficacious and Forced Work

For the piston to move and produce work a differential pressure must exist between the engine working fluid on the internal face of the piston, and the surrounding fluid on the external face of the piston. Pressure from the surrounding fluid is termed buffer pressure (P_b). For engines without enclosed or pressurized crank cases, the buffer pressure is the atmospheric pressure surrounding the engine, and can be considered to be constant. Buffer pressure has an important influence on the calculation of the indicated work, and as will be discussed in subsequent sections, effects the mechanical efficiency of the engine as described in the work of Senft [29]. For engines operating at cycle pressures entirely above the buffer pressure, calculation of indicated work is as described in section 1.2.5.

If the buffer pressure is between the minimum and maximum pressures of the engine cycle, the portions of the cycle that contribute to positive and negative work are altered. As shown in Figure 1.10, portions of the expansion and compression stroke end up acting against the pressure differential that existed when the stroke began. The portion of the cycle where the work space is expanding and producing positive work, is termed efficacious expansion work [29]. Conversely, the portion of expansion that produces negative work is termed expansion forced work [29]. Similarly, for the compression portion of the cycle, positive work segments are termed efficacious compression work, and negative segments are termed compression forced work.

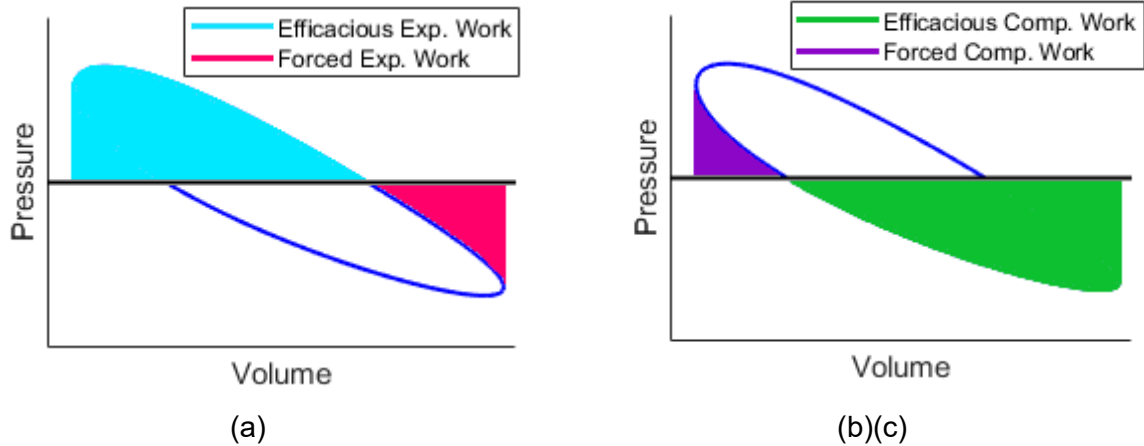


Figure 1.10 – Pressure volume indicator diagram showing (a) efficacious and forced work of expansion and (b) the efficacious and forced work of compression

These segments are conceptualized mathematically by the following equations:

$$\int_{V_{min}}^{V_{max}} P_{exp} \cdot dV = \begin{cases} W_{eff}, & P_{exp} > 0 \\ W_{FW}, & P_{exp} < 0 \end{cases} \quad 1.12$$

$$\int_{V_{max}}^{V_{min}} P_{comp} \cdot dV = \begin{cases} W_{eff}, & P_{comp} > 0 \\ W_{FW}, & P_{comp} < 0 \end{cases} \quad 1.13$$

- where:
- W_{eff} = efficacious work [J]
 - W_{FW} = forced work [J]
 - V_{max} = maximum engine volume [m³]
 - V_{min} = minimum engine volume [m³]
 - P_{exp} = engine gauge pressure during expansion [Pa]
 - P_{comp} = engine gauge pressure during compression [Pa]
 - V = engine volume [m³]

The indicated work is calculated as the net of the efficacious work and the forced work components of the cycle as:

$$W_{ind} = W_{eff} - W_{FW} \quad 1.14$$

Combining the indicator diagrams shown in Figure 1.10(a) and Figure 1.10 (b) while taking into account equations 1.12 through 1.14 results in the indicator diagram shown in Figure 1.11. The indicated work is still the area enclosed by the P-V curve, while

forced work can be envisioned as the any area between the P-V and the 0 gauge pressure line of the cycle. A well designed engine will have a buffer pressure that, relative to the cycle, minimizes the forced work segments of the cycle [29].

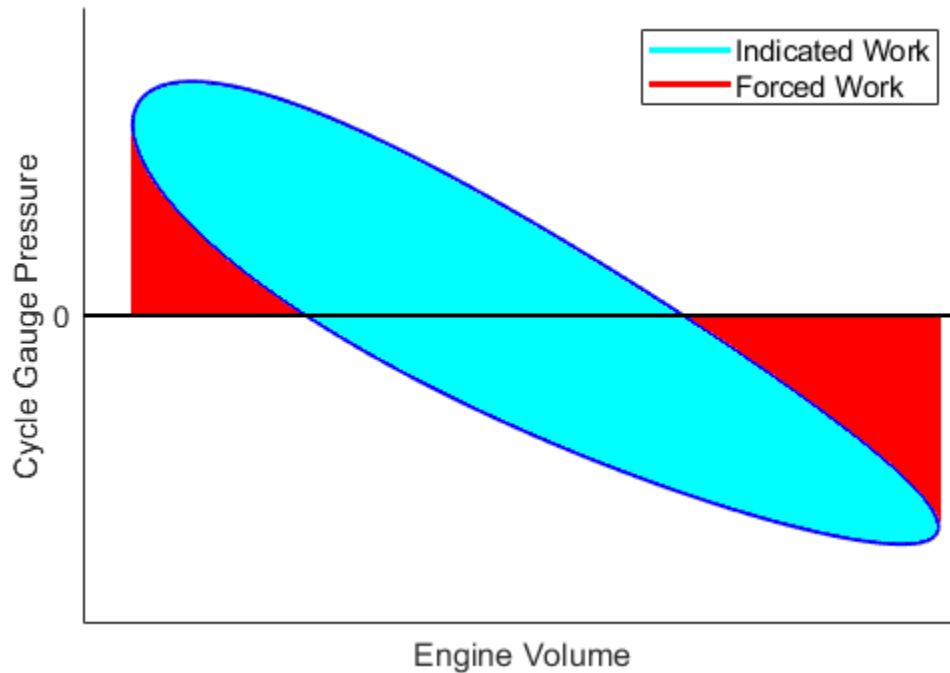


Figure 1.11 – Indicator diagram depicting the components of indicated work and forced work

1.3.6 Shaft Work and Shaft Power

Maximizing the shaft power of a LTD gamma type Stirling engine is the principal goal of this investigation. Shaft power is calculated as the rate at which shaft work is output from an engine as:

$$p_s = W_s \cdot f \quad 1.15$$

where: p_s = shaft power [W]
 W_s = shaft work [J]
 f = cycle frequency [s^{-1}]

Work is product of force and displacement. Shaft work is defined as the torque that is applied through one complete rotation of the output shaft as:

$$W_s = \tau_s \cdot 2\pi \quad 1.16$$

where: $W_s =$ shaft work [J]
 $\tau_s =$ torque of output shaft [Nm]

Working equation 1.16 into equation 1.15 and substituting ω in place of $2\pi \cdot f$ the calculation for shaft power becomes:

$$p_{shaft} = \tau_{shaft} \cdot \omega \quad 1.17$$

where: $p_s =$ shaft power [W]
 $\tau_s =$ torque of shaft [Nm]
 $\omega =$ angular frequency [rads/s]

1.3.7 Mechanism Effectiveness

The fundamental efficiency theorem developed by Senft [29] conceptualizes a relationship between indicated work (W_{ind}), forced work (W_{FW}), and a term called mechanism effectiveness (E), in order to determine the theoretical shaft work (W_s) output of a heat engine. Figure 1.12 shows a schematic representation of the engine and drive mechanism depicted in Figure 1.7. The figure shows the energy flows through the components of the engine from the engine working space through to work output.

Following the energy flow of the engine working space in Figure 1.12 it can be noted that the efficacious work from the cycle acts through the piston. Any losses in the piston, such as friction, will reduce the work delivered to the mechanism (W_{M+}) such that $W_{eff} \geq W_{M+}$. Work delivered to the engine flywheel from the mechanism (W_{F+}) is also subject to losses such that $W_{M+} \geq W_{F+}$. The rotational inertia of the flywheel acts as a kinetic energy battery for the cycle, and provides the energy for the forced work segments of the cycle. The flow of energy from the flywheel into the engine is subject to losses of the mechanism such that $W_{F-} \geq W_{M+} \geq W_{FW}$.

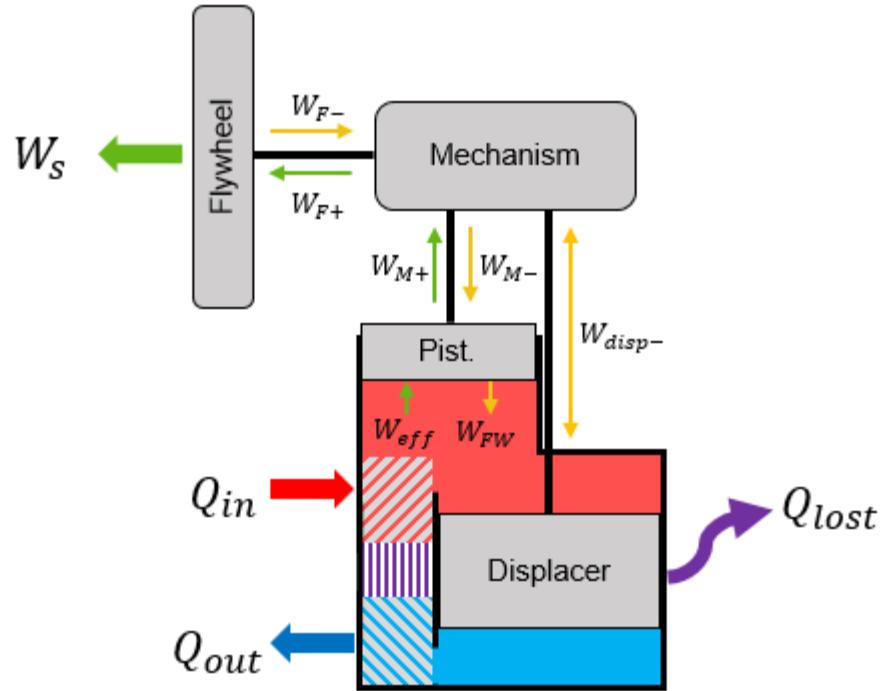


Figure 1.12 – Schematic of a gamma engine showing the energy flows through components of the engine drive mechanism (adapted from Senft [29])

The net result is that the shaft work of the engine (W_s) is less than the indicated work of the cycle, and is equal to the balance of energy entering and exiting the flywheel back to the engine as described by:

$$W_s = W_{F+} - W_{F-} \quad 1.18$$

In order to relate the shaft work of the cycle to the indicated and forced work segments of the thermodynamic cycle, a discounting factor is applied to the indicated work and forced work. As conceptualized by Senft [29], this discounting factor named mechanism effectiveness (E), is merely the ratio between the actual work delivered to the flywheel, and the work that would be delivered in an ideal, zero loss mechanism. This term is conceptually the instantaneous efficiency of the mechanism, but has been termed effectiveness so as to not be equated to the mechanical efficiency of the engine as a whole. The mechanism effectiveness is inherently variable as the loads on engine components change at every instantaneous position of the thermodynamic cycle. As dynamic relationships between drive mechanism components change throughout a

cycle so do components of force that cause friction. In order to provide an estimation of shaft work mechanism effectiveness is assumed to be constant in the following relationship:

$$W_s = E \cdot W_{ind} - \left(\frac{1}{E} - E\right) \cdot W_{FW} \quad 1.19$$

where: $W_s =$ Shaft work [J]
 $E =$ Mechanism effectiveness ($0 \leq E \leq 1$)
 $W_{ind} =$ Indicated work [J]
 $W_{FW} =$ Forced work [J]

Examining equation 1.19 it becomes apparent how important forced work is, as any amount of forced work overcome requires a greater amount of work to overcome mechanism losses incurred twice. Also worth noting is that any friction or pumping losses incurred by the motion of the displacer must also come through the engine mechanism. If shaft work, indicated work, and forced work are known, the value of constant mechanism effectiveness can be calculated by rearranging equation 1.19 into a quadratic form as shown below:

$$0 = E^2(W_{ind} + W_{FW}) + E(-W_s) - W_{FW} \quad 1.20$$

It becomes apparent from this theory that any modification of the engine drive mechanism may reduce the shaft work by decreasing the effectiveness of the mechanism, even if that modification increases indicated work. Thus, any proposed mechanism modification should also aim to reducing mechanism losses. When considering the energy balance of the engine, the frictional losses of the engine mechanism are a sub set of general losses that occur. A general balance of the energy flow through the heat engine is thus:

$$Q_{in} = W_s + Q_{out} + Q_{lost} \quad 1.21$$

where: $Q_{in} =$ heat transfer from thermal source
 $W_s =$ shaft work of engine
 $Q_{out} =$ heat transfer to thermal sink
 $Q_{lost} =$ heat loss from engine to ambient conditions (ambient conditions may or may not be thermal sink)

1.4 Drive Mechanism Modifications in Pursuit of a More Ideal Thermodynamic Cycle

Considering all that has been discussed regarding the compromise of the thermodynamic overlap imposed by the practical kinematic engine drive mechanism, it is no surprise that there have been prior attempts at improving engine performance by optimizing motion of the pistons to extract more work from the thermodynamic cycle. Many of the investigations into thermodynamic cycle optimization have targeted low temperature engines. Some optimizations have seen incidental outcomes of mechanism improvement aimed at other design considerations.

Kolin [26] concluded that discontinuous displacer motion was important for lowering the operating temperature differential and improving power output of small scale gamma type engines. The results were from building and testing of 16 designs of LTD gamma Stirling engines over 10 years. The designs incorporated various methods of dwelling the displacer and included slotted and forked delaying linkages to move the displacer in a discontinuous motion profile.

Investigations by Senft [32] into ultra low temperature Stirling engines showed positive outcomes from discontinuous motion of the displacer in both free piston displacer engines, as well as in kinematic engines. A slotted link on the displacer mechanism was used to produce dwelled displacer motion in Senft's P-19 ultra low temperature gamma engine [29] which was demonstrated to be able to run off of a temperature difference of just 0.5 °C.

Boutammachte and Knorr [41] explored using discontinuous displacer motion in an experimental low-temperature solar gamma type Stirling engine. The displacer motion was driven by a cam with lobes arranged to hold the displacer piston stationary at TDC and BDC during the expansion and compression phase of the cycle. Results from testing the engine showed that the discontinuous motion increased the area of the indicator diagram, and claimed improvement to power output of the engine. It was noted that the high accelerations of the displacer due to the discontinuous motion had unspecified negative impacts on the engine mechanical stability and was not preferred for long term operation.

The often discussed Rhombic drive mechanism [42] is commonly employed by beta type Stirling engines [5] was developed as a mechanism that allowed for elimination of side loads on the displacer and piston rods to reduce friction. Analysis of the mechanism design by Aksoy et al. [43] found that the mechanism produced more discontinuous displacer and piston motion that was advantageous for engine power when compared to a conventional slider crank drive mechanism. This work led the same group to develop an engine with a slotted lever designed to dwell the displacer at TDC and BDC to improve thermodynamics [44]. Testing of a prototype engine with the slotted lever showed to produce more power than an engine of larger volume with a conventional drive mechanism at similar operating conditions.

Other methods of achieving a more ideal cycle have been proposed but not tested experimentally. Proposals include modified four bar linkages [45], as well as a system utilizing non-circular gearing to dwell both the displacer and piston was conceptualized by Fang and Herold [46]. Fang and Herold's analytical results of their thermodynamic model suggested improvements over a conventional slider-crank design could be achieved. A patent by McWaters [47] describes a modified rhombic drive mechanism utilizing non-circular gears to better effect the ideal Stirling cycle in a beta type Stirling engine but contains no analysis.

Overall there is little published quantified evaluations of the effectiveness of dwelled cycle optimizations when compared to conventional motion designs operating at the same engine conditions. The most well documented investigations involve very small engines with a goal of reducing the operating temperature difference [29],[26], not of improving their power, and so the findings may not be applicable to larger engines with more complex designs. In the examined literature there is no deliberate effort to provide control mechanism effectiveness of the modified motion mechanism in a way that can indicate that improvements in power were not attributable lower mechanism losses, as opposed the dwelling of the the displacer. There is also a lack of investigation into the dwelling of the piston in addition to the displacer. Available evidence suggests that dwelling has the potential to improve engine performance but it has yet to be deliberately investigated empirically.

1.5 A Gamma Stirling Engine with Non-Circular Gearing

After a review of the published designs that featured dwelled displacer and piston motion in low temperature Stirling engines efforts were taken to conceptualize an engine design that would allow deliberate investigation of motion modification of engine pistons to improve thermodynamic performance. To expedite the investigation it was decided early on adapting a new drive mechanism to an existing engine within the lab. The available engine was a LTD gamma type Stirling engine with unpressurized air as the working fluid known as the EP1 [40][48]. The author had assisted in the design and construction of the EP1 engine prior to undertaking this investigation. A set of criteria for the new drive mechanism was laid out as follows:

- Ability to independently manipulate the motion of the displacer, piston, as well as manipulating both pistons together.
- Ability to configure the drive mechanism as close as possible to a conventional kinematic engine to provide a comparison baseline and control the influence of mechanism effectiveness on the investigation
- Changes between motion configurations must minimize disturbance to the engine.
- Should allow numerous motion modifications and combinations to provide points of comparison
- Minimize mechanism losses by minimizing friction.

Numerous mechanisms were considered for the application, including dwelling linkages, axial cam drives, and swashplate drives. A critical consideration of the design was the ability to dwell the piston, which had not been explored empirically in the reviewed literature. Since cycle work is recovered from the piston the method of motion manipulation would need to be suitable from transmitting force or torque to the engine mechanism. Many of the displacer dwelling mechanisms described in the literature used variations of sliding linkages, which are suitable to the low force requirements for the displacer, but were less suitable for the force transmission requirements of the piston. A design was developed that would utilize interchangeable non-circular gears to modify the motion profiles of the displacers and piston in a manner similar to the proposed

mechanisms of Fang and Herold [46] and McWaters [47]. Figure 1.13 shows a simplified model of the design adapted to a gamma Stirling engine. The design met the investigation criteria and featured the ability to replicate a conventional kinematic engine easily by using round gears instead of non-circular gears, all changing the engine or the rest of the mechanism.

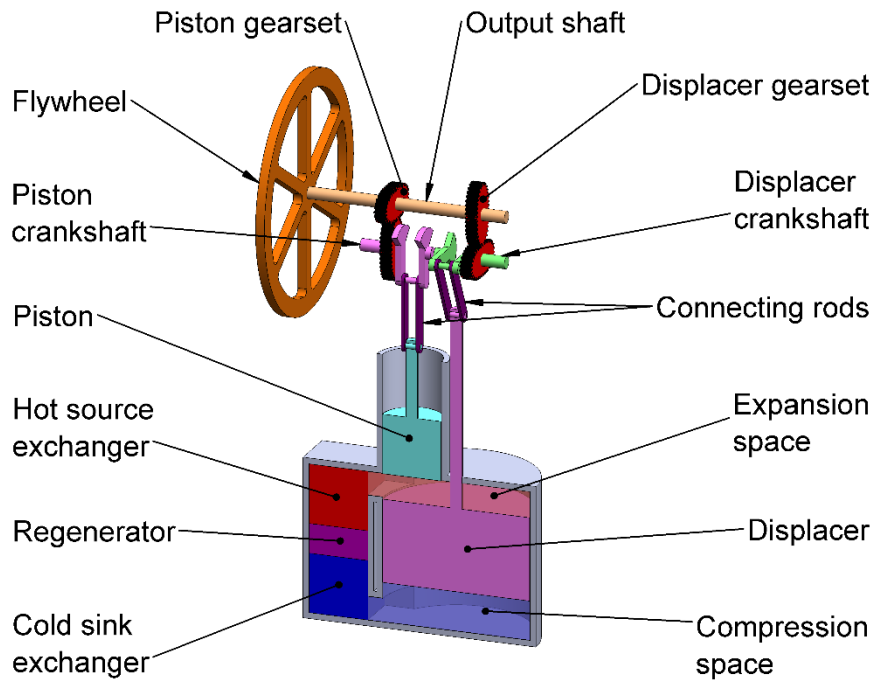


Figure 1.13 – Conceptual embodiment of a gamma Stirling engine with a drive mechanism using non-circular gears

1.6 Thesis Objective and Structure

The objective of this thesis was to investigate if it is possible to modify the drive mechanism of an existing LTD gamma Stirling engine to better replicate the ideal Stirling thermodynamic cycle and improve the power producing performance of the engine when compared to a conventional mechanism design. Information presented will detail how the proposed modified drive mechanism was developed to allow modification of the displacer motion, the piston motion, and the combined motion of both pistons simultaneously with the use of non-circular gearing on the displacer and piston crankshafts. Validation of the concept was done using a thermodynamic model that will be developed to include the kinematics of the proposed mechanism. Having found favourable results from the model using input parameters from previously reported performance of the investigation engine [40], the concept was built onto the existing engine. A series of experiments was run on the modified engine which assessed the effectiveness of the modified motion against a baseline case emulating a conventional kinematic drive mechanism. A final judgement on the utility of the mechanism modifications on improving engine power over the baseline case was made as well as an assessment of the accuracy of the model's predictions.

Chapter 2 describes the thermodynamic and kinematic modelling techniques used to predict the performance of the proposed drive mechanism adapted to the EP1 Stirling engine. Results of the modeling are presented.

Chapter 3 describes in detail the experimental LTD Stirling engine used in this investigation along with data collection instruments, and engine support systems used to quantify the engine performance.

Chapter 4 describes the experimentation plan and procedure used during the collection of data as well as steps taken to control variables outside the scope of the investigation.

Chapter 5 describes the data processing methodology used to calculate results from the experiments.

Chapter 6 presents the results of the experimental trials of the modified motion for all tested configuration against the baseline performance of the conventional kinematic engine analog configuration.

Chapter 7 presents comparisons of the empirical indicator diagrams against the predictions of the updated thermodynamic model.

Chapter 8 provides concluding statements on the investigation as well as suggestions for future works.

2 PERFORMANCE MODELING

This chapter details the thermodynamic modeling techniques used to predict performance of the modified Stirling engine. The isothermal model as described by Urieli and Berchowitz [31] was used to predict performance of the conceptualized drive mechanism modification to the EP1 low temperature difference Stirling engine. The isothermal model was adapted to utilize the kinematics of non-circular gearing. The theory of fundamental efficiency as proposed by Senft [29] is introduced to estimate shaft power output using the P-V indicator diagrams produced by the isothermal model to evaluate the effectiveness of the concept.

2.1 Isothermal Model of the Stirling engine

The isothermal thermodynamic model is a simple model used to predict performance of a Stirling cycle heat engine. The model presented is described by Urieli and Berchowitz [31] as being reasonably accurate for a prediction of cycle work, but of limited use for predicting efficiency and heat transfer. Versions of the model have been used to optimize engine geometry, including mechanism geometry [44].

2.1.1 Model description

The ideal isothermal model breaks the working space of the Stirling engine into distinct volume sections as shown in Figure 2.1 (a). These volumes change throughout the engine cycle as the engine pistons displace under the control of the drive mechanism kinematics. Each of these volume spaces is prescribed a temperature that is invariant through the cycle, hence the name isothermal model. A one dimensional temperature profile of the spaces is shown in Figure 2.1 (b). Relying on the ideal gas law and assumptions regarding the working fluid, the engine pressure can be calculated as a function of the variations in the working space volumes. The model is therefore useful in investigating how different drive mechanisms control the volume variations of the engine and influence the power output [31].

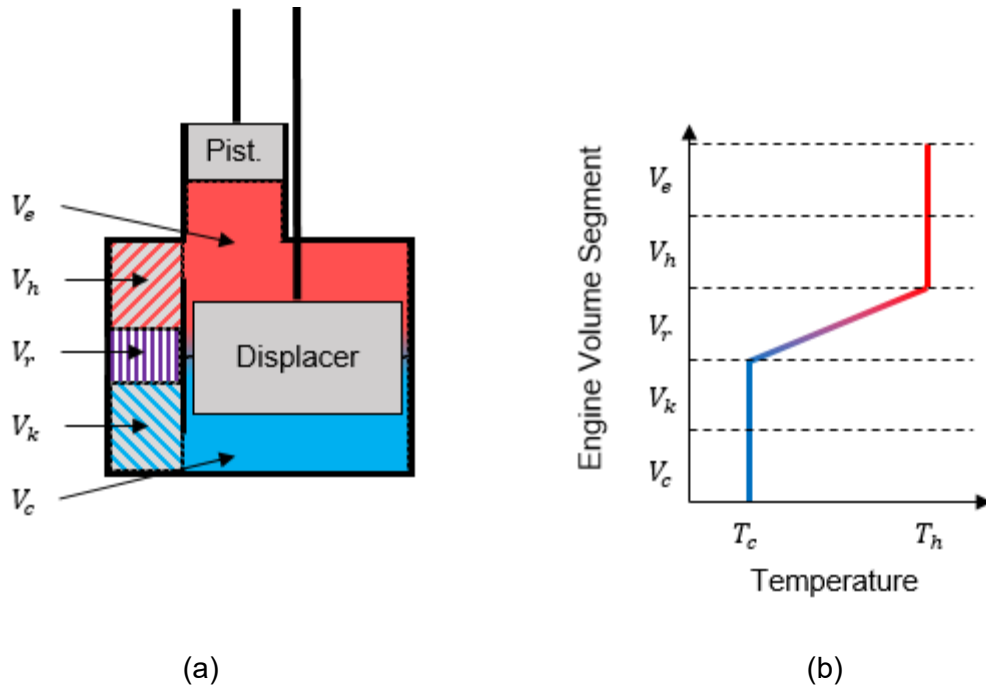


Figure 2.1 – Graphical representation of the isothermal model for a gamma Stirling engine showing the (a) working space volumes and (b) the prescribed temperature profile of the spaces

2.1.2 Model assumptions

The isothermal model makes numerous simplifying assumptions regarding the working spaces of the engine. The assumptions are laid out below:

- Working spaces are isothermal and all heat exchange into engine spaces is perfectly effective.
- Total mass of the working fluid in the engine is constant (no leaks).
- All working spaces of the engine are part of one of five serially connected volume spaces as shown in Figure 2.1 (a):
 - o expansion space V_e
 - o heater V_h
 - o regenerator V_r
 - o cooler V_k
 - o compression space V_c
- Each space is a homogeneous entity and all working fluid within has uniform instantaneous properties of:

- mass m
 - absolute temperature T
 - volume V
 - pressure P .
- There is no pressure drop through the volume spaces and thus pressure is uniform throughout the engine at any instant.
 - The ideal gas law applies to the working fluid.
 - Cyclic steady state is achieved.
 - Kinetic and potential energies of the gas are neglected.

In the case of a gamma type engine the expansion space volume and the compression space volume do not correlate to volume spaces of a particular piston cylinder as is the case for alpha type engines. Examining Figure 2.1 it can be seen that the displacer separates the expansion and compression ends of the engine. The piston can be modeled as its own space with its own properties, but for simplicity it is modeled as part of the expansion space or the compression space depending on which side of the engine it is mounted to.

2.1.3 Model Analysis and Equations

The goal of the model analysis is to provide an estimate of the cyclic work done by the engine. As discussed in section 1.2.5 the indicated cyclic work is calculated by taking the enclosed area of the pressure-volume indicator diagram. To begin the analysis assumptions are made as to the engine operating conditions. These assumptions include the type and total mass of working fluid in the engine m , the absolute temperatures of the engine spaces, and the nature of the volume variations in those engine spaces.

The mass of working fluid is dictated by the initial charge of working fluid added to the engine working space prior to sealing it. This can be arbitrary or dictated by the engine design. For reasons noted in section 1.3.4 and 1.3.7 it is desirable to have the mass of working fluid be such that the mean pressure of the cycle matches the buffer pressure of the engine [29]. This is an iterative process as determining the cycle mean pressure

is done from the results of the isothermal model analysis. An initial estimate of the working fluid mass is thus required.

Decisions about the engine temperature profile is dictated by thermal source and thermal sink that the engine is designed to utilize. Using the source and sink temperatures for the working spaces temperatures is an available starting point for modeling that assumes perfect heat transfer. If an estimate of the actual working fluid temperature is available or can be inferred by data from engines of similar architecture, using these temperatures will yield more realistic model results.

The temperature distribution through the regenerator is assumed as being linear as depicted in Figure 2.1 (b). The effective regenerator temperature as derived by Urieli and Berchowitz [31] is given by:

$$T_r = \frac{T_h - T_k}{\ln \frac{T_h}{T_k}} \quad 2.1$$

where: $T_r =$ effective regenerator temperature
 $T_h =$ heater space temperature
 $T_k =$ cooler space temperature

The volumes of the working fluid is dictated by the geometry of the engine working spaces. Typically the engine heater, cooler, and regenerator working spaces are invariant. Volumes of the expansion and compression spaces must change in sequence through an engine cycle to undertake an efficacious Stirling cycle. Volume variations of these spaces is dictated by the displacement profiles of the engine pistons. For kinematic Stirling engines the displacer and piston motion profiles are functions of the drive mechanism position θ .

Applying the ideal gas law to an individual working space x with the assumed properties results in the following equation for instantaneous pressure:

$$P_x(\theta) = \frac{m_x \cdot R \cdot T_x}{V_x(\theta)} \quad 2.2$$

where: $P_x(\theta)$ = workspace x pressure at cycle position θ [Pa]
 m_x = working fluid mass in workspace x [kg]
 R = working fluid specific gas constant [J/kg·K]
 T_k = absolute temperature of workspace x [K]
 $V_x(\theta)$ = workspace x volume at cycle position θ [m³]

Applying the no pressure drop assumption and known engine working space properties, the individual working space equations combine to give:

$$P(\theta) = m \cdot R \cdot \left(\frac{T_e}{V_e(\theta)} + \frac{T_h}{V_h} + \frac{T_h - T_k}{V_r \cdot \ln T_h/T_k} + \frac{T_k}{V_k} + \frac{T_c}{V_c(\theta)} \right) \quad 2.3$$

With the values of P and V being a function of the mechanism position θ , P-V indicator diagrams can be made for the expansion space V_e and compression space V_c . All volume spaces can also be combined to produce an indicator diagram for the complete engine working space V . The indicated work for the expansion and compression spaces can be calculated by taking the contour integral of the P-V curve as:

$$W_{es} = \oint P(\theta) \cdot dV_e(\theta) \quad 2.4$$

$$W_{cs} = \oint P(\theta) \cdot dV_c(\theta) \quad 2.5$$

where: W_{es} = expansion space indicated work [J]
 $P(\theta)$ = engine pressure [Pa]
 $V_e(\theta)$ = expansion space volume [m³]
 $V_c(\theta)$ = compression space volume [m³]

Equations 2.4 and 2.5 are differentiated from equations 1.5 and 1.6 in that they consider the complete cycle of an engine working space, as opposed to the whole engine as is the case for the total engine volume indicator diagram. The net of the expansion space and compression space work is the engine indicated work:

$$W_{ind} = W_{es} - W_{cs} \quad 2.6$$

2.1.4 Model Implementation

The first implementation of a closed form solution of the isothermal model was described by Schmidt [49] assuming sinusoidal piston motion in 1871. The Schmidt isothermal model can still be used in preliminary analysis of Stirling engines of any type. To evaluate the modification of the piston motion in this investigation the isothermal model was implemented numerically in MATLAB. The MATLAB script documenting a later implementation of the model is documented in Appendix E.1. In order to predict the performance of the experimental engine the isothermal model was adapted to the conceptual design. Equations for the compression work space volume and the expansion workspace volume were adapted to take independent input puts of angular positions of the displacer crankshaft θ_d and the piston crankshaft θ_p respectively. As noted in section 2.1.2 the displacer splits the expansion and compression space such that the linear displacement of the displacer results in volume variations of the expansion and compression space equal to the following:

$$dV_{e_d} = -dV_{c_d} = A_d \cdot dh_d(\theta_d) \quad 2.7$$

where: dV_{e_d} = change in displacer expansion space [m³]
 dV_{c_d} = change in displacer compression space [m³]
 A_d = cross-sectional displacer area [m²]
 $dh_d(\theta_d)$ = change in displacer position as a function of displacer crankshaft position [m]

The displacer expansion space (V_{e_d}) and compression space (V_{c_d}) combined are equal to the swept displacer volume (V_{s_d}). In the case of the EP1 engine used in this investigation, the piston is attached on the expansion side of the engine and is considered as part of the expansion space volume. Details of the engine design are described in section 3.1. The change in the expansion space volume attributed to piston motion is described by the following:

$$dV_{e_p} = A_p \cdot dh_p(\theta_p) \quad 2.8$$

where: dV_{e_p} = change in displacer expansion space [m³]
 A_p = cross-sectional piston area [m²]
 $dh_p(\theta_p)$ = change in piston position as a function of piston crankshaft position [m]

The displacer position (h_d) and piston position (h_p) are functions of the displacer crankshaft and piston crankshaft by way of slider-crank mechanisms equations. The slider crank equation as derived by Norton [50] with respect to the piston's bottom dead center (BDC) position is:

$$h = r \cdot \cos \theta + \sqrt{l_{cr}^2 - r^2 \cdot \sin^2 \theta} - l_{cr} + r \quad 2.9$$

where: h = piston wrist pin / crosshead location [m]
 r = crank pin radius [m]
 θ = angular position of crankshaft [°]
 l_{cr} = connecting rod length [m]

Imputing the necessary engine geometry data and assuming the properties of the working fluids within the engine spaces allows for the final calculation of engine pressure as a function of the angular positions of the displacer and piston crankshafts. A numerical integration scheme was used to calculate the segments indicated work and forced work from the model results. The details of the numerical integration approximation used is documented in section 5.3.3. Table 2.1 list the input variables of the isothermal model and the preliminary values used in this investigation. These values came from a variety of sources, including experimental results of the EP1 as determined by Stumpf [40], as well as details of the planned modifications to the EP1 as described in chapter 3.

Table 2.1 –Preliminary isothermal modeling parameters for analysis of the EP1-M

Model Parameter	Variable(s)	Value	Units
Displacer swept volume	V_{sd} (V_{ed} and V_{cd})	5.69	L
Power piston swept volume	V_{sp} (V_{ep})	1.78	L
Heater and expansion side dead volume	V_h	1.93	L
Cooler and compression side dead volume	V_k	1.37	L
Regenerator volume	V_r	0.11	L
Expansion space and heater temperature	T_e, T_h	70	°C
Compression and cooler space temperature	T_c, T_k	20	°C
Effective regenerator temperature	T_r	44.3	°C
Working fluid	-	Dry air	-
Specific gas constant of air [20]	R	0.287	kJ/kg·K
Buffer pressure	P_b	92.5	kPa
Mass of working fluid	m	derived	kg
Angular position of displacer crank	θ_d	variable	°
Angular position of piston crank	θ_p	variable	°
Radius of displacer crank	r_d	58.0	mm
Radius of piston crank	r_p	45.0	mm
Displacer connecting rod length	l_d	385.0	mm
Piston connecting rod length	l_p	185.0	mm

The angular positions of the displacer and piston crankshafts were governed by the kinematic equations of the conceptual drive mechanism using the proposed non-circular gearing. The theory and kinematics of the non-circular gears is presented in section 2.2. The results of the preliminary isothermal modeling is presented in section 2.3.

2.2 Kinematics of Oval Non-Circular Gears

The next stage of modeling was to establish the kinematics of the non-circular gears used in the conceptualized drive mechanism modification. The non-circular gears were selected to change the velocities of the displacer and piston crankshafts to achieve the desired motion profiles. The information in this section is presented from the works of Litvin [51] on non-circular gearing theory. Litvin [51] describes gears as pairs of planar curves called centrodes that roll over each other without slipping. For conventional gears the pitch circles of the pair would be the centrodes [52]. An example of an elliptical non-circular centrode and mating pair is shown in Figure 2.2. The curves will contact one another at the instantaneous point of contact J , which is located on the straight line vector between the centers of rotation for each pair O_1 and O_2 , where O_1 is the rotation input, and O_2 is the rotation output. To make gears involute teeth are cut along the centrode curves and the meshing teeth transmit force between the rotating centrodes. For round gear pairs the centrodes are circles, and the point J is fixed, resulting in a constant derivative function (commonly called speed ratio) between the two centrodes. For non-circular centrodes, the derivative function varies depending on the shape of the centrodes. In continuous motion machines such as those with rotating shafts, a requirement for centrodes is that they are closed form periodic curves. This investigation focuses on elliptical mating centrodes.

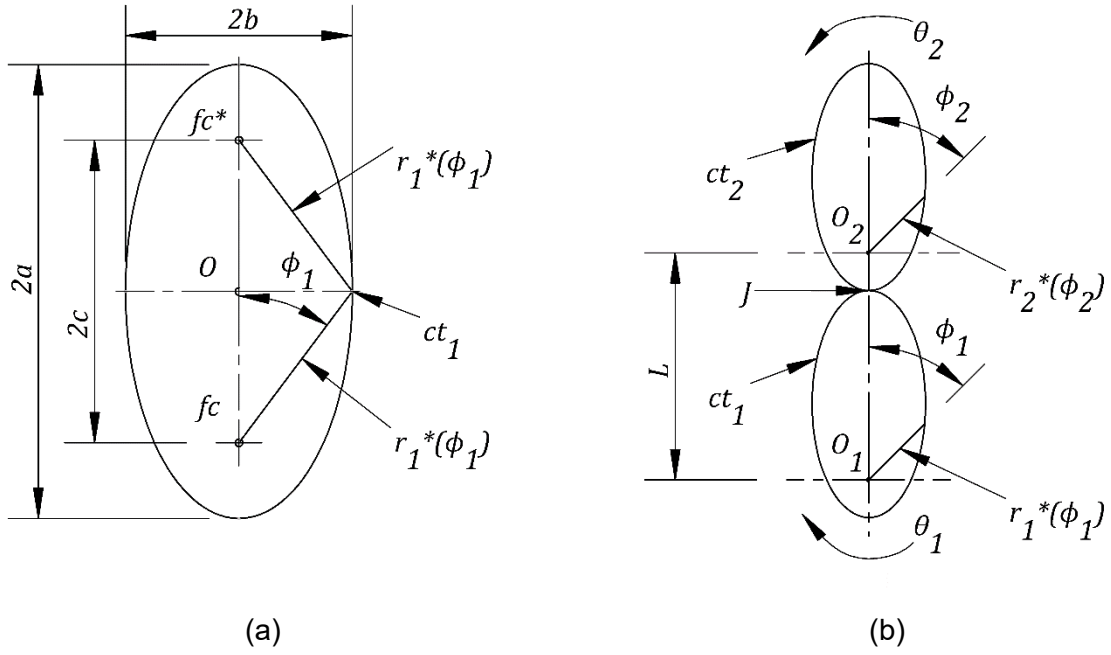


Figure 2.2 – Elliptical centrodes showing (a) basic geometry elements and (b) a mating pair of identical elliptical centrodes (modified from Litvin [51])

2.2.1 Ellipse Geometry

An elliptical centrode pair is shown in Figure 2.2 (b) where the principal geometry elements of the centrodes are annotated. To form a mating pair each centrode must rotate about one of the two foci, O_1 and O_2 , of the ellipse. The definition of an ellipse dictates that the vectors from either foci to a point on the perimeter is a constant, and equal to twice the major axis as shown in equation 2.10:

$$r_1 + r_1^* = 2a \tag{2.10}$$

- where: $r_1 =$ vector from foci fc to centrode perimeter
 $r_1^* =$ vector from foci fc^* to centrode perimeter
 $a =$ major axis of an ellipse

Figure 2.2 (a) shows the relationships between elements of ellipse geometry. Using the Pythagorean Theorem we get a relationship for the axes of the ellipse as follows:

$$b = \sqrt{a^2 - c^2} = a\sqrt{1 - e^2} \quad 2.11$$

where: $b =$ minor axis of an ellipse
 $a =$ major axis of an ellipse
 $c =$ foci distance
 $e =$ ellipse eccentricity

The second part of equation 2.11 introduces a new ellipse property known as the ellipse eccentricity e which is defined by the following relation:

$$e = \frac{c}{a} \quad 2.12$$

where: $e =$ ellipse eccentricity
 $c =$ foci distance
 $a =$ major axis of an ellipse

With an identical pair of ellipses mated as depicted in Figure 2.2 (b), the center distance L between the two rotation points equivalent to the twice the ellipse major axis a as defined by:

$$L = 2a \quad 2.13$$

It is important to note that in order for the centrodes to roll over each other at a fixed center-to-center distance L , the center of rotation of each centrode must be located at one of the foci of the ellipses.

The polar equations that define the curve of a centrode of an ellipse about the foci is derived in detail in the works of Litvin [51]. For an ellipse the centrode is defined as:

$$r_n(\varphi_n) = \frac{a(1 - e^2)}{1 - e(\cos \varphi_n)} \quad 2.14$$

where: $r_n(\varphi_n) =$ radius vector of centrode as a function of polar angle φ_n
 $a =$ major axis of an ellipse
 $e =$ ellipse eccentricity

2.2.2 Kinematics of Mating Ellipses

With the geometry of a basic elliptical centrode defined, the kinematics of mating elliptical centrodes can be defined. In general gear theory the derivative function of a mating pair of centrodes defines the relative angular motion of one centrode in relation to the first. From this point forward with respect to gear sets, the driving gear will be identified as gear 1 while the driven gear is identified as gear 2. The derivative function is defined in relation to the radii of the two centrodes at the point of contact J . For non-circular gears, the location of contact point J on the vector L between the two centers of rotation of each centrode varies throughout rotation. The following equation describes the derivative function with regard to the geometry of both centrodes:

$$k_{21} = \frac{d\theta_2}{d\theta_1} = \frac{r_1(\theta_1)}{r_2(\theta_1)} = \frac{r_1(\theta_1)}{L - r_1(\theta_1)} \quad 2.15$$

where: k_{21} = derivative function of centrodes 2 with respect to centrode 1
 $r_1(\theta_1)$ = radius of centrode 1 along vector L at rotational position θ_1 of centrode 1
 $r_2(\theta_1)$ = radius of centrode 2 along vector L at rotational position θ_1 of centrode 1
 L = center to center distance of mating pair

Substituting equation 2.14 defining the radii of centrode 1 into equation 2.15 results in the derivative function being as follows

$$k_{21} = \frac{1 - e^2}{1 + e^2 - 2e(\cos \theta_1)} \quad 2.16$$

Finally, the relative rotation of both centrodes about their respective centers of rotation is given by the transmission function of the mating pair. The closed form solution for mated elliptical centrodes as depicted in Figure 2.2 (b) is defined by equation 2.17.

$$\tan \frac{\theta_2}{2} = \frac{1 - e}{1 + e} \tan \frac{\theta_1}{2} \quad 2.17$$

- where: $\theta_2 =$ angular position of centrodes 2 about its center of rotation
 $\theta_1 =$ angular position of centrodes 1 about its center of rotation
 $e =$ ellipse eccentricity of mating centrode pair

The gear pair shown in Figure 2.2 (b) results in a derivative function that varies with a period of 2π . For the conceptual drive mechanism modification of the EP1 Stirling engine the derivative function of angular velocity variations needs to repeat twice per cycle for the displacer and piston crankshafts: once for dwelling at TDC, and once at BDC. This requires applying a modifying factor w to the elliptical centrodes. A modification factor of 2 results in a twice per cycle variation suitable for the design. Applying a modification factor of 2 to elliptical centrodes is a specific type of elliptical centrode termed an oval. A pair of mating oval centrodes is shown in Figure 2.3.

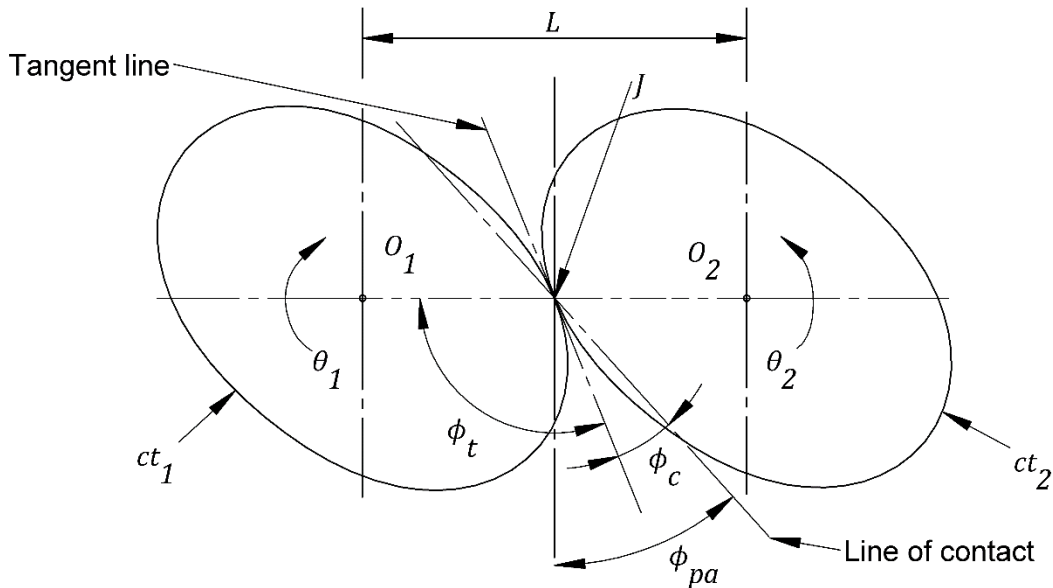


Figure 2.3 – Modified elliptical centrodes forming a mating pair (modified from Litvin [51])

Oval non-circular gears are one of the most common non-circular gears varieties and have application in some positive displacement flow meters [53]. Litvin [51] derived equations for the polar equation, derivative function, and transmission function for elliptical gears with modifying factor $w = 2$ as follows:

$$r_n(\varphi_n) = \frac{a(1 - e^2)}{1 - e(\cos(w \cdot \varphi_n))} = \frac{a(1 - e^2)}{1 - e(\cos(2\varphi_n))} \quad 2.18$$

$$k_{21} = \frac{1 - e^2}{1 + e^2 - 2e(\cos(w \cdot \theta_1))} = \frac{1 - e^2}{1 + e^2 - 2e(\cos(2\theta_1))} \quad 2.19$$

$$\tan \frac{w \cdot \theta_2}{2} = \frac{1 - e}{1 + e} \tan \frac{w \cdot \theta_1}{2} = \tan \theta_2 = \frac{1 - e}{1 + e} \tan \theta_1 \quad 2.20$$

2.2.3 Design of Oval Non-Circular Centroides

Using the modified ellipse centroide equation 2.18 the polar curves for mating oval centroides can be generated by selecting a centre-to-center distance $L = 2a$ and a suitable eccentricity e . For this work a 3 inch center-to-center distance was selected based on the availability of commercially available oval gear pairs from Cunningham Industries, Inc. [54]. Commercially available gears were planned to be used as substitutes in the drive mechanism retrofit to the EP1 in the event that planned 3D printing of gears proved insufficiently accurate. Detailed design of the oval non-circular gears is documented in section 3.2. The 3 inch center-to-center distance chosen offered sufficient clearance between the main output shaft and the crankpins to allow the necessary displacer and piston stroke lengths of the EP1. This avoided the need for multiple gear stages to provide clearance for the engine crankshafts.

The planned modified motion required two pairs of identical oval centroides to investigate the effects of dwelling and a set of centroides to emulate the conventional motion profiles. For the conventional case a set of round centroides with a constant derivative function were designed. The 1:1 derivative function of the round centroides would replicate the speed of a conventional crankshaft and therefore conventional piston motion. Round centroide can be described using the same equations as the modified elliptical centroides by selecting an eccentricity of $e = 0$. The two oval centroide profiles were selected to vary the derivative ratios incrementally. The first set varied the derivative function k_{21} between the crankshafts and the output shaft to ratios between 1.5:1 and 0.75:1. The second set varied the derivative function k_{21} to a ratio that varied

between 2:1 and 0.5:1. These derivative function ranges are achieved by modified oval elliptical centrodes of eccentricities of $e = 1/5$ and $e = 1/3$ respectively. From this point forward the centrodes and gear sets are identified by their design eccentricities: $e = 0$, $e = 1/5$, and $e = 1/3$.

The kinematic equations for the oval centrodes were programmed into MATLAB for use in the Isothermal model and later data processing equations. The sub function for the centrode kinematics is documented in Appendix E.2. A plot of the derivative function for a single rotation of the input centrodes is shown in Figure 2.4. The polar curves of the modified elliptical centrodes generated using equation 2.18 are shown in Figure 2.5.

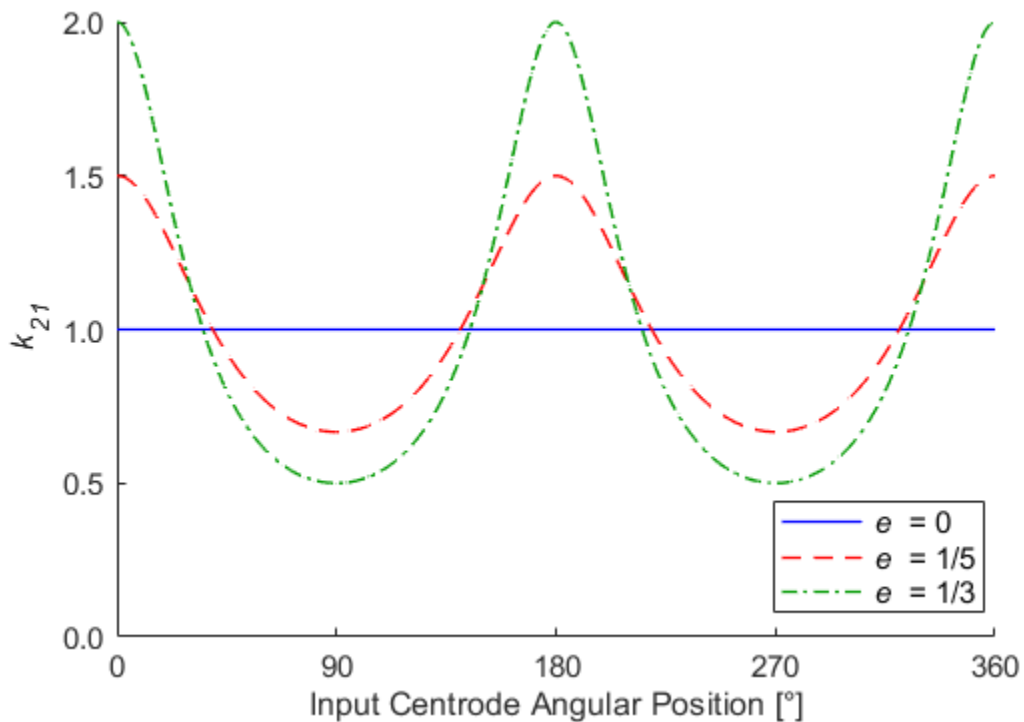


Figure 2.4 – Derivative function results for the investigated oval non-circular centrode pairs

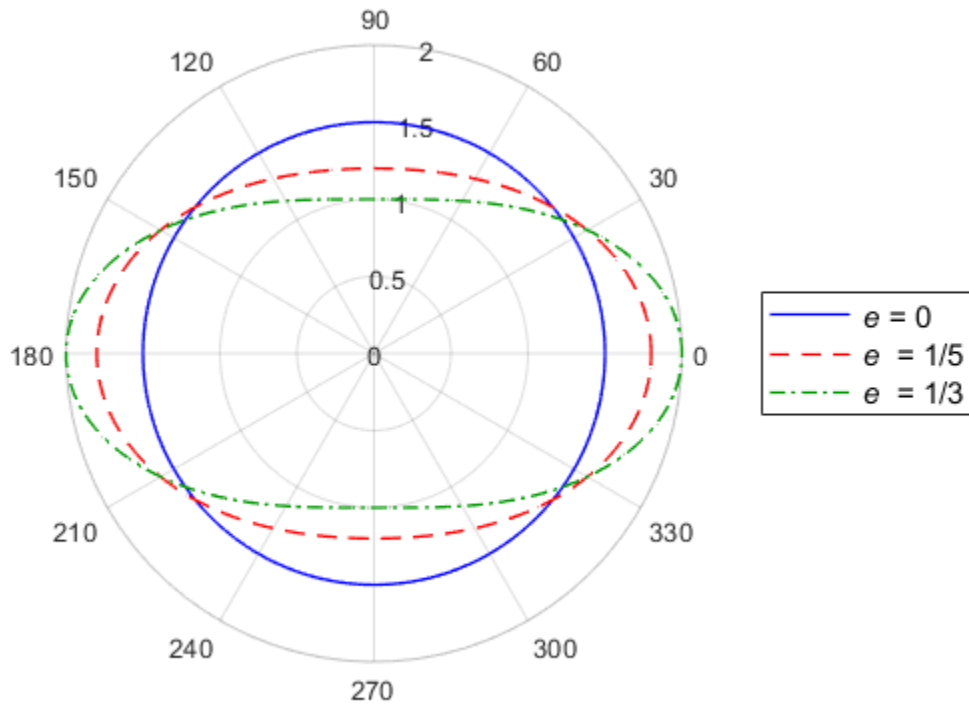


Figure 2.5 – Polar plot of the modified oval elliptical centrodes

2.3 Results of the Isothermal Modeling

The kinematics of the oval non-circular centrodes was integrated into the isothermal model to generate predictions of indicated work for the engine. A final element was added to the model to predict shaft work out of the engine by integrating Senft's fundamental efficiency theorem as introduced in section 1.3.7. Equation 1.19 was integrated into the model assuming a constant mechanism effectiveness $E = 0.80$. The assumed mechanism effectiveness taken from the results of Stumpf's optimizations of the EP1 [40]. Equation 1.19 used the inputs of the numerical integration of the model indicator diagram for W_{ind} and forced work W_{FW} . It was anticipated that the addition of more mechanical elements to the drive mechanism would reduce the mechanism effectiveness, but E of 0.80 was considered a good start point. The model parameters used are those listed in Table 2.1 and were held constant across all motion modifications.

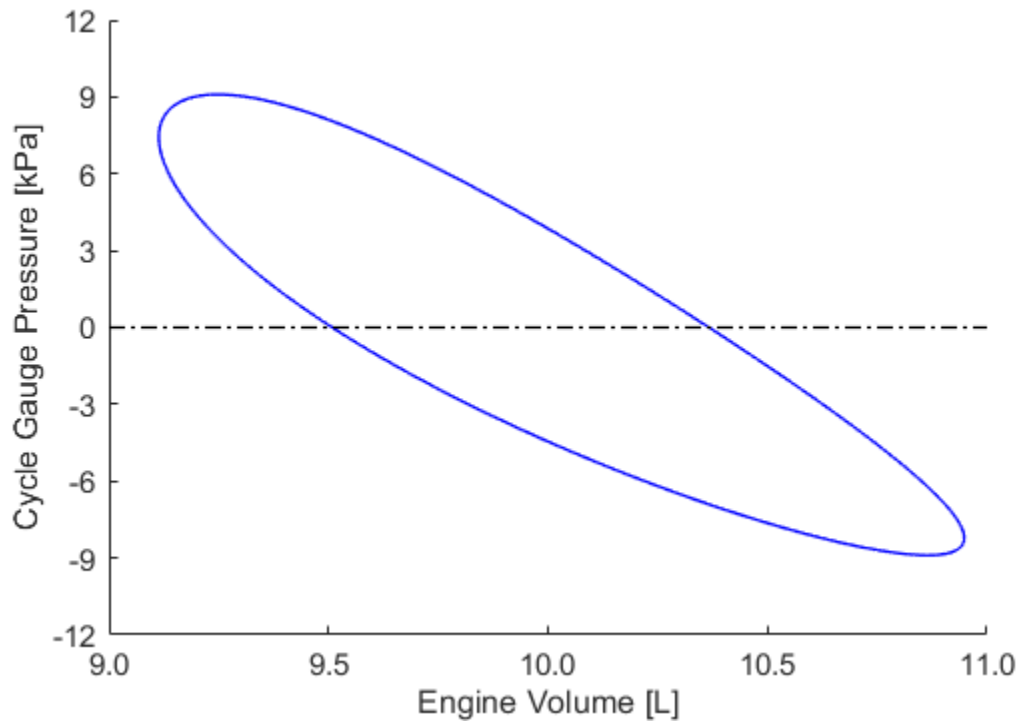
Modeling initially investigated motion modification for a single crankshaft, first for dwelling the displacer and then the piston. Modeling then progressed to motion modification of both pistons combined. Results are arranged by sequential model numbers and present the model indicator diagrams, as well as tabulation of the calculated engine work components of the cycle.

2.3.1 Baseline Conventional Motion Results

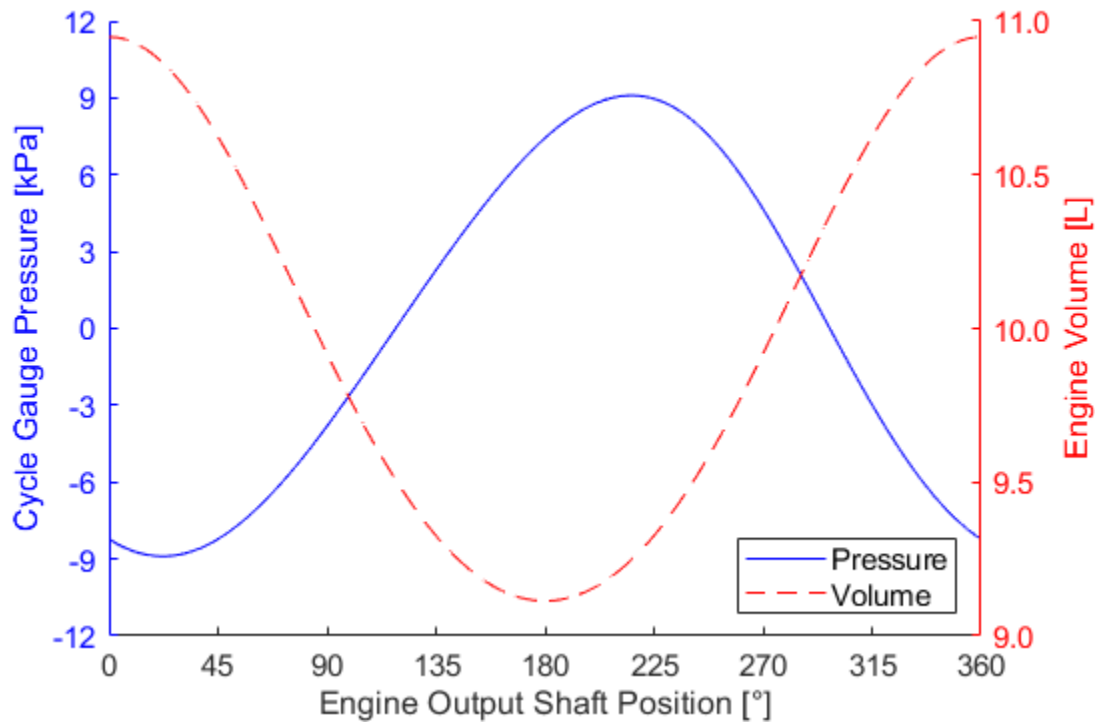
The baseline conventional motion model uses the round centrodes of $e = 0$ for both the displacer and piston to emulate a drive mechanism with a conventional crankshaft and slider-crank piston connections. These results serve as the basis of comparison for the models with modified motion.

Examining Figure 2.6(a) the P-V indicator diagram of the model is as expected for a conventional kinematic Stirling engine. The ends of curves are distinctly rounded when compared to the ideal Stirling cycle indicator diagram curve shown in Figure 1.3. Figure 2.6(b) provides a double Y-axis plot showing the engine pressure and volume as a function of the engine output shaft position. The volume curve is as anticipated, as it is directly proportional to the position of the piston. The shape of the pressure curve also

closely follows the shape of the displacer motion profile for the conventional motion case as shown in Figure 1.8(b). The overlap in pressure and volume changes can clearly be seen and are a result of the overlaps in displacer and piston motion profiles. The results of the calculation of engine work is shown in Table 2.2. Forced work is about ~25% of the calculated indicated work, and reduces the shaft power output to ~66% of the indicated work.



(a)



(b)

Figure 2.6 – Model no. 1 baseline isothermal (a) indicator diagram and (b) pressure and volume curves

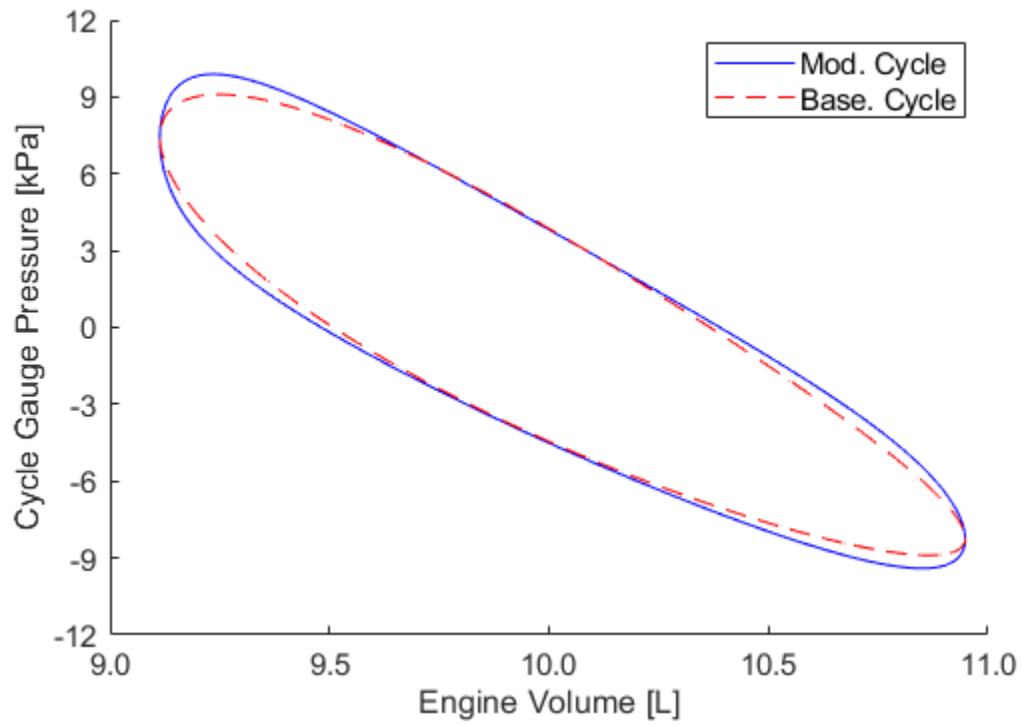
Table 2.2 – Baseline isothermal modeling results

Model Parameter	Model No.	Centrode e		Value	Units	Diff. over Baseline [%]
		Disp.	Pist.			
Indicated work W_{ind}	1	$e = 0$	$e = 0$	12.06	J	-
Forced work W_{FW}	1	$e = 0$	$e = 0$	3.14	J	-
Estimated shaft work W_S	1	$e = 0$	$e = 0$	8.24	J	-

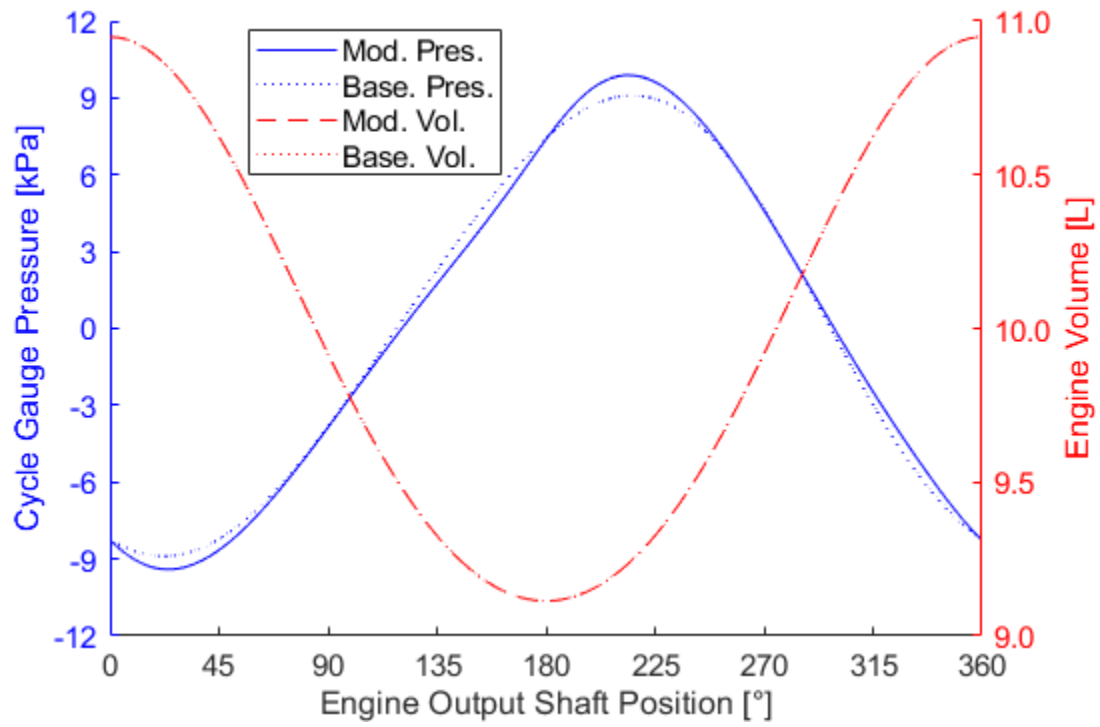
2.3.2 Displacer Dwelling

The displacer dwelling model uses non-circular centrode equations for the relationship between the engine output shaft position and the displacer crankshaft position. Model number 2 dwells the displacer with the $e = 1/5$ centrode profile, while model number 3 dwells the displacer with the $e = 1/3$ centrode profile. The motion is phased in such a way as to prolong the displacer dwell at its TDC and BDC positions. All further references to “dwelling” in this work refer to this phasing and prolongation of time that either piston spends at TDC or BDC. The theoretical advantage of this dwelling is to prolong the duration of engine working fluid being predominantly in the expansion or compression space during the piston motion. With more gas in either section the model should predict higher engine expansion and compression pressures.

Examining the results shown in Figure 2.7(a) it can be observed that the dwelling of the displacer with the $e = 1/5$ centrode has the anticipated effect of expanding the indicator diagram at the corners when compared to the baseline case from model no. 1. The effect is even more pronounced with the longer dwell period of the displacer with the $e = 1/3$ centrode as shown in Figure 2.8(a) results. Examining the pressure and volume curves of Figure 2.7(b) and Figure 2.8(b) it can be noted that the increasing the indicator area arises from an increase in peak cycle pressures at the beginning of the piston expansion and compression stroke. The pressures are not prolonged at the midpoint of the expansion and compression strokes so no gains are seen in the middle section of the indicator diagram.

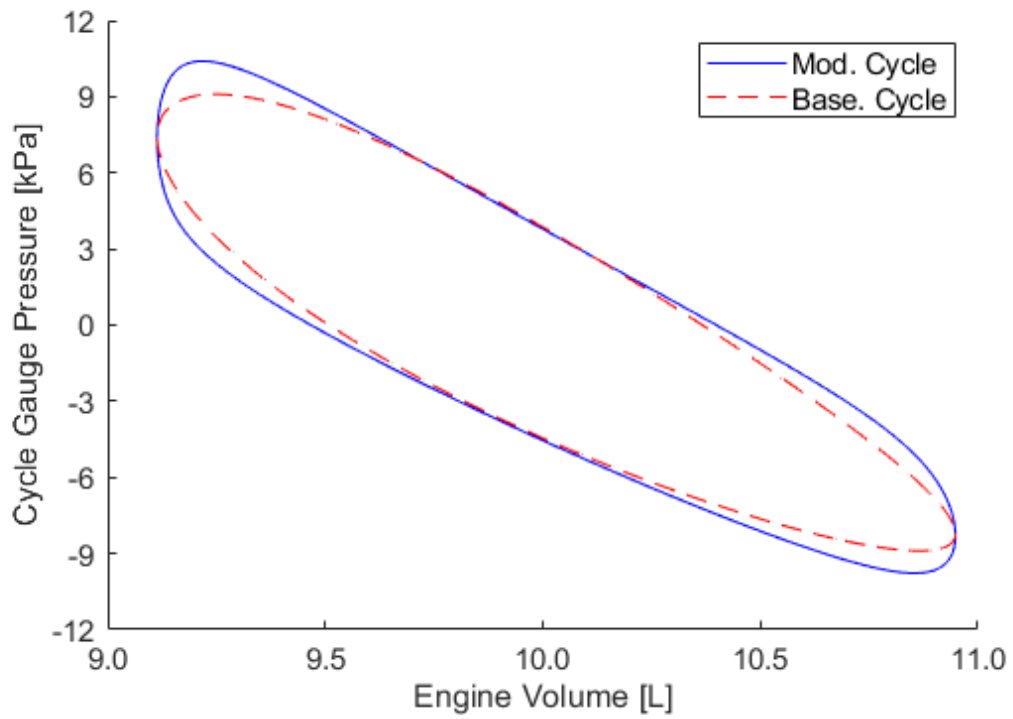


(a)

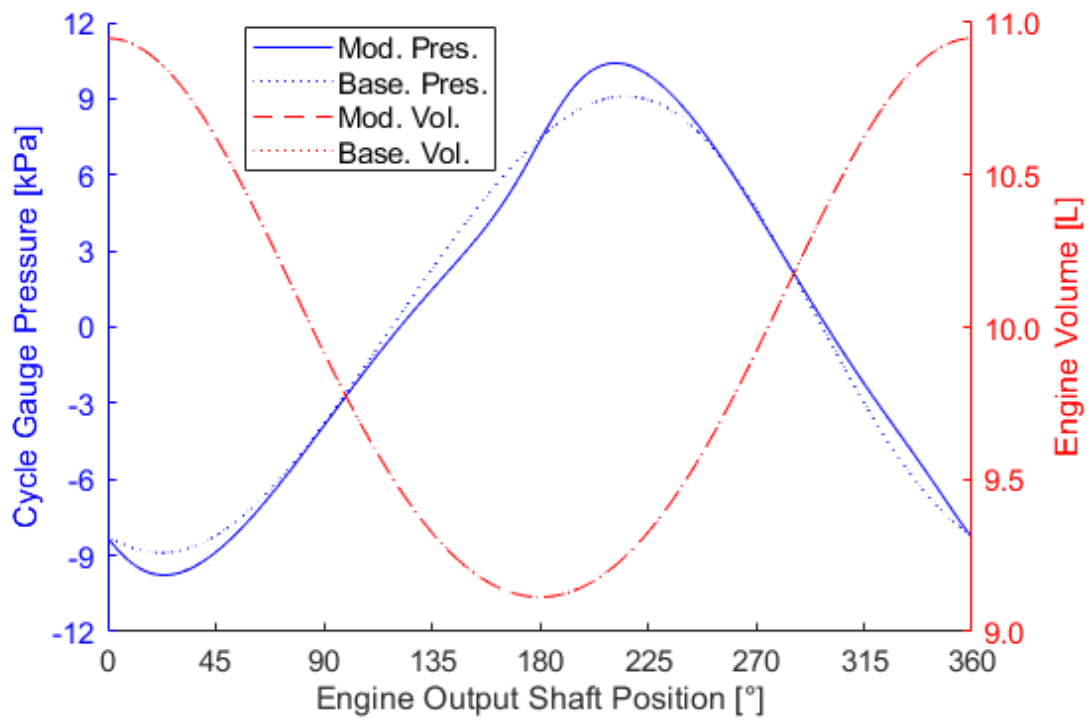


(b)

Figure 2.7 – Model no. 2: dwelled displacer $e = 1/5$ isothermal (a) indicator diagram and (b) pressure and volume curves



(a)



(b)

Figure 2.8 – Model no. 3: dwelled displacer $e = 1/3$ isothermal (a) indicator diagram and (b) pressure and volume curves

The results of the work predictions for the models are listed in Table 2.3. Results suggest that the dwelling of the displacer piston has the potential to increase the shaft work of the cycle by 13.0% and 20.2% for the centrodos of eccentricity $e = 1/5$ and $e = 1/3$ respectively.

Table 2.3 – Displacer dwelling modeling results

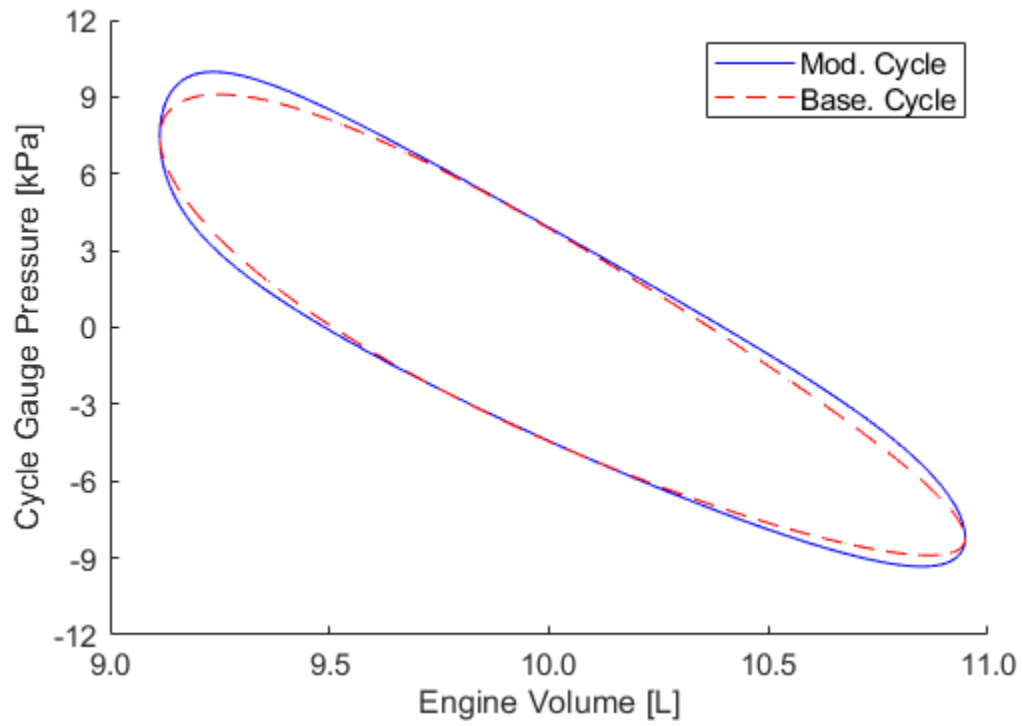
Model Parameter	Model No.	Centrode e		Value	Units	Diff. over Baseline [%]
		Disp.	Pist.			
Indicated work W_{ind}	2	$e = 1/5$	$e = 0$	13.14	J	8.9
Forced work W_{FW}	2	$e = 1/5$	$e = 0$	2.68	J	-14.6
Estimated shaft work W_S	2	$e = 1/5$	$e = 0$	9.31	J	13.0
Indicated work W_{ind}	3	$e = 1/3$	$e = 0$	13.74	J	13.9
Forced work W_{FW}	3	$e = 1/3$	$e = 0$	2.42	J	-23.0
Estimated shaft work W_S	3	$e = 1/3$	$e = 0$	9.90	J	20.2

2.3.3 Piston Dwelling

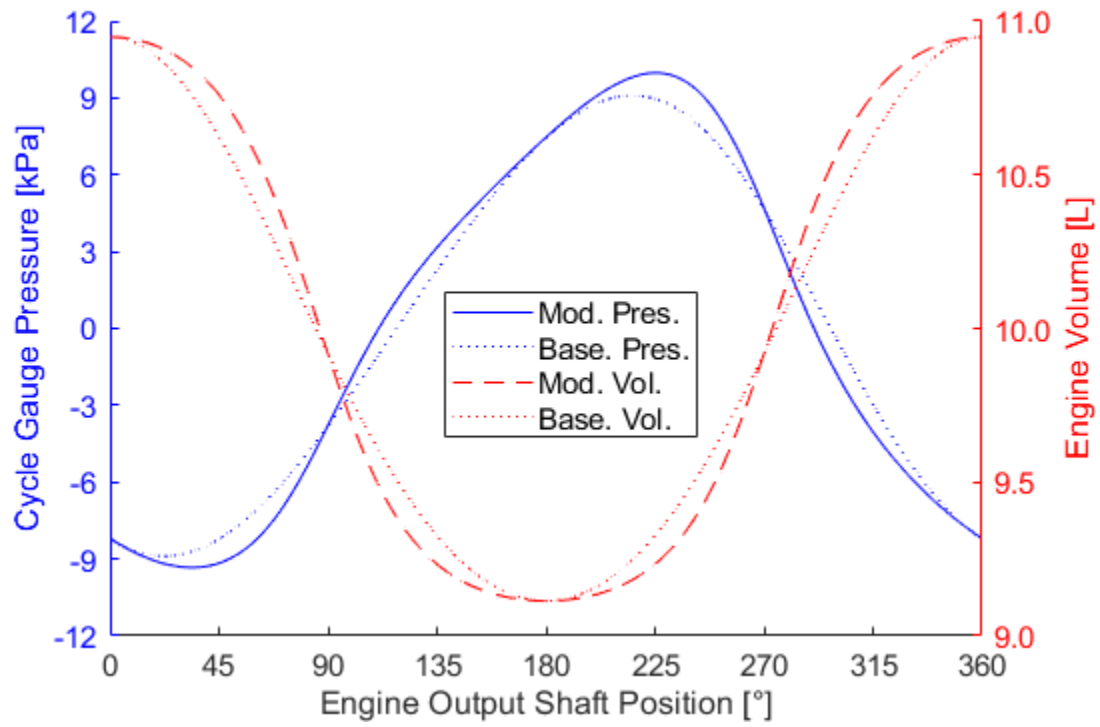
The piston dwelling modeling uses non-circular centrode equations for the relationship between the engine output shaft and the piston crankshaft, while maintaining a conventional motion profile for the displacer. Model number 4 dwells the piston with the $e = 1/5$ centrode profile, while model number 5 dwells the piston with the $e = 1/3$ centrode profile. The motion is phased in such a way so as to dwell the piston at TDC and BDC. The advantage of this dwelling pattern is to shorten the duration expansion and compression strokes of the piston so that they take place during the maximum and minimum cycle pressures. Conceptually this should have similar results as the displacer dwelling explored in section 2.3.2, but with shortening a portion of the cycle instead of prolonging one.

Results plotted in Figure 2.9(a) displays a similar filling out of the corners of the indicator diagram as compared to Figure 2.7(a) as anticipated. The similarity remains for the $e = 1/3$ centrode dwelled cycle as shown in Figure 2.10(a), which bears a strong resemblance the dwelled displacer counterpart Figure 2.8 (a).

Examining the pressure and volume curves of Figure 2.9(b) and Figure 2.10(b) it can be noted that the dwelling of the piston has the anticipated effect of changing the volume variation of the cycle. Of note is that the shape of the pressure curves change more substantially than for the dwelled displacer models, as both the peak pressures are changed as well as distorted towards the mid piston stroke points when compared to the baseline model results.

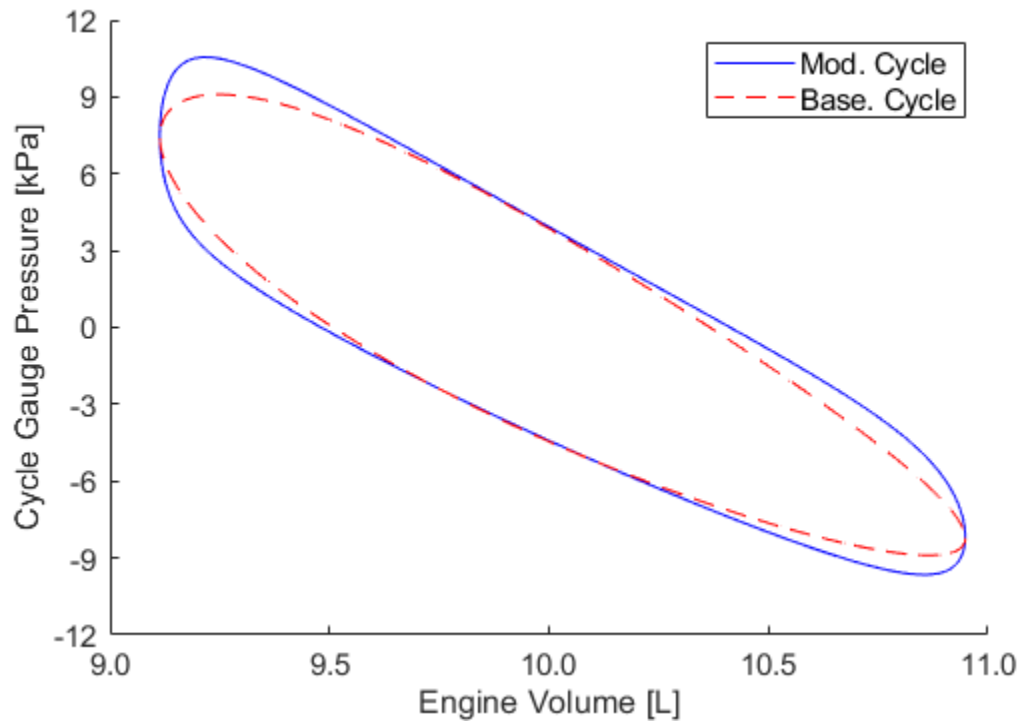


(a)

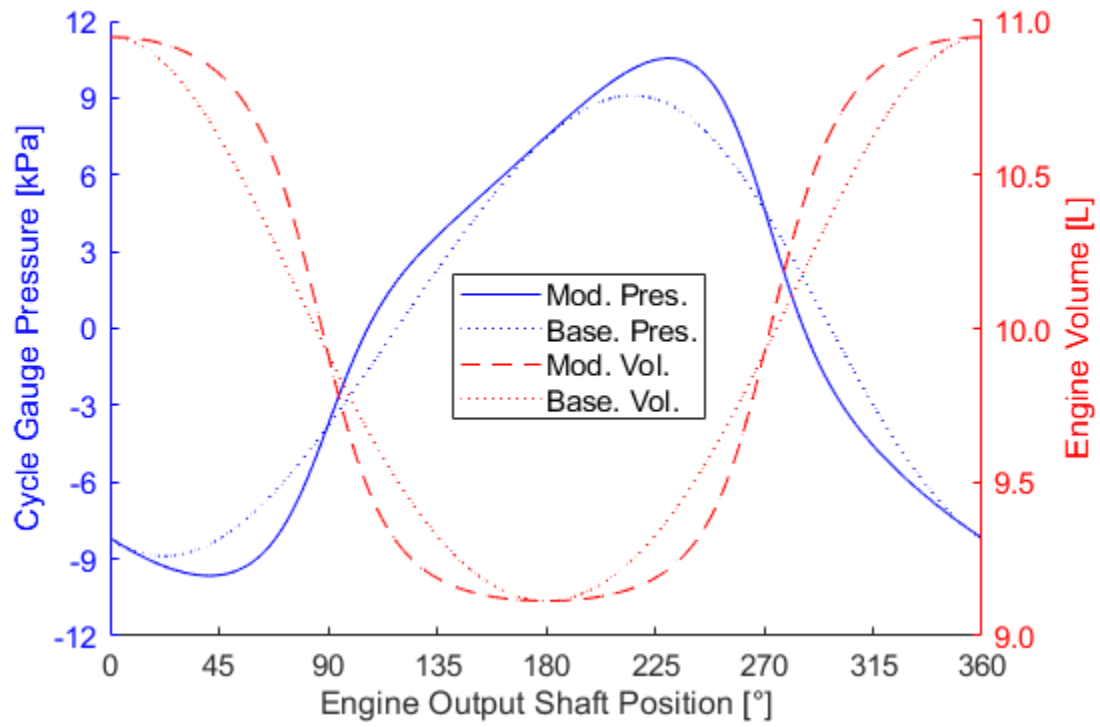


(b)

Figure 2.9 – Model no. 4: dwelled piston $e = 1/5$ isothermal (a) indicator diagram and (b) pressure and volume curves



(a)



(b)

Figure 2.10 – Model no. 5: dwelled piston $e = 1/3$ isothermal (a) indicator diagram and (b) pressure and volume curves

The results of the work predictions of the models are listed in Table 2.4. In further support of the model similarities between the dwelled displacer and the dwelled piston, the percent differences in the model results when compared to the baseline case are <1% different when comparing to the results in Table 2.3. Results suggest that the dwelling of the piston has the potential to increase the shaft work of the cycle by 13.2% and 20.5% for the centrodies of eccentricity $e = 1/5$ and $e = 1/3$ respectively based on the model parameters. Both results suggest that piston dwelling has the potential to improve engine work.

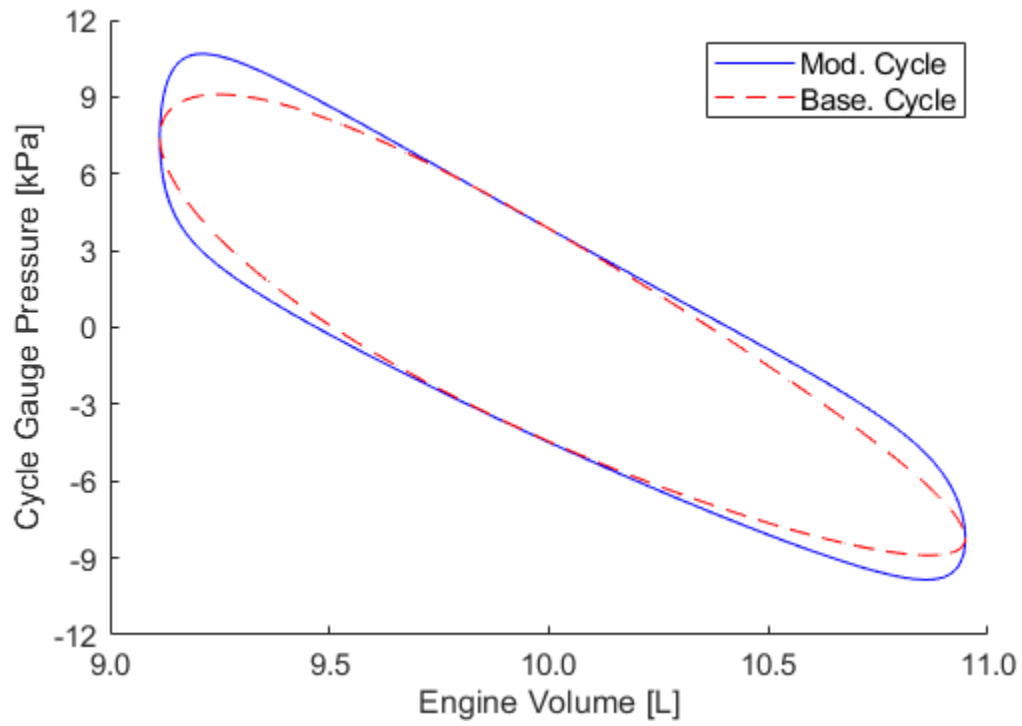
Table 2.4 – Piston dwelling modeling results

Model Parameter	Model No.	Centrode e		Value	Units	Diff. over Baseline [%]
		Disp.	Pist.			
Indicated work W_{ind}	4	$e = 0$	$e = 1/5$	13.15	J	9.0
Forced work W_{FW}	4	$e = 0$	$e = 1/5$	2.67	J	-15.0
Estimated shaft work W_S	4	$e = 0$	$e = 1/5$	9.32	J	13.2
Indicated work W_{ind}	5	$e = 0$	$e = 1/3$	13.76	J	14.1
Forced work W_{FW}	5	$e = 0$	$e = 1/3$	2.40	J	-23.7
Estimated shaft work W_S	5	$e = 0$	$e = 1/3$	9.93	J	20.5

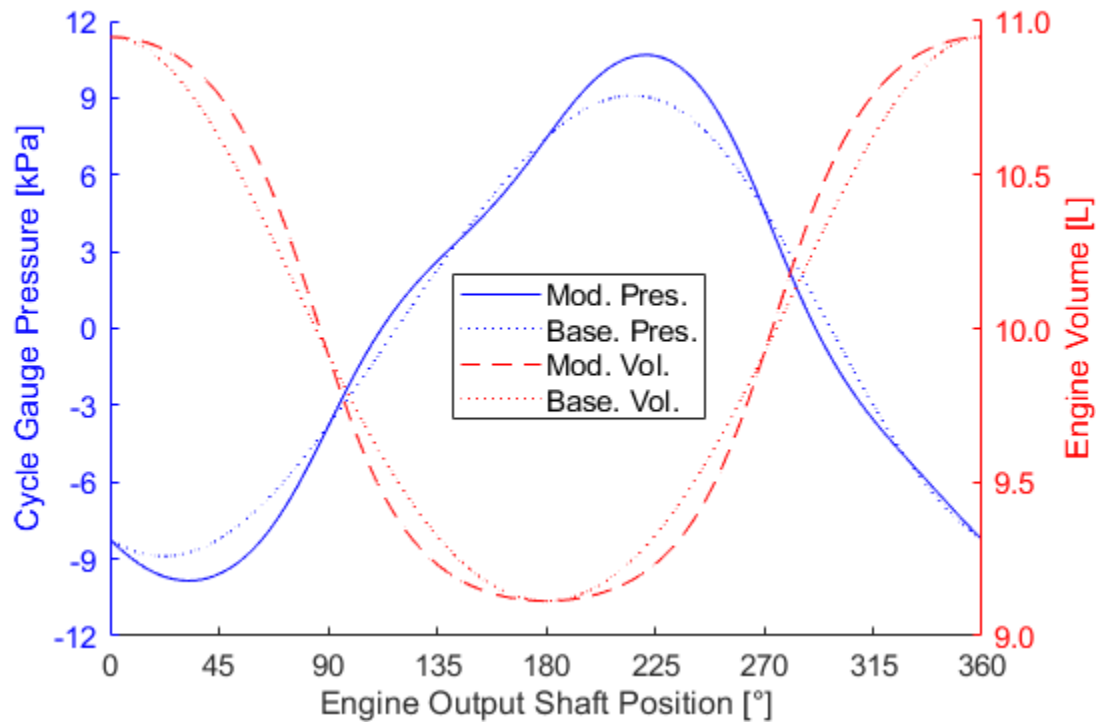
2.3.4 Combined Displacer and Piston Dwelling

The next batch of models included the simultaneous dwelling of both the displacer and piston via the non-circular centrode transmission functions. Two models were made. Model 6 applied $e = 1/5$ centrode relationships to the displacer crankshaft and the piston crankshaft. The centrodes were phased 90° apart relative to the output shaft so as to alternate dwelling of the the displacer and the piston during the cycle. Model number 7 is configured the same as model 6 but uses the $e = 1/3$ centrode relationships. It was decided to not model variations using the $e = 1/3$ centrode in combination with the $e = 1/5$ centrode as it was felt these variations would be redundant as the results would lie between model 6 and 7. It was anticipated the combined dwelled results would most closely resemble an ideal Stirling cycle out of all the motion modifications modeled as the combined dwelled cycles have the least overlap in displacer and piston motion profiles.

Examining the model indicator diagrams shown in Figure 2.11(a) and Figure 2.12(a) the effects of the combined dwelling trend towards the shape of the ideal indicator diagram. There are clear trends towards filling out the corners in both the $e = 1/5$ dwelled model and more significantly in the $e = 1/3$ dwelled model. Examining the pressure and volume curves in Figure 2.11(b) and Figure 2.12(b) it can be seen the increase in indicator diagram area is attributable to both the increase in the maximum and minimum pressures obtained by the cycles just prior to the expansion and the compression strokes of the piston when compared to the baseline cycle. The curves also share the characteristics of dwelled displacer and dwelled piston models as expected.

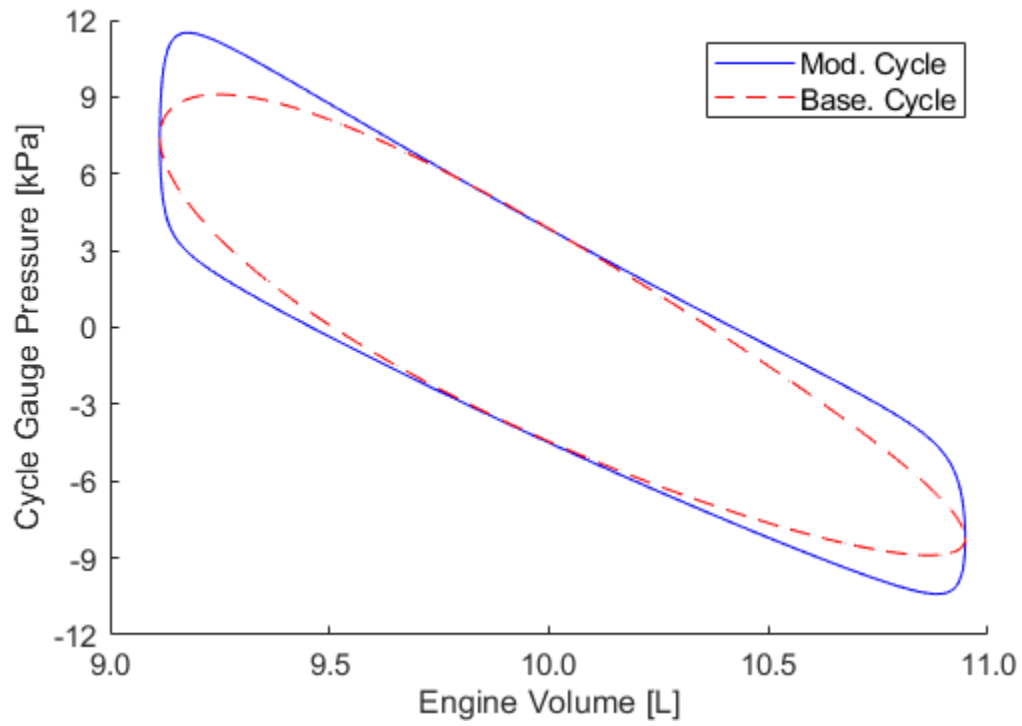


(a)

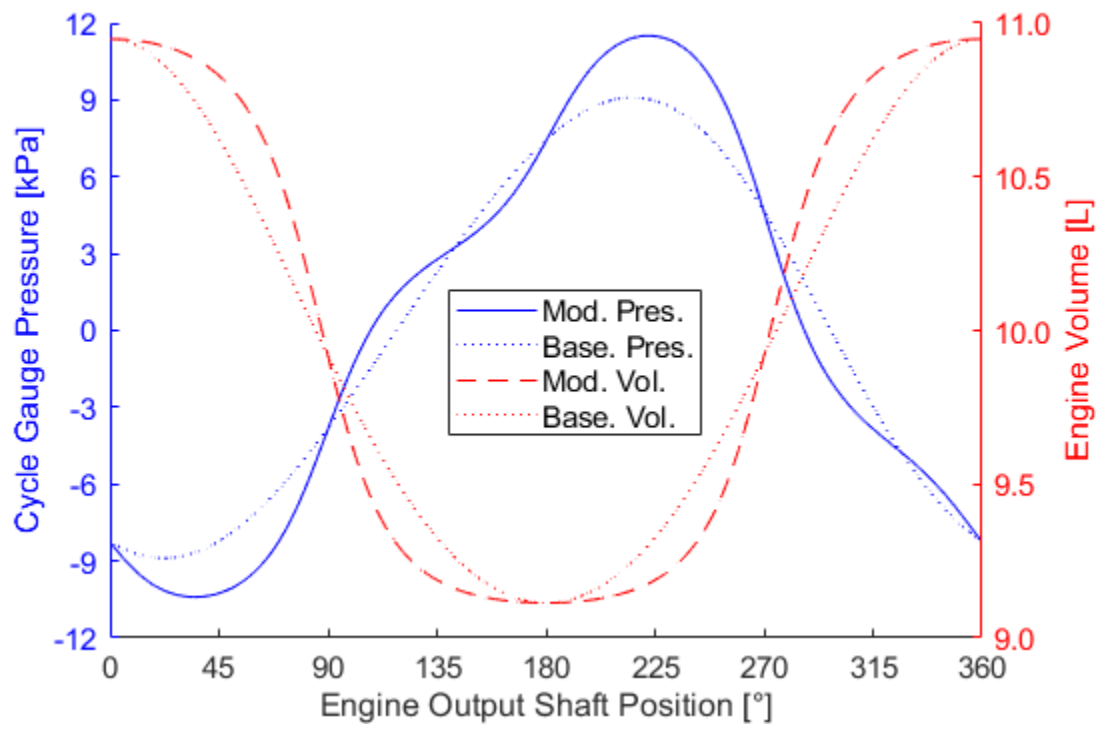


(b)

Figure 2.11 – Model no. 6: combined dwelled piston $e = 1/5$ and displacer $e = 1/5$ isothermal (a) indicator diagram and (b) pressure and volume curves



(a)



(b)

Figure 2.12 – Model no. 7: combined dwelled piston $e = 1/3$ and displacer $e = 1/3$ isothermal (a) indicator diagram and (b) pressure and volume curves

The results of the work predictions of the combined dwell models are listed in Table 2.5. The results show the most substantial increases in the indicator diagram area and estimates of shaft work of all model results. Results suggest that the dwelling both the displacer and the piston has the potential to increase the shaft work of the cycle by 22.9% and 31.8% for the centrodcs of eccentricity $e = 1/5$ and $e = 1/3$ respectively when compared to the shaft power estimate of the baseline case.

Table 2.5 – Combined displacer and piston dwelling modeling results

Model Parameter	Model No.	Centrode e		Value	Units	Diff. over Baseline [%]
		Disp.	Pist.			
Indicated work W_{ind}	6	$e = 1/5$	$e = 1/5$	13.95	J	15.7
Forced work W_{FW}	6	$e = 1/5$	$e = 1/5$	2.31	J	-26.3
Estimated shaft work W_S	6	$e = 1/5$	$e = 1/5$	10.12	J	22.9
Indicated work W_{ind}	7	$e = 1/3$	$e = 1/3$	14.68	J	21.7
Forced work W_{FW}	7	$e = 1/3$	$e = 1/3$	1.98	J	-37.0
Estimated shaft work W_S	7	$e = 1/3$	$e = 1/3$	10.85	J	31.8

2.3.5 Triangle Displacer Motion with Dwelled Piston

A range of models were also investigated using an alternative phasing of the displacer using the $e = 1/5$ centrode relationships. This arrangement had the displacer centrode phased 90° ahead of the phasing evaluated in number 2. The concept behind this arrangement was to dwell the displacer at mid stroke rather than at TDC or BDC, which resulted in a displacement profile that resembled a triangular wave as shown in Figure 2.13. From this point forward this variety of motion modification is referred to as triangular motion.

This motion profile was investigated on the basis that the centrodes could be phased such that the maximum displacer velocities during the cycle could be lowered, which might have favourable results on pressure drop from flow friction in real engines [31]. The isothermal model however assumes no pressure drop occurs in the engine so likely real world results would not be reflected in the modeled results. In addition, this phasing would have the effect of shortening the time for the displacer at TDC and BDC, resulting in greater cycle component overlap, in contrast to goal of reducing cycle overlap to optimize the thermodynamic cycle. To counteract this overlap, the piston was modeled dwelled using the same arrangement as in models 4 and 5.

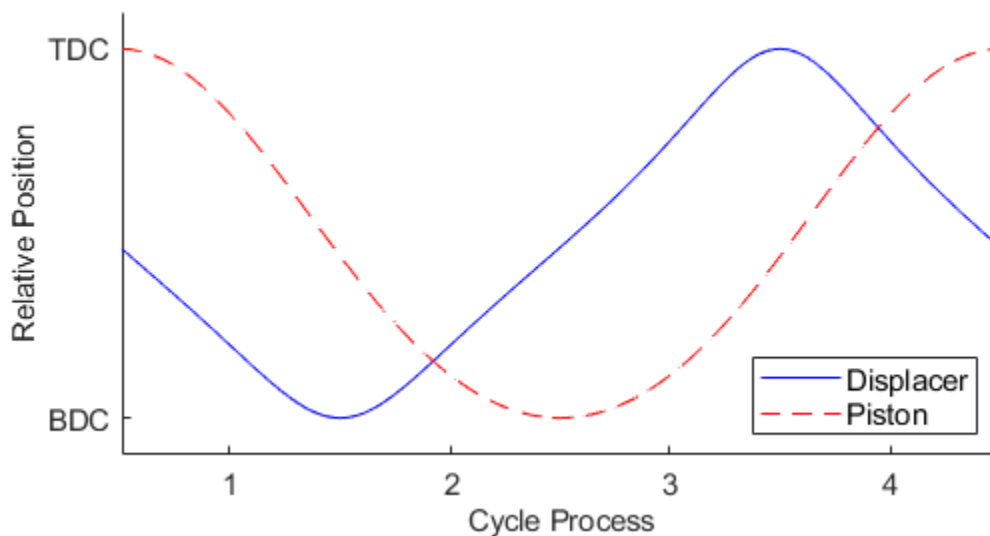


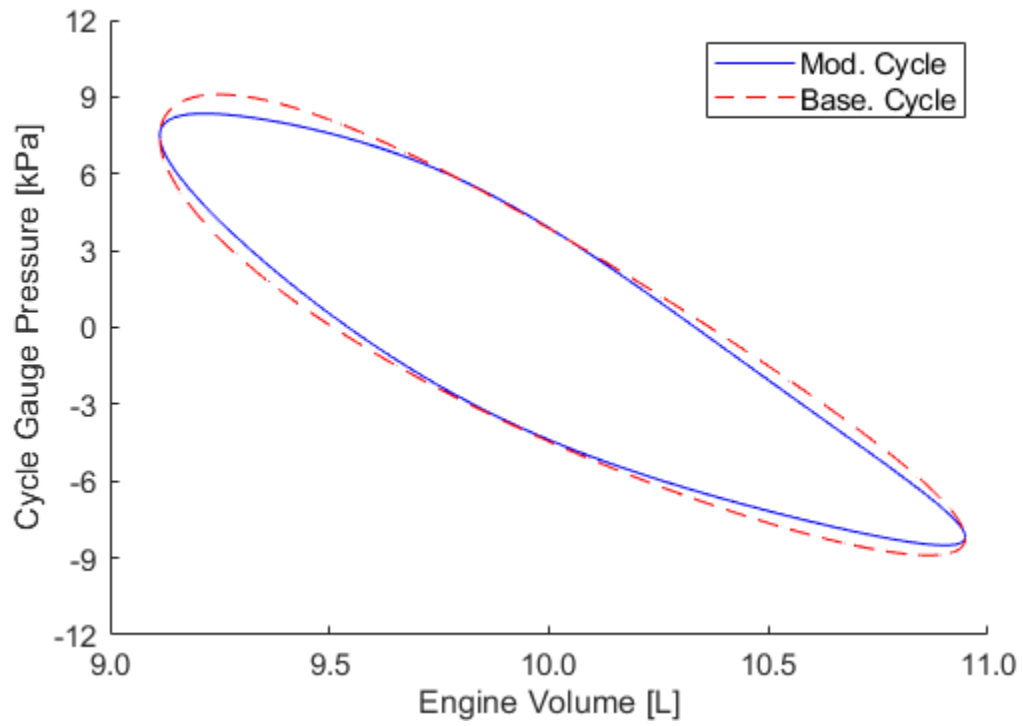
Figure 2.13 – Displacement profile of engine pistons for a displacer crankshaft phased $e = 1/5$ centrode and a conventional $e = 0$ centrode piston crankshaft

Model 8 uses the triangular displacer motion with the $e = 1/3$ centrode and conventional piston motion using the $e = 0$ centrode relationship serving as a control case for the triangular motion modification. Models 9 and 10 use the triangular displacer motion in conjunction with dwelling the piston using the $e = 1/5$ centrode and $e = 1/3$ centrode relationships accordingly.

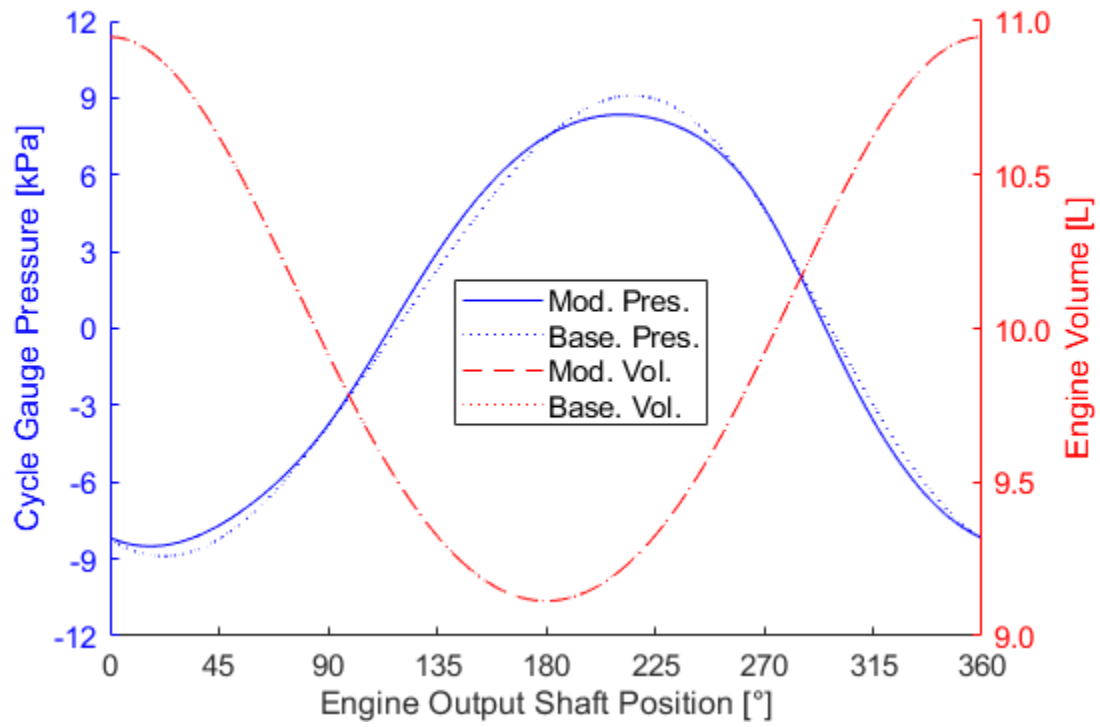
Figure 2.14(a) shows the results from model 8 with the triangular displacer motion paired with conventional piston motion. The results show the anticipated decrease in indicator diagram area resulting from increases in cycle overlap. Examining the pressure and volume curves shown in Figure 2.14(b) it is apparent that the increased process overlap had the effect of reducing the maximum and minimum cycle pressure swing prior to the expansion and compression stroke.

Figure 2.15(a) shows the interesting results from model Models 9 which utilized both $e = 1/5$ centrodes in phase with one another, moving the displacer in a triangular motion profile while dwelling the piston. The combined effect produced an indicator diagram that was nearly identical to the baseline conventional motion case. Examining the pressure and volume curves shown in Figure 2.15(b) reveals that despite the near identical indicator diagram there were changes to the pressure and volume curve when compared to the baseline case.

Figure 2.16 (a) shows the results from model 10 with the triangular displacer motion and the dwelled piston using the $e = 1/3$ centrodes. The indicator diagram shows a modest increase in the indicator area. This was anticipated given that the increased overlap of the cycles due to the triangular motion of the displacer should have been entirely counteracted by the dwelled piston such that the process overall would be less than the baseline case. Examining the pressure and volume curves shown in Figure 2.16 (b) reveals strong similarities to the model 4 results shown in Figure 2.9 (b). There are increases to the cycle pressure swing prior to expansion and compression strokes of the power piston.

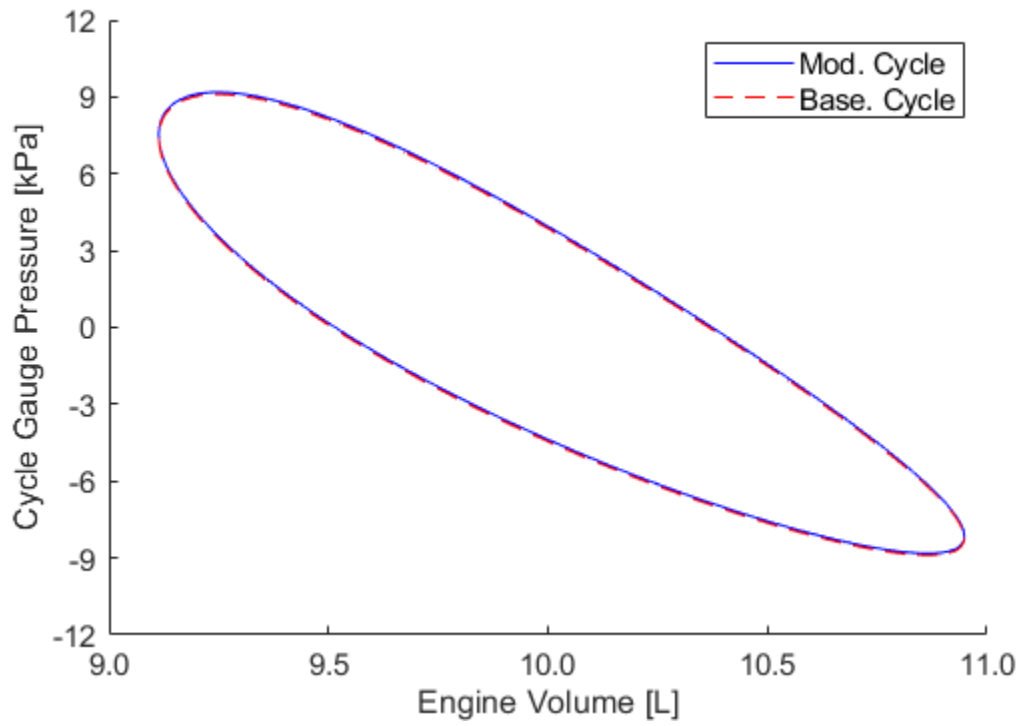


(a)

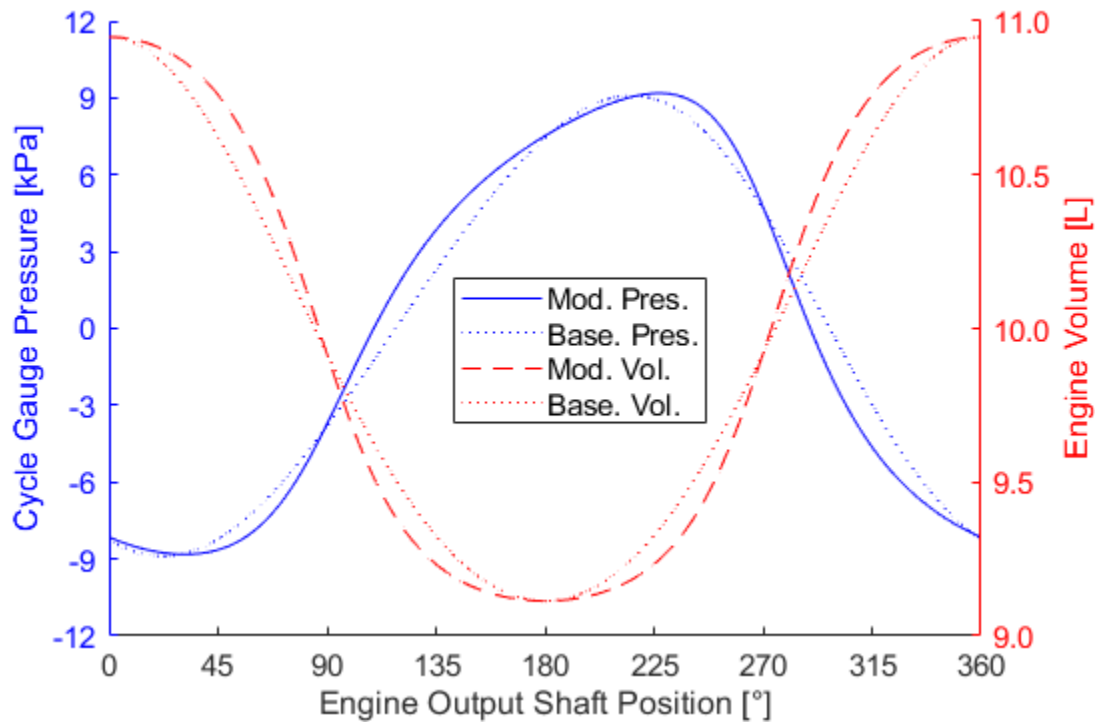


(b)

Figure 2.14 – Model no. 8: triangle displacer $e = 1/5$ and conventional piston $e = 0$ isothermal (a) indicator diagram and (b) pressure and volume curves

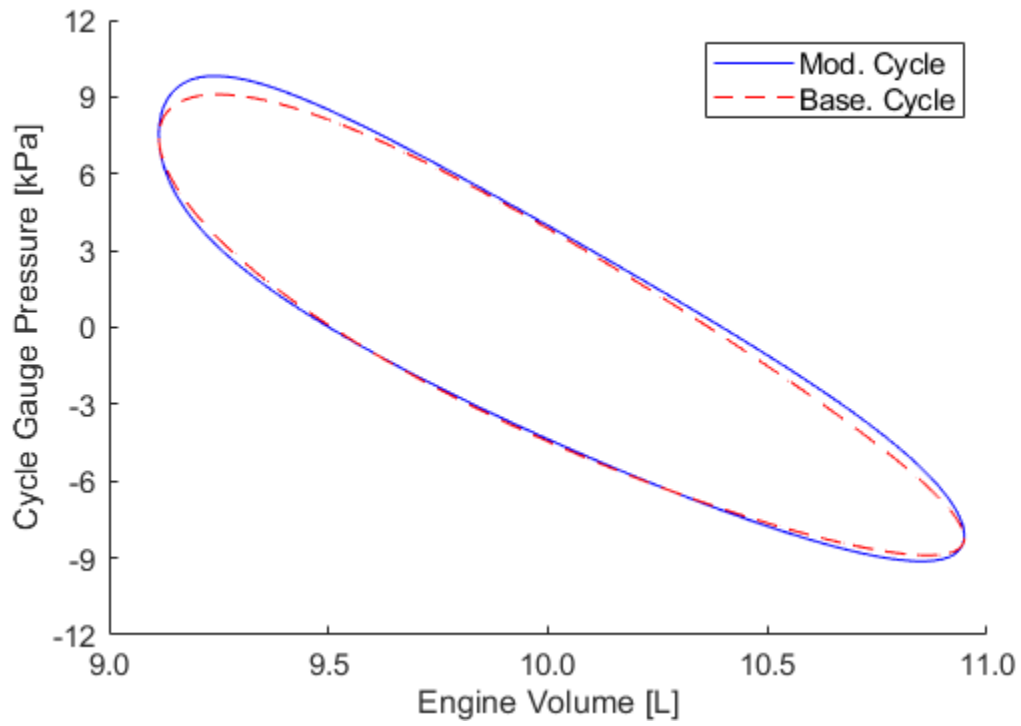


(a)

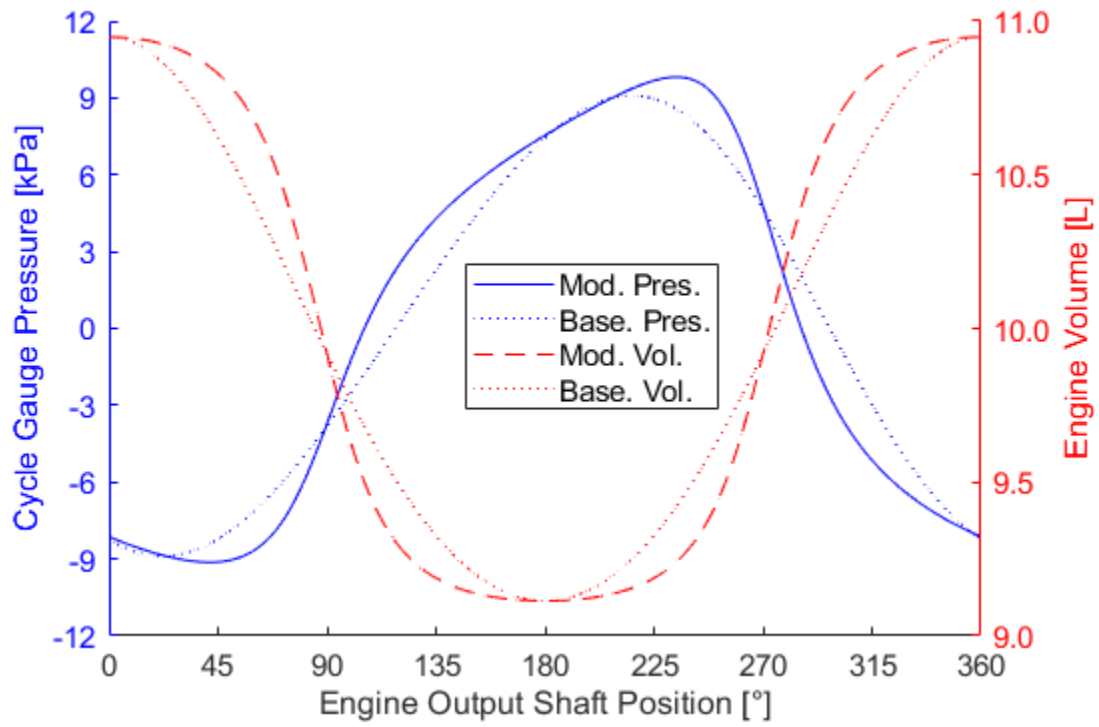


(b)

Figure 2.15 – Model no. 9: triangle displacer $e = 1/5$ and conventional piston $e = 1/5$ isothermal (a) indicator diagram and (b) pressure and volume curves



(a)



(b)

Figure 2.16 – Model no. 9: triangle displacer $e = 1/5$ and conventional piston $e = 1/3$ isothermal (a) indicator diagram and (b) pressure and volume curves

The results of the work predictions for the triangular motion models are listed in Table 2.6. The results from model 8 are unfavourable, showing not only a decrease in indicated work, but also a substantial increase to forced work, resulting in a estimated loss of shaft work of -15.8% when compared to the baseline case. As discussed earlier, the results from model 9 indicate the shaft work from the cycle is anticipated to be nearly identical to the baseline case, differing by only 0.2%. Model 10 shows the greatest potential of the group of triangular motion configurations, with an estimated increase in shaft work of 9.8%.

Table 2.6 – Triangle displacer and dwelled piston modeling results

Model Parameter	Model No.	Centrode e		Value	Units	Diff. over Baseline [%]
		Disp.	Pist.			
Indicated work W_{ind}	8	$e = 1/5^*$	$e = 0$	10.74	J	-11.0
Forced work W_{FW}	8	$e = 1/5^*$	$e = 0$	3.67	J	17.1
Estimated shaft work W_S	8	$e = 1/5^*$	$e = 0$	6.94	J	-15.8
Indicated work W_{ind}	9	$e = 1/5^*$	$e = 1/5$	12.07	J	0.1
Forced work W_{FW}	9	$e = 1/5^*$	$e = 1/5$	3.13	J	-0.4
Estimated shaft work W_S	9	$e = 1/5^*$	$e = 1/5$	8.25	J	0.2
Indicated work W_{ind}	10	$e = 1/5^*$	$e = 1/3$	12.87	J	6.7
Forced work W_{FW}	10	$e = 1/5^*$	$e = 1/3$	2.78	J	-11.3
Estimated shaft work W_S	10	$e = 1/5^*$	$e = 1/3$	9.05	J	9.8

2.4 Model Result Discussion and Limitations

The results from the isothermal model support theory that non-circular gearing can be applied to a Stirling engine drive mechanism in the pursuit of increasing indicated work. The dwelling of the displacer and piston had the anticipated effect of reducing overlap of the cycle thermodynamic processes in the engine and achieving a more ideal cycle indicator diagram.

The results of the isothermal model are predicated on many assumptions as listed in section 2.1. These assumptions limit the accuracy of the model when considering the performance of a real engine. The prescribed temperatures of the engine working spaces, and consequently the engine working fluid, is a significant assumption. With regards to the modeled motion modifications, it is unclear what impact the motion modifications will have on the heat transfer in the engine spaces. Using the results of the derivative function as shown in Figure 2.4, the displacement speeds of the pistons using the modified motion will increase to twice the speed of a conventional motion profile when using the $e = 1/3$ centrode set.

The effects of piston speed on pressure drop from working fluid flow in the engine is also not accounted for by the isothermal model, as it explicitly assumes no pressure drop in the engine. The isothermal model results show that most of the the gains in indicated work and shaft work are derived from increases in the maximum and minimum pressure swing of the engine. If the pressure drop resulting from the flow friction is substantially increased from motion modification the gains seen in the model may not be realized for a real engine.

Finally, the calculation of shaft work relies on the assumption of a constant mechanism effectiveness, which as noted in section 1.3.7 is a simplifying assumption. If the use of non-circular centrodes in the drive mechanism substantially decreases the mechanisms effectiveness by increasing mechanism friction losses, then gains of indicated work may not result in any gains to shaft power, and in the worst case my results in negative shaft work and an inability of the engine to run.

3 EXPERIMENTAL EQUIPMENT AND INSTRUMENTATION

This chapter provides a detailed description of the experimental set up used in this investigation, including a detailed description of the retrofit of the EP1 LTD Stirling engine into the tested EP1-M Stirling engine. Details of the experiment support equipment and instrumentation used for engine data collection is also provided. Detailed drawings of the complete engine assembly, as well as the lower engine pressure she assembly, are located in Appendix F.

3.1 The EP1-M LTD Gamma Stirling Engine

The EP1-M engine as described in this work is an evolution of an experimental low temperature differential engine designed and built by the Dynamic Thermal Energy Conversion Laboratory (DTECL) at the University of Alberta in 2017 with support from Terrapin Geothermics Ltd. This engine was designated the EP1 engine. It was first run in 2018 after a redesign of the piston from a conventional piston cylinder to a pleated elastomer bellow. A series of performance tests and optimizations of the EP1 was done by Stumpf [40]. These examined changing phase angle (α) and Compression ratio (CR) to optimized engine power output at a thermal source temperature of 95° C and a thermal sink temperature of 5° C. The recommendations from this optimization were carried forward into the drive mechanism retrofit to the engine to examine piston motion modification. The engine designation was changed to EP1-M to distinguish it from the original configuration. This section will describe the key design features of the EP1-M engine as tested in this investigation. A partial section view of the EP1-M solid model is depicted in Figure 3.1 with annotations identifying key components.

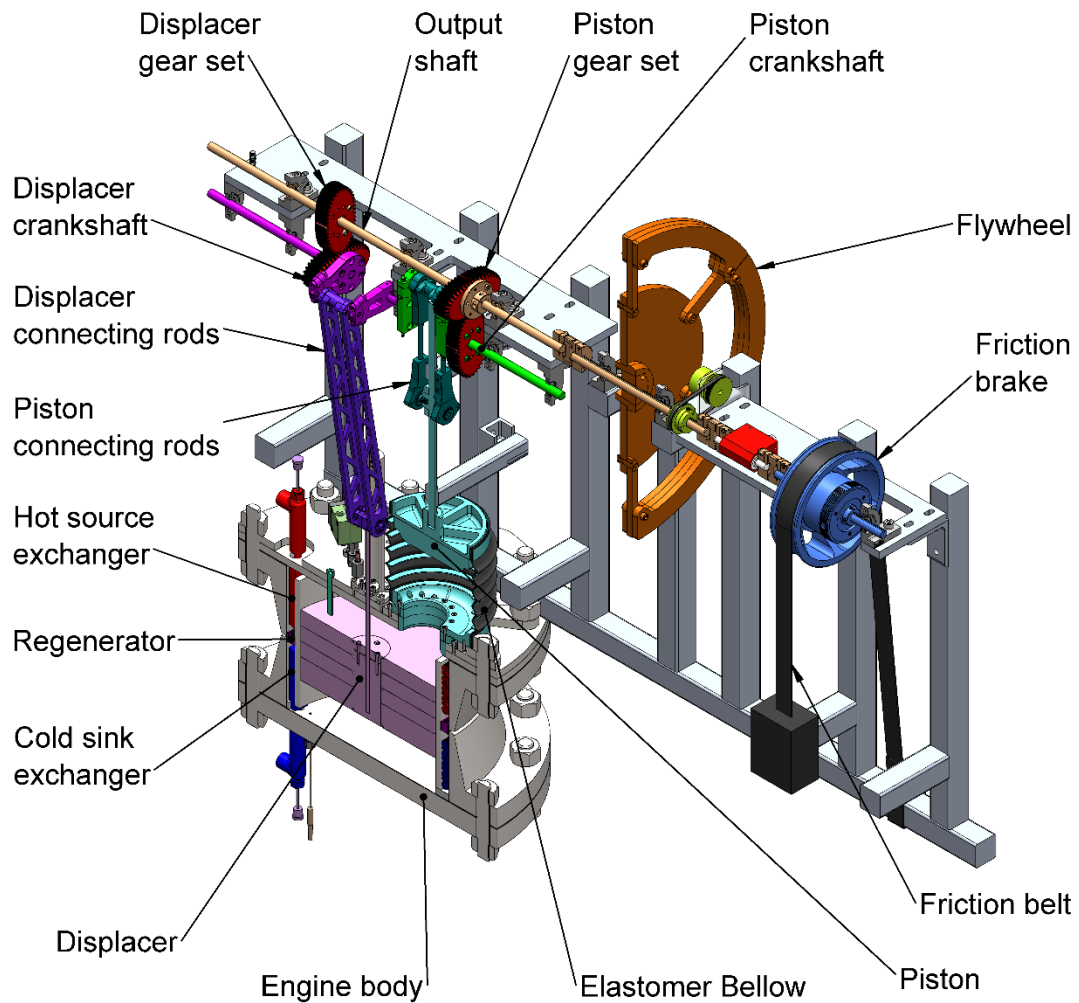


Figure 3.1 – Annotated partial section view of the EP1-M low temperature Stirling engine identifying key components

3.1.1 Engine Body Pressure Shell

The EP1 as initially conceived was going to be operated mean cycle pressures above atmospheric pressure. To retain the pressurized working fluid the engine body shell was manufactured from two ASME B16.5 12in class 150 weld neck flanges mounted back to back, resulting in a 12in internal diameter bore. The internal diameter housed annular heat exchangers, the regenerator, as well as the expansion and compression spaces formed by the sweep of the displacer. The compression space is capped by a class 150

blind flange machined with access ports for the cold side heat exchanger and measurement instruments. The cap of the expansion space is manufactured from two 1in thick plates of acrylic plastic. The expansion space cap has penetrations for the hot side heat exchanger, instruments, the displacer rod, as well as the access port to the bellow piston. A section view of the pressure shell solid model is shown in Figure 3.2.

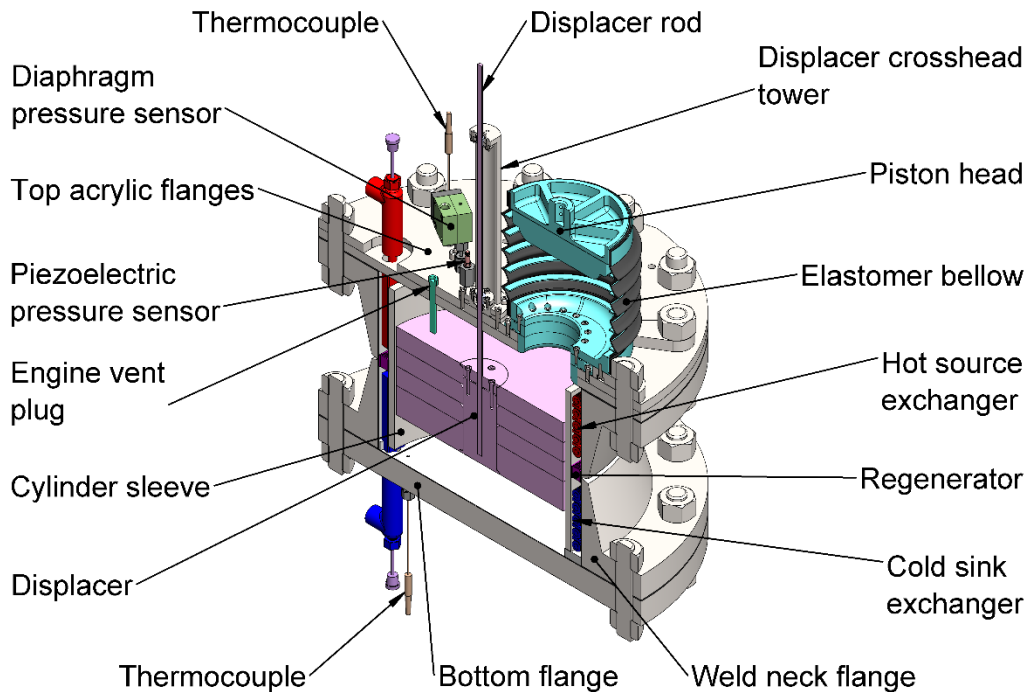


Figure 3.2 – Section view of the EP1-M engine body

3.1.2 Finned Tube Heat Exchangers & Regenerator

The heat exchangers of the EP1-M are mounted in the annular gap between the pressure shell and the displacer cylinder. Given the small annular volume, a finned tube coil heat exchanger was used in the design. Source and sink exchangers are identical in-line stacks of 5 copper finned tubes. The tube banks are fed from an inlet manifold and emptied from a mirrored outlet manifold that pass through the pressure shell caps and connect to the source and sink loops. Improvements to EP1 the heat exchanger included the addition of flow diverters between the exchanger coils to force the flow of

working fluid back on to the center of the next coil as shown in the heat exchanger solid model shown in Figure 3.3.

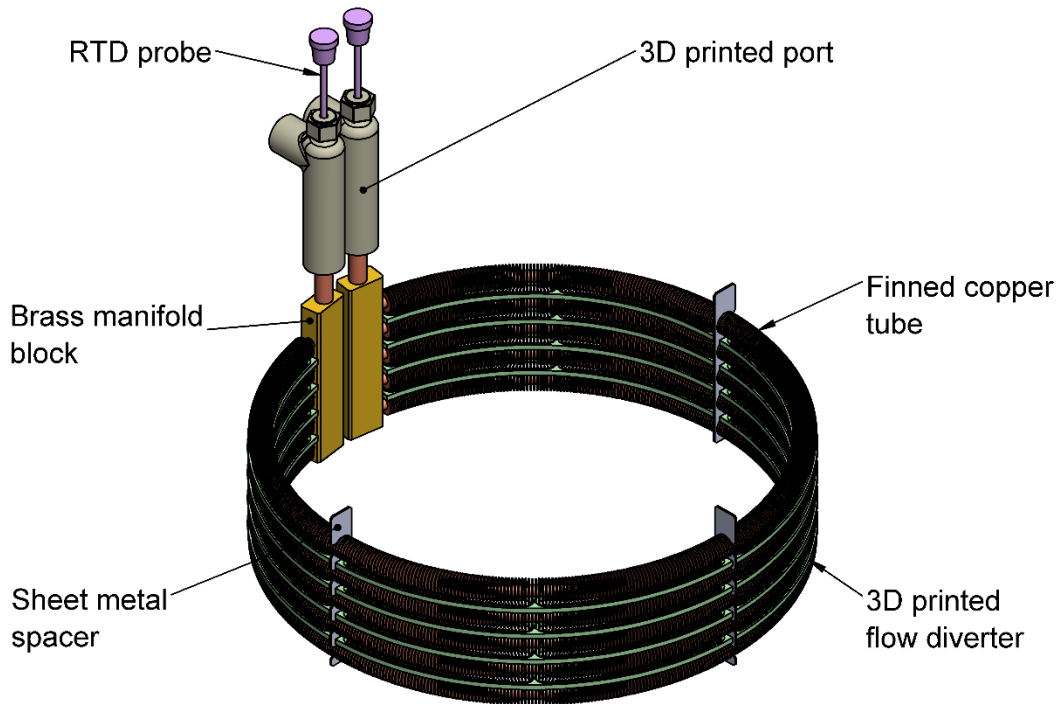


Figure 3.3 – Annotated view of the EP1-M heat exchangers and regenerator stack

A simple regenerator was designed to fit between the hot exchanger and cold exchanger in the annular gap. It consists of sections of thin radial rectangular channels 3D printed in ABS plastic. The rectangular channels have a hydraulic diameter of 1.5mm wide by 11.5mm tall and have a length of 15mm and are shown in Figure 3.4. The rectangular channel regenerator was designed minimize flow loss. Geometric details of the heat exchanger coils and regenerator are listed in Table 3.1 and Table 3.2 respectively.

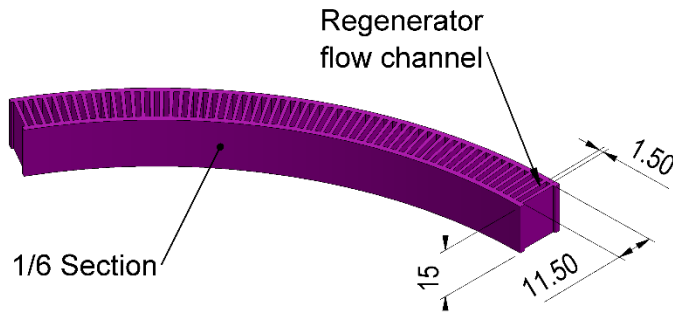


Figure 3.4 – Solid model of 3D printed regenerator section annotated with flow channel dimensions

Table 3.1 – Heat exchanger properties

Property	Value
Heat exchanger material	Copper & Brass
Finned tube ID [mm]	4.6
Finned tube OD [mm]	12.7
Working fluid exposed surface area [m ²]	0.553
Component dead volume [L]	0.36

Table 3.2 – Regenerator properties

Property	Value
Regenerator material	ABS
Working fluid exposed surface area [m ²]	0.182
Component dead volume [L]	0.11

3.1.3 Elastomer Bellow Piston

The piston of the EP1-M consists of a 3D printed resin piston head that is fixed to a cylindrical pleated elastomer bellow. A detailed partial section view of the modeled piston with annotations is shown in Figure 3.5. The design was departure from more conventional piston cylinder designs and offers some unique advantages. Expansion and compression of the bellow permits engine volume changes with no sliding seals which reduces friction. The bellow design also accommodates large misalignment

between the piston head and the engine which that facilitated manufacture of the engine without precision machining. Additional reinforcement structures were added to the bellow pleats to limit radial expansion and compression of the piston that cannot be captured by the piston head and output to the engine mechanism.

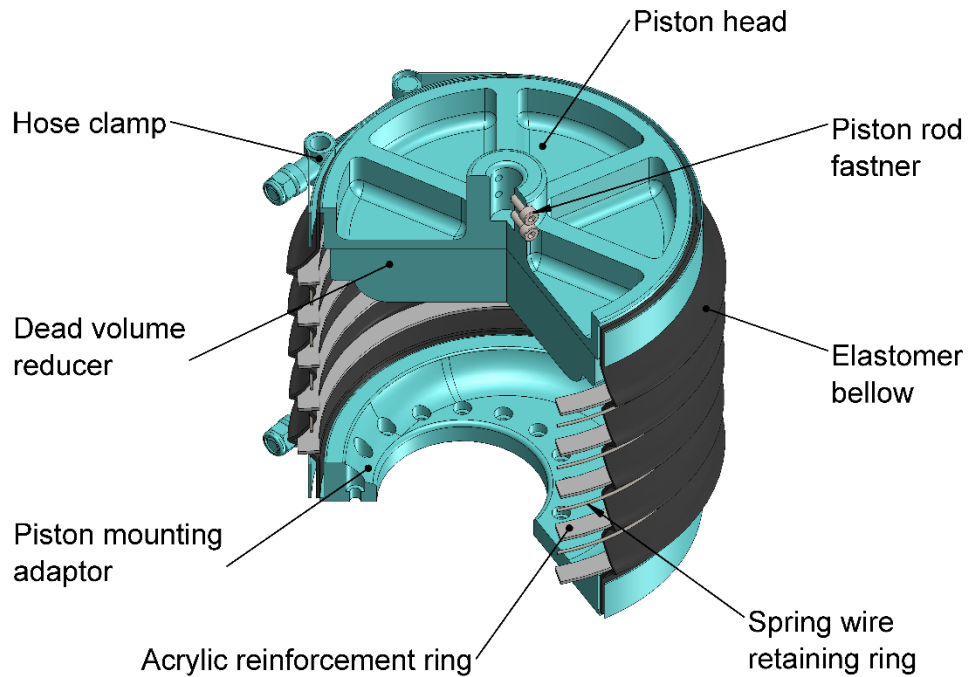


Figure 3.5 – Partial section view of the solid model of the EP1-M elastomeric piston bellow and internal structures

The base of the piston assembly is affixed to the engine top flange via a 3D printed resin piston mounting adaptor that connects the piston working space with the engine working space. The adaptor was made necessary as the original EP1 piston was of a smaller diameter. A hollow dead volume reducer is affixed to the piston head to take up dead volume in the piston as its minimum stroke height. Details for the piston design are listed in Table 3.3.

Table 3.3 – Piston properties

Property	Value
Piston materials	Resin, Elastomer, ABS, Acrylic, Steel
Piston swept volume [L]	1.78
Piston dead volume [L]	0.49

Figure 3.6 depicts the piston connection to the piston crankshaft. The 1/2 inch aluminum piston rod is constrained by PTFE linear bushings mounted to directly to the drive mechanism frame. The piston rod drives the crosshead block which transmits force to the piston connecting rods. The rod lengths are adjustable to accommodate changes to stroke length and adjustments to minimized dead volume at BDC. All the radial bearings on the connecting rod pivots are open ball bearings to minimize friction.

The piston swept volume can be changed by adjusting the length of the crank arms of the piston crankshaft. First the connecting rod axle is separated from the end of the crank arms, and then then spacer blocks are added between the arm and the axle to change stroke as can be seen in Figure 3.10.

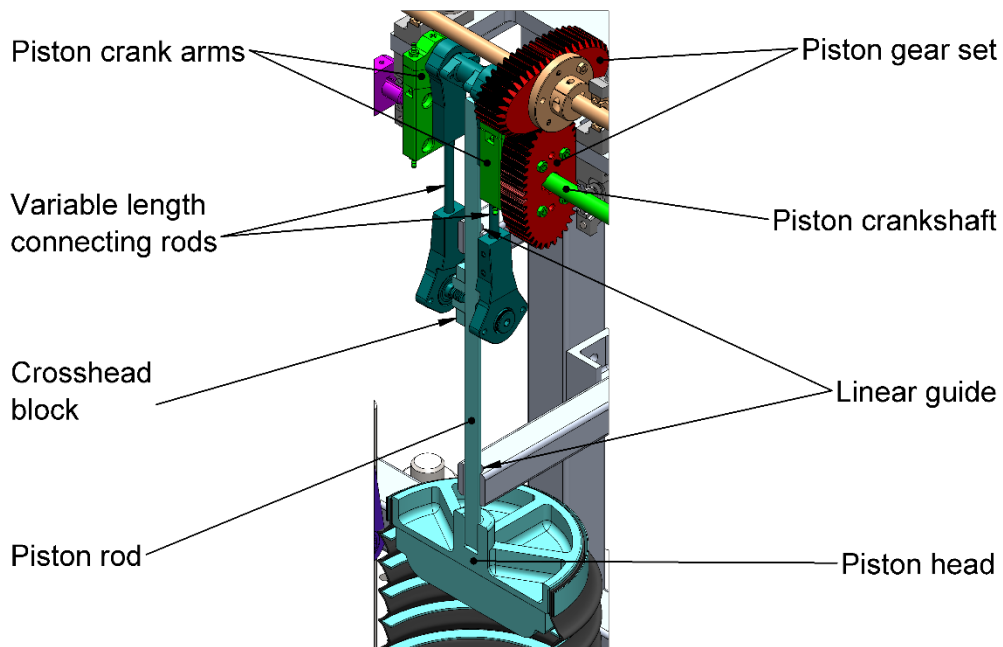


Figure 3.6 – Piston crosshead, connecting rods, and piston crankshaft

3.1.4 Displacer and Crosshead

The displacer of the EP1-M consists of a stack of closed-cell rigid polystyrene foam that is coupled via a 1/4 inch rod to the engine drive mechanism. A partial section view of the displacer is shown in Figure 3.7. The emphasis of the displacer design was to be light weight and effectively separate the engine compression and expansion spaces from one another thermally. Any gaseous fluids that exists within the pressure boundary of the engine must be limited so as to no contribute to additional dead volume within the engine. For both these reasons a closed cell rigid foam material was an ideal choice. The foam disks are held together with a 3D printed mandrel that connects the displacer to the piston rod.

A small diameter rod is ideal as the rod pierces the engine working space boundary, and thus the cross-sectional area of the rod acts as miniature piston. The volume displaced by the rod also slightly changes the expansion space volume. For the EP1-M the volume of the rod that enters and leaves the engine is 3.67mL, while the swept volume of the piston is 1.78L. The change in volume due to the displacer rod is thus considered negligible.

The radial movement of the displacer is constrained by PTFE linear bushings located in the engine top flange and at the top of the displacer crosshead tower, as can be seen in Figure 3.2. There is no shaft seal for the displacer rod at the pressure boundary as the lack of seal reduces friction, and allows a small leak point that is advantageous for equilibrating the mean cycle pressure to the atmospheric buffer pressure. General displacer properties are noted in Table 3.4.

Table 3.4 – Displacer properties

Property	Value
Displacer materials	Polystyrene foam and ABS
Displacer swept volume [L]	5.69

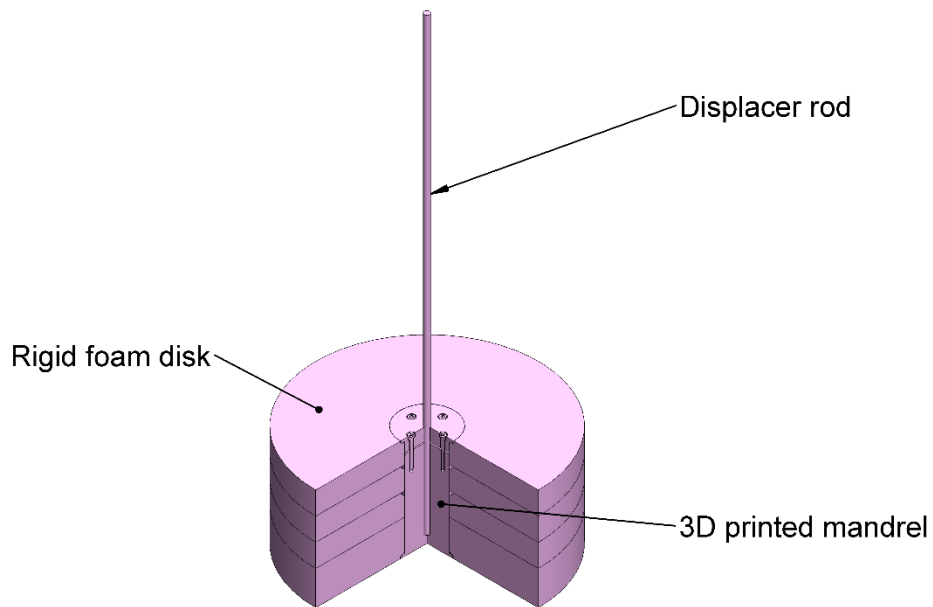


Figure 3.7 – Partial section view of the displacer solid model

Figure 3.8 shows detail of the displacer connecting rod and crank shaft. The connecting rods for the displacer are of a fixed length and were laser cut from acrylic sheet material. The bearings at the crosshead block pivots and on the displacer crankpin are open ball bearings to reduce friction. The crank pin at the end of the crank arms is removable to accommodate changing of the displacer gear set. The stroke length of the displacer is fixed at 116mm by the displacer crank arms.

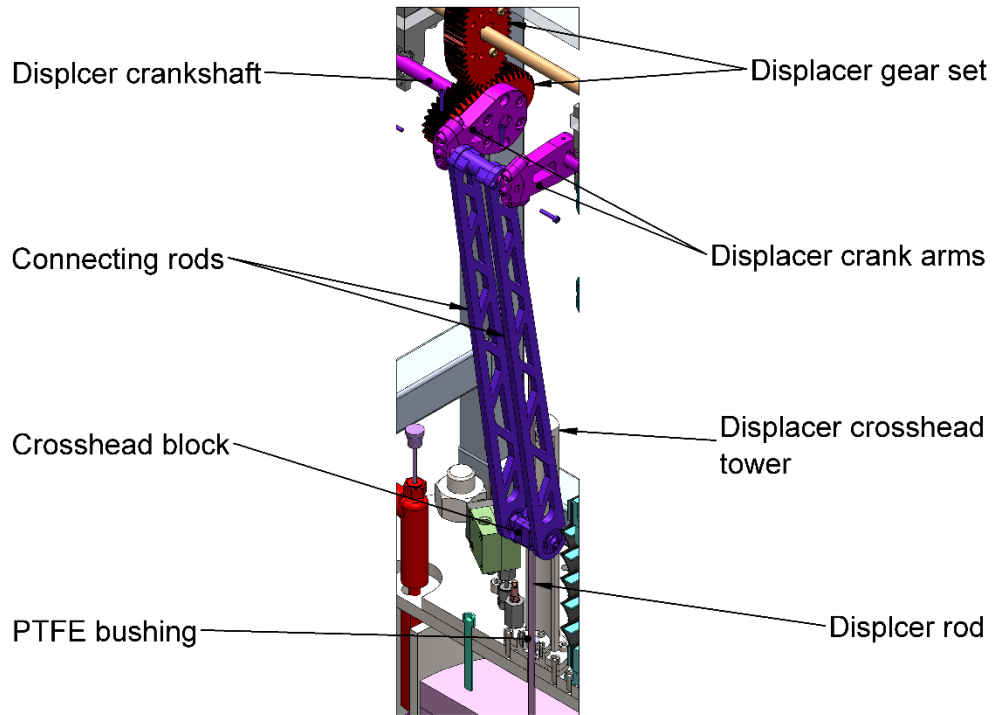


Figure 3.8 – Displacer crosshead, connecting rods, and piston crankshaft

3.1.5 Drive Mechanism and Engine Brake

The engine drive mechanism re-design was the most substantial upgrade of the EP1-M. The main components include the engine output shaft, the geared half crankshafts of the displacer and piston, and the engine flywheel. After the flywheel the engine instrumentation system is coupled to the output shaft, which includes a rotary encoder, a torque sensor, and the engine loading or brake system. A profile view of the engine drive mechanism is depicted in Figure 3.9.

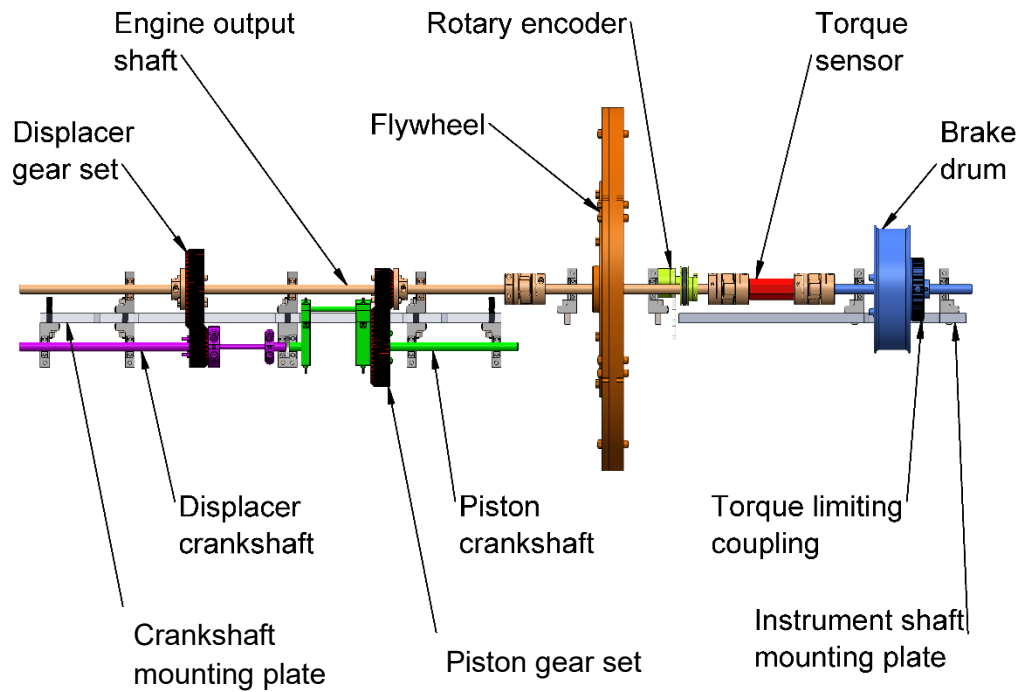


Figure 3.9 – Profile view of the EP1-M engine drive mechanism and instrumentation output

The multi-shaft design of the EP1-M was the physical implementation of the conceptual drive mechanism. The displacer and piston crankshafts are collinear and are spaced 3 inches axis to axis with parallel output shaft. Both sets of shafts are supported by ball bearings mounted in bearing blocks on either side of a common crankshaft mounting plate. All shafts are 12mm in diameter and have a standard 4mm keyway running their whole length. The design and manufacture of the gears is detailed in section 3.2. The gears are designed with keyways to ensure repeatable mounting and correct phasing.

The multi-piece design of the crankshafts permits the crankpins to be removed from the crank arms along with the connecting rods in order to change gear sets for different trials. An exploded view of the engine crank plate assembly is shown in Figure 3.10 with components disassembled for a gear change.

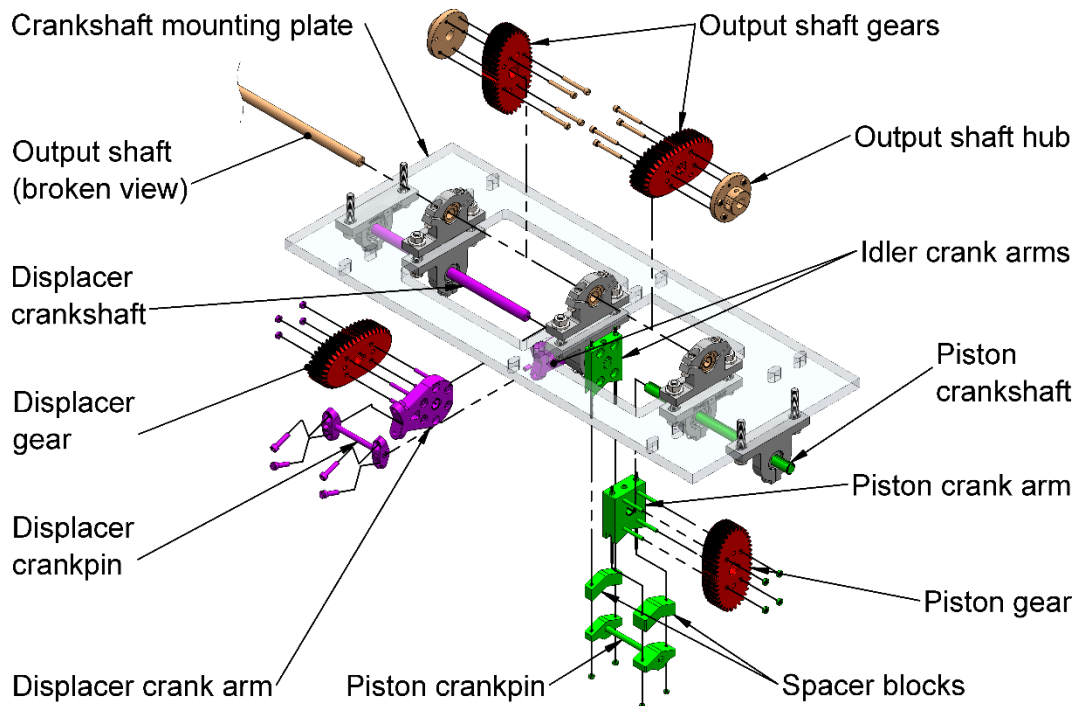


Figure 3.10 – Explode view of the engine crankshaft mounting plate used for swapping out the crank shaft gear sets.(mounting plate shown transparent for clarity)

The engine flywheel was recycled from a different engine for use on the EP1-M. The flywheel of the engine acts as a mechanical battery that smooths the intermittent mechanical power produced from the piston, and provides the force necessary to accomplish forced work sections of the cycle as discussed in section 1.3.7. This mechanical battery relies on the moment of inertia of the flywheel about its rotational axis. The flywheel design as used on the EP1-M was optimized by Miller [55] and features a ring of additional mass as shown in Figure 3.11. The derivative functions of the non-circular gears relies on the assumption that the engine output shaft rotates at a relatively constant speed. As such having a flywheel with as much moment of inertia as possible is important to the investigation.

The rotary encoder is mounted just after the engine flywheel and is used to measure the position of the engine output shaft. The encoder has a 1:1 rotation relationship with the output shaft by way of a toothed timing belt and pulleys. Models of the encoder and belt are shown in Figure 3.11. The pulley position is calibrated to engine top dead center

(TDC) as part of the experiment procedure of each trial. Details of the flywheel design are noted in Table 3.5.

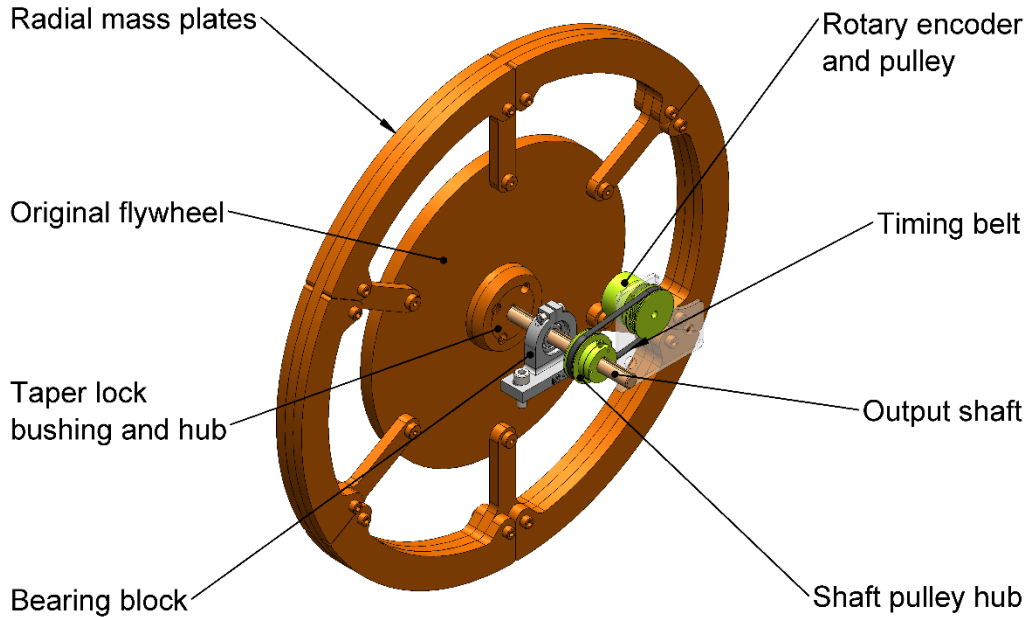


Figure 3.11 – Annotated view of flywheel and rotary encoder

Table 3.5 – Flywheel properties

Property	Value
Flywheel material	Steel
Mass [kg]	17.97
Polar Moment of Inertia [kg m ²] [55]	0.5995

The final two elements of the engine drive mechanism assembly is the torque sensor and the engine brake system as depicted in Figure 3.12. The torque produced from the engine driving against the load of the brake is measured by the torque sensor mounted in-line with the engine output shaft and the brake shaft. Load is applied to the engine by friction from a weighted belt draped over the brake drum as shown in Figure 3.12. During trials the belt was loaded with mass in increments of 71g to increase the brake friction. The mass increment is arbitrary as the exact value of the friction is not important, only in that it results in a load to counter engine torque. Friction can be

applied up to a threshold set by a magnetic hysteresis clutch, which acts as a torque limiting coupling between the brake drum to the engine output shaft. The clutch limits torque to $\tau \approx 1.2\text{Nm}$ before slipping to protect the torque sensor from overload above its maximum capacity of $\tau = 1.5\text{Nm}$ in the event of sudden engine overloads or stoppages. Part of the EP1-M upgrades included turning and polishing the brake drum to ensure that the application of load torque was consistent at all angular positions of the output shaft.

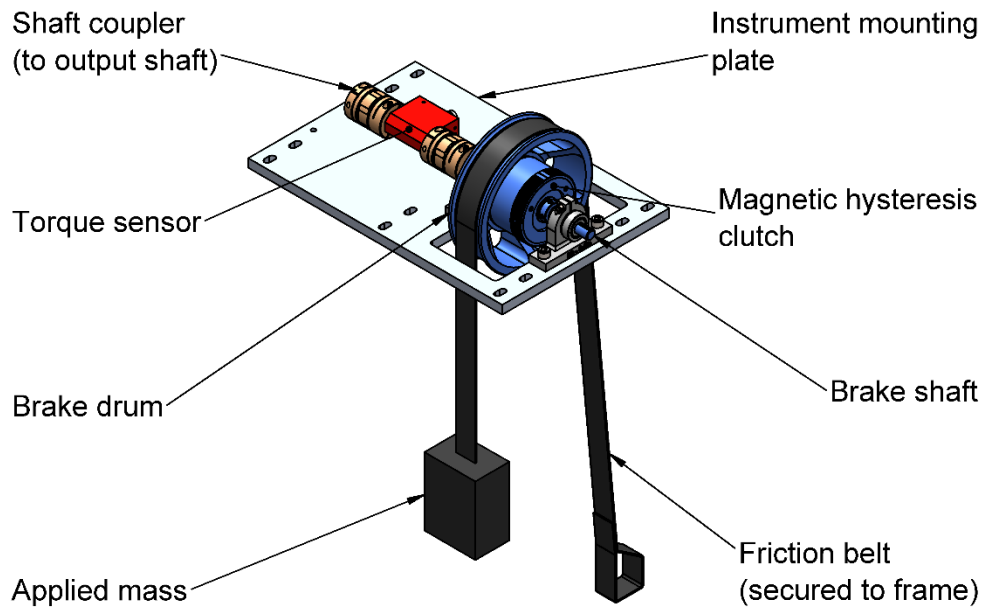


Figure 3.12 – Annotated view of instrument plate and friction brake assembly

3.2 Modeling and Manufacture of Oval Gears

With the theory of the oval non-circular centrodes established in section 2.2, it was necessary to generate the fully toothed profiles to produce gears for use in the engine drive mechanism. Toothed profiles were designed in commercial software and solid modeled with features necessary to integrate them into the drive mechanism design. For the experimental engine, three unique pairs of oval gears were 3D printed from ABS plastic using fused filament fabrication (FFF) methods.

3.2.1 Modeling the Non-Circular Involute Gears

Once selection of the target derivative function and the necessary non-circular centrodes was known, properties necessary for adding involute teeth were investigated. For detailed derivation of the theory of involute gearing for non-circular gears refer to the works of Litvin [51].

The following description makes reference to Figure 2.3. Assuming both centrodes had infinite friction, they would be able to transmit a force vector to one another at the instantaneous point of contact J , with the force vector oriented along the instantaneous tangent line of the two centrodes at J . For conventional round gears this tangent line is fixed and perpendicular to the vector between the centers of rotation for each gear. For non-circular centrodes, the angle of tangent line is continuously variable as defined by:

$$\tan \varphi_t = \frac{r(\theta)}{\frac{dr(\theta)}{d\theta}} \quad 3.1$$

where: $\varphi_t =$ angle of tangent line
 $r(\theta) =$ radius of the centrode as a function of angular position of the centrode about its axis

Instead of relying on friction between centrodes, involute gearing has meshing tooth profiles that permit the smooth transmission of force between mating centrodes. Through rotation a meshing involute curve makes rolling contact at points that lie along the line of contact. The involute curves are shaped such that each point on the involute curve is always normal to the line of contact for every contact point J of the centrodes. The instantaneous transmission force vector for the gear set is in line with the line of

contact. The angle of the line of contact relative to a line perpendicular to vector between the two centers of rotation is known as the gear pressure angle (φ_{pa}) of the gear pair.

For gears pairs the line of contact is offset from the tangent line of contact of the centrodes by a fixed angle φ_c which corresponds to the rack cutter angle used to cut the tooth profiles. The cutter angle is a property selected by the gear designer. The equation for the gear pair pressure angle is thus a function of the angle of the tangent line φ_t and the selected rack cutter angle φ_c as defined by:

$$\varphi_{pa} = \varphi_t + \varphi_c - 90^\circ \quad 3.2$$

Because the tangent line of round gears is always perpendicular to the vector between both centers of rotation, the gear pressure angle φ_{pa} is equivalent to φ_c . A plot of the pressure angles for the two modeled oval centrode pairs is shown as a function of the angle θ_1 of the input gear is shown in Figure 3.13. It is recommended to keep the pressure angle of a gear set between $-50^\circ < \varphi_{pa} < 50^\circ$ [51]. This is to limit the components of force trying to separate the two shafts when transmitting torque between the two gears. If the gears are cut with a standard rack cutter angle $\varphi_c = 20^\circ$ [56][52], the maximum pressure angle case is for of the modified $e = 1/3$ oval centrode and is $\varphi_{pa} = 55.3^\circ$. This is slightly over the recommended maximum pressure angle, but was deemed acceptable for an experimental engine running for a limited total duration.

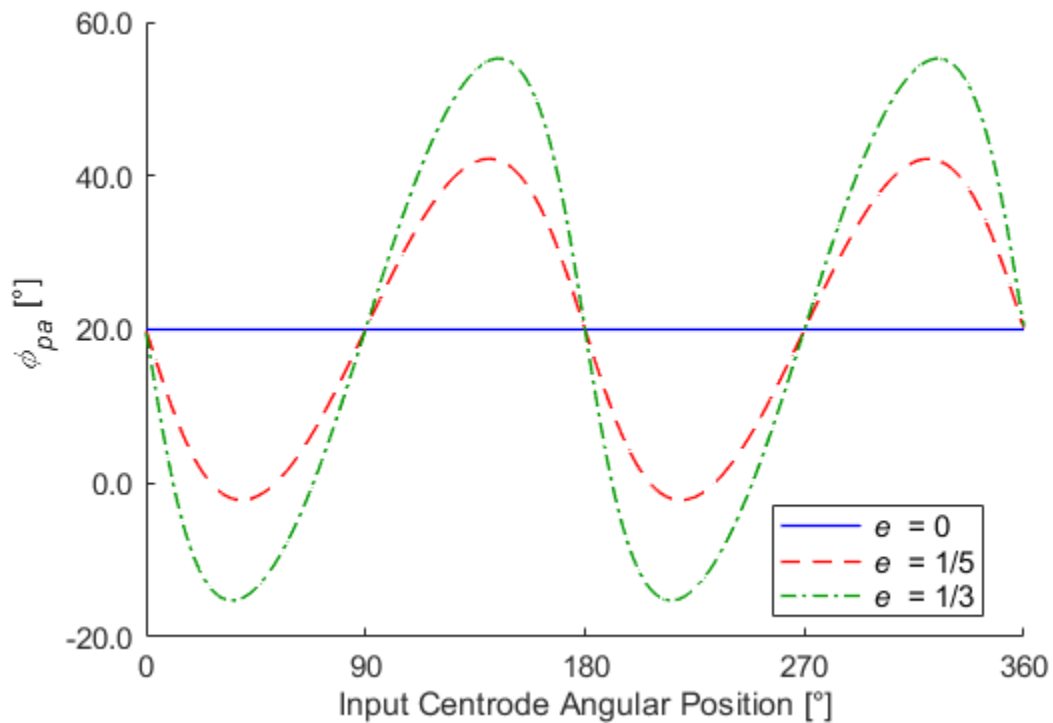


Figure 3.13 – Pressure angle plot for the complete rotation of a driving gear for the modified oval centrode pairs investigated

To determine the suitable size of the involute teeth to be cut consideration must be given to avoiding undercutting. Undercutting occurs when a selected tooth profile is too big for the centrode that the teeth are cut into, requiring the removal of material at the tooth base to enable proper meshing [57]. The American Gear Manufacturers Association (AGMA) has standardized tooth shapes and sizes which are used for commercial gear production. To maintain similarity with the use of commercial non-circular gears available from Cunningham Industries, Inc [54] if needed, it was decided to use U.S. specification gear standards as laid out by Budynas and Nisbett [58]. Tooth size is described by the diametral pitch (p_d) as defined by:

$$p_d = \frac{N}{d} = \frac{N}{2r_{min}} \quad 3.3$$

where: p_d = diametral pitch
 N = number of teeth on the centrode
 d = pitch circle diameter
 r_{min} = minimum radius of curvature of centrode

For round gears the pitch circle diameter is equivalent to the centrode curve. For non-circular gears the minimum radius of curvature must be used to determine an equivalent pitch circle diameter. In the case of the oval centrodes the point and value of the minimum radius of curvature for the $e = 1/3$ centrode is shown in Figure 3.14. The minimum radius of curvature was measured using SOLIDWORKS CAD after importing the polar curve for centrodes into the program. The results from SOLIDWORKS were compared to the following from equation from Litvin [51]:

$$r_{min} = \frac{a}{2}(1 - e^2) \quad 3.4$$

Using the center-to-center distance $L = 3\text{in}$ and equation 2.13, which specifies that $= L/2$, equation 3.4 confirms that the smallest radius of curvature of the $e = 1/3$ oval centrode is equal to $r_{min} = 0.67\text{in}$.

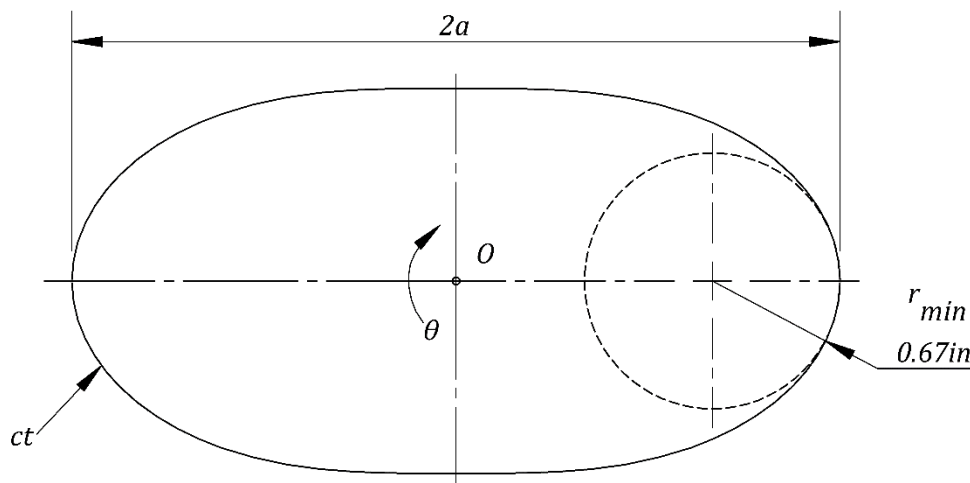


Figure 3.14 – Modified oval elliptical centrode of eccentricity $e = 1/3$ showing the minimum radius of curvature as determined from SOLIDWORKS

With a minimum radius of curvature known, the number of teeth for the centrode was determined. A minimum tooth number can be established by avoiding undercutting of the gear teeth [58]. The number of teeth necessary to avoid undercutting is related to the rack cutter pressure angle φ_c is determined by the following:

$$N_{min} = \frac{2}{\sin^2 \varphi_c} \quad 3.5$$

where: N_{min} = minimum tooth number for the centrode
 φ_c = rack cutter pressure angle

With the selected standard rack cutter angle of $\varphi_c = 20^\circ$ the minimum number of teeth necessary to avoid undercutting is $N_{min} = 18$. Substituting $N = 18$ and $r_{min} = 0.67$ in into equation 3.3, the maximum diametral pitch becomes $p_d = 13.5$ in⁻¹. Standard diametral pitches are whole integers so $p_d = 14$ in⁻¹ was selected for the centrodes. These are the largest teeth possible teeth for the designed centrode curves and provided the greatest cross-sectional profile to manufacture the gears for strength of the teeth. The total number of teeth for the centrodes is determined using equation 3.3 and solving for N . All three centrodes are the the same curve length, so for uniformity of tooth profile the same diametral pitch was used for all three centrodes despite the different minimum radii of curvature. The total number of teeth for the gears is $N = 42$.

With the properties of the designed gears decided it was possible to generate the complete gear profiles. This was done using a piece of commercial 3D CAD software (Gearotic v3.06, Artsoft) that specializes in gear modeling. The program simulates a single tooth cutter profile that is traced about the profile of a centrode in the same way a single pint rack cutter would contour the gear [59]. The program has a non-circular gear modeling module that takes as input any polar curve of the centrode to be toothed. Polar curve files for the centrodes were output from the MATLAB centrode model based on equation 2.18. The diametral pitch of $p_d = 14$ and the total tooth number $N = 42$ was specified in the program to generate the non-circular involute toothed gear profile along with the matching gear. An annotated screen capture of the software user interface is shown in Figure 3.15 and shows the generated profile of the oval gear pair of

eccentricity $e = 1/3$. Properties of the gears were held constant over all three gear sets to provide geometric similarity and are summarized in Table 3.6.

Table 3.6 – Gear properties

Gear Profile	$e = 0$	$e = 1/5$	$e = 1/3$
Center Distance [in]	3	3	3
Diametral Pitch [in ⁻¹]	14	14	14
Teeth	42	42	42
Cutter Pressure Angle [°]	20	20	20
Max Effective Pressure Angle [°]	20	42.2	55.3

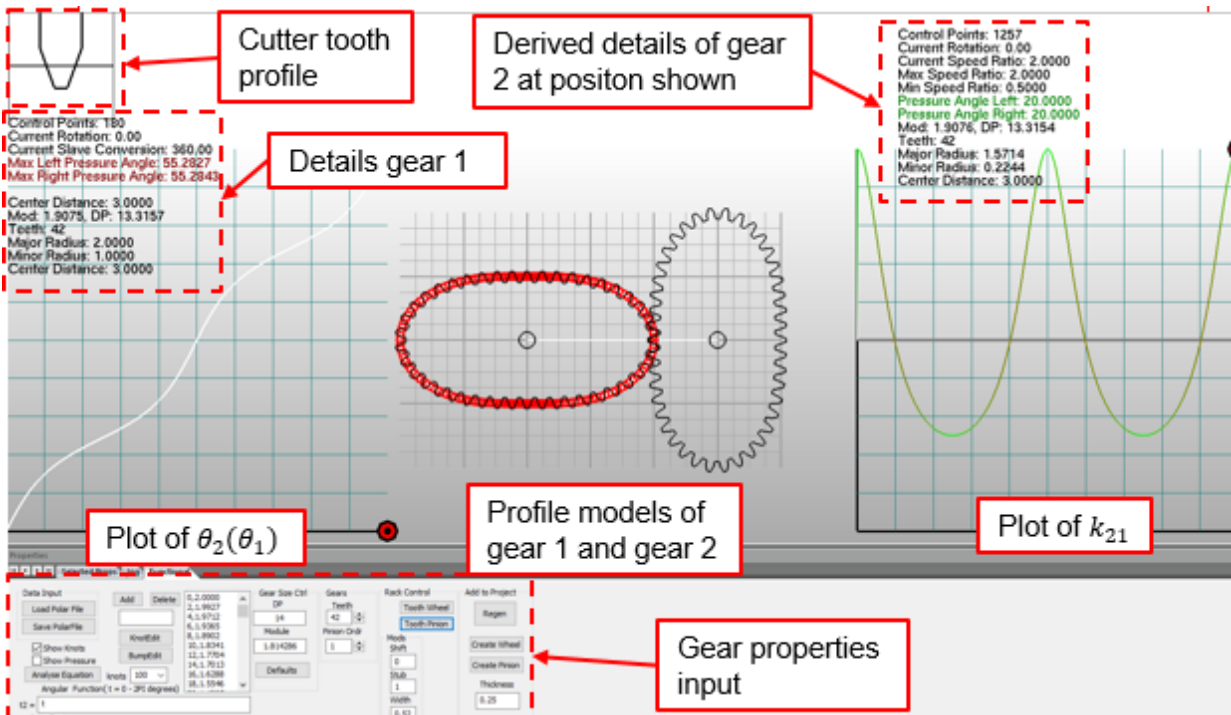


Figure 3.15 – Annotated view of Gearotic 3.06 user interface modeling a toothed oval $e = 1/3$ gear pair

The profiles of each wheel and pinion were then exported from the program as *.stl models. The profiles were imported into SOLIDWORKS CAD program to add additional design features and be integrated into the engine solid model. Features added include the central bore, keyways, and hardware holes necessary for mounting the gears with repeatable accuracy. The depth of the 2D gear profile was 25mm and ensured a line of

contact of a minimum of 20mm between gears to maximize the force distribution over the tooth face in the available space of the engine drive mechanism. Detailed orthogonal drawings of all three designed gears are provided in Appendix F.

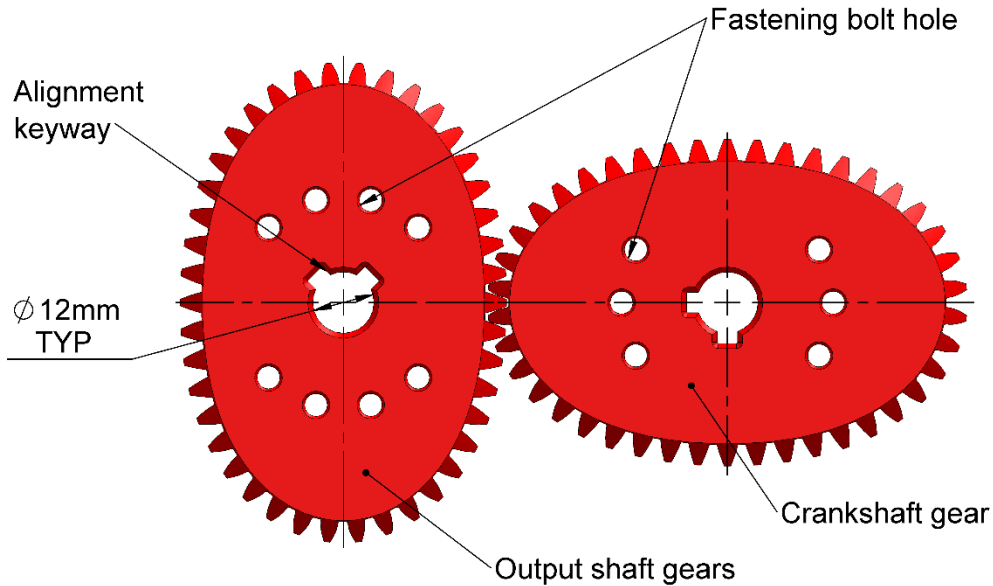


Figure 3.16– Solid model of the $e = 1/5$ eccentric gear pair for the displacer crank

3.2.2 Manufacturing and Final Fitting of Gears

The highly unique tooth geometry of the gears made manufacture of the gears using standard gear machining techniques very difficult, so it was decided to use 3D printing technology available in the lab to manufacture the gears. Due to the low anticipated power output of the engine it was deemed that the printed gears would be sufficiently accurate and strong for the limited running time of the trial engine. The process of manufacturing the gears was iterative and the methods described here were the final processes adopted.

The gears were printed using ABS plastic using a fused filament fabrication 3D printer (Ultimaker 2+, Ultimaker BV). A series of test prints were made to refine the print

settings to achieve the desired surface finish at an acceptable print speed. The printer settings of the final production run are noted in Table 3.7.

Table 3.7 – Gear printing settings

Property	Value
Nozzle diameter [mm]	0.4
Layer height [mm]	0.15
Shell layers	7
Bottom and top layers	12
Infill density [%]	25
Infill pattern	Grid
Approximate print time [h]	~12

The wall thicknesses chosen resulted in solid walls for all functional geometry of the gear with a partially hollow core. The hollow core was necessary to ensure a reasonable print time of ~12 hours per gear. A cross section of a failed gear print is shown in Figure 3.17 and shows the details of the printed gear structure.

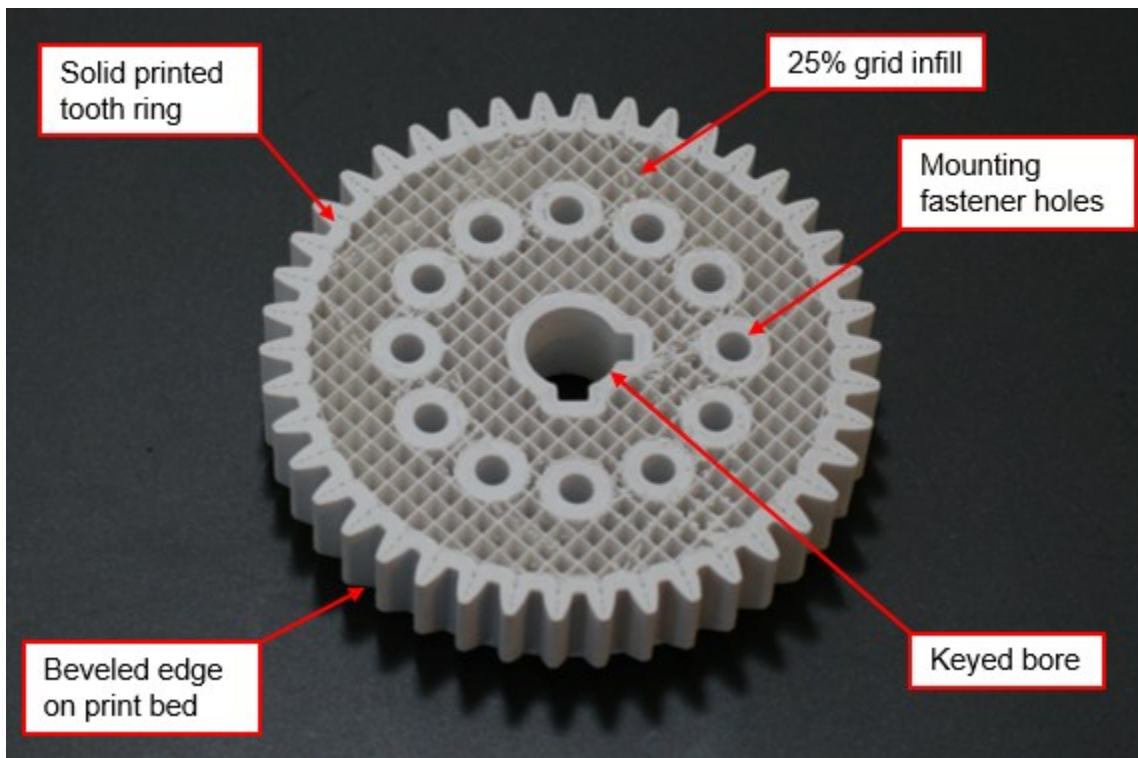


Figure 3.17 – Internal structure of the printed gears from a failed print

Finishing machining steps were taken to improve the fit of the gears. The flat faces of the gears were sanded and checked for parallelism by sweeping them with a dial indicator on the bed of a CNC vertical milling machine. The gears were then mounted to the bed and the bores of the gears were reamed using a 12mm spiral fluted reamer to ensure concentricity of the bore with the tooth profile and to clear away any over extrusions from the printing process.

Final fitting involved manually filing any over extrusion from the tooth profiles and testing the gears to when mounted to the mechanism. This included hand filing to fit the under sized keyways. Any pair with excessive tightness or backlash was either matched with another gear, or rejected and reprinted. Fitted pairs were marked and indexed and the gear backlash uncertainty was measured. Gear backlash contributing to shaft position uncertainty is detailed in Appendix B.6.1. An assortment of the fitted pairs is shown in Figure 3.18.

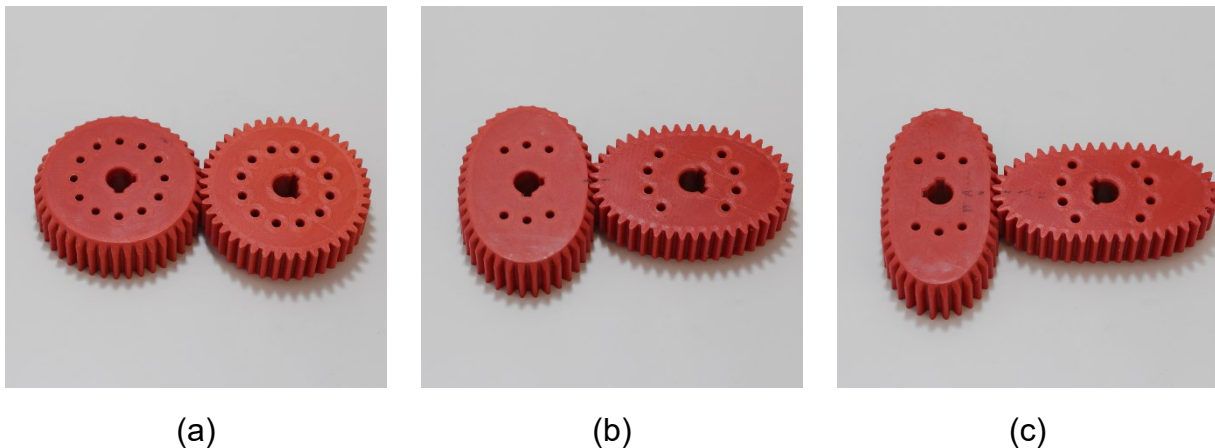


Figure 3.18 – Assortment of the final printed gears of (a) $e = 0$ centrode, (b) $e = 1/5$ centrode, and (c) $e = 1/3$ centrode

3.3 Working Space Volumes of the EP1-M

To determine the volumes of working fluid of the engine the solid model of the engine was assessed using SOLIDWORKS models of the engine components. A subtractive process was used for the volume of components inside of the inside the pressure shell. The engine pressure shell space was built up of basic geometric of volumes consisting of the displacer swept volume cylinder, and the concentric cylindrical volumes of the hot source exchanger, the regenerator, and the cold sink exchanger. The volumes of engine components occupying parts of these basic geometric shapes were determined using SOLIDWORKS's evaluate tool and were subtracted from the relevant space to leave the volumes of those zones.

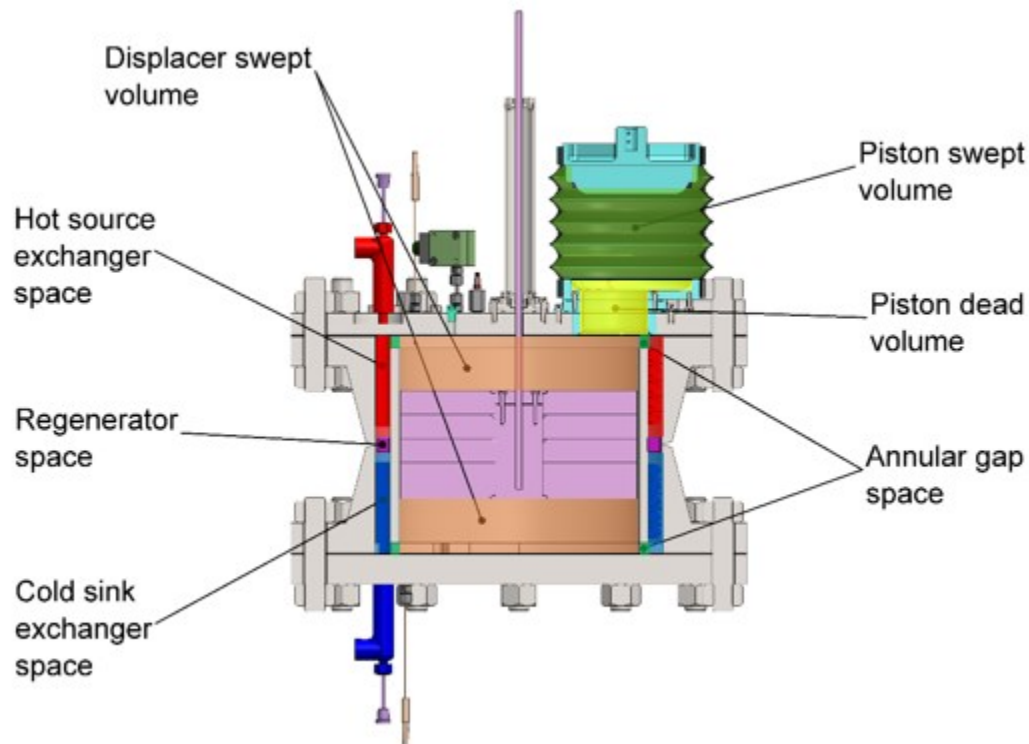


Figure 3.19 – Section view of EP1-M with colour coded working space volume areas

Volumes outside the engine pressure shell (beyond the internal edge of the top flange) were added to the total engine volume. These volumes were calculated various ways. For volumes up to the edge of the elastomer bellow cuff, the solid models of the piston mount were inverted and the volumes of the formerly negative spaces of the

model were taken using the evaluate tool in SOLIDWORKS. For the swept volume of the power piston, the maximum elastomer bellow volume taken from bellow volume calibration data detailed in section 4.3. The volumes of the internal structures inside the bellow volume was then subtracted in the same manner as for the volumes inside the engine pressure shell. These internal volumes consisted of the elastomer bellow material thickness, the structural rings of the bellow, and the dead volume reducer of the piston head. Figure 3.19 shows an annotated section view of the engine volume space.

Table 3.8 lists the volumes of the engine occupied by working fluid in the EP1-M as well as classifying the volumes as fitting the descriptions of engines spaces described in section 2.1. The compression ratio (CR) of the engine is 1.196 as calculated using equation 1.8

Table 3.8 – EP1-M working fluid volume spaces

Engine Space	Model Variable	Volume [L]
Displacer swept volume	V_{sd}	5.69
Displacer dead volumes	V_h of V_k	0.49
Hot source exchanger	V_h	1.10
Cold sink exchanger	V_k	1.03
Regenerator	V_r	0.11
Annular gap passages	V_h of V_k	0.19
Piston dead volumes	V_h	0.49
Engine minimum volume	V_{min}	9.11
Piston swept volume	V_{sp}	1.78
Engine maximum volume	V_{max}	10.90

3.4 Operation and Support System

The engine operation was supported by heating and cooling loops to provide the thermal source and sinks necessary to run the Stirling engine. Energy from the source and sink was delivered to the engine via circulating water. Water was chosen for both thermal loops for reasons laid out below:

- Remains liquid between the source and sink temperatures of 95° C and 5° C
- High heat capacity and good heat transfer properties
- No special material handling or toxicity concerns for use in the lab environment
- Compatibility with available equipment and piping materials

The heating loop was supplied from a 13L circulating bath (KH-12101-41, Cole-Parmer Canada Company). A supplementary immersion heater (T1, Messgerate-Werke Lauda) was also deployed in the circulating bath when it was observed that the temperature of the bath would drop 2° C below the set point at high engine running speeds. The cooling loop was supplied from a 28L circulating bath (KH-12111-21, Cole-Parmer Canada Company).

A schematic of the engine thermal loops is shown in the engine instrumentation diagram shown in Figure 3.20. The thermal fluid was delivered to the engine heat exchangers through a network of clear 3/8 in PVC tubing. The tubing was insulated with flexible rubber foam pipe insulations. The flow rate of both thermal loops was regulated with a dual-head programmable peristaltic pump (07551-20, MasterFlex Cole-Parmer Instrument Company) located before input to the engine heat exchangers.

Table 3.9 – Heating and cooling loop specifications

Property	Value
Heating loop bath model	KH-12101-41
Manufacturer	Cole-Parmer Canada Company
Capacity [L]	13
Thermal fluid	Water
Heating capacity [W]	1000
Nominal temperature setting [°C]	90
Heating loop immersion heater model	T1
Manufacturer	Messgerate-Werke Lauda
Heating capacity [W]	1050
Nominal temperature setting [°C]	90
Cooling loop bath model	KH-12111-21
Manufacturer	Cole-Parmer Canada Company
Capacity [L]	28.4
Thermal fluid	Water
Heating capacity [W] @ 20°C ambient	700
Nominal temperature setting [°C]	5
Peristaltic pump model	07551-20 (L/S 18 tubing)
Manufacturer	MasterFlex Cole-Parmer Instrument Co.
Heads	2
Nominal flow setting [L/min]	2.065

The actual delivery flow rates for the programmable peristaltic pump was determined through a calibration procedure that was conducted with the loops warmed up to operational temperatures. Details of the calibration procedure are noted in Appendix B.1. The calibrated thermal fluid mass flow rates used through the trials is noted in Table 3.10.

Table 3.10 – Calibrated thermal fluid delivery rates for the hot source and the cold sink loops

Loop	Variable	Value	Uncertainty	Unit
Hot source loop	\dot{m}_h	32.37	± 0.19	g/s
Cold sink loop	\dot{m}_c	29.14	± 0.10	g/s

3.5 Engine Instrumentation and Data Acquisition

Numerous engine parameters are measured directly using a digital data acquisition system. The variables that are recorded directly from instruments on the engine or support equipment is listed in Table 3.11. A schematic diagram of the engine instrumentation and support equipment shown in Figure 3.20.

Table 3.11 – Directly recorded engine parameters

Engine Property	Symbolic Variable	Instrument
Heating source input temperature	T_{Hin}	Resistance temp. detector
Heating source output temperature	T_{Hout}	Resistance temp. detector
Cooling sink input temperature	T_{Cin}	Resistance temp. detector
Cooling sink output temperature	T_{Cout}	Resistance temp. detector
Engine Time	t	DAQ
Expansion space gas temperature	T_e	Thermocouple
Compression space gas temperature	T_c	Thermocouple
Engine working space pressure	P_e	Piezoelectric pressure transducer and Diaphragm pressure transducer
Engine buffer / atmospheric pressure	P_{atm}	MEMS pressure sensor
Engine output shaft position	θ_{out}	Digital rotary encoder
Engine output torque	τ	Digital torque transducer

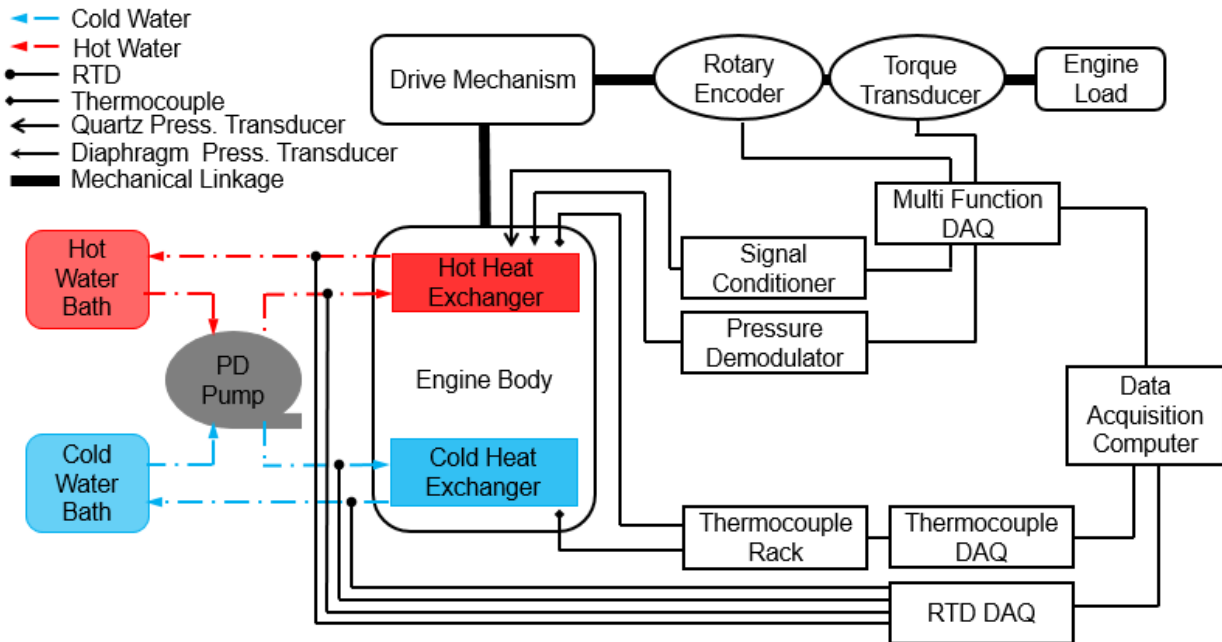


Figure 3.20 – Schematic of engine instrumentation and data acquisition system

3.5.1 Source and Sink Temperature Measurements

Measurements of source thermal fluid temperatures (T_{Hin} , T_{Hout}) and sink thermal fluid temperatures (T_{Cin} , T_{Cout}) were measured using immersion resistance temperature detectors (RTDs) mounted at the inlet and outlet manifolds of the source (hot) and sink (cold) heat exchangers. The RTD probes (RTD-810, Omega Engineering Inc.) were mounted in resin 3D printed manifolds that placed them in line to the fluid flow just above the distribution manifolds of the heat exchangers as can be in Figure 3.21. Instrument specifications are detailed in Table 3.12.

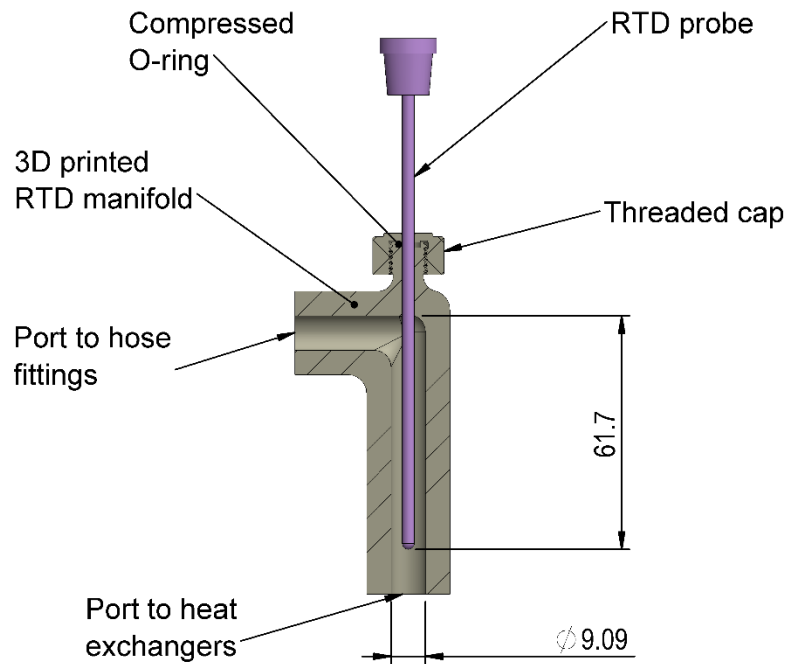


Figure 3.21 – Section view of RTD measurement location on EP1-M heat exchanger manifold

An RTD DAQ system comprising an ADC DAQ module (NI 9217, National Instruments Corp.) was used to record the temperature measured by the RTDs. The digital output from the ADC DAQ module was recorded by the DAQ computer as voltage measurements. As the flow rate and temperature of the thermal fluid should be constant over a steady state trial and the sought value was only for average temperatures over a data set, the response time of the devices was not critical.

Table 3.12 – RTD Sensor specifications

Device Model	Mfg.	Range	Mode
RTD-810 Sensor	Omega Engineering Inc.	-200 °C to 750 C	Trial average

RTDs were selected are suitable for use in potentially conductive fluids like the thermal fluid as they are grounded. Additionally, the measurement range and response time of the selected RTDs was adequate for the measurement of average thermal source and sink temperatures over the trial.

The specifications and standard uncertainties of the RTDs is discussed in Appendix B.1. A calibration procedure was performed to verify the linearity and establish a calibration constant for the recorded output from the RTD DAQ and is described in Appendix B.1. An example of the calibration curve for RTD1 is shown in Figure 3.22. As can be seen a linear fit aligns with the recorded data within the uncertainty of the instrument. Calibration data used in the data processing is presented in Table 3.13.

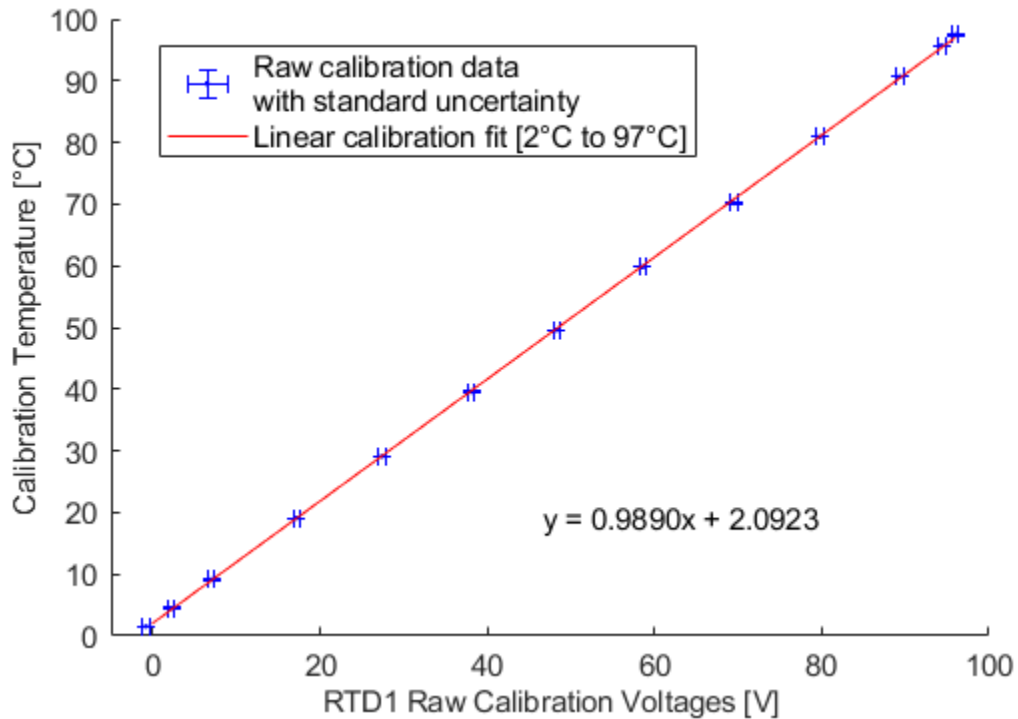


Figure 3.22 – Plot of RTD1 calibration curve and linear calibration constant

Table 3.13 – Processing and calibration data for RTDs

Instrument ID	Measurement	Calibration Eq	Unit
RTD1	T_{Hin}	$T_{Hin} = 0.9890 M_{RTD1} + 2.0923$	°C
RTD2	T_{Hout}	$T_{Hout} = 1.0109 M_{RTD2} - 1.6290$	°C
RTD3	T_{Cin}	$T_{Cin} = 0.9863 M_{RTD3} - 0.8588$	°C
RTD4	T_{Cout}	$T_{Cout} = 0.9865 M_{RTD4} - 0.8409$	°C

3.5.2 Working Fluid Temperature

Measurements of the working fluid temperature in the engine expansion space (T_e) and the engine compression space (T_c) were measured using thermocouples. The thermocouples were type-T (TTSS-116E-6, Omega Engineering Inc.) with an exposed junction. The bead of the exposed junction measured approximately 0.75mm in diameter. The working fluid thermocouples were located at the exit gap from the annular heat exchangers as can be seen in Figure 3.23. The expansion space thermocouple, identified as T0, protruded into the exit gap steam by ~10mm can be seen in detail A of Figure 3.23. The compression space thermocouple, identified as T1, was flush mounted to the bottom flange as can be seen in detail B of Figure 3.23 due to an overlap between the instrument hole and the displacer swept volume. As such, measurements from T1 are not from the free stream working fluid exiting the cold side heat exchangers. Instrument specifications are detailed in Table 3.14 .

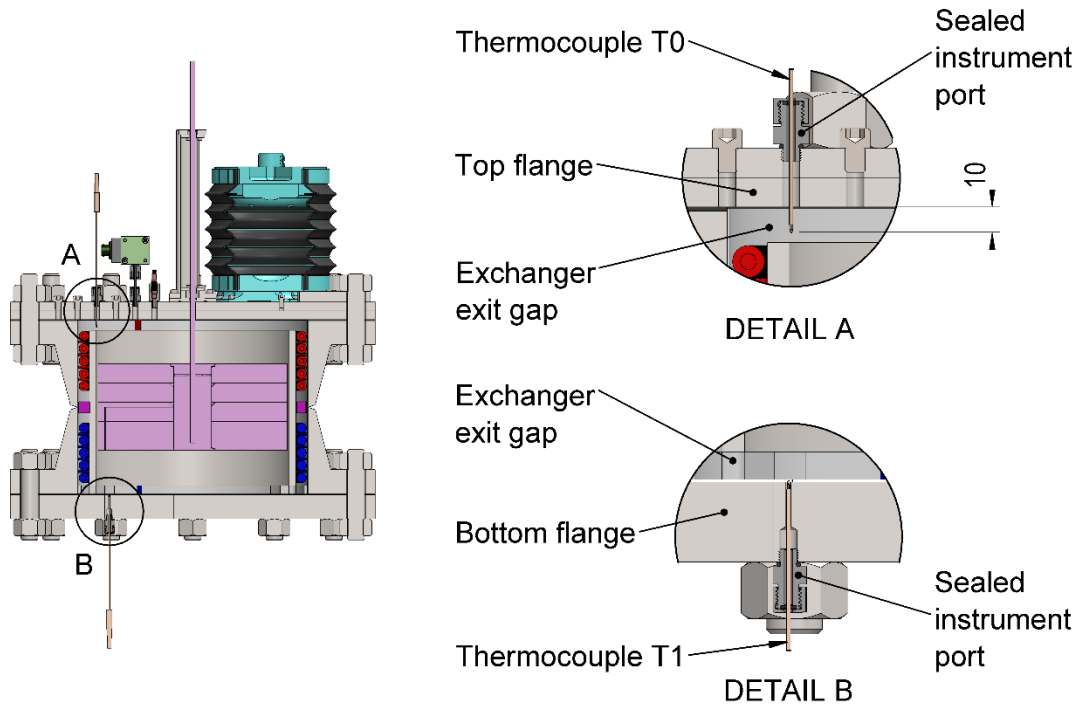


Figure 3.23 – Section view engine body showing the location of the expansion space thermocouple T0 and compression space thermocouple T1

Table 3.14 – Thermocouple sensor specifications

Device Model	Mfg.	Range	Mode
Type-T Thermocouple	Omega Engineering Inc	-0°C to 260°C	Cycle average

Measurements from the Thermocouple probes were collected by a series of DAQ devices. The leads from the probe were first plugged into a rack mount adapter (TC 2095, National Instruments Corp.). The rack adaptor groups individual field leads into the input for the signal conditioning module (SCXI-1102B, National Instruments Corp.). The signal conditioner outputs into a low noise digitizer chassis (SCIX-1600, National Instruments Corp.) in which is mounted. The chassis then outputs to the DAQ computer to be recorded.

The specifications and standard uncertainties of the Thermocouples is discussed in Appendix A. A calibration procedure was performed to verify the linearity and establish a calibration constant for the recorded output from the Thermocouple DAQ and is described in Appendix A. An example of the calibration plot for T0 is shown in Figure 3.24. A can be seen a linear fit aligns with the recorded data within the uncertainty of the instrument and is applied to processing the data. Calibration equations used in the data processing is presented in

Table 3.15 .

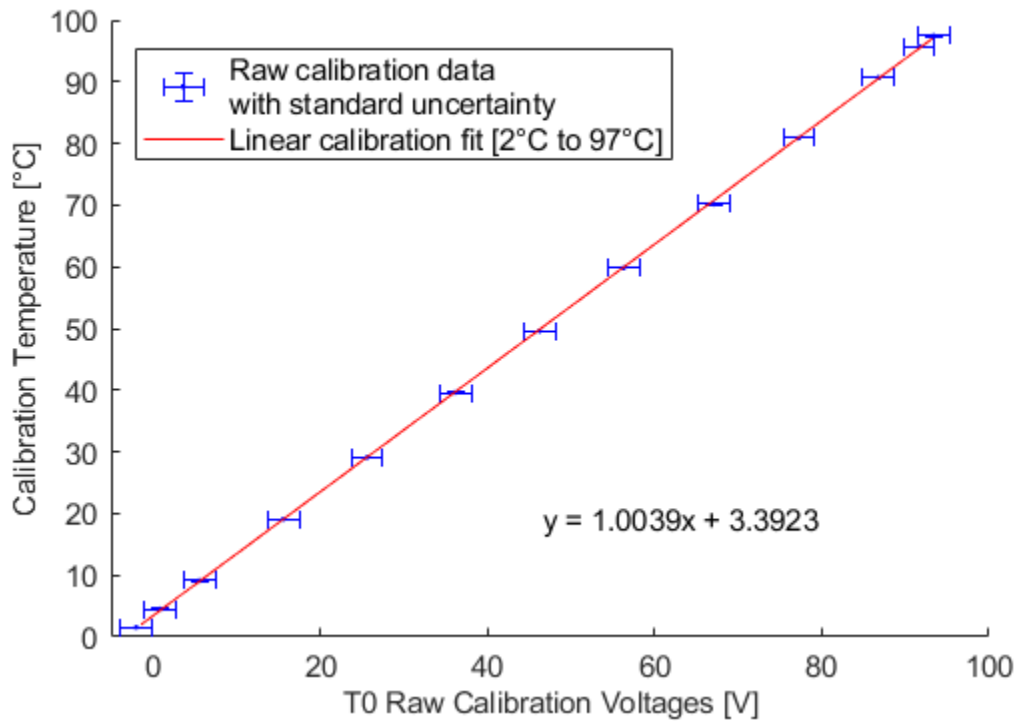


Figure 3.24 – Plot of T0 calibration curve and linear calibration constant

Table 3.15 – Processing and calibration data for thermocouples

Instrument ID	Measurement	Calibration Eq	Unit
T0	T_e	$T_{Hin} = 1.0039 M_{T0} + 3.3923$	°C
T1	T_c	$T_{Cout} = 1.0037 M_{T1} - 3.3704$	°C

3.5.3 Engine and Pressure Measurements

Measurements of pressure (P_e) inside the shell of the engine was measured by two devices, a piezoelectric pressure transducer (113B21, PCB Piezotronics Inc.) and a diaphragm pressure transducer (DP15, Validyne Engineering). The sensors were mounted in the engine top flange as close to the engine displacer centerline as possible. The instruments access the engine expansion space as shown in the detail view of Figure 3.25. Instrument specifications are detailed in Table 3.16.

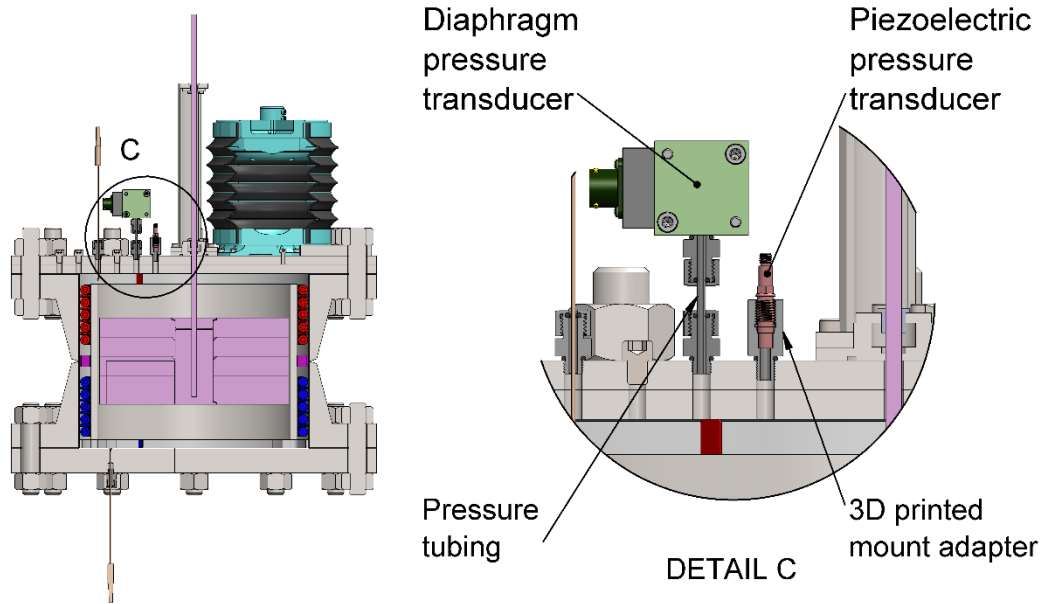


Figure 3.25 – Section view engine body showing the location of the working fluid pressure sensors

Table 3.16 – Pressure sensors specifications

Device Model	Mfg.	Range	Mode
DP15 /w DP15 3-36	Validyne Engineering	34.5kPag (5psig)	Instantaneous
113B21 (SN: LW35042)	PCB Piezotronics Inc.	1380kPa (200psi)	Instantaneous

Two pressure sensors were used in conjunction to measure the working space pressure of the engine. The piezoelectric pressure sensor has a very short time response of $\leq 1 \mu\text{s}$ which made it suitable to track the dynamic pressure changes occurring in the engine. The measurement signal of the piezoelectric sensor will only respond to changes in pressure, and will “relax” to output a 0 measurement equivalent to the mean pressure of the engine, which may not match the initial charge pressure of the engine. The absolute gauge pressure between the engine working space and the atmospheric buffer pressure is what drives the piston and cannot be accurately measured by the piezoelectric sensor. The diaphragm pressure transducer is designed to measure gauge pressure and so was selected for use for that purpose. There was concern that the diaphragm pressure transducer response time might not be sufficient to capture pressure changes occurring at high engine speeds. Using measurements from both sensors provided a redundant set of measurements, where the shortcomings of either instrument could be rectified by the other.

Measurements from the piezoelectric pressure sensor were output to a signal conditioner (482C05, PCB Piezotronics Inc.) which applied a x100 gain to the signal. Measurements from the diaphragm pressure transducer were output to a multi-channel carrier demodulator (CD280-8, Validyne Engineering). Both conditioned signals were passed to a high speed multifunction USB I/O device (NI-USB-6211, National Instruments Corp.) and finally recorded by the DAQ computer.

The specifications and standard uncertainties of the pressure sensors is discussed in Appendix B.4 and B.5. Appendix B.5 also includes a detailed description of the calibration procedure used to calibrate the diaphragm pressure transducer using a large manometer. The results of the calibration are shown in Figure 3.26 and a clear linear trend in the instrument is evident. Calibration equations used for both sensors in the data processing is presented in Table 3.17.

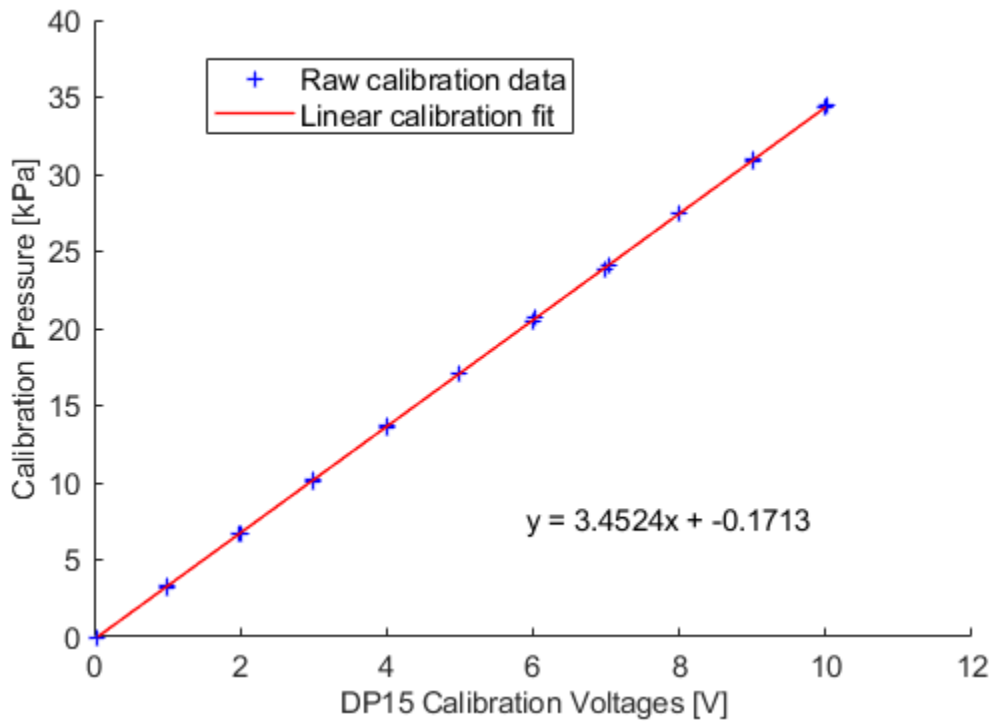


Figure 3.26 – Plot of DP15 manometer calibration and linear calibration constant

Table 3.17 – Processing and calibration data for engine pressure sensors

Instrument ID	Measurement	Calibration Eq	Unit
P1 (DP15)	P_e	$P_{e_VAL} = 3.4524 M_{P1} - 0.1713$	kPa
P2 (PCB)	P_e	$P_{e_PCB} = \frac{1000}{3.519} M_{P2}$	°kPa

3.5.4 Buffer pressure measurement

The buffer pressure of the engine was atmospheric air conditions in the laboratory. It was not possible to directly control this variable so it was recorded for every data set prior to recording the data set. The absolute atmospheric pressure was taken using the microelectromechanical systems (MEMS) absolute pressure sensor of a smartphone (SM-A520W (Galaxy A5 2017), Samsung). The sensor data was accessed using the Science Journal application (Version 3.5346039689, Google LLC). Instrument specifications are detailed in Table 3.18.

Table 3.18 – Atmospheric pressure measurement device properties

Device Model	Mfg.	Range	Mode
SM-A520W	Samsung	Unknown	Trial average

The sensor provided an absolute pressure measurement for the engine buffer pressure. The sensor was calibrated against a mercury barometer to provide the data processing calibration offset as shown in Table 3.19. Details of the calibration are presented in Appendix B.8.

Table 3.19 – Processing and calibration data for atmospheric pressure sensor

Instrument ID	Measurement	Calibration Offset	Unit
A5	P_{atm}	$P_{atm} = P_{SM-A520W} + 0.211$	kPa

3.5.5 Output Shaft and Crankshaft Rotary Position

Measurements of the output crankshaft position (θ_{out}) were measured using a 500 position rotary encoder (15S-19M1-0500MV1ROC-F03-S1, Encoder Products Company) that was coupled to the engine output shaft via a tensioned timing belt with a 1:1 transmission ratio. A depiction of the mounting arrangement is shown in Figure 3.11. The rotary encoder was installed to output a binary voltage signal two channels. The first channel (Z-pulse) output a single pulse once every rotation, while the second (A-pulse) output 500 evenly spaced pulses throughout a revolution. The excitation power supplied to the encoder was 5V supplied by a programmable DC power supply (GPD-3303S, Good Will Instrument Co., Ltd). The sensor output an “on” pulse reading 5V at

each encoder “tick”, and otherwise output 0V between “ticks”. The specifications of the encoder are shown in Table 3.20. Each channel was passed to a high speed multifunction USB I/O device (NI-USB-6211, National Instruments Corp.) and finally recorded by the DAQ computer.

Table 3.20 – Crankshaft position measurement device properties

Device Model	Mfg.	Range	Mode
15S-19M1-0500MV1ROC-F03-S1	Encoder Products Company	1 pulse / rev (Z) 500 pulses/rev.(A)	Instantaneous

Positions of the piston and displacer crankshaft were derived using the transmission function described by equation 2.20 with respect to the position measurement of the output shaft. As such the position of the crankshafts is subject to uncertainty from any backlash of the gears. This was accounted for by introducing an uncertainty term for the gear backlash as discussed in Appendix B.6. For every trial the rotary encoder Z-pulse was calibrated to the piston top dead center position using a dial indicator. Data from all the direct measurement values are grouped and averaged to the relevant rotary encoder position. Angular position of the output and crankshafts thus becomes the fundamental measurement of the engine at any instant, along with the recorded time stamp of the DAQ. The data processing scheme is discussed in section 5.2.1.

3.5.6 Output Torque

Output torque of the engine (τ) was measured using a non-contact shaft to shaft rotary torque sensor (TRS600 FSH01994, FUTEK Advanced Sensor Technology, Inc). The sensor was connected between the engine output shaft and the engine brake system as described in section 3.1.5. The sensor output a positive or negative voltage between 0 and ± 5 VDC with a linear relationship with applied torque and the applied direction. Excitation voltage required by the sensor was 20VDC supplied by a programmable DC power supply (GPD-3303S, Good Will Instrument Co., Ltd). Specifications of the torque sensor are shown in Table 3.21. The sensor output was passed to a high speed multifunction USB I/O device (NI-USB-6211, National Instruments Corp.) and finally recorded by the DAQ computer. Instrument specifications are detailed in Table 3.21.

Table 3.21 – Engine output torque measurement device properties

Device Model	Mfg.	Range	Mode
TRS600 FSH01994	FUTEK Advanced Sensor Technology, Inc	1 Nm	Instantaneous

Calibration of the torque sensor was performed by the device manufacturer. The linear fit from the calibration data used in data processing is noted in Table 3.22. Details of the calibration and uncertainty sources are presented in Appendix B.7.

Table 3.22 – Processing and calibration data for torque sensor

Instrument ID	Measurement	Calibration Eqn.	Unit
TOR	τ	$\tau = 0.1953 M_{TOR} + 0.131$	Nm

3.6 Data Acquisition System Details

The sensors for the data acquisition system usually output to supporting signal conditioners or digitizers as described in section 3.5. The signals from the various sensors was condensed to three DAQ units as can be seen on the P&ID diagram shown in Figure 3.20. The tree units include: RTD ADC DAQ module (NI 9217, National Instruments Corp.), thermocouple signal conditioner and digitizer (SCXI-1102B and SCIX-1600, National Instruments Corp.), and the multi function I/O device (NI-USB-6211, National Instruments Corp.). All three units output to USB connections that were collected by the DAQ computer running a code written in LabWindows / CVI (LabWindows / CVI Vserison 2010 SP1, National Instruments Corp.) for use with multiple engines within the lab.

The UI for the data collection script is shown in Figure 3.27 with annotations identifying program functions. Channels for each DAQ module are selected depending on which plug the instruments are connected to. The sampling rate and duration for each signal is configurable for the three modules. Collection rate decisions are discussed in section 3.6.1. Live readout charts show the raw signal voltages to allow diagnostics of the instruments in real time. There is also readout charts of engine speed, power, and torque that permits engine monitoring. Watching engine speed also serves as a good indicator of the engine achieving steady state after a load change. Additional functionality includes a Z-pulse rotary encoder alignment tool that displays a bright green box when the Z-pulse is on, as required by the alignment calibration detailed in section 4.5.1. A section on the right of the UI allows trial data to be input including the measurement of atmospheric buffer pressure. Trial information is them used to populate the data file titles once recorded.

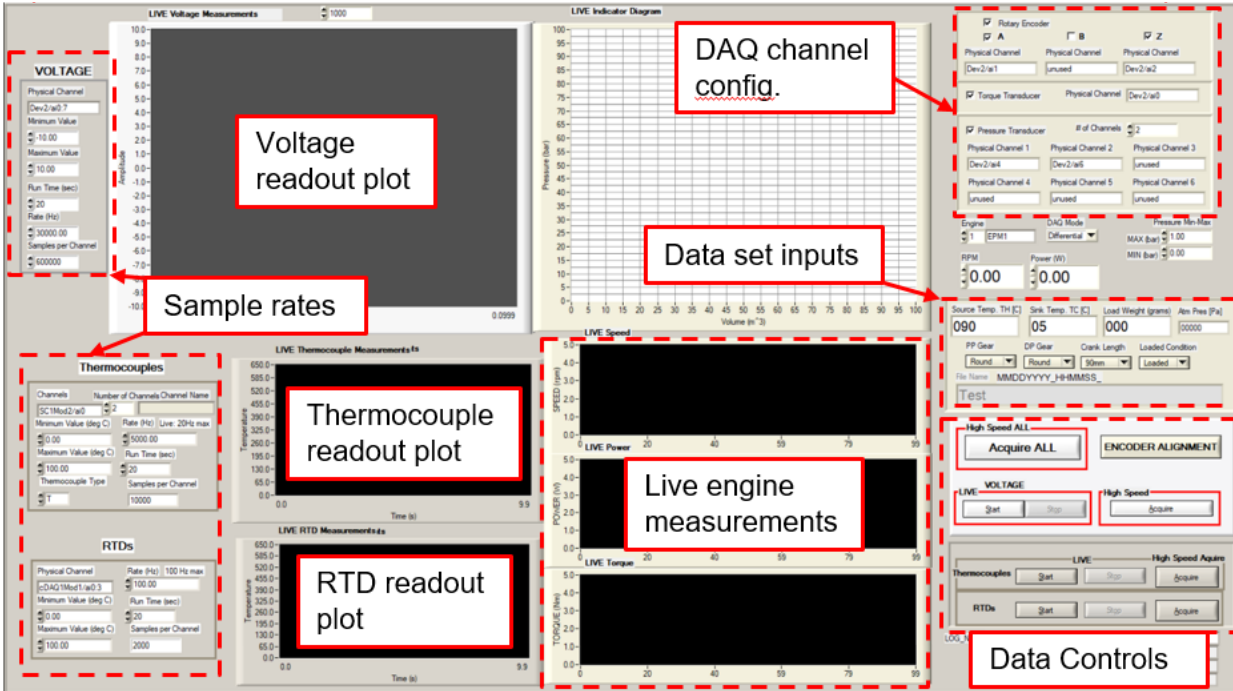


Figure 3.27 – User interface of LabWindows CVI data capture program with annotations

When recording a set the life outputs must be disabled and the Acquire All button will initiate the data collection for the specified sample rate and duration. Once all data is acquired *.log files are created for each of the DAQ modules. The *.log files are structured as tab delimited files with each row corresponding to the recording time, and each column the measurement signal of an instrument. An example of the first few rows of a *.log file output by the computer DAQ acquisition program is shown in Figure 3.28 Acquired signals will also be displayed in the live readout charts and can be checked for completeness.

11252020_151643_090_05_0000_92289_12C_F_Volt.log - Notepad

File	Edit	Format	View	Help
Date	11-25-2020		Time	15:17:03
Volts	Volts	Volts	Volts	Volts
A	Z	TOR	P1	P2
Start	0.08822450			
End	20.05872850			
0.1281	0.1327	0.0626	-1.6004	-1.0756
0.1274	0.1320	0.0642	-1.5990	-1.0585
0.1268	0.1317	0.0656	-1.5974	-1.0549
0.1268	0.1317	0.0675	-1.5987	-1.0756
0.1264	0.1314	0.0692	-1.5997	-1.0605
0.1268	0.1310	0.0705	-1.5994	-1.0549
0.1268	0.1314	0.0712	-1.5984	-1.0737
4.9199	0.1284	0.0715	-1.5964	-1.0674
4.9327	0.1274	0.0715	-1.5948	-1.0826
4.9350	0.1274	0.0708	-1.5951	-1.0589

Figure 3.28 – Sample of the first few rows of the acquired *.log file for the multi function I/O device

3.6.1 Data Collection Rates

The DAQ programme allows specification of separate collection rates and durations for all three DAQ module devices. Sampling rate for each instrument was based of the sampling-rate theorem as described by Wheeler and Ganji [60] which states that the minimum sampling rate must be twice the highest frequency component of the original signal to avoid aliasing as described by the following equation:

$$f_{sample} > 2f_{signal} \quad 3.6$$

where: f_{sample} = Sampling / measurement frequency [Hz]

f_{signal} = highest frequency of the of the signal to be measured

For measurements from sensors operating in instantaneous mode for engine properties, the signal rate was dictated by the anticipated engine frequency and the number of data points per cycle that were to be collected. The anticipated engine speed was informed by previous work and testing of the EP1 by Stumpf [40] which saw maximum engine speeds of up to $\omega \approx 150$ rpm, or $f_{engine} = 2.5$ Hz. To add a buffer in

the event the EP1-M ran faster, the anticipated maximum speed was increased by 20% to $\omega \approx 180$ rpm, or $f_{engine} = 3$ Hz. To capture instantaneous measurements of the engine the data processing and collection scheme was built around taking engine data coordinated to each of the 500 measurable positions of the rotary encoder. Lastly, to reduce the random uncertainty of the sensor measurements, at least 10 measurement signals were collected to be averaged at each encoder position. These factors came together to prescribe a sample rate for the multi function I/O device as follows:

$$f_{I/o \text{ sample}} = 2(f_{engine} \cdot n_{encoder} \cdot n_M) = 2(3 \cdot 500 \cdot 10) = 30 \text{ kHz} \quad 3.7$$

The thermocouple devices were run in a cycle average mode so a slower sampling rate was calculated based on engine speed and to collect a minimum of 1 point per encoder position measurement ($n_{encoder}$) per cycle. The specified collection rate was arbitrarily chosen as:

$$f_{therm \text{ sample}} > 2f_{engine} \cdot n_{encoder} = 2(3 \cdot 500) \quad 3.8$$

$$\text{Chosen } f_{therm \text{ sample}} = 5 \text{ kHz}$$

Lastly the RTDs measuring the hot source and cold sink loops were not anticipated to change much through the course of a steady state trial and were run to collect a cycle average measurement. To minimize uncertainty of the calculated average at least 15 measurement points were to be collected per cycle. The sample rate was rounded up to a convenient number as described by:

$$f_{RTD \text{ sample}} > 2f_{engine} \cdot n_M = 2(3 \cdot 15) \quad 3.9$$

$$\text{Chosen } f_{RTD \text{ sample}} = 100 \text{ Hz}$$

The total collection duration was decided on the desire based on interest in capturing a minimum of 10 cycles per data set for all DAQ modules. The EP1 was capable of running at minimum speeds of to $\omega \approx 30$ rpm, or $f_{engine} = 0.5$ Hz. It was not anticipated the EP1-M would run slower than the EP1, thus the dataset collection duration was described by the following:

$$t_{sample} = \frac{n_M}{f_{engine}} = \frac{10}{0.5 \text{ s}} = 20 \text{ s} \quad 3.10$$

Details of data collection rates and durations per DAQ module and sensor are summarized in Table 3.23.

Table 3.23 – DAQ data collection properties

DAQ Module	Instrument ID	Measurement	Sample Rate	Sample Duration
I/O device NI-USB-6211	P1 (DP15)	P_e	30 kHz	20 s
	P2 (PCB)	P_e		
	ENC	θ_{out}		
	TOR	τ		
RTD ADC DAQ NI 9217	RTD1	T_{Hin}	5 kHz	20 s
	RTD2	T_{Hout}		
	RTD3	T_{Cin}		
	RTD4	T_{Cout}		
Thermocouple DAQ SCXI-1102B and SCIX-1600	T0	T_e	100 Hz	20 s
	T1	T_c		

4 EXPERIMENTAL PROCEDURES AND PRELIMINARY TESTING

This chapter documents the testing procedures of the experiments carried out on the modified drive mechanism of the EP1-M low temperature Stirling engine. To ensure consistency between trials for controlled variables detailed procedures for engine running and data collection were developed. These procedures had their basis in initial trials of the precursor EP1 engine, along with preliminary testing to the EP1-M modifications. Results from that preliminary testing is documented in this section. Details of the elastomer bellow volume calibration testing is also presented, which was an undertaking made necessary by the unique characteristics of the elastomer below power piston of the EP1 / EP1-M. With the procedures and calibrations established, the core steady state experimentation plan of the modified drive mechanism was organized. The experiments were organized in test groups that reproduced the gearing configurations explored in the engine modeling, but in an order that was logistically simpler to implement on the engine.

4.1 Preliminary Engine Testing

Pre-trial testing was undertaken to evaluate and establish guidelines for the running the engine under test conditions. These tests were run concurrently with development of the experimentation plan and the final stages of the digital isothermal engine modeling. After adding all the manufacturing of upgrades bring the EP1 up to EP1-M standard the engine was run to evaluate performance of the engine and make any necessary improvements.

4.1.1 Source and Sink Temperature and Piston Stroke Optimization

The initial work by Stumpf [48] on the EP1 used a nominal thermal source temperature T_H of 95 °C and a nominal sink temperature (T_C) of 2 °C to run the EP1. Their investigation allowed for variable piston stroke, for which the optimal value was a piston stroke of $r_p = 50\text{mm}$.

It was initially planned to run the EP1-M at the same source and sink temperatures and at the piston stroke of $r_p = 50\text{mm}$ to provide results comparable to the works of Stumpf [40]. However, very early initial testing of the conventional gearing EP1-M revealed that the improvements to the drive mechanism as part of the EP1-M upgrades had reduced mechanical friction in the drive mechanism when compared to the EP1. This was observed when apply load to the friction brake to try and find the stall point of the EP1-M, the magmatic hysteresis clutch began slipping significantly above the stall point. The clutch slip point was set at $\tau \approx 1.2\text{Nm}$ to protect the torque sensor, which is only calibrated to provide accurate results in the range of $\tau = -1.0\text{Nm}$ to 1.0Nm . As finding the stall point of the engine was deemed important early, it was decided to reduce the temperature difference of the engine to the nominal source and sink values of $T_H = 90\text{ °C}$ and $T_C = 5\text{ °C}$ respectively. The isothermal modelling parameters were adjusted as well.

Reducing the temperature has an impact on the optimum compression ratio (CR) of the engine as noted in section 1.3.4. Using equation 1.11 and the new temperature bounds of the EP1-M, the optimum compression ratio was calculated to be $CR = 1.19$. It was decided to reduce the piston stroke from $r_p = 50\text{mm}$ to $r_p = 45\text{mm}$ using the adjustable spacer blocks of the piston crank arms as described in section 3.1.5. This would also have the benefit of reducing the bellow elastomer stretch and prolong its life. It was observed that after the elastomer volume calibration (discussed in section 4.3) that the volume variation of the piston at $r_p = 45\text{mm}$ corresponded to a $CR = 1.196$, which was very close to the ideal predicted by Stumpf [40]. It was also possible to stall the engine with conventional gears with loads that did not exceed the slip condition of the clutch.

Finally the maximum free running speed of the engine was observed using the DAQ to confirm the data collection rates specified in section 3.6.1. The observed maximum free running speed was $\omega \approx 150$ rpm, which was less than the $\omega \approx 180$ rpm specified by the data collection rates.

4.1.2 Manufacture and Break-in of 3D Printed Non-Circular Gears

As a result of the FFF manufacturing method of the 3D printed gears, the surface finish of the gears had distinct layers of material. The layers at the bottom of the print ended up getting compressed more than the remaining layers of the gears. The original design of the printed gears had a straight profile as shown in Figure 4.3, which when combined with the layer compression on the print bed, resulted in a flared edge with a larger tooth profile.

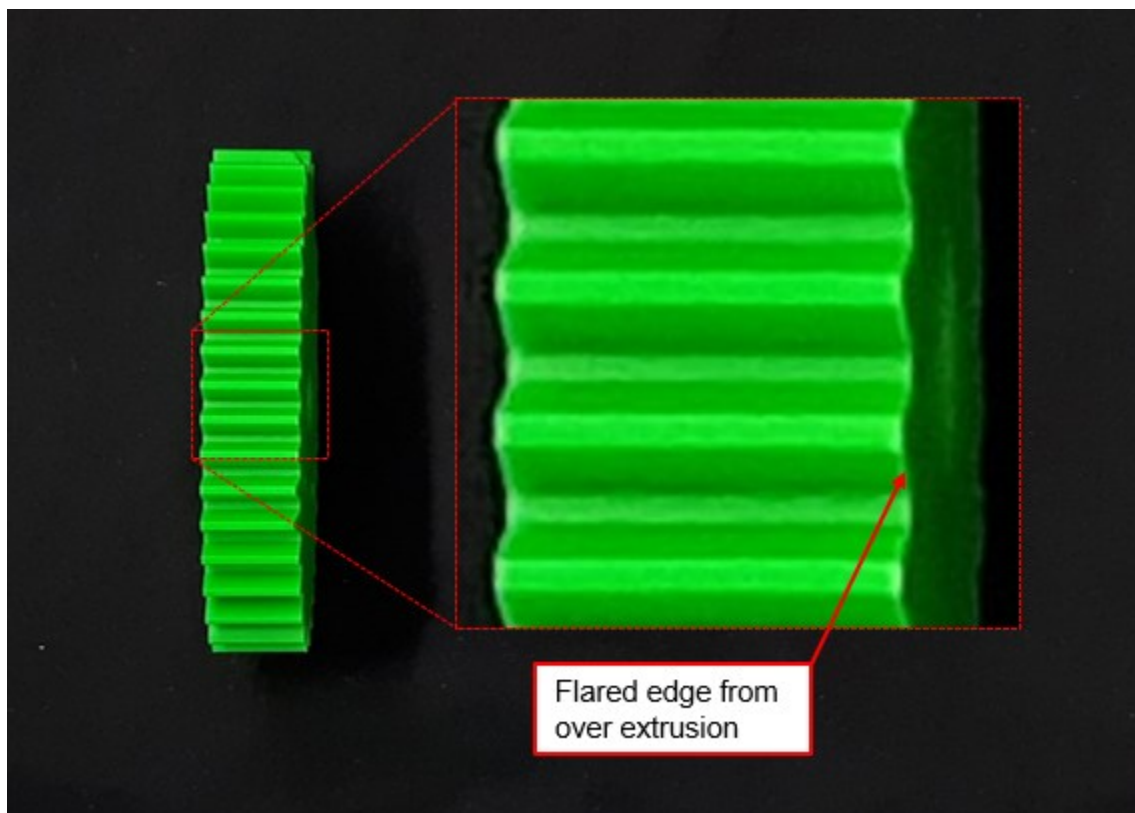


Figure 4.1 – Early 3D printed oval gear showing straight profile design and a detail view of the flared edge resulting from printing over extrusion

It was found during the initial engine testing that the flare was resulting in the gears running too tight, and that the flare would wear unevenly. The uneven wear would result

in greater backlash during parts of the cycle while the being tight in other portions of the rotation.

The initial gears were also bored to the 12mm shaft diameter using a drill press and a twist drill. The bore was not consistently parallel with the gear profile, further compounding the backlash problems caused by the printing flare.

After iterating the design of the gears, solutions for the observed problems would come with the improved manufacturing methods detailed in section 3.2.2. These included adding a bevel to the tooth profile that preventing the printing flaring, and using a much more rigid boring method to finish the gear bores using a spiral reamer and a CNC milling machine. These gears were worn in by running them for at least 1 hour on the engine and applying a lubricating grease to the teeth.

4.2 Engine Transient Testing

Only data regarding steady state engine running conditions was of interest for this investigation. Given that the application in mind of these engines is low temperature power generation, it is not anticipated that the engine will operate with highly variable operating conditions. Applying different loading to the engine between data sets were thus waited out until steady state had been achieve for that loading condition prior to recording data.

To establish a minimum time between load change and data collection, a series of transient trials were recorded for a data collection period of 120s. The engine was operated at normal testing conditions, and configured to the conventional $e = 0$ gearing configuration for the test. A load of 426g was applied the brake and the engine was allowed to come to steady state for 10 minutes. The data recording was commenced after the ten minutes and the within a few seconds of beginning recording the load on the brake was reduced to 215g. After the data collection had complete the engine was again allowed 10 minutes to achieve steady state. Afterwards the same transient test was repeated, only this time loading the engine back to 415g on the brake. This cycle was repeated three times.

Figure 4.2 depicts the calculated moving average of instantaneous output shaft velocity for the middle trials of the transient test. The moving average is for 500 data

points which correspond to a full rotation of the rotary encoder, and thus provide a moving average for 1 cycle of the engine. As can be seen, the engine achieves a near steady operating speed within ~30s of the load change. The small jogs at the beginning and the end of the speed curves are artifacts of the moving mean function which truncates the window at the ends of the data arrays.

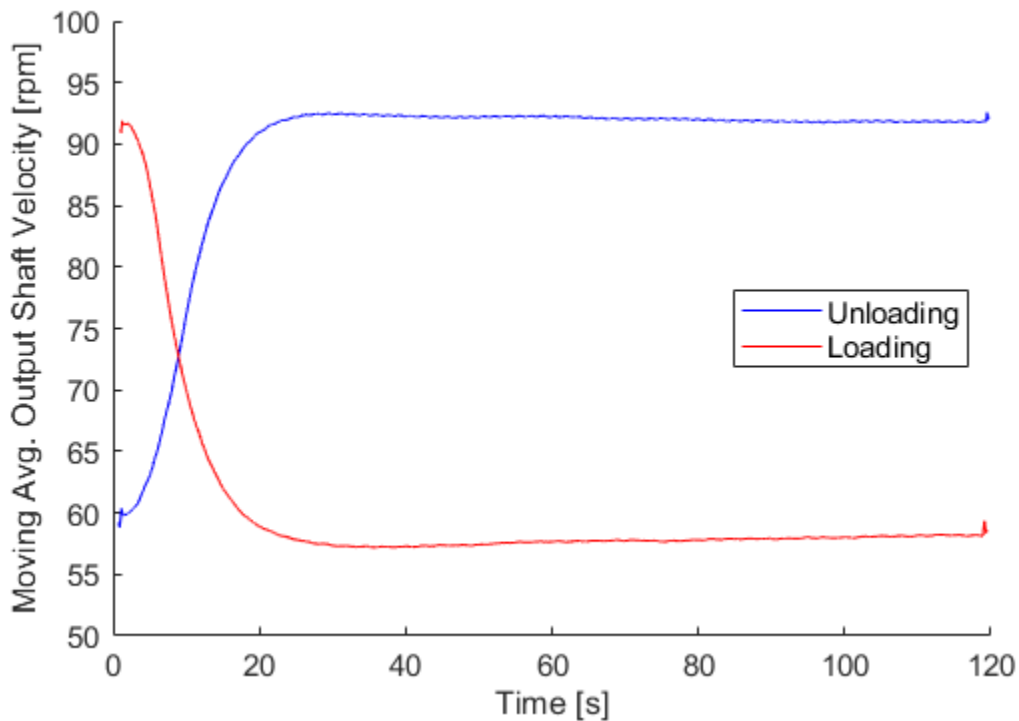


Figure 4.2 – Instantaneous engine speed recorded for a step change in engine loading

After ~30s the engine has a very gradual change in average cycle velocity that trends slightly faster after loading, and slightly slower after initial unloading. It has been observed that Stirling engines have a tendency to “acclimatize” to new loading conditions [61], asymptotically trending towards a steady state running speed after a load change. It has been theorized that this is attributable to the thermal equilibrium changing within the engine at the new loading conditions [61]. Considering the very gradual changes after 30s seen in Figure 4.2 it was deemed there was not significant advantage gained in prolonging the waiting beyond a 120s period for collecting steady state trial data given the large number of data sets collected and the risk of breaking an engine component through extended running. The minimum waiting period after load variation was included in the data collection procedure detailed in section 4.5.

4.3 Bellow Volume Variation Calibration and Measurement

The pleated shape of the bellow and the elastomeric material make it difficult to exactly determine the internal volume of the working fluid of the piston at any given position. The results of Stumpf [48]s relied on assumptions regarding the internal volume of the elastomer bellow as measured from solid modeling. The calculated uncertainty of this was deemed to be too high to adequately observe the changes to the indicator diagram and so a new method of volume variation calibration was explored. It was decided measure the bellow volume variation with digital imaging calibration to improve the accuracy of the working space volume measurement of the engine. A method was used by Michaud [62] that took an illuminated profile image of a static elastomer bellow in order to more accurately model the volume of the object. Michaud [62] was working on an alpha Stirling engine with similar elastomer bellows within the research group. A limitation of Michaud's method [62] was that it only profiled the bellow under static conditions, and still relied on correlating the bellow position via the drive mechanism.

The improved method used during the EPM-1 calibration involved taking backlit profile images of the piston while the engine was running and correlating the volume calibration directly to the output shaft rotary encoder position. The images were processed to calculate the internal volume of working fluid in the piston to correlate piston volume with specific rotary encoder position measurements throughout a full engine cycle. With the correlation the change in volume of the engine could be accurately determined for each trial by apply the derivative function of the gear set in use for the piston crankshaft.

4.3.1 Volume Variation Calibration Experimental Setup

To take suitable images of the bellow piston and support frame were modified to allow an unobstructed view of the piston to be captured by a digital camera (acA800-510um, Basler AG) with a variable 12.5mm to 75mm zoom lens (No. 64610, Cosmocar). The engine bellow was back lit with a white screen reflecting light from an LED studio light (CN-600SA, NanGuang) to produce a diffuse source. The camera was set up at a long distance to capture the convolutions of the bellow with minimal parallax error. The

camera was triggered by a function generator (AFG3021B, Tektronix) set to output a square wave trigger signal. The trigger signal was split, going to the camera, and also to an open voltage measurement channel on the engine DAQ multi function I/O device (NI-USB-6211, National Instruments Corp.). This allowed the camera images to be calibrated to the rotary encoder position they were taken at. The trigger signal for the camera was set to 10Hz. The image capture computer was set to take the first 100 images sent from the camera. An image of the calibration setup and view of the image capturing camera is shown in Figure 4.3.

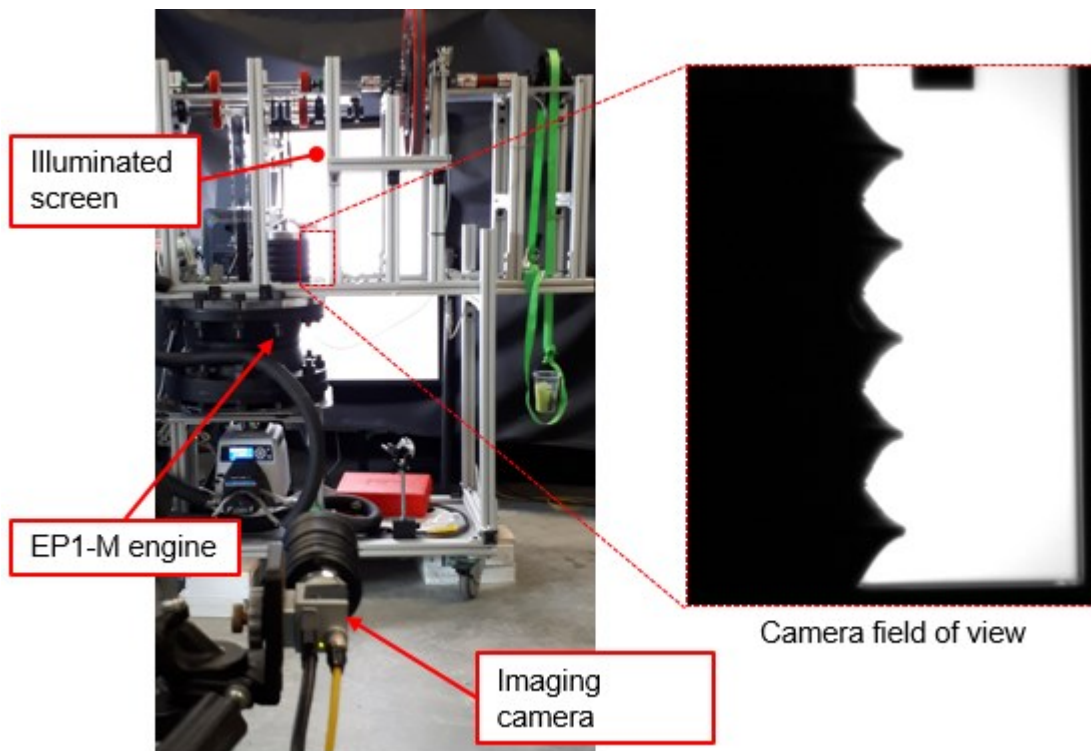


Figure 4.3 – Volume variation calibration trial setup showing the camera and EP1-M with the bellow profile as captured by the imaging camera

The engine piston head was modified with a 3D printed target arm as shown in Figure 4.4. The edge of the target arm is found in the later image processing and has a known distance from the centerline of the piston. The baseline trial configuration with the $e = 0$ gear pairs was used for volume variation trial set.

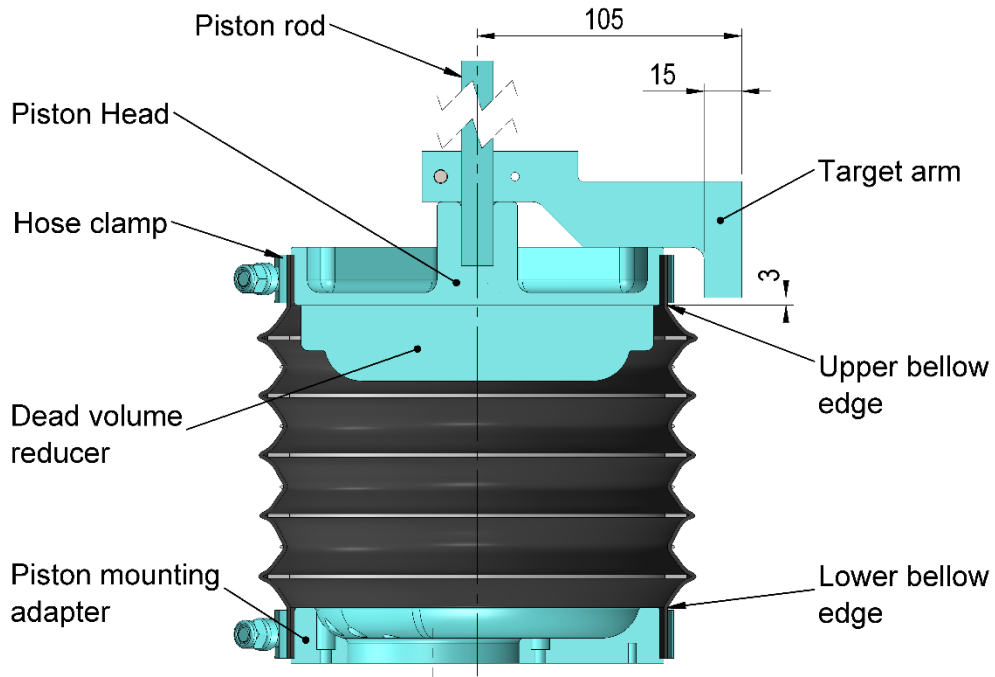


Figure 4.4 – Annotated section view of EP1-M piston with target arm and relevant dimensions

4.3.2 Volume Variation Experimental Procedure

Once the experimental set was configured for the volume variation calibration trial the camera was turned on and the area of interest was verified to be in frame. A series of pixel space calibration images were taken to convert the pixel resolution into direct measurements. An example of such a calibration image is shown in Figure 4.5.

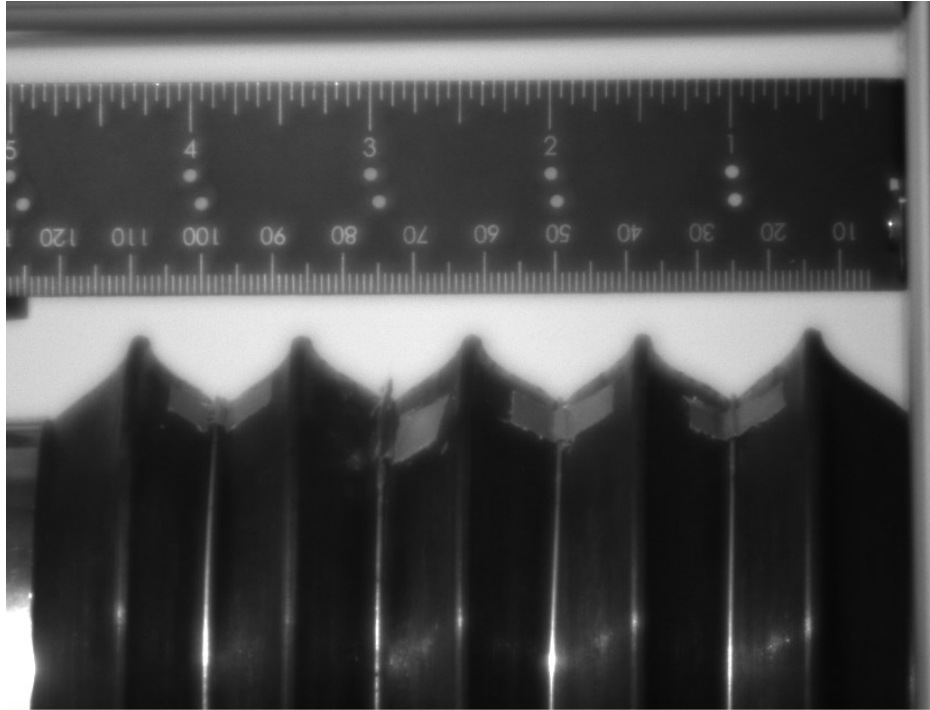


Figure 4.5 – Unprocessed pixel space calibration image from volume variation calibration

To perform the engine image capture trial the engine was started using the procedure as described in section 4.5.1. Once the engine was running the diffuse light source was turned on and the lab lights turned off. Three trials were completed back to back, capturing a total of 300 calibration images. The steady-state trial data collection procedure as described in section 4.5.2 was modified in the following ways to capture data for the volume calibration sets:

- Engine loaded to produce ~1Hz engine speed
- once 30s data sample recording is commenced, the function generator pulse stream is manually initiated ~5s into capture

4.3.3 Volume Variation Image Processing

The images taken by the camera were indexed to the crank angle position as recorded by the rotary encoder position that aligned to the camera trigger pulse. The indexed raw images were sorted into crank position order and each image was processed to determine the exterior volume of the bellow over a complete cycle. To translate between physical and pixel space a series of calibration images were captured

with a ruler mounted in plane with the profile of the bellow. An example image is shown in Figure 4.5. The pixel space relation defined by the calibration images was 0.16mm/pixel.

First the raw image is adjusted to improve edge definition to improve accuracy of the edge detection. A highpass filter was applied to remove low frequencies in the image that corresponded to gradual gradients, mostly in the background. The MATLAB function *imadjust* was then used to push grey towards either maximum or minimum brightness. This had the effect of boosting the white around sharp edges. The effects of this processing can be seen in the example images shown pre and post processing in Figure 4.6.

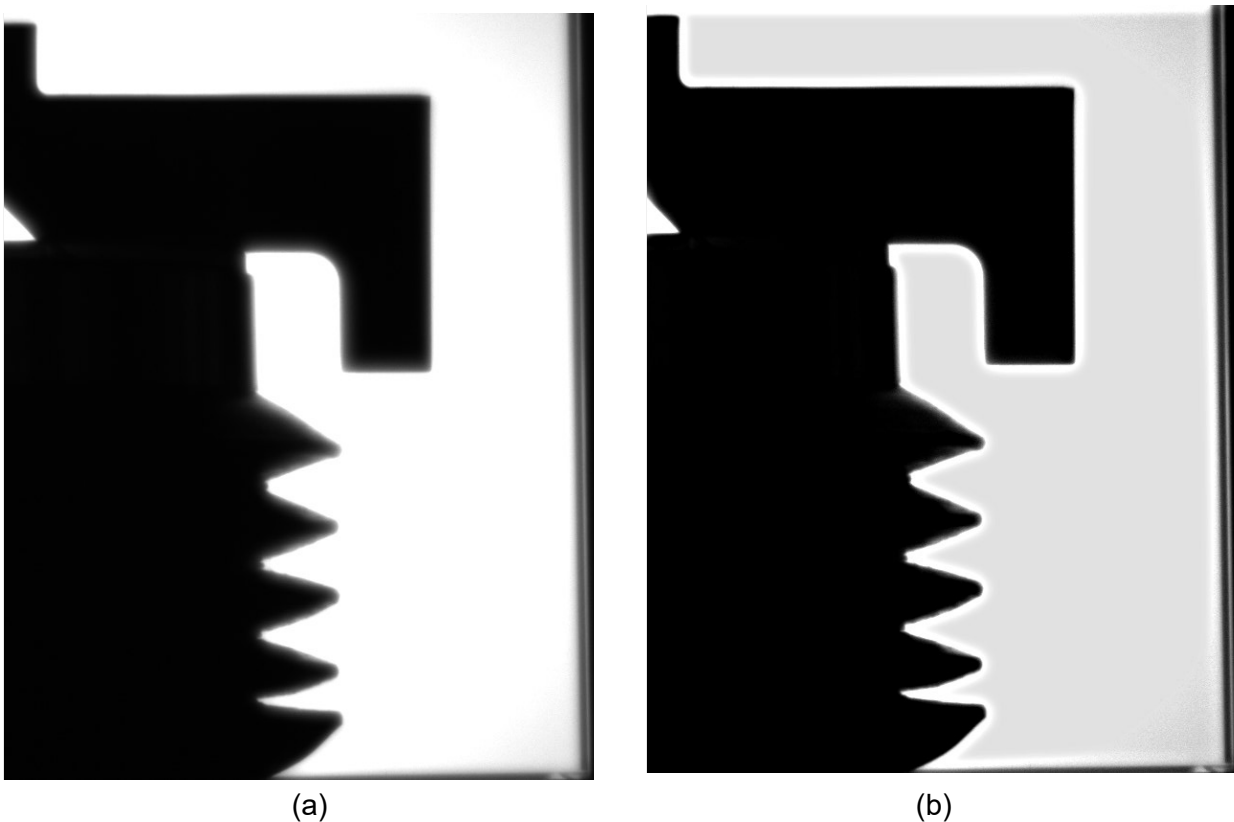


Figure 4.6 – Comparison of a (a) raw captured image and the (b) initial processed image with highly defined edges

With the improved image, an edge detection scheme was used to identify features with known physical dimensions. The cropping scheme is described in relation to Figure 4.7 (a). First the bottom edge is cropped to the bottom the bellow (line 1). This edge is fixed across all camera images so a simple offset crop was sufficient. Next the area

between the blue vertical lines (2) where the target arm moves is scanned for abrupt changes in image intensity from top to bottom. The second change is the bottom of the target arm (line 3). The edge of the bellow is a fixed offset distance from the edge of the target arm as shown in Figure 4.7. Applying this offset determines the top crop of the bellow image (line 4). Next, a region above the edge of the target arm bounded by blue lines (5) is scanned for changes of image intensity to find the outside edge of the target arm (line 6). Applying an arbitrary fixed offset from the target arm creates the right edge of the cropped image (line 7). The offset distance for the bellow centerline to the target arm edge is larger than the captured area of the image, so additional pixels are added to expand the image to the bellow centerline to form the left edge of the image (line 8). Applying the crop lines 1, 4, 7, and 8 results in an image that captures the full profile radius of the bellow between the bottom edge of the piston head and the upper edge of the bellow mounting adaptor as seen in Figure 4.6(b).

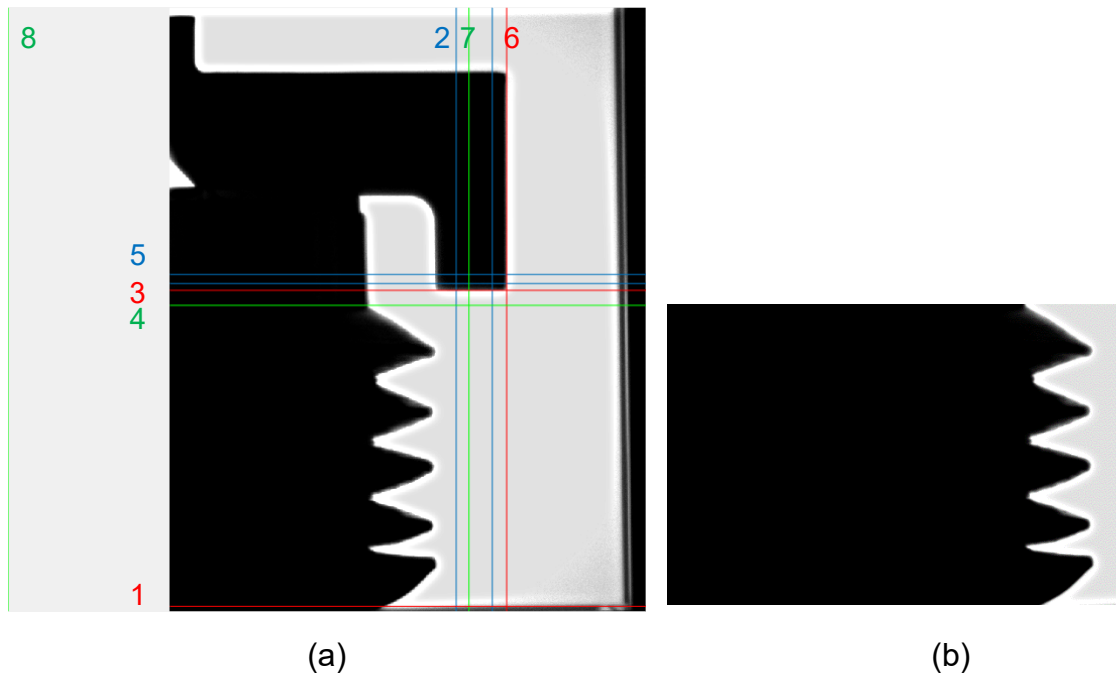


Figure 4.7 – Annotated view of (a) cropping lines used on bellow image and (b) the cropped image of the bellow radii

After cropping the convolution edge was then binarized and pixel intensity inverted, with solid bellow pixels attributed with an image array value of 1, and negative space assigned a value of 0. The final processed image is shown in Figure 4.8.

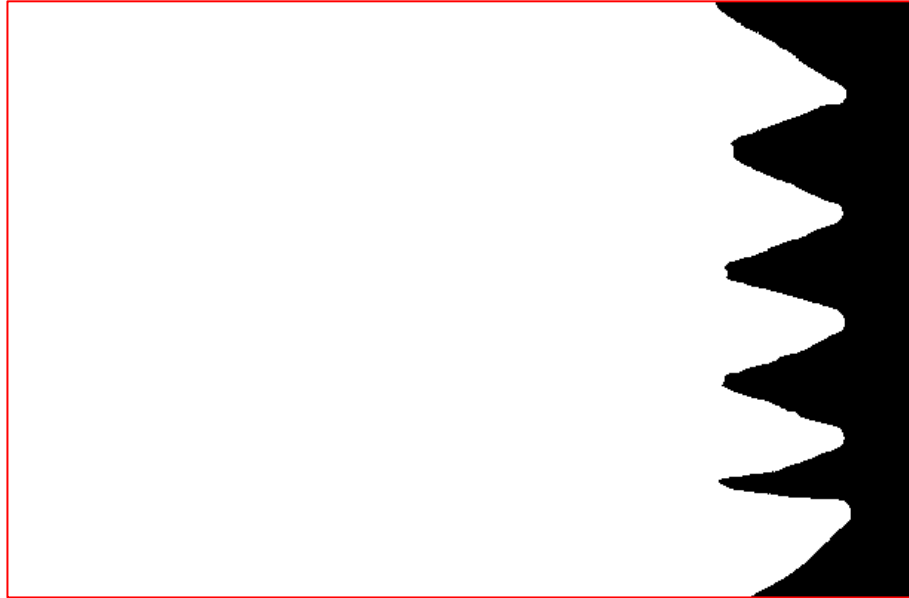


Figure 4.8 – Fully processed (average, cropped, and inverted) pixel space radial profile of bellow (red bounding box added to establish full image size)

With the fully processed image the volume of the bellow was calculated as a sum of disks, each 1 pixel in width as described by the following equation:

$$V_{bellow} = \sum_{i=1}^n A_i \cdot h = \sum_{i=1}^n \left(\pi \cdot \left(\sum row_i \cdot \frac{0.16mm}{pixel} \right)^2 \right) \cdot \frac{0.16mm}{pixel} \quad 4.1$$

where:

- V_{bellow} = external volume of the bellow
- A_i = area of row disk
- h = height of row (1 pixel)
- $\sum row_i$ = sum of pixels per image row

A critical assumption of the calibration is that bellow maintains a substantially cylindrical shape through expansion and compression, and that the captured image of the bellow radius profile is representative of its radius at any section about its axis. Observing the bellow while running qualitatively validated this assumption as no one side flexed or deform noticeably asymmetrically. Multiple trials were taken over many cycles and aggregated together to form the volume – position calibration. A bellow

profile image captured at TDC during the volume variation trials was subsequently loaded into SOLIDWORKS to model the bellow accurately with measured material thickness. The solid model of the bellow as seen in Figure 4.4 and other figures is this solid model.

The core image processing script was written by Linda Hasanovich, and was integrated into the data processing scripts by the author. The MATLAB script for the image processing is documented in Appendix E.6.

4.3.4 Volume Variation Results

Data from the three volume variation calibration trials was aggregated into a compound curve that was fitted to produce a volume lookup table for each encoder position. A spline fit was made using a window of volumes at each integer rotary encoder position from 0 to 499. This method was used to account for subtle changes in the curve that were not adequately captured by other fitting methods examined. Tested fits included a sine fit and a linear spline scheme of the complete volume calibration.

The fitted splines were a second order polynomial generated by the *polyfit* function in MATLAB over a window of 47 volume data points either side of encoder position in question. Using the *polyval* function in MATLAB an external bellow volume value was calculated for the encoder position in question, along with a standard uncertainty prediction. The standard uncertainty prediction, when doubled, provides a roughly 95% confidence interval [63] and was used as the uncertainty value for the volume lookup table $u_{V,cal}$. The calculated fit is presented in Figure 4.9 with the image calibration data points. The spread of images taken account for random and systematic uncertainty in the in the drive mechanism between the piston head and the rotary encoder during the calibration trial.

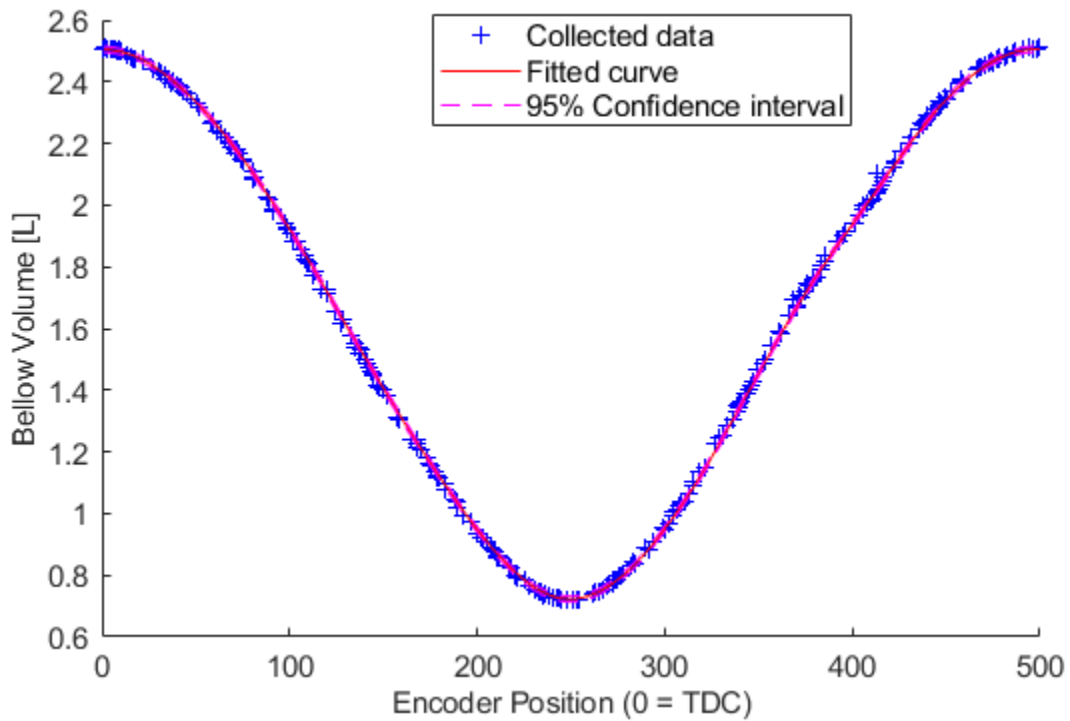


Figure 4.9 – Fitted curve of bellow external volume at each rotary encoder position for the volume variation calibration trial

To calculate the working fluid volume contained within the piston, the internal volumes associated with internal structures discussed in section 3.3 were subtracted from the external bellow volume results. Uncertainty in the rotary encoder position and calibration during trial data processing are noted in Appendix B.6.

4.4 Testing Sequence

Test trials were structured such that a complete suite of trials was collected for all the modeled displacer and piston motion configurations noted in section 2.3. A set of baseline trials was run the very beginning of the test sequence to establish a case for conventional piston motion against which the variations in motion would be evaluated. Trials were arranged to independently test displacer dwell, piston dwell, as well as combinations of dwelling both pistons. The final test group was the triangular displacer motion with piston dwelling piston. A final set of baseline trials was also run at the end of all testing to verify if the performance of the engine had drifted over the course of testing. No substantial drift was observed. The test trial sequence and gearing configurations is displayed in Table 4.1

Table 4.1 – Test group trial sequence

Manipulated Variable	Sequential Test Group	Trials	Piston Gear Set	Displacer Gear Set
Baseline	1	3	$e = 0$	$e = 0$
	11	2	$e = 0$	$e = 0$
Displacer dwell	2	2	$e = 0$	$e = 1/5$
	10	2	$e = 0$	$e = 1/3$
Piston dwell	6	2	$e = 1/5$	$e = 0$
	7	2	$e = 1/3$	$e = 0$
Displacer and piston dwell	5	2	$e = 1/5$	$e = 1/5$
	9	2	$e = 1/3$	$e = 1/3$
Triangular displacer and piston dwell	3	2	$e = 0$	$e = 1/5$ *
	4	2	$e = 1/5$	$e = 1/5$ *
	8	2	$e = 1/3$	$e = 1/5$ *

Testing of the gears was performed over a period of 30 days with 9 individual test days. The trials were arranged in a sequence that facilitated the change of gears with minimal effort and disruption to the engine. Additionally, trials employing the $e = 1/3$ gear sets were grouped at the end of test trials as it was anticipated that these gears would introduce the most stress on the engine components. This was based on the severity of the motion modification resulting in high accelerations in drive mechanism components and the high pressure angle of the gears as can be seen in Figure 3.13.

A summary of the chronological data collection plan is presented in Appendix D along with reproductions of the trial logs that note the trial dates and any noteworthy observations during engine operation. At the beginning of test group 9 a small tear between the pleats of the elastomer bellow was discovered during the pre-trial testing procedure. The bellow was replaced with a spare identical bellow from the same supplier. A 1 hour long break-in session was run at ~ 1 Hz engine speed prior to resuming data collection to break-in the replacement bellow. No other major engine changes or stoppages were observed during testing.

4.5 Steady State Engine Trial Procedures

This section describes the general procedures used when collecting data during the steady state trials. The procedures are separated for initial engine start-up, trial data collection, and changing of gears. Many steps involve interacting with the LabWindows CVI DAQ UI, an annotated image of which is shown in Figure 3.27.

4.5.1 Engine Start and Warm-up Procedure

To start the engine and data collection system the following procedure was performed to ensure engine performance consistency between trials:

Step	Procedure
1	Inspect and turn on heating and cooling baths <ul style="list-style-type: none">- Add water as necessary.- Inspect flow loop lines, ensure pump heads are disengaged, and ensure valves are closed.- Turn on bath and verify set point.- Slowly open flow loop valves to circulate thermal fluid and preheat engine. Inspect for flow loop leaks.- Wait minimum of 1hr prior to running engine.
2	Engine general inspection <ul style="list-style-type: none">- Ensure engine pressure vent plug is removed.- Ensure engine drive mechanism locks are engaged.- Switch over drive mechanism gears as needed.- Apply gear lubricant as needed.- Inspect engine fasteners and instruments. Tighten as needed.
3	DAQ power on <ul style="list-style-type: none">- Turn on DAQ computer.- Turn on NI.- Turn on power supply and set to output. Verify outputs (CH1 5V, CH2 20V).- Turn on Pezotronic pressure demodulator.- Open LabWindows CVI and run UI.- Turn on live voltage output.
4	Engine pressure integrity test <ul style="list-style-type: none">- Disengage drive mechanism lock.- Move piston to TDC.- Press finger over pressure vent plug and apply pressure to engine by rotating output shaft slowly by hand.

-
- Observe DAQ live pressure readout and inspect for leaks resulting in decrease in engine pressure (engine will have slow leak at displacer rod for equalization during engine running).
 - Move piston to BDC.
 - Press finger over pressure vent plug and apply vacuum to engine by rotating output shaft slowly by hand.
 - Observe DAQ live pressure readout and inspect for leaks resulting in increase in engine pressure (engine will have slow leak at displacer rod for equalization during engine running).
 - Repair any leaks as necessary.
-

5 Engine rotary encoder alignment

- Turn on Encoder Alignment window in DAQ UI to display encoder Z-pulse.
 - Mount dial indicator to engine frame to read out piston head height.
 - Rotate engine output shaft by hand to bring the piston head to TDC by observing dial indicator maximum point of travel.
 - At TDC, observe DAQ Encoder Alignment window. If lit, encoder is aligned with TDC, if not proceed.
 - Engage drive mechanism lock.
 - Loosen set screw on the shaft pulley of the rotary encoder belt
 - Adjust pulley until DAQ Encoder Alignment window is lit.
 - Disengage drive mechanism lock and verify TDC alignment with dial indicator and Encoder Alignment window.
-

6 Engine start and warm up

- Load brake with 5 x 71g load units.
 - Rotate output shaft until piston is at half stroke.
 - Partially insert pressure vent plug.
 - Pull on flywheel to kick engine rotation.
 - If engine begins to run, close pressure vent plug.
 - Observe DAQ live readouts and verify instruments are outputting as expected.
 - Let engine run at ~1Hz for 0.5 hrs prior to running trials to allow engine temperatures to equilibrate to running condition.
-

4.5.2 Steady State Trials

The procedure for collection of steady state data applied to any complete trial for data collection. A trial for any gear configuration involved allowing the engine to run unloaded, and progressively load the engine up to stall, and then progressively unload the engine back down to free running. The procedure is used in conjunction with the data collection plan / logs, which have been reproduced in Appendix D

Step	Procedure
1	<p>Pre-trial engine running and parameter verification</p> <ul style="list-style-type: none">- Ensure the engine has been running for at least 15 minutes prior to data collection.- A prior trial run is sufficient for pre-running.- The engine should be pre-run at ~1Hz.- Verify the readouts of data collection instruments using the “LIVE” data readouts on the DAQ UI.- Inspect the water bath temperatures are within ± 2 °C of the set point.
2	<p>Update DAQ filename output information & verification</p> <ul style="list-style-type: none">- Update the DAQ UI with the configuration specifications for the trial.- Verify data collection rates, duration, and channels.
3	<p>Engine free running: first data point</p> <ul style="list-style-type: none">- Remove any applied engine load masses and remove load strap from engine brake.- Set timer for 2 minutes minimum to achieve steady state running.- Proceed to step 4.
4	<p>Data point data recording procedure</p> <ul style="list-style-type: none">- Update the DAQ UI with data set specifications from the collection plan- Record atmospheric pressure for 10s and update value in DAQ UI- Inspect the water bath temperatures are within ± 2 °C of the set point.- Observe the live engine speed plot on UI for attainment of steady state condition- Once steady state timer has elapsed and the engine speed plot shows minimal fluctuation data may be recorded:<ul style="list-style-type: none">o Stop “LIVE” readoutso Select “Acquire ALL”o Do not touch engine or UI during the next 20s while data is recordedo Wait for recorded data to be displayed on UI windows- Observe for any irregularities in recorded data meriting a re-record- Update the data collection log- Turn on “LIVE” data readouts

5 Engine loading

- Apply engine loading strap to brake wheel if not present.
- Add load mass to the strap in increments as dictated by the collection plan using the mass units of 35.5g.
- If engine has stalled after applying load, remove 1 mass unit at a time while trying to restart engine.
- Repeat until running.
- Observe data readouts for any irregularity in engine performance.
- Set timer for 2 minutes minimum to achieve steady state running
- Proceed to step 4.
- Repeat until engine has stalled consistently and cannot be restarted without going below last recorded load increment.
- Record a second data point at the maximum loading increment with unloading load code.

6 Engine unloading

- Remove load mass from the strap in increments as dictated by the collection plan using the mass units of 35.5g.
- Observe data readouts for any irregularity in engine performance.
- Set timer for 2 minutes minimum to achieve steady state running.
- Proceed to step 4.
- Repeat until engine has no more applied mass units.

7 Engine free running: last data point

- Remove load strap from brake drum.
- Observe data readouts for any irregularity in engine performance.
- Set timer for 2 minutes minimum to achieve steady state running.
- Proceed to step 4.
- Once final data point is recorded, re-apply load strap and apply load mass units until engine is running at ~1Hz.

8 Post-trial engine running and parameter verification

- Inspect the water bath temperatures are within ± 2 °C of the set point.
 - Inspect engine for any irregularities such as:
 - o Excess drive train noise.
 - o Sounds of air leaking.
 - o Bellow noise or leaks.
 - If a second trial is to be run in this configuration proceed to step 2 and repeat procedure after 2 minutes.
 - If engine is to be reconfigured or stopped:
 - o Remove engine vent plug slowly.
 - o Observe engine as it comes to a stop.
 - o Apply engine rotation locks.
 - To restart engine follow step 6 of engine start procedure.
-

5 DATA PROCESSING

This chapter describes the data processing scheme used to process the data from the collected data. A discussion regarding measurement uncertainty is presented first and is incorporated into the data processing of measured values. The last portion of this section described the methods and formulas used to calculate engine performance metrics from the measured data.

5.1 Calculation of Uncertainties

Uncertainty in were calculated for all directly measured variables. Random uncertainty was accounted for for all sampled variable were calculated for a 95% confidence interval assuming a two tailed normal distribution for collected measurements. Random uncertainties were combined with systematic uncertainties pulled from manufacturer information using standard uncertainty calculation methods described in the work of Wheeler and Ganji [60], and by Coleman and Steele [64]. Uncertainty was propagated through the equations of calculated variables provide the combined standard uncertainty intervals for all measured values. It was assumed that the sources of uncertainty were not correlated Detailed descriptions of the equations used are presented in Appendix A.

For certain instruments a set of calibrations was performed to reduce uncertainty of a measured variable as much as possible to improve the quality of quantified variables. As was previously presented in section 4.3, a calibration of the volume variation of elastomer bellow was done to provide a volume – output shaft, but a side benefit of the calibration was a significantly reduced uncertainty measurement of the engine volume change. Michaud [62] utilized a static imaging technique for calculation of a bellow volume of a similar design and reported an average uncertainty interval of ± 0.05 L for instantaneous volume variation measurements. Through the calibration method used in this investigation the uncertainty interval for instantaneous volume variation measurements was reduced to just ± 0.009 L. Calibration of the diaphragm pressure transducer was undertake with a large scale manometer specifically to reduce

uncertainty. Stumpf [40] reported a uncertainty interval of ± 0.44 kPa using the same diaphragm pressure transducer as used in this investigation, while after calibration for this investigation gauge pressure measurement uncertainty was reduced to ± 0.17 kPa. Low uncertainties for pressure and volume were critical to the accurate determination P-V indicator diagram calculations at the core of this investigation.

An area where uncertainty was particularly high in this investigation was the propagated uncertainty of the temperature differences between the inlet and outlet temperatures of the thermal source and sink flow loops. The individual combined standard uncertainty of the RTDs was determined to be ± 0.46 °C, and when propagated through when calculating ΔT it rose to ± 0.57 °C. This became an issue due to the fact that the observed temperature drop from inlet to outlet was quite small on average, < 5 °C. This resulted in a relative uncertainty on the order of 15% to 20%. This high relative uncertainty dominated the propagated calculations of heat transfer in (Q_{in}) and out (Q_{out}) of the engine, as well as calculations of engine thermal efficiency (η_T). These results were not critical to the investigation, but could be improved for future work with more precise calibration or by allowing the drop in temperature of the thermal loops to be more substantial by lowering the mass flow rate for the thermal loops.

5.2 Data Processing Methodology

This section describes the data processing methodology applied to the raw data recorded from the individual data sets and how it was aggregated into data for trials. All raw data consisted of *.log files of the voltage outputs collected by the LabWindows CVI code. Each DAQ module was recording at an independent sampling rate as discussed in section 3.6.1. Three *.log files were created, one from each DAQ module. An example of the *.log data structure is shown in Figure 3.28. At the top of the file the date, time, and recorded channels of that module are noted. The global beginning and end time of the sampling is also noted, which shares a common clock across all DAQ module *.log files. Each sample of the channels is then recorded in tab delimited rows for the complete duration of the sampling. For example, the multi function I/O device was sampled at a rate of 30 kHz for the 20s sampling duration, resulting in each captured data *.log file having 600,000 rows of data.

A set of processing scripts were written in MATLAB to load the trial *.log files and process them. The MATLAB data processing script is documented in Appendix E.3 for reference. The first step was interpreting the relevant trial parameters from the name of the *.log files, which recorded details regarding the trial. Data included:

- Trial date and time
- Nominal source and sink temperature
- The nominal mass applied to the brake for that data set
- The gear set code for the piston and the displacer
- Atmospheric pressure recorded for that data set
- Whether the trial was a free running, loading, unloading, or end free running load condition (load code)

The arrays of voltage data recorded for each instrument was then processed.

5.2.1 Determination of Angular Positions

The processing approach taken was to organized and average values to each recorded rotary encoder position of the output shaft position. The logic behind this was to have data points of instantaneous engine performance evenly spaced over the

engine cycles. To establish the first rotary encoder position, raw voltage data for the encoder Z channel was analyzed. The channel output a binary signal of 0 volts when “off”, and a 5 volt value when it was “on”. From the encoder calibration procedure, the middle of the pulse was calibrated to piston TDC and represents the output shaft position of 0°. The index of the loaded data array corresponding to this 0° value was noted. The first binary pulses of the encoder A channel aligns with the Z channel, and the processing code subsequently identified the middle of following pulses, ascribing them a value of $i + 1$ with $i = 1$ being the first Z pulse detected. A visual representation of this scheme is depicted in Figure 5.1, where the raw pulse trains Z, A, and M are organized into indexed arrays of Z*, A*, and M*. The MATLAB implementation of this scheme is shown in Appendix E.5.

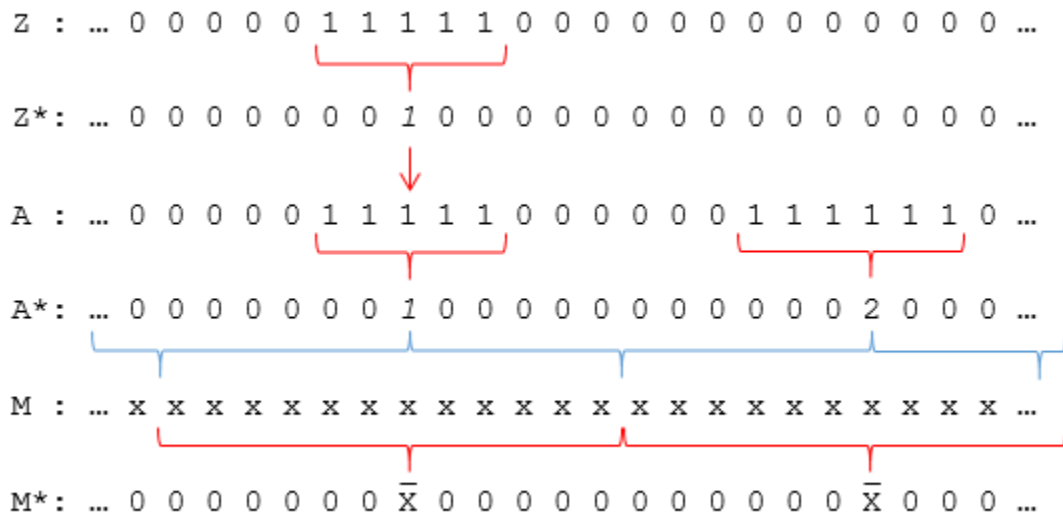


Figure 5.1 – Visualization of rotary encoder discretizing and signal averaging scheme

All data arrays from a *.log group share the same array dimensions. With the indexes of all the sequential rotary encoder position “ticks” known, the raw data measurements were averaged to produce measurement mean values \bar{M}_x at the same index position as the encoder position ticks for each recorded channel. The calculation of these values was a simple mean of the recorded data captured in the range between the mid point between each rotary encoder position index, as can be visualized in Figure 5.1. The bias uncertainty for each averaged data point was calculated using the bias uncertainty

methods and taking a 2-tailed t -score value with a 95% confidence interval using built in MATLAB calculations of standard deviation.

The index of each pulse increment was noted by the script, and a new vector was created with the index values of the encoder pluses, creating an array of each encoder pulse index over the experiment sampling set. The script called each index to produce vectors of data with each row corresponding to the sequential encoder position index, or “tick”. These vectors formed a sequential recording of the engine performance at each $2\pi/500$ position θ of the engine output shaft. The voltage data vectors included:

- Position θ (ticks and radians)
- Average voltage values of TOR, P1, P2
- Bias uncertainties of TOR, P1, P2
- DAQ Time of the specific position index

5.2.2 Thermocouple and RTD Data Alignment

The next process of the script was to align the recorded data from the thermocouple DAQ and the RTD DAQ to a corresponding rotary encoder position. The thermocouple *.log data points had recorded time values that were universal across all three *.log files. The script matched the closest matching voltage time values to the recorded thermocouple time values. Indices of the matches were noted and the midpoints between indices them were used to form averaging windows for calculating the mean thermocouple data in vectors that aligned with the voltage data. A visualization of this scheme is shown in Figure 5.2. The bias uncertainty for each averaged thermocouple data point was calculated in same way as for voltage data points.

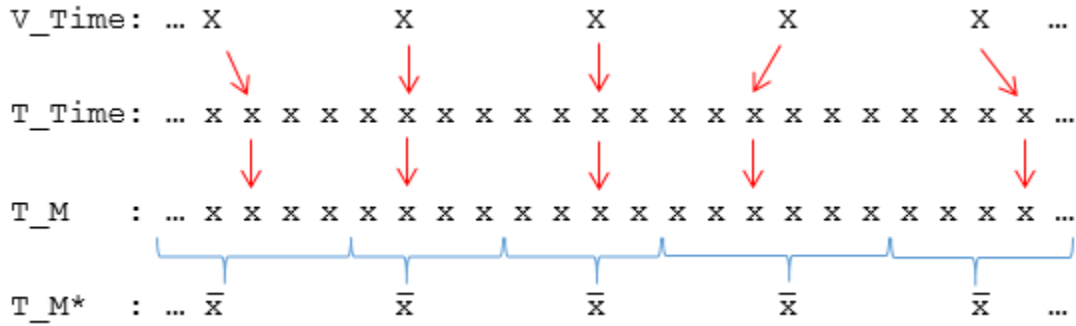


Figure 5.2 – Visualization of thermocouple data to voltage data alignment and averaging scheme

Alignment for the RTD measurements was done in much the same way as for the thermocouple data, except that data was aligned for each cycle of the engine rather than for each rotary encoder positions. The time value for each 500th rotary encoder positions was matched to a measured time for RTD data, and the RTD measurements were averaged in windows bounded by each matched time index. The mean values of RTD measurements for the whole cycle were ascribed to each rotary encoder positions within that cycle. The bias uncertainty for each averaged RTD cycle value was calculated in same way as for voltage data points and thermocouple data points.

5.2.3 Data Cropping to Complete Cycles

The complete data vectors were cropped at the ends to include only complete cycles. Bases on the indexing scheme, this resulted in data arrays cropped from the first position array multiple of 500, and ended by the last complete integer multiple of 500 ticks. The total number of cycles recorded was determined by the data vector lengths by 500.

5.2.4 Determination of DP and PP Crankshaft Position

The crankshaft position of the displacer θ_d and the piston θ_p was determined using the transmission function as described by equation 2.20 for the gear set used in the trial. A sub function in the data processing script applies the appropriate centrode geometry to the transmission function based on the gear set configuration data

interpreted from the *.log file titles. Uncertainty for the crankshaft positions u_{θ_d} and u_{θ_p} is applied based on the backlash uncertainty calibration as described in Appendix B.6.1.

5.2.5 Determination of Engine Volume

The volume of the engine is determined from the piston crankshaft position θ_p . The volume of the elastomer bellow piston was calibrated to the position of the engine output shaft using the round $e = 0$ gear set and thus with the 1:1 transmission function of the calibration, the piston crankshaft position θ_p was able to correlate to the θ -volume lookup table generated from the calibration detailed in section 4.3. A linear interpolation is used if the input values of θ_p that fall between tabulated values of θ . The volume of the piston V_{θ_p} was added to the minimum volume V_{min} of the engine working space as documented in section 3.3 to obtain a measurement of the total engine volume in m^3 .

Uncertainty in the determined value of engine volume is determined by taking the minimum and maximum value of $\theta_p \pm u_{\theta_p}$ and using the lookup table to find the volume uncertainty interval V_{min, θ_p} and V_{max, θ_p} . The maximum value of the uncertainty interval from V_{θ_p} established the positions uncertainty of volume $u_{V_{\theta_p}}$. Finally, the uncertainty of $u_{V_{\theta_p}}$ was propagated with the calibration volume uncertainty $u_{V,cal}$.

5.2.6 Data Conversion

To obtain the true values from all the aligned and averaged measurement vectors the conversion equations for each measured value was applied. The conversion equations for the measurement instruments is documented in section 3.5. Conversions are also applied to the uncertainties for each measurement.

5.2.7 Data Organization and Averaging

The final data processing operation applied to the data set measurements was to break up the linear sequential cycle arrays into a matrix for each measurement. A modulo operation was applied to the encoder position vector and each sequential measured engine property of at the same encoder position was added to a new column of the 500 row matrix. Data from each row of a measurement matrix was then averaged to determine the average measurement of an engine variable for each rotary encoder positions over the full range of cycles captured during the sampling duration.

5.3 Calculated Parameters

For each processed engine data set numerous engine parameters were calculated as listed in Table 5.1. Subsections discuss the methods and equations used to calculate these parameters for any given trial data set and any relevant assumptions.

Table 5.1 – Calculated engine parameters

Engine Property	Symbolic Variable	Units
Engine speed	ω	[rad/s] [rpm]
Shaft work	W_s	[J]
Shaft power	p_s	[W]
Indicated work	W_{ind}	[J]
Forced work	W_{FW}	[J]
Efficacious work	W_{EFF}	[J]
Mechanism effectiveness	E	-
Heat transfer rate into engine	\dot{Q}_{in}	[W]
Heat transfer rate out of engine	\dot{Q}_{out}	[W]
Thermal efficiency	η_T	-
Engine global losses	\dot{Q}_L	[W]

5.3.1 Calculation of Engine Speed

The data set averaged output shaft angular velocity, presented in this work simply as engine speed, is the average output shaft angular velocity as measured by the rotary encoder for the measured 20s data collection sample. The efforts noted in the data collection procedures as described in section 4.5.2 to maintain steady state operational conditions support the assumption that the cycle average velocity over the trial was unlikely to change. For engine speed, the number of complete cycles was determined from the rotary encoder Z-pulse measurement (as described in 5.2.3). The total number of engine cycles was then divided by the difference between the time stamp of the last included Z-pulse and the first Z-pulse. This method is represented in equation form as:

$$\omega = \frac{n_{cycles} \cdot 2\pi}{\Delta t} = \frac{n_{cycles} \cdot 2\pi}{(t_{zn} - t_{z1})} \quad 5.1$$

where: ω = Shaft angular velocity [rad/s]
 n_{cycles} = Count of complete engine cycles per data set
 Δt = duration of the data cropped set from beginning cycle to end cycle $(t_{zn} - t_{z1})$ [s]

The uncertainty propagation for shaft work and shaft power is presented in Appendix C.1. Of note, engine speed is typically reported in units of revolutions per minute [rpm] as is common when describing engines.

5.3.2 Calculation of Shaft Work and Shaft Power

The shaft work and shaft power were straightforwardly calculated from engine measured data using equations 1.16 and 1.17. The equations are presented here again for completeness.

$$W_s = \tau_s \cdot 2\pi \quad 5.2$$

where: W_s = Shaft work [J]
 τ_s = Torque of output shaft [Nm]

$$p_s = \tau_s \cdot \omega \quad 5.3$$

where: p_s = Shaft power [W]
 τ_s = Torque of shaft [Nm]
 ω = Angular frequency [rads/s]

The uncertainty propagation for shaft work and shaft power is presented in Appendix C.2.

5.3.3 Indicator Diagram Work Components

Components of work are calculated in MATLAB using an integration approximation scheme from the vectors that make up the engine indicator diagram. Calculated work components are: efficacious work (W_{EFF}), forced work (W_{FW}), and indicated work (W_{ind}). The indicator diagram is generated from the closed curve formed from cycle pressure (P_{avg}) and cycle volume (V_{avg}) values at each of the 500 rotary encoder positions

averaged over a trial. A trapezoid approximation of the integration of the P-V curve was coded in MATLAB as described by equation 5.4:

$$W_x = \int_{V_{min}}^{V_{max}} P_{avg} \cdot dV_{avg} \cong \sum_{i=1}^{500} \left(P_{avg,i} \cdot \frac{(V_{avg,i+1} + V_{avg,i-1})}{2} \right) \quad 5.4$$

where: W_x = Work of segment x [J]
 V_{max} = Maximum engine volume [m³]
 V_{min} = Minimum engine volume [m³]
 P_{avg} = Trial average gauge pressure [Pa]
 V_{avg} = Trial average volume [m³]
 i = Rotary encoder index

The approximation yields the same results as the *polyarea* function of MATLAB. Efficacious and forced work segments were determined by their definitions as described in section 1.3.4. In cases where $dV_{avg,i}$ = the sign of $P_{avg,i}$ the area component was added to total efficacious work. In cases where $dV_{avg,i} \neq$ the sign of $P_{avg,i}$ the area component was added to total forced work. The indicated work was calculated as the net of efficacious work and forced work as described in equation 1.14.

The propagated uncertainty for the integration approximation scheme for calculating work segments is detailed in Appendix C.3

5.3.4 Estimation of Mechanism Effectiveness

With calculated values of shaft work, indicated work, and forced work a calculation of mechanism effectiveness can be made by using equation 1.20 and the quadratic equation. Coefficients of the quadratic equation are drawn from equation 1.20 as follows:

$$E = \frac{-c_2 + \sqrt{c_2^2 - 4c_1c_3}}{2c_1} \quad 5.5$$

where: c_1 = $W_i + W_{FW}$
 c_2 = $-W_s$
 c_3 = $-W_{FW}$

Propagation of uncertainty through the quadratic equation was determined with guidance from the NIST/SEMATECH e-Handbook of Statistical Methods [65] and is detailed in Appendix C.4.

5.3.5 Calculation of Heat Transfer rates and Engine Efficiency

For the control volume of the engine the heat transfer rate \dot{Q}_{in} is supplied by the steady flow hot source loop. It is assumed that the kinetic energy changes in the loop are negligible and the potential energy change is also negligible as the loop returns to the bath. Likewise, a portion of the energy leaving the engine is taken by the cold sink flow loop as the heat transfer rate \dot{Q}_{out} . The cold loop operates under similar assumptions as the hot source loop. The general equation describing the heat transfer rate is as follows:

$$\dot{Q} = \dot{m} c_p \Delta T = \dot{m} c_p (T_{in} - T_{out}) \quad 5.6$$

where: \dot{Q} = Heat transfer rate [J/s]
 \dot{m} = Mass flow rate of thermal fluid [kg/s]
 c_p = Specific heat capacity [J/kg·K]
 T_{in} = Temperature of fluid entering the engine exchanger [K]
 T_{out} = Temperature of fluid leaving the engine exchanger [K]

The heat capacity for water used in the thermal loops is assumed constant as the typical temperature drop of the thermal loops was ~ 5 °C in all trial conditions. The values and properties used in the calculation of thermal flows is presented in Table 5.2.

Table 5.2 – Heat transfer variables and uncertainties

Variable	Value	Uncertainty Variable	Uncertainty Value	Unit	Notes
\dot{m}_h	3.237×10^{-2}	$u_{\dot{m}_h}$	$\pm 1.9 \times 10^{-4}$	kg/s	See Appendix B.1
\dot{m}_c	2.914×10^{-2}	$u_{\dot{m}_c}$	$\pm 1.0 \times 10^{-4}$	kg/s	See Appendix B.1
c_{p_h}	4206	$u_{c_{p_h}}$	Negligible	[J/kg·K]	Taken from [66] saturated water at 90 °C
c_{p_c}	4205	$u_{c_{p_c}}$	Negligible	[J/kg·K]	Taken from [66] saturated water at 5 °C
$T_{h\ in}$	Variable per trial	$u_{T_{h\ in}}$	Variable per trial	[°C]	Converted to [K] for calculation in equation 5.6
$T_{h\ out}$	Variable per trial	$u_{T_{h\ out}}$	Variable per trial	[°C]	Converted to [K] for calculation in equation 5.6
$T_{c\ in}$	Variable per trial	$u_{T_{c\ in}}$	Variable per trial	[°C]	Converted to [K] for calculation in equation 5.6
$T_{c\ out}$	Variable per trial	$u_{T_{c\ out}}$	Variable per trial	[°C]	Converted to [K] for calculation in equation 5.6

Details of the uncertainty calculation of the heat transfer rates is detailed in Appendix C.5.

5.3.6 Engine Efficiency and Global Losses

With the heat transfer rates into and out of the engine known, as well as the shaft power, the thermal efficiency of a heat engine [20] can be determined by the following equation:

$$\eta_T = \frac{p_s}{\dot{Q}_{in}} \quad 5.7$$

where: η_T = Thermal efficiency of the engine
 p_s = Shaft power out of the engine
 \dot{Q}_{in} = Thermal energy delivered to the engine

This investigation examines thermal efficiency of the engine from inputs of thermal energy to the delivered shaft power. Parasitic loads on the engine, such as pumping energy required by the thermal loops, is not considered. This was because the focus of the research was on the engine cycle itself, rather than the particular arrangement of the experimental engine and supporting equipment. The pump utilized for the investigation emphasized accuracy over efficiency. In a practical deployment of the system to an application further consideration of the parasitic loads on the engine performance would need to be considered to determine the brake efficiency of the engine.

An encompassing calculation of the energy lost from the engine control volume can be determined by taking the heat transfer rate delivered to the engine and subtracting the know energy flows out of the engine as described by the following:

$$\dot{Q}_{Lost} = \dot{Q}_{in} - p_s - \dot{Q}_{out} \quad 5.8$$

where: \dot{Q}_{Lost} = Thermal efficiency of the engine
 \dot{Q}_{in} = Thermal energy delivered to the engine
 p_s = Shaft power out of the engine
 \dot{Q}_{out} = Thermal energy taken by the cold sink loop

This lost energy includes thermal loses to the ambient conditions, friction loses from the mechanism, and any other losses not captured by these three measured energy flows.

The propagations of uncertainties for both the engine efficiency and the engine global loss variable is presented in C.6.

5.3.7 Recalculation of Isothermal Modeling Results

As part of the evaluation of the isothermal model's utility in predicting the performance of low temperature Stirling engines the results of the model as implemented were compared to the empirical results obtained from testing the EP1-M. To obtain a fair assessment of the model, the input parameters of the model were updated with values observed during testing for the maximum power producing data set of a test group. These variables include:

- Heater and expansion space temperatures T_e, T_h
- Cooler and compression space temperatures T_c, T_k
- Engine buffer pressure P_b
- Mechanism effectiveness E

The other implementation parameters noted in Table 2.1 were accurate to the EP1-M and were kept constant. Results of the recalculated results are presented in section 7 where they are evaluated against the empirical performance of the engine.

6 EVALUATION ENGINE PERFORMANCE

This chapter presents the results of the steady state trials for the performance modifications made to the drive mechanism of the EP1-M. Results are organized by test groups as laid out in section 4.4. Each section presents results summarizing the complete test group, itself made up at least two trials conducted as identically as possible. Each trial within a test group is comprised of data sets of recorded and processed data for each loading condition of the engine, as was recorded in the collection plan / logs (see Appendix D). In total there were 11 test groups of data collected, comprised of 23 trials made up from 473 total data sets processed.

The concerns of this work are around improving the performance of low temperature Stirling engines in the context of maximum power production potential. In addition to summaries of test group performance, the details of the maximum power producing data set of each test group is also discussed. Comparisons are made between the performance of the motion modification test groups and the baseline test. The comparison serves as a basis to measure the success of modified piston and displacer motion as an effective way of improving the power potential of a low temperature kinematic Stirling engine.

Test conditions were held as constant as possible over the course of the trials. Table 6.1 lists the constant engine control variables that were applied to all test group trials. Tables within the results note any variations to test group conditions for that group.

Table 6.1 – General experimental controlled variables for all test groups

Property	Variable	Nominal Value	Actual Value	Unit
Hot source temperature	T_{Hin}	90	see results	°C
Hot source mass flow rate	\dot{m}_h	34.41	32.37	g/s
Cold sink temperature	T_{Cin}	5	see results	°C
Cold sink mass flow rate	\dot{m}_c	34.41	29.14	g/s
Engine working fluid	-	Room air	Room air	-
Engine fill / buffer pressure	P_{buff}	Atmosphere	Atmosphere	kPa

6.1 Result Plots Generation and Format

The section also introduces methodology used to produce the plots that present the results of the experimental trials. It also discusses and how these were used in the context of evaluating experimental results. Not all plots presented here will be replicated for each test group / motion modification discussion.

6.1.1 Test Group Trial Comparisons

All trials within a test group were compared to observe if there was substantial variation in engine performance between trials. Atmospheric pressure P_{atm} was not able to be controlled across all trials and certain trials were conducted days apart. Comparing the trial results also influenced the decision as to whether the results from both trials would be aggregated into a single test group result, or it would suffice to select a single trials to be representative of the test group.

Figure 6.1 and Figure 6.2 displays the torque and power curves for the three trials making up the baseline test group 01. Individual data set results for power and torque are plotted and grouped according to the loading condition for the data set. Dashed lines link data sets taken during the sequential loading of the engine, and dotted lines link data points taken during the sequential unloading of the engine.

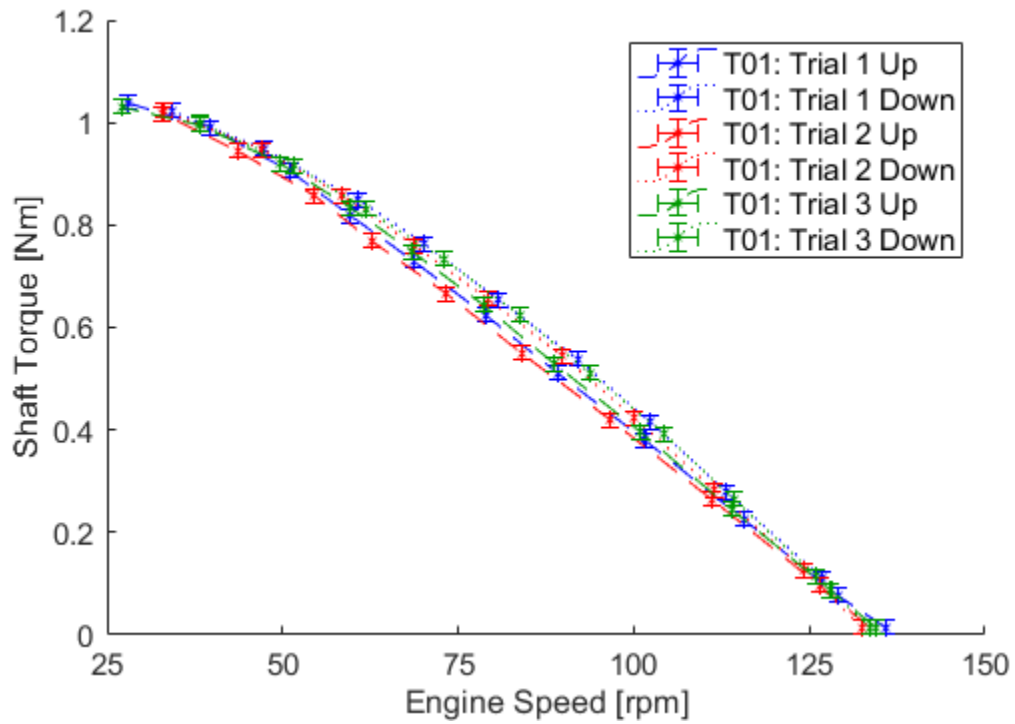


Figure 6.1 – Test group 01 torque curves across trials

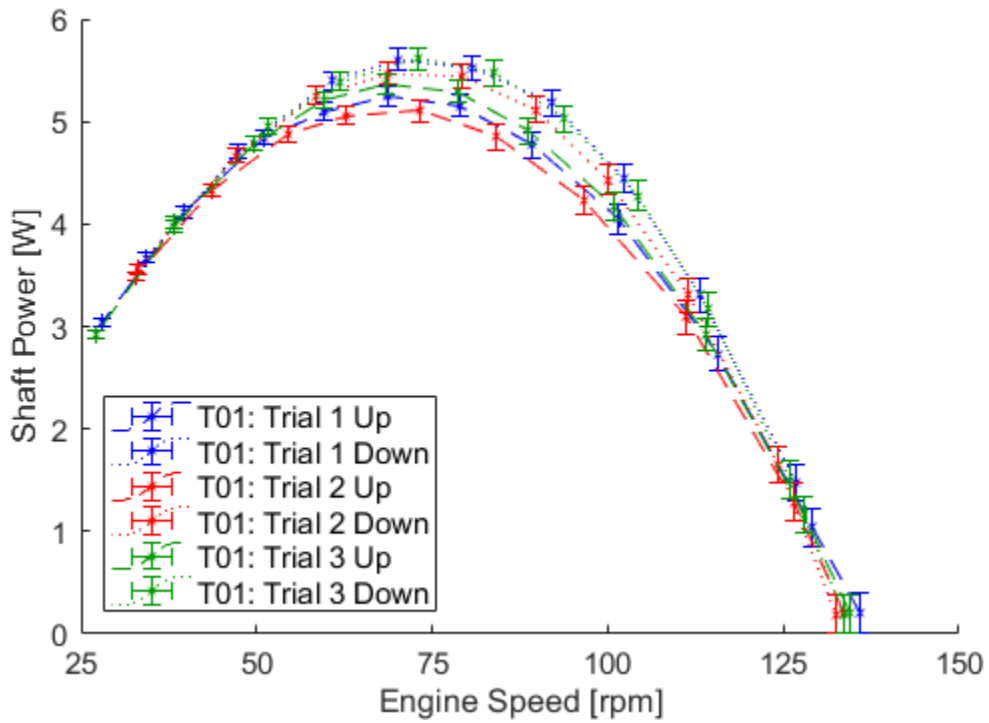


Figure 6.2 – Test group 01 power curves across trials

Observing Figure 6.1 it can be seen that at each recorded load increment the shaft torque of the engine is consistent across loading and unloading. There is also consistency across trials, within torque measurement uncertainty, from free running to the near stall loads. The torque curves are nearly linear, up until near the stall point of the engine where the torque measurement linearity reduces slightly. The friction brake system can be concluded as not substantially changing torque characteristics of the range of engine loads. The most noticeable trend in the torque curves of Figure 6.1 is the difference in engine running speed between the loading and unloading curves. The difference in steady state speed between points at the same torque loads is most significant in the middle of the trial span, while there is minimal difference at the fully loaded or fully unloaded trials. The likely reason for the difference is the tendency of the engine to asymptotically settle towards its steady state running speed, as can be observing Figure 4.2. Data was taken at consistent time intervals from when engine load was changed but it is possible that the final steady state running speed required waiting longer than the procedure specified. However, given the volume of data points required, it was decided once trials had started that waiting longer than the 120s minimum was not practical for the remaining small change in engine speed. . .

Examining Figure 6.2 it can be seen that the differences in speed at particular loading points has a compounded effect on the calculated power curve of the engine. This is obvious when noting that power is the product of average engine output torque and running speed.

Examining the same plots for other test groups revealed that overall there was good consistency between trials within all test groups. All configurations of the engine and had the tendency for the unloading data sets to run slightly faster at the same applied load as the loading data sets. Given the consistency between trials it was decided to select a single trial from each test group from which comparisons across groups were made. The trial selected was that which recorded the highest calculated power output. Furthermore, while both the loading and unloading data sets were used for calculations of engine performance, only the unloading data sets were plotted in comparative figures of results. This was done in order to reduce the clutter of plots and facilitate better comparisons of results across trial groups

6.1.2 Test Group Power and Torque Curves

Three groups of figures were developed to plot the results of test families to compare the measured performance of the drive mechanism modifications against the baseline conventional engine configuration of test group 1. The first of these plots is the torque curve, shown in figure Figure 6.3, which resembles Figure 6.1, but includes data from the maximum power trial for each test group that featured the motion modification being evaluated. The second comparative curve is the power curve, shown in Figure 6.4. The power curve likewise includes data from the maximum power trial for each test group being compared. All torque and power curves are plotted on a common set of axes to facilitate comparisons. As noted in section 6.1.1, these only include unloading data sets for each trial and thus progress from right to left.

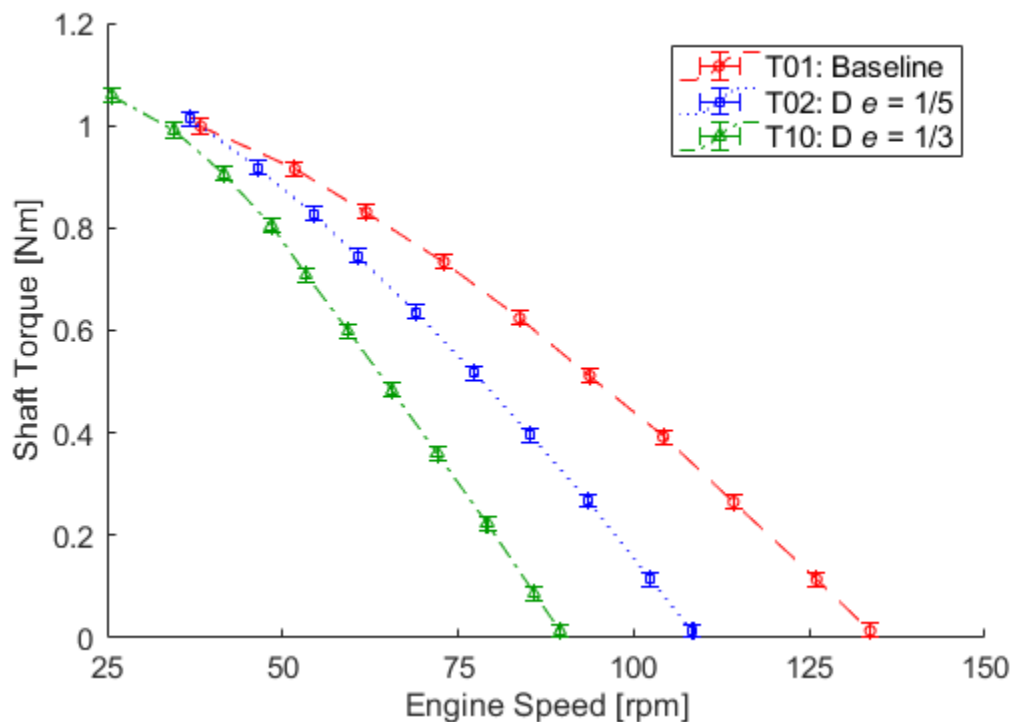


Figure 6.3 – Comparative torque curves for displacer dwelling test groups 02 and 10

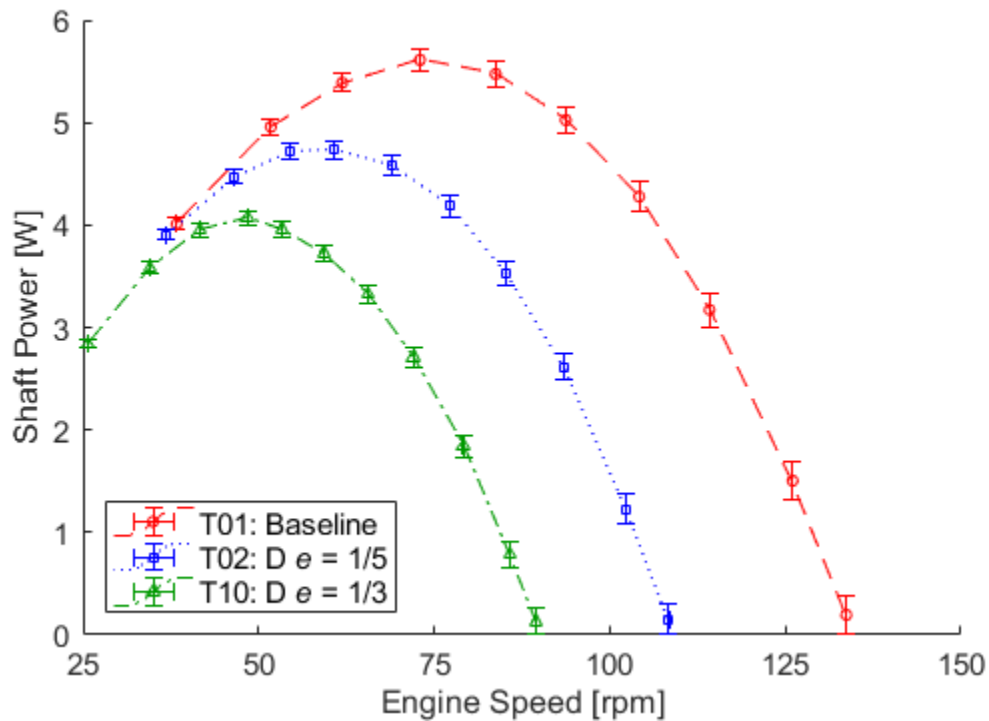


Figure 6.4 – Comparative power curves for displacer dwelling test groups 02 and 10

6.1.3 Maximum Power Data Sets Results

Figure 6.5 shows an example of the P-V indicator diagram for the data set of the test group with which produced the maximum shaft power output measured for the test group, in this case the baseline test group. A selection of points at intervals of 25 points are also plotted with the cumulative standard uncertainty. The P-V indicator diagrams are useful tools for comparing the effects of the manipulated piston profiles against the baseline P-V indicator diagram, as well as against the results of the isothermal models. All P-V plots share a common set of axes to facilitate comparisons.

The cumulative standard uncertainties of pressure and volume as plotted in Figure 6.5 demonstrate that the calibration procedures taken for the volume variation and the cycle pressure have yielded uncertainties that makes comparisons of results across test groups feasible. In comparative plots of P-V indicator diagram, the cumulative standard uncertainty error bars are typically removed for clarity. Figure 6.6 shows both the cycle pressure and the cycle volume curves plotted against the output shaft position. Both

curves are comprised of the full data for all 500 rotary encoder shaft position measurements. Figures like Figure 6.6 are used when evaluating the performance of a test group against the isothermal modeling results.

Along with the analysis of the maximum power data set indicator diagrams, other calculated metrics of the data set are presented to provide a complete perspective on the performance of the engine. These results include the calculated average constant mechanism effectiveness, the thermal loop heat transfer rates, and a calculation of the thermal efficiency of the engine. As is noted in section 5.3.6 the calculated engine efficiency is determined from the point of delivery and rejection of heat to the engine to the output of shaft power. It is not a calculation of engine brake efficiency with consideration to parasitic engine loads. There was no variations in engine load between trials and test groups beyond those applied by the friction brake.

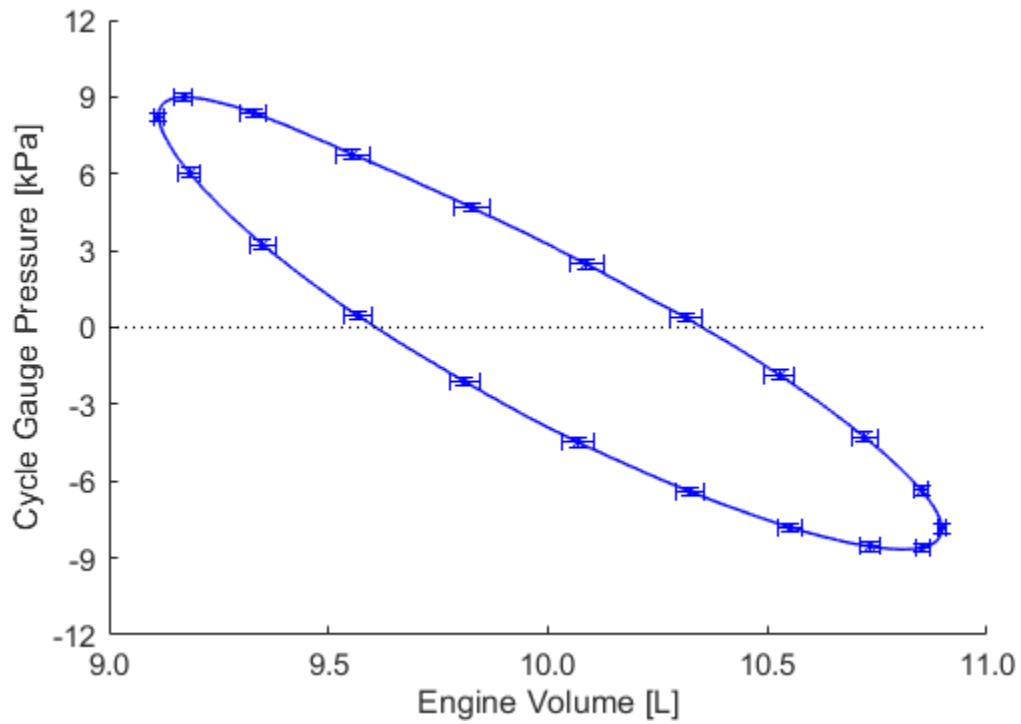


Figure 6.5 – Example maximum power data set P-V indicator diagram

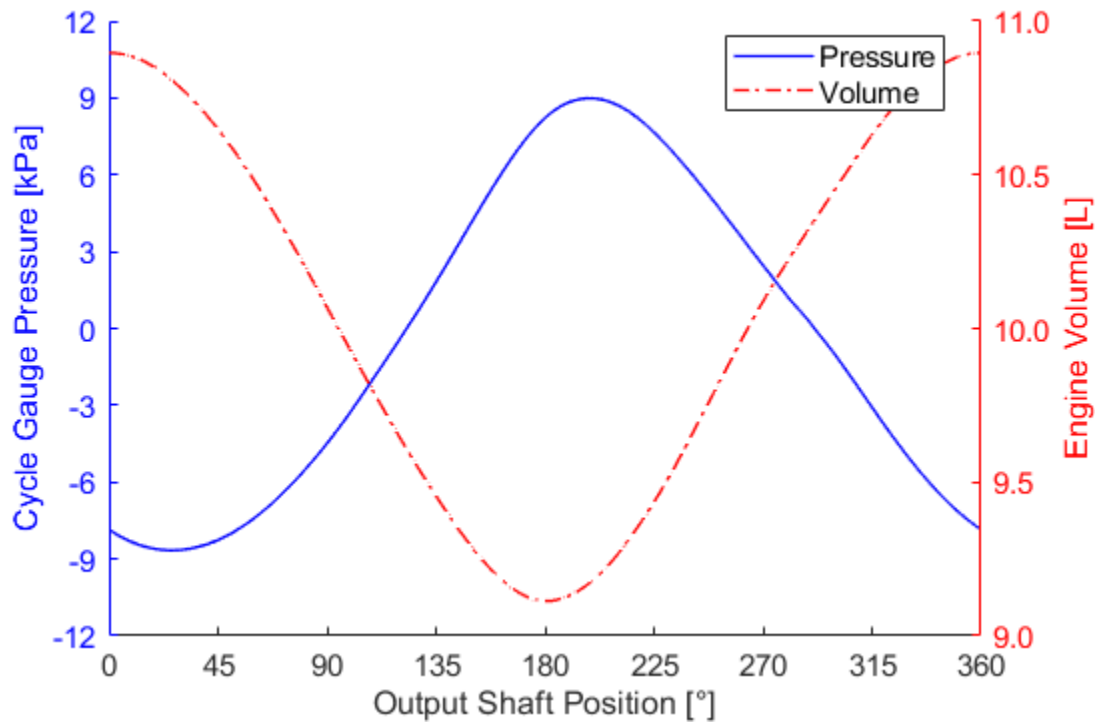


Figure 6.6 – Example maximum power data set Pressure and Volume curves plotted for a full engine cycle

6.1.4 Test Group Work Curves

Curves of the calculated indicated work, forced work, shaft work, and mechanism effectiveness are plotted for the maximum power trial of a test group. An example of the work plot for the baseline case is shown in Figure 6.7. From the work component plot it is possible to broadly interpret if the indicator diagrams of an engine changes over the course of applying load to the engine without individually examining the P-V indicator diagram of the complete trial. All variables of work are plotted on a common right-side y -axis, while mechanism effectiveness is plotted on the left side y -axis. They are plotted against a normalized engine load variable expressed as a percentage, which is the measured torque value of the data set τ_x , which is normalized over the highest measured value of engine torque observed from all trials of 1.05 Nm. The torque measurement is a direct analogue for the amount of load applied to the engine via the brake system. Also noteworthy is that shaft work is calculated as $2\pi \cdot \tau$ as per equation 5.2, and so will have a direct linear relationship with the normalized load of the engine. All plots of work share a common set of axes allowing for easy comparison between test groups. An annotated red box highlights the individual data set of the trial that produced the maximum power.

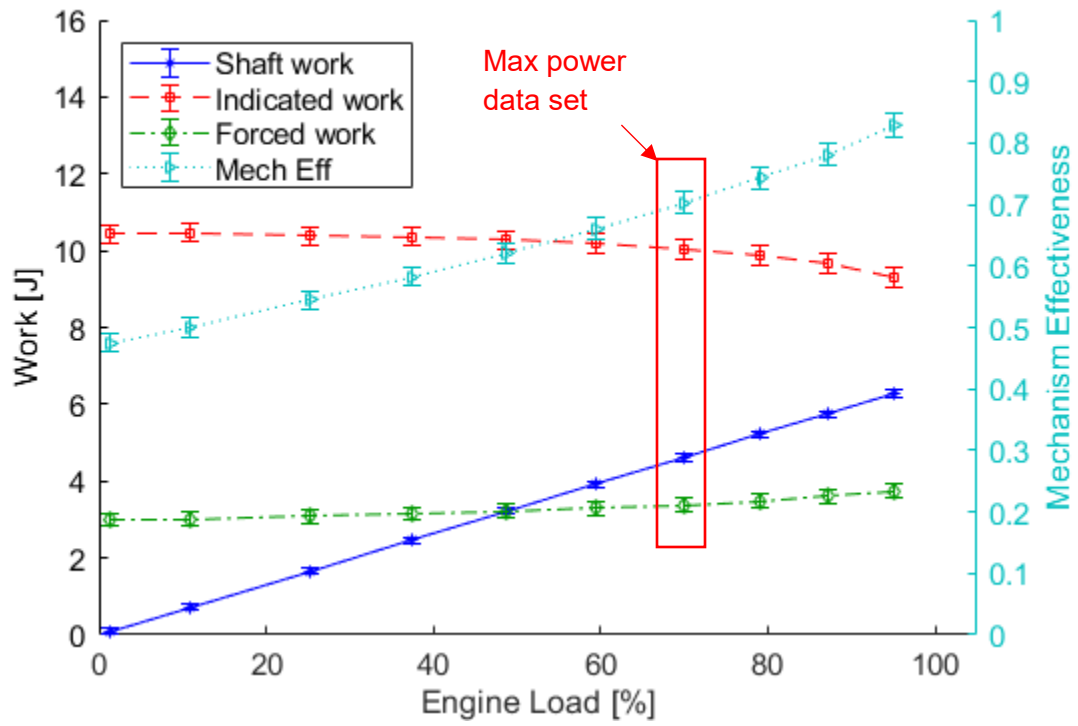


Figure 6.7 – Example diagram of trends for indicator work components and mechanism effectiveness for trial

6.2 Baseline Motion: Test Group 01

The baseline motion tests were the best emulation of a conventional crank driven kinematic Stirling engine on the EP1-M platform. The test configuration used round gears of eccentricity $e = 0$ to drive the displacer and piston crankshafts with a 1:1 derivative function with respect to the engine output shaft. This “conventional” configuration maintained the same mechanical elements and transmitted engine forces through gears of identical design specifications and construction as the non-circular gears. This permitted the baseline motion trial to be compared to the modified motion with a minimal number of variations.

The pattern of presented results and analysis of each test group will be similar to this test group, with repetitive or inconsequential portions omitted as necessary. The actual test conditions of the baseline test group trials listed in is Table 6.2. The maximum power data set was identified in trial 3.

Table 6.2 – Test conditions of baseline motion test group 01

Property	Variable	Nominal Value	Actual Value	Unit
Displacer gear set	-	$e = 0$	$e = 0$	-
Piston gear set	-	$e = 0$	$e = 0$	-
Hot source temperature	T_{Hin}	90	92.6	°C
Cold sink temperature	T_{Cin}	5	4.9	°C
Total trials	-	3	3	-
Maximum power trial	-	-	3	-

6.2.1 Indicator Diagram for Baseline Test

Figure 6.8 shows the empirical P-V indicator diagram of the maximum power data-set from the baseline test group 01. The shape of the indicator diagram shape is very similar to the preliminary isothermal model for the convention motion case as depicted in Figure 2.6 (a). Further comparison between the empirical indicator diagram and the recalculated isothermal model indicator diagram is presented in section 7. This indicator diagram forms the basis of comparison for the indicator diagrams for the modified motion test groups and is plotted along side their results for easy comparison.

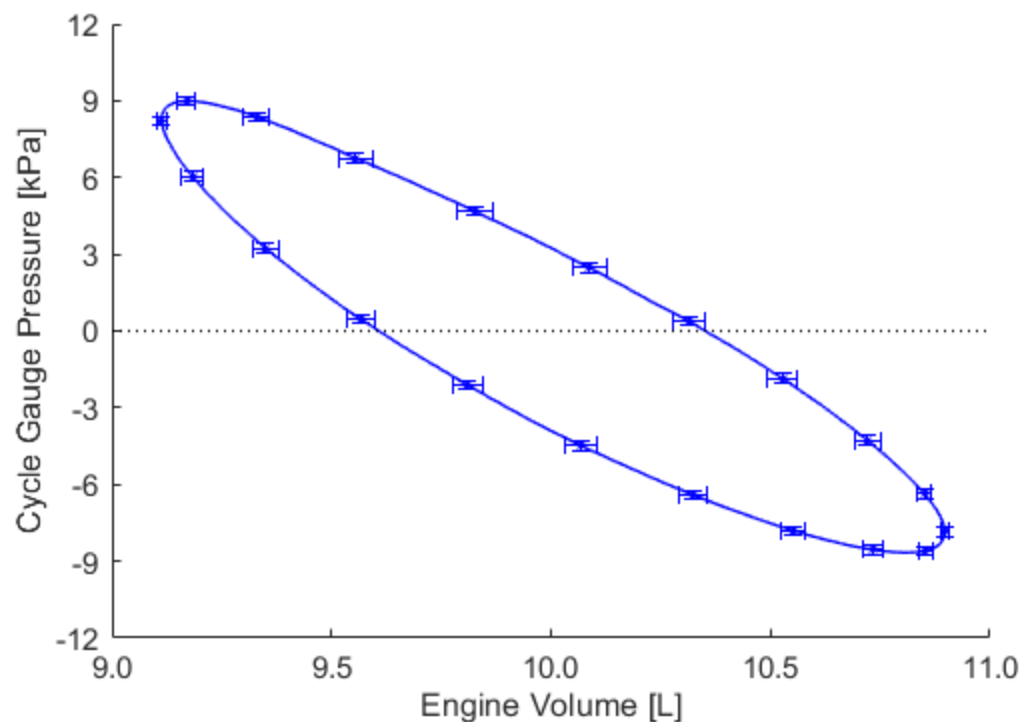


Figure 6.8 – Test group 01 maximum power data set P-V indicator diagram

Table 6.3 notes the calculated values of work from the indicator diagram, along with the results for shaft work and calculation of mechanism effectiveness for the maximum baseline data set. These values will form the basis of comparison for modified cycles moving forwards. Of note is the calculated mechanism effectiveness of $E = 0.70 \pm 0.02$ which is smaller, but within standard uncertainty, for the value of $E = 0.80 \pm 0.2$ found by Stumpf [40] during their optimization of the EP1.

Table 6.3 – Test group 01 maximum power data set values

Property	Var. x	Baseline		Test Group 01		Diff. [%]	Unit
		Value	Std. $\pm u_x$	Value	Std. u_x		
Shaft Power	p_s	5.61	0.10	5.61	0.10	-	W
Shaft Work	W_s	4.61	0.09	4.61	0.09	-	J
Indicated Work	W_{ind}	10.03	0.25	10.03	0.25	-	J
Forced Work	W_{FW}	3.39	0.18	3.39	0.18	-	J
Mech. Effectiveness	E	0.70	0.02	0.70	0.02	-	-
Thermal Efficiency	η_T	1.1	0.2	1.1	0.2	-	%

6.2.2 Indicator Diagram Trends for Baseline Test Group 01

From examination of Figure 6.9 it is noted that the calculated work and the forced work components of the indicator diagram remain steady through the loading of the engine. There is a slight decrease in indicated work at the very maximum engine load as well as a slight increase in forced work. To lend insight as what is happening to the indicator diagrams at the extremes of shaft work production, the maximum and minimum shaft work indicator diagrams were plotted along with the maximum power indicator diagram in Figure 6.10. From the comparison of P-V diagrams it can be seen that the width of the diagram decreases at the maximum shaft power data set when compared to the maximum power and minimum shaft work data sets. As all three trials undergo the same volume variation as controlled by the piston kinematics, the cause of the decrease in diagram width is likely reduced pressure swing in the cycle at high shaft work conditions. Reduction in pressure may be due to greater leakage of gas at slower running speed due to longer times spent at maximum and minimum pressures of the cycle.

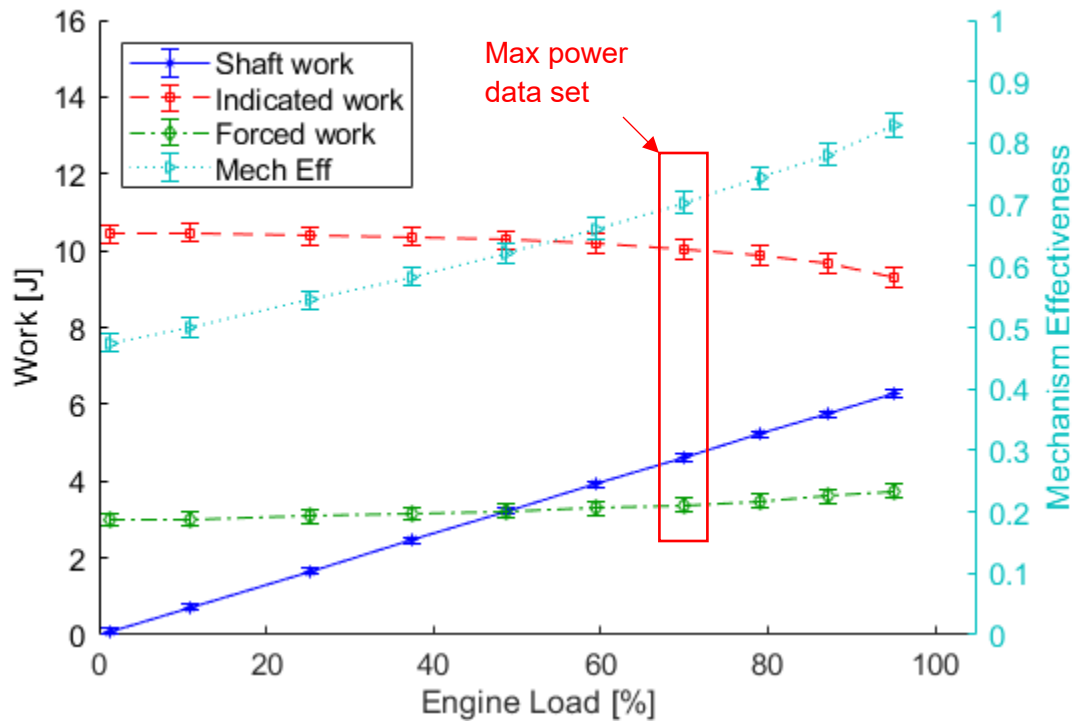


Figure 6.9 – Test group 01 trial trends for indicator diagram work components and mechanism effectiveness

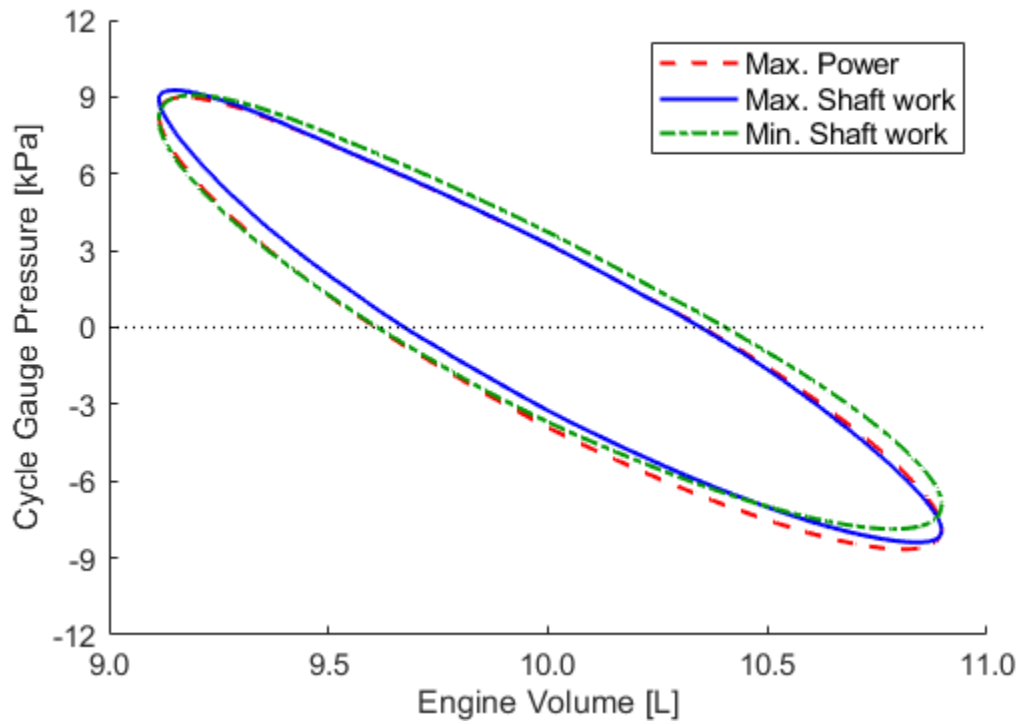


Figure 6.10 – Comparison of P-V indicator diagrams over the range of shaft work output for test group 01 maximum power trial

Overall the reduction in indicated work and the slight increase in forced work is minimal. Similar trends were observed in the trial indicator work component diagrams of other test groups. The comparative plots of the P-V indicator diagrams from the low shaft work to the high shaft work data points revealed similar trends of decreased pressure swing between the expansion and compression strokes of the engine.

6.3 Displacer Dwelling: Test Groups 02 and 10

This section presents the results from the test groups where non-circular gearing was used to dwell the displacer at TDC and BDC. Test group 02 used a non-circular gear pair with eccentricity of $e = 1/5$ and the conditions for the test group trials is noted in Table 6.4. Test group 10 used a non-circular gear pair with eccentricity of $e = 1/3$ and the conditions for the test group trials is noted in Table 6.5. Results for both test groups are discussed in the following subsections.

Table 6.4 – Test conditions of displacer dwelling motion test group 02

Property	Variable	Nominal Value	Actual Value	Unit
Displacer gear set	-	$e = 1/5$	$e = 1/5$	-
Piston gear set	-	$e = 0$	$e = 0$	-
Hot source temperature	T_{Hin}	90	91.2	°C
Cold sink temperature	T_{Cin}	5	4.7	°C
Total trials	-	2	2	-
Maximum power trial	-	-	1	-

Table 6.5 – Test conditions of displacer dwelling motion test group 10

Property	Variable	Nominal Value	Actual Value	Unit
Displacer gear set	-	$e = 1/3$	$e = 1/3$	-
Piston gear set	-	$e = 0$	$e = 0$	-
Hot source temperature	T_{Hin}	90	94.2	°C
Cold sink temperature	T_{Cin}	5	4.7	°C
Total trials	-	2	2	-
Maximum power trial	-	-	2	-

6.3.1 Displacer Dwelling: Torque and Power Curves

The results of the maximum power trials of the two displacer dwelling test groups reveal that there was a dramatic reduction in the engine running speed at comparable loading conditions across test groups. This result can be clearly seen in Figure 6.11. For low load conditions (load is analogous to torque) the engine ran significantly slower. The effects of increasing the displacer dwelling time at TDC and BDC when moving from the $e = 1/5$ to the $e = 1/3$ non-circular gear reduced the engine running speeds by a similar margin.

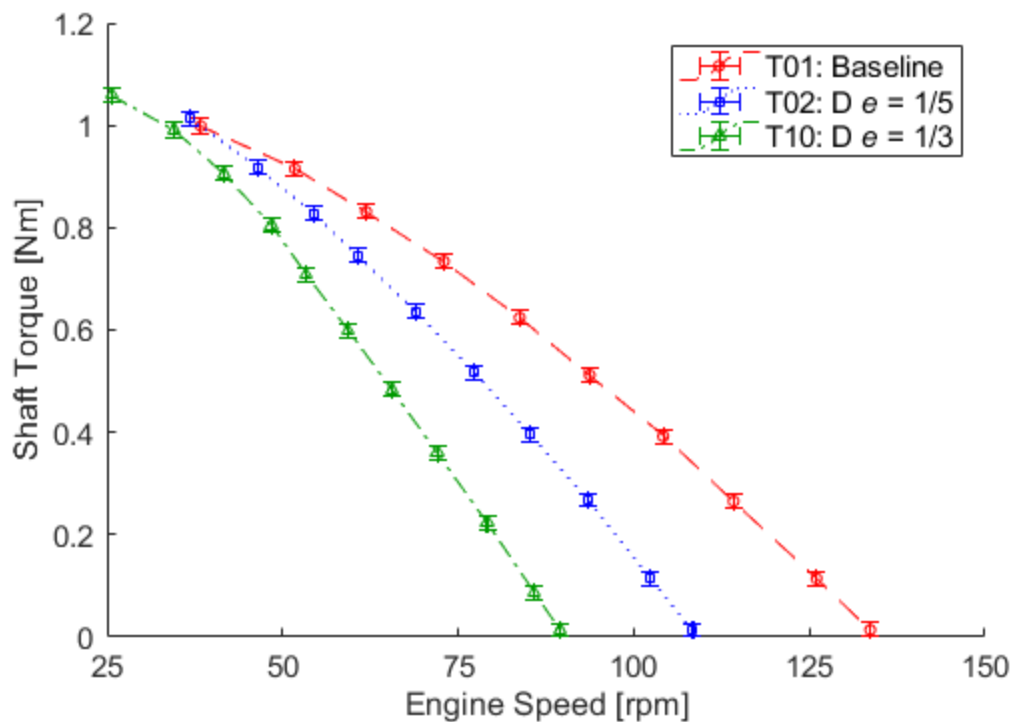


Figure 6.11 – Comparative torque curves for displacer dwelling test groups 02 and 10 and the baseline

Examining the power curve of the displacer dwelling test groups shown in Figure 6.12 shows the compounded effect that decreases in engine running speed have on power output of the engine. As is noted later in Table 6.6 the maximum power produced from test group 02 was -15.6% less than for the baseline case. The effect is more pronounced for test group 10 using the $e = 1/3$ gear, as noted in Table 6.7 the peak power of the dwelled cycle had a maximum power output 27.4% lower than the baseline case.

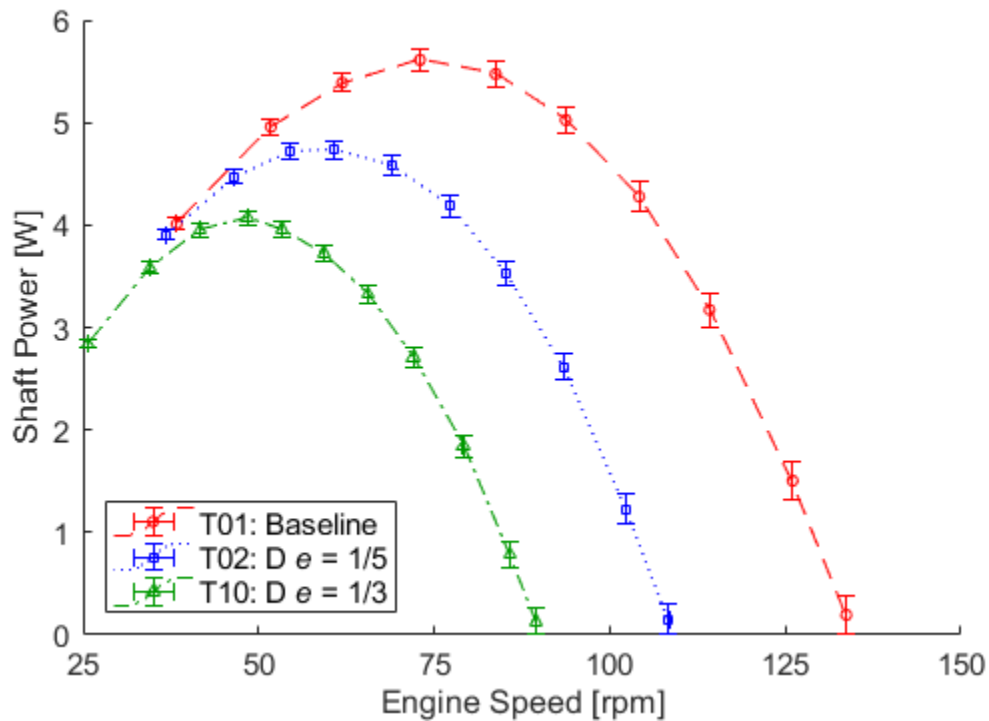


Figure 6.12 – Comparative power curves for displacer dwelling test groups 02 and 10 and the baseline

6.3.2 Displacer Dwelling: Maximum Power Indicator Diagrams

Figure 6.13 shows a comparative plot of the indicator diagrams of the maximum power data sets for the dwelled displacer test groups as well as the baseline case. At the upper and lower corner of the diagrams the dwelling of the displacer had the intended effect of expanding the indicator diagrams towards a more ideal case, as was anticipated by the isothermal modeling results. The calculations of the work components of the indicator diagrams are presented in Table 6.6 and Table 6.7. They reveal that indeed there was a 4.1% and 4.6% increase in indicated work for the $e = 1/5$ and $e = 1/3$ dwelling respectively. Shaft work of the cycle for these maximum cases was also increased by 1.5% and 9.5% over the baseline in test group 02 and 10 respectively.

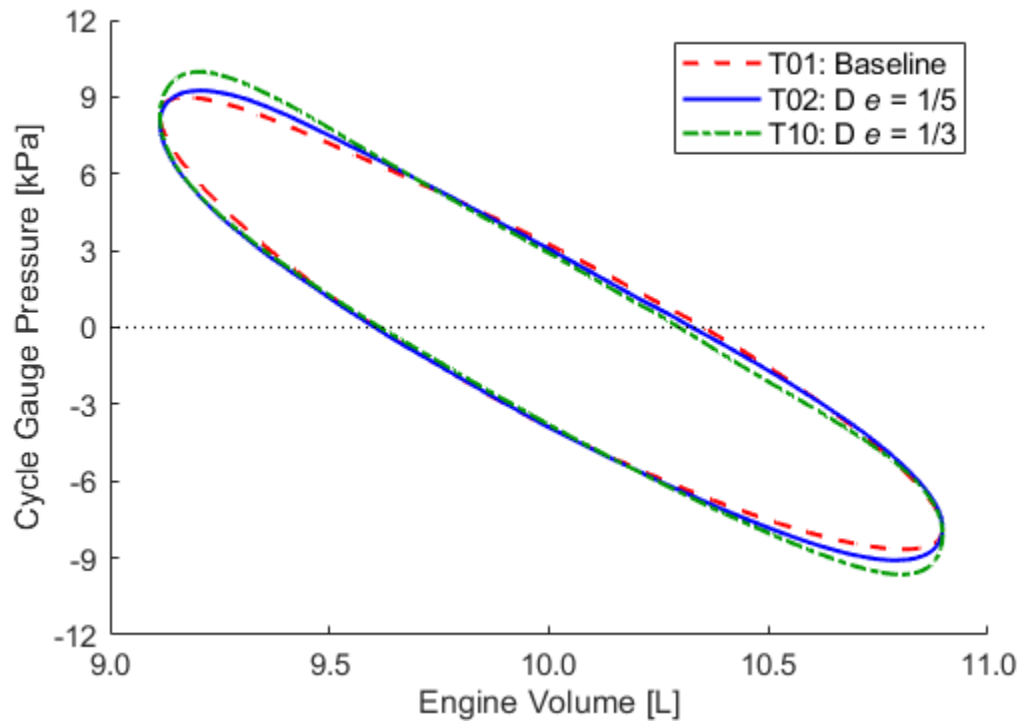


Figure 6.13 – Maximum power data set P-V indicator diagrams for test group 02 and 10 compared to the baseline indicator diagram

Table 6.6 – Test group 02 maximum power data set values

Property	Var. x	Baseline		Test Group 02		Diff. [%]	Unit
		Value	Std. $\pm u_x$	Value	Std. u_x		
Shaft Power	p_s	5.61	0.10	4.73	0.09	-15.6	W
Shaft Work	W_s	4.61	0.09	4.68	0.09	1.5	J
Indicated Work	W_{ind}	10.03	0.25	10.45	0.25	4.1	J
Forced Work	W_{FW}	3.39	0.18	3.25	0.17	-4.0	J
Mech. Effectiveness	E	0.70	0.02	0.69	0.02	-2.2	-
Thermal Efficiency	η_T	1.1	0.2	1.51	0.4	39.4	%

Table 6.7 – Test group 10 maximum power data set values

Property	Var. x	Baseline		Test Group 10		Diff. [%]	Unit
		Value	Std. $\pm u_x$	Value	Std. u_x		
Shaft Power	p_s	5.61	0.10	4.07	0.07	-27.4	W
Shaft Work	W_s	4.61	0.09	5.05	0.09	9.5	J
Indicated Work	W_{ind}	10.03	0.25	10.50	0.26	4.6	J
Forced Work	W_{FW}	3.39	0.18	3.48	0.18	2.6	J
Mech. Effectiveness	E	0.70	0.02	0.71	0.02	1.2	-
Thermal Efficiency	η_T	1.1	0.2	0.8	0.1	-25.0	%

6.3.3 Indicator Diagram Trends over Trials of the Displacer Dwelling Test Groups

The plots of the trial indicator diagram trends for test group 02 and test group 10 are shown in Figure 6.14 and Figure 6.15 respectively. These plots bear a strong resemblance to same plot, Figure 6.9, from the baseline test group 01. There does not appear to be significant changes in the indicator diagrams over the course of engine loading over the trials. Also of note is that for all test groups examined so far, the maximum power data sets occur around the ~70% of full engine load mark. The mechanism effectiveness also displays very similar trends. The maximum power cases of all the dwelled displacer trials and the baseline case, the calculated mechanism effectiveness was all within standard uncertainty values of one another at about $E = 0.7$. This indicates that there does not seem to be significant additional mechanical losses in the mechanism when changing between the different non-circular gears. This holds true when examining the calculated mechanism effectiveness from the low load and high load data sets.

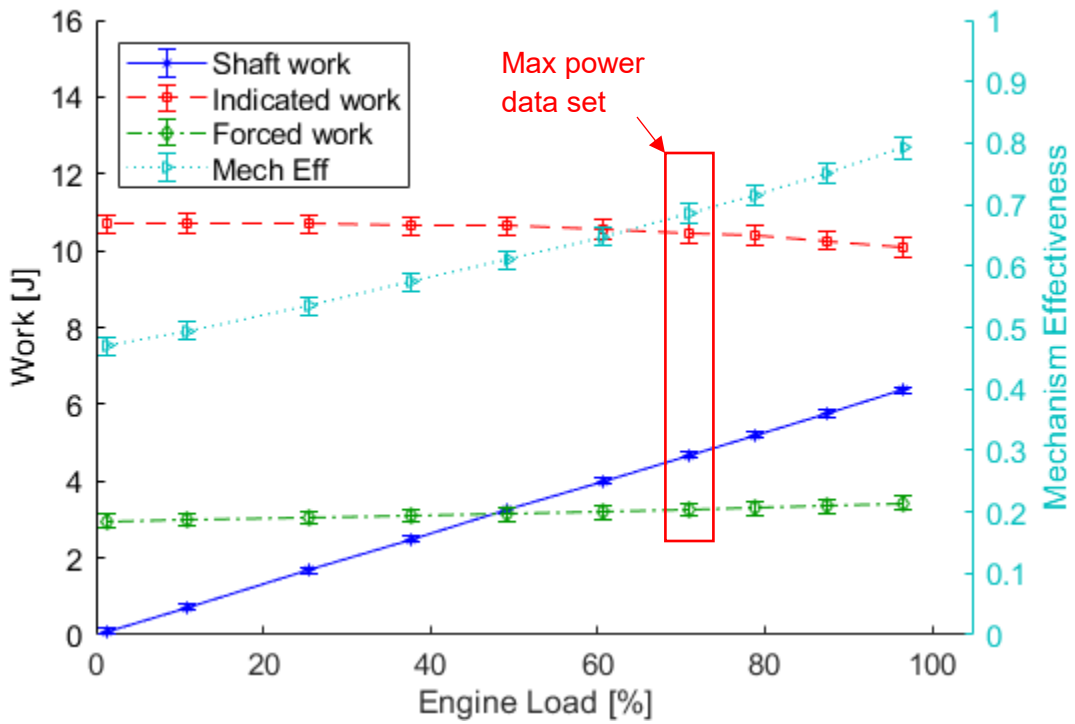


Figure 6.14 – Test group 02 trends for indicator diagram work components and mechanism effectiveness

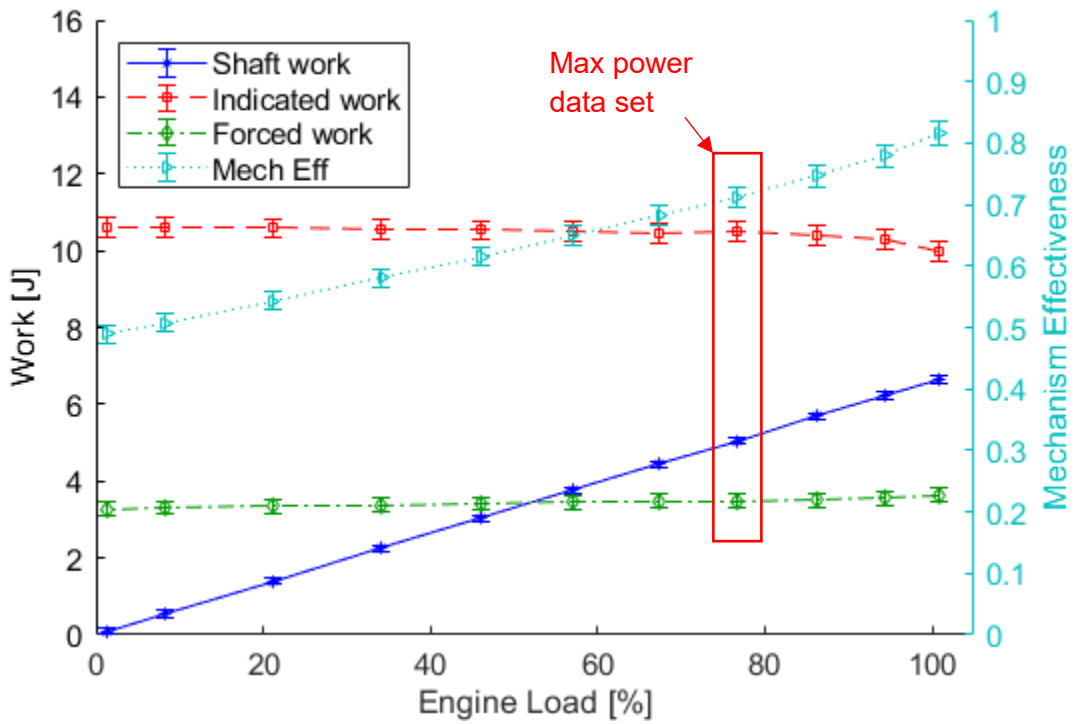


Figure 6.15 – Test group 10 trends for indicator diagram work components and mechanism effectiveness

6.3.4 Dwelled Displacer Conclusions

From the results of the displacer dwelling test group the modification of the displacer motion had the intended effect of slightly increasing the indicated work, and shaft work of the engine cycle when compared to the baseline conventional motion case. However, gains in the indicator diagram did not manifest in higher engine output power, as the engine ran consistently slower with dwelled displacer cycle when compared to the baseline under the same engine loads. The engine was simply not able to complete as many cycles in the same time, despite those cycles being improved.

Some theories as to why this was the case can be formed when examining the spread of the power and torque curves shown in section 6.3.1, as the gap is consistent. When examining the plot of the transmission function of the oval elliptical non-circular gears plotted in Figure 2.4, the peak angular velocity of the displacer crankshaft shaft varies by an even amount when changing between $e = 0$, $e = 1/5$, and $e = 1/3$ eccentricities. Given the near sinusoidal relationship between piston velocity and crankshaft angular velocity from the slider crank relationships, the displacer piston moves twice as fast during a movement from TDC to BDC in the dwelled configuration with the $e = 1/3$ gearing configuration. If the displacer piston peak translation speed is what limits the engine speed, then the expectation is that the $e = 1/3$ dwelled displacer, moving at the same speed as the $e = 0$ geared displacer, would result in an output shaft angular velocity of the inverse of the maximum transmission function value of 2. Examining the power and torque curves shown in section 6.3.1 that indeed appears to be the case, as the $e = 1/3$ dwelled displacer test group 10 runs consistently at ~60% the speed of the $e = 0$ baseline case.

Losses associated with higher displacer translation speed include flow friction losses of the as being driven through the exchangers faster. There may also be increase mechanical friction, or reduced gas temperatures from changes to the exchanger to gas heat exchange. However, when examining other features such as the indicator diagram pressure swings, gas temperatures, and mechanism effectiveness results of the dwelled test groups, these effects are not observed in the data.

6.4 Piston Dwelling: Test Groups 06 and 07

This section presents the results from the test groups where non-circular gearing was used to dwell the piston at TDC and BDC. Test group 06 used a non-circular gear pair with eccentricity of $e = 1/5$ and the conditions for the test group trials is noted in Table 6.8. Test group 07 used a non-circular gear pair with eccentricity of $e = 1/3$ and the test conditions for the test group trials is noted in Table 6.9. Results for both test groups are discussed in the following subsections.

Table 6.8 – Test conditions of piston dwelling motion test group 06

Property	Variable	Nominal Value	Actual Value	Unit
Displacer gear set	-	$e = 0$	$e = 0$	-
Piston gear set	-	$e = 1/5$	$e = 1/5$	-
Hot source temperature	T_{Hin}	90	91.76	°C
Cold sink temperature	T_{Cin}	5	4.81	°C
Total trials	-	2	2	-
Maximum power trial	-	-	2	-

Table 6.9 – Test conditions of piston dwelling motion test group 07

Property	Variable	Nominal Value	Actual Value	Unit
Displacer gear set	-	$e = 0$	$e = 0$	-
Piston gear set	-	$e = 1/3$	$e = 1/3$	-
Hot source temperature	T_{Hin}	90	91.82	°C
Cold sink temperature	T_{Cin}	5	4.82	°C
Total trials	-	2	2	-
Maximum power trial	-	-	1	-

6.4.1 Piston Dwelling: Torque and Power Curves

In contrast to the results of the dwelled displacer, the results of the maximum power trials of the piston dwelling test groups revealed that there was not much change in the engine running speed at comparable loading conditions across test groups. This result can be clearly seen in Figure 6.16. Test group 06 appear to very closely overlay the baseline configuration, with there is a slight reduction in maximum running speed for test group 07 power piston. A notable achievement of the dwelled piston test groups was that both groups produced the a very high maximum torque data set, surpassing the calibrated measurement range of the torque transducer and recording a maximum torque measurement of $\tau = 1.06$ Nm for test group 06. The transmission function of the non-circular has an inverse effect on the mechanical advantage of the gears. Thus, when undergoing rapid expansion and compression strokes, the piston has a mechanical advantage when transmitting torque to the engine output shaft when compared to the conventional drive mechanism.

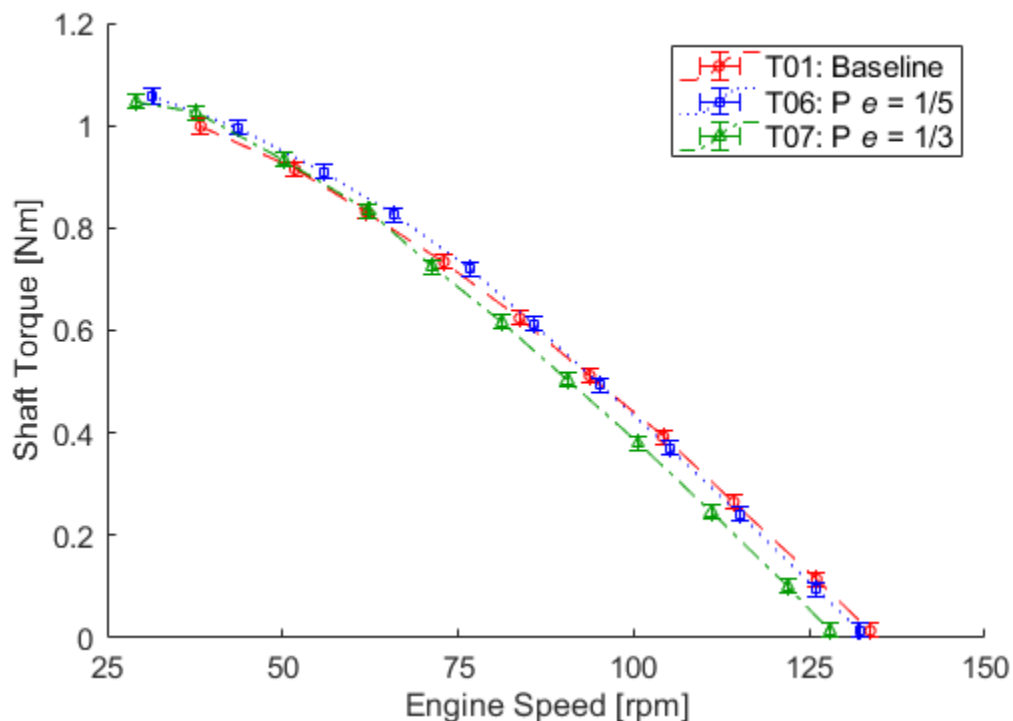


Figure 6.16 – Comparative torque curves for piston dwelling test groups 06 and 07 and the baseline

Examining the power curve of the piston dwelling test groups shown in Figure 6.17 shows the effects of the slight speed difference on produced power. For the first time a modified configuration of the engine produces more power than the baseline conventional configuration. That trial is the 06 test group dwelling the power piston with the $e = 1/5$ gear set. Conversely the 07 test group using the the $e = 1/3$ gear set to dwell the power piston showed a slight decrease in maximum engine power.

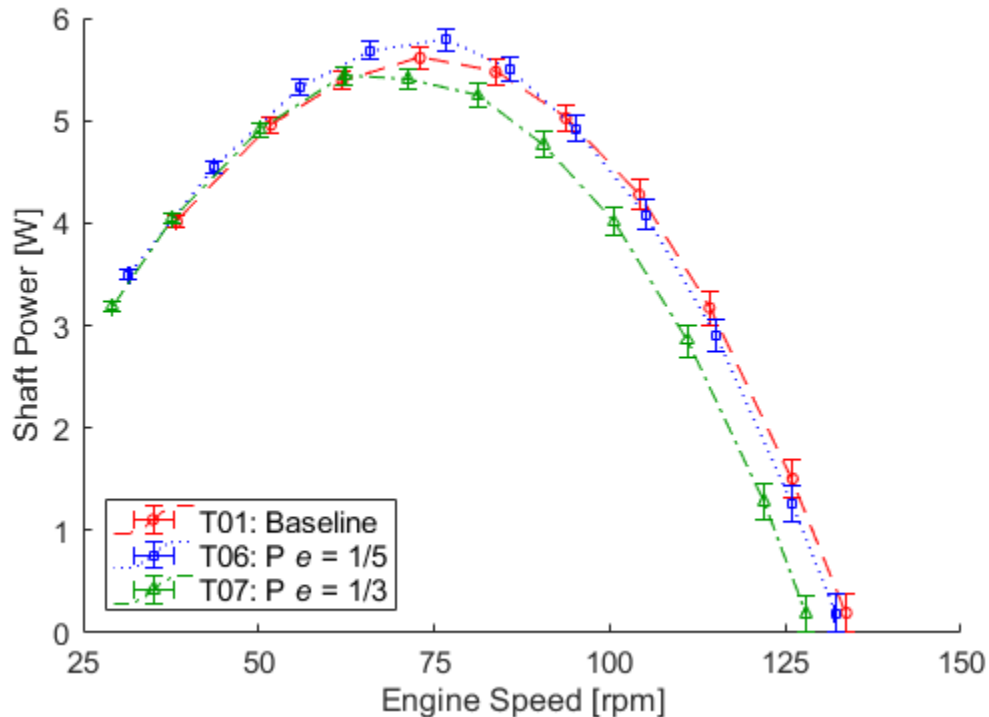


Figure 6.17 – Comparative power curves for piston dwelling test groups 06 and 07 and the baseline

6.4.2 Piston Dwelling: Maximum Power Indicator Diagrams

Figure 6.18 shows a comparative plot of the indicator diagrams of the maximum power data sets for the dwelled piston test groups as well as the baseline case. As with the dwelled displacer test groups the upper and lower corners of the indicator diagrams demonstrated the intended effect of expanding the indicator diagram towards a more ideal shape. In addition to the corners being pushed out slightly, there is significant area gained in the middle of the indicator diagram where there appears to be a more substantial difference between the expansion and compression pressures of the cycle.

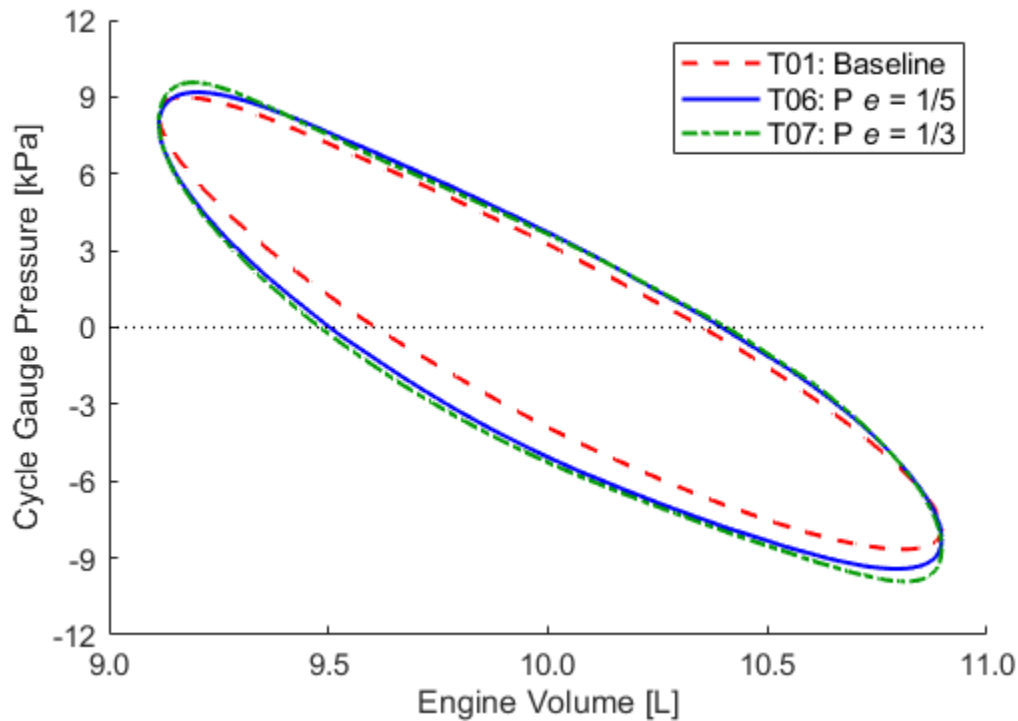


Figure 6.18 – Maximum power data set P-V indicator diagrams for test group 06 and 07 compared to the baseline indicator diagram

The calculations of the work components of the indicator diagrams are presented in Table 6.10 and Table 6.11. The results reveal that there was a significant increase in the indicated work over the baseline: for test group 06 there was an increase of 24.8% and for test group 07 the increase was 29.4%. There was also a substantial reduction in forced work for test group 06 of -18.5% and -21.3% for test group 07. These gains did not translate to measured increases in shaft work, which only saw modest gains of 13.5% for test group 07, and actually decreased by -1.9% for test group 06.

To mathematically reconcile these outcomes, the calculated mechanism effectiveness for the two dwelled piston test groups was determined to be $\sim E = 0.60$ for the motion modification from both gear sets tested, a difference of -14.9% when compared to the baseline case.

Table 6.10 – Test group 06 maximum power data set values

Property	Var. x	Baseline		Test Group 06		Diff. [%]	Unit
		Value	Std. $\pm u_x$	Value	Std. u_x		
Shaft Power	p_s	5.61	0.10	5.79	0.11	3.1	W
Shaft Work	W_s	4.61	0.09	4.53	0.09	-1.9	J
Indicated Work	W_{ind}	10.03	0.25	12.53	0.26	24.8	J
Forced Work	W_{FW}	3.39	0.18	2.76	0.18	-18.5	J
Mech. Effectiveness	E	0.70	0.02	0.60	0.02	-14.9	-
Thermal Efficiency	η_T	1.1	0.2	1.3	0.2	22.9	%

Table 6.11 – Test group 07 maximum power data set values

Property	Var. x	Baseline		Test Group 07		Diff. [%]	Unit
		Value	Std. $\pm u_x$	Value	Std. u_x		
Shaft Power	p_s	5.61	0.10	5.44	0.09	-3.1	W
Shaft Work	W_s	4.61	0.09	5.24	0.09	13.5	J
Indicated Work	W_{ind}	10.03	0.25	12.99	0.26	29.4	J
Forced Work	W_{FW}	3.39	0.18	2.67	0.18	-21.3	J
Mech. Effectiveness	E	0.70	0.02	0.61	0.02	-12.8	-
Thermal Efficiency	η_T	1.1	0.2	1.5	0.3	34.7	%

6.4.3 Indicator Diagram Trends Over Trials of the Piston Dwelling Test Groups

The plots of the trial indicator diagram trends for test group 06 and test group 07 are shown in Figure 6.19 and Figure 6.20 respectively. When compared to the displacer dwelling and baseline trends there is a more substantial drop off in indicated work towards the higher engine load side. Both the group 06 and 07 indicator diagrams show substantially higher indicated work and lower forced work when compared to previous results. However, these gains in the cycle were not translated to direct improvements to directly measured shaft power of the engine. As was noted in the previous section, the calculation of mechanism effectiveness reconciles this discrepancy by determining a mechanism effectiveness for both dwelled piston motion cycles that is on average ~15% below that of the baseline trials.

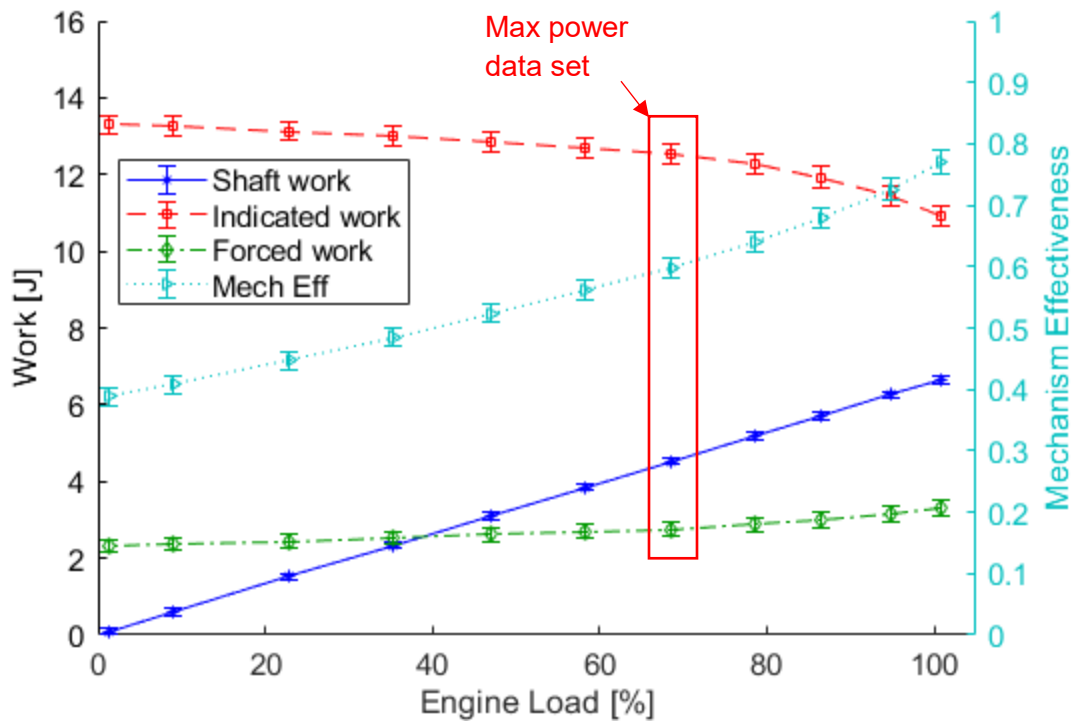


Figure 6.19 – Test group 06 trends for indicator diagram work components and mechanism effectiveness

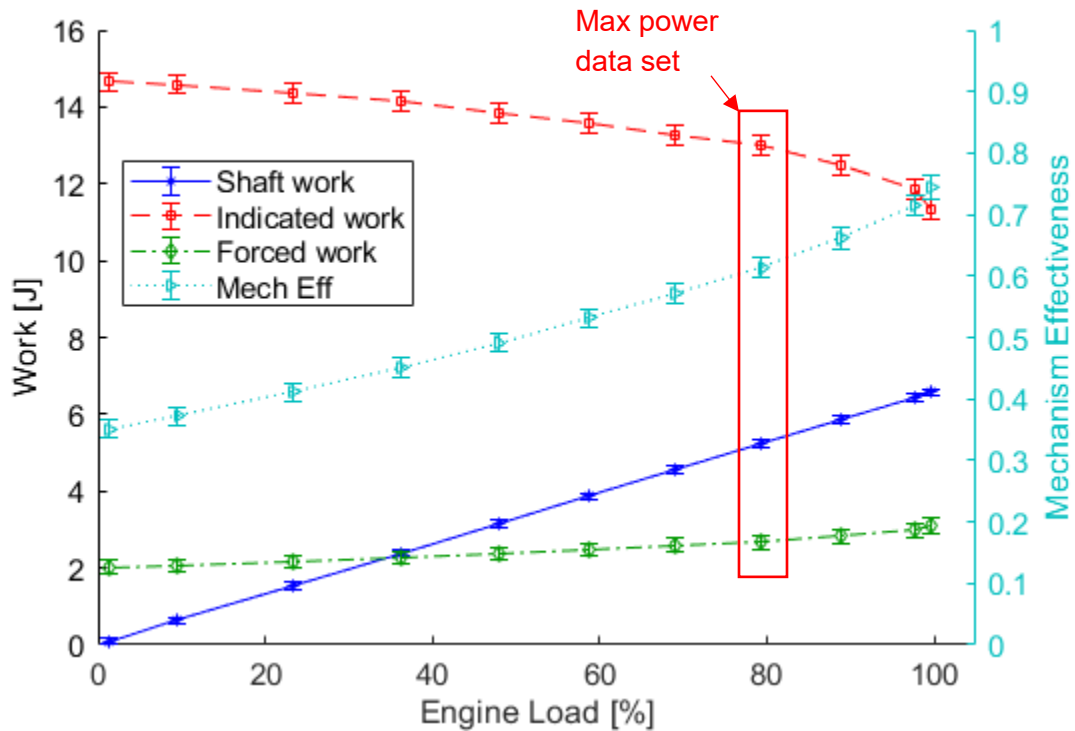


Figure 6.20 – Test group 07 trends for indicator diagram work components and mechanism effectiveness

Results indicate that dwelling of the piston via the non-circular gears produces consistent mechanical losses in the drive –mechanism that independent of engine load conditions. As was mentioned in section 6.4.1 the mechanical advantage of the dwelled piston changes continuously throughout the cycle because of the non-circular gears, so mechanical friction due to forces on the drive mechanism may increase. It may also be the case in the opposite direction, when energy from the flywheel acts to drive the piston through forced work sections of the cycle, the change in mechanical advantage increases losses.

Further instrumentation to measure the torque and force transmission through the various elements of the drive mechanism to produce a more comprehensive model of mechanical losses in the drive mechanism. This would provide better insight as to where the reduction in mechanism effectiveness is occurring for the engine.

6.4.4 Piston Dwelling Conclusions

Results from the piston dwelling test group reveal that the speed at which the engine can complete thermodynamic cycles is not impaired by dwelling of the piston, as was the case with the dwelled displacer. Overall there was a slight improvement in the maximum power produced by the modified drive mechanism using the $e = 1/5$ gear set to dwell the power piston, however the improvement was a small 3.1%, nearly within the standard uncertainty bounds for the measurements. It was found to be possible to increase the indicator diagram area substantially as was predicted by the engine modeling, but those gains were not able to be translated into substantial improvements to the shaft work or power of the engine.

6.5 Combined Displacer and Piston Dwelling: Test Groups 05 and 09

This section presents the results from the test groups where both the displacer and piston were dwelled out of phase to minimize the amount of overlap in their motions. Test group 05 used two non-circular gear sets with eccentricity of $e = 1/5$ and the conditions for the test group trials is noted in Table 6.12. Test group 09 used two non-circular gear sets with eccentricity of $e = 1/3$ and the test conditions for the test group trials is noted in Table 6.13. Results are discussed in the following subsections.

Table 6.12 – Test conditions of combined displacer and piston dwelling motion test group 05

Property	Variable	Nominal Value	Actual Value	Unit
Displacer gear set	-	$e = 1/5$	$e = 1/5$	-
Piston gear set	-	$e = 1/5$	$e = 1/5$	-
Hot source temperature	T_{Hin}	90	92.58	°C
Cold sink temperature	T_{Cin}	5	4.69	°C
Total trials	-	2	2	-
Maximum power trial	-	-	1	-

Table 6.13 – Test conditions of combined displacer and piston dwelling motion test group 09

Property	Variable	Nominal Value	Actual Value	Unit
Displacer gear set	-	$e = 1/3$	$e = 1/3$	-
Piston gear set	-	$e = 1/3$	$e = 1/3$	-
Hot source temperature	T_{Hin}	90	94.16	°C
Cold sink temperature	T_{Cin}	5	4.56	°C
Total trials	-	2	2	-
Maximum power trial	-	-	2	-

6.5.1 Combined Dwelling: Torque and Power Curves

Not surprisingly the results of the combined motion test groups show a combination characteristics of the results of the individually dwelled displacer and dwelled piston test groups. Examining the torque curves shown in Figure 6.21 it can be seen that there is a substantial decrease in in engine speed when using the more modified motion profiles. The spread is similar to the results for the dwelled displacer torque curve shown in Figure 6.11. Additionally, for test group 05 using the $e = 1/5$ gears, the group recorded the highest measured torque value of all trial a $\tau = 1.08$ Nm. High torque measurements where characteristic of the dwelled piston test groups.

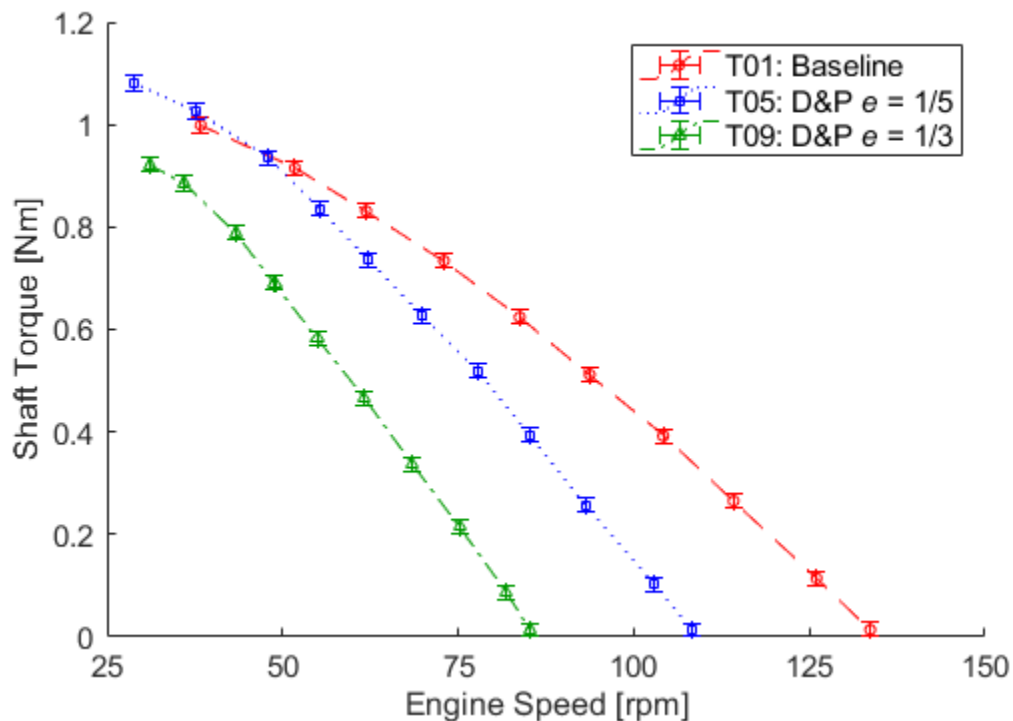


Figure 6.21 – Comparative torque curves for combined displacer and piston dwelling test groups 05 and 09 and the baseline

Examining the power curve of the combined motion test groups shown in Figure 6.22 it can be clearly seen that the reduced running speed of the double dwelled test groups has a very detrimental effect on the power producing potential of the EP1-M. Test group 09 in particular, using both sets of $e = 1/3$ gears recorded the lowest maximum power data set at 3.57 ± 0.06 W, which was a reduction of 36.4% when compared to the maximum power data set of the baseline configuration.

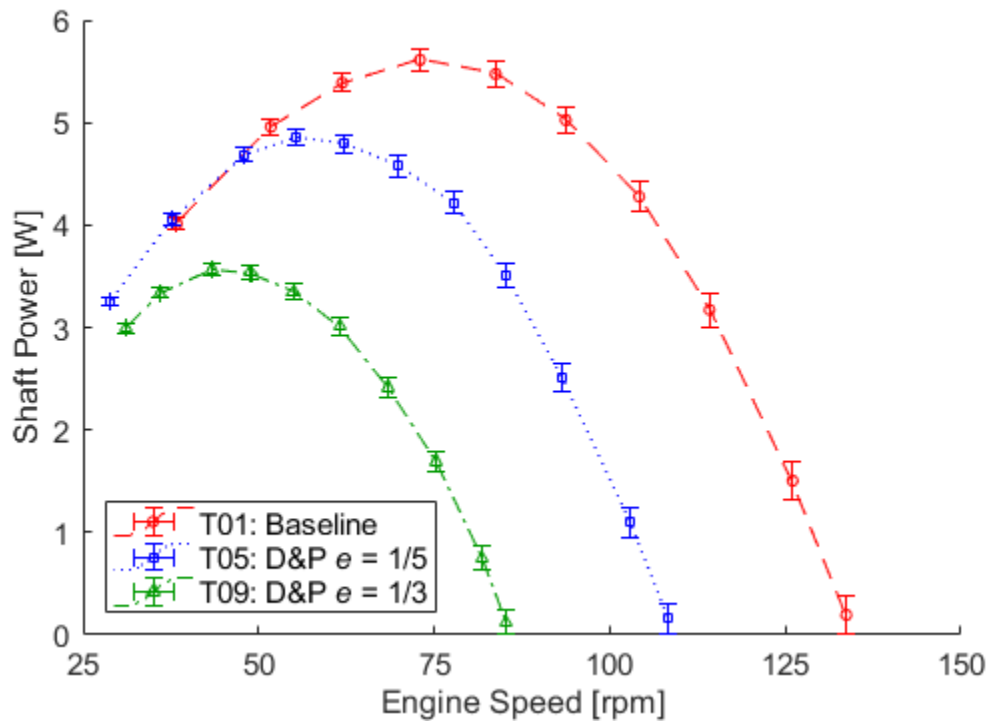


Figure 6.22 – Comparative power curves for combined displacer and piston dwelling test groups 05 and 09 and the baseline

6.5.2 Combine Dwelling: Maximum Power Indicator Diagrams

The comparative plot of the indicator diagrams of the maximum power data sets for combined test groups and the baseline test group is shown in Figure 6.23. The combined dwelling cycles were predicted by the model to produce indicator diagrams that most closely approximated the ideal Stirling cycle case. Examining Figure 6.23 indeed shows that the corners of the indicator diagrams are indeed more squared, pulling substantially up at the ends and producing a very large pressure swing at the extremities of the indicator diagram. The gains that were seen pressure swing in the middle of the expansion and compression phases of the cycle is not as significant as it was for the dwelled piston test groups.

The calculations of the work components of the indicator diagrams are presented in Table 6.14 and Table 6.15. Across both test groups the gains made to the indicated work: for the $e = 1/5$ dwelled cycle the indicated work increased by 23.1%, and for the $e = 1/3$ dwelled cycle the indicated work increased by 11.6% over the baseline case.

Contrary to the dwelled piston test groups, the increased indicated work as translated to meaningful increases to shaft work. For the $e = 1/5$ dwelled cycle the shaft work increased by 13.9%, and for the $e = 1/3$ dwelled cycle the shaft work increased by 7.3% over the baseline case. All of these indicator diagram work improvement however, were completely erased when it came to power production as the cycle frequency of the engine was substantially below the baseline case. The maximum power data set for the $e = 1/5$ dwelled test group 05 produced a maximum shaft power of 4.85 ± 0.08 W, while the maximum power data set for the $e = 1/3$ dwelled test group 09 produced a maximum shaft power of 3.57 ± 0.06 W. These maximum power measurements were a 13.6% and 36.4% reduction in power when compared to the baseline case respectively.

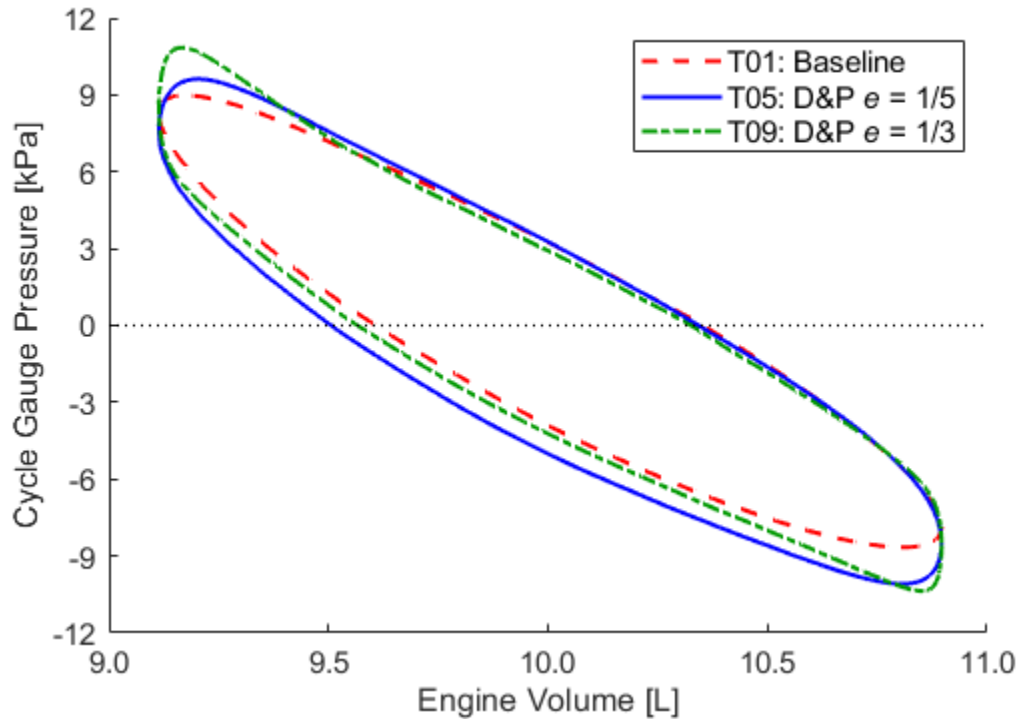


Figure 6.23 – Maximum power data set P-V indicator diagrams for test group 05 and 09 compared to the baseline indicator diagram

Table 6.14 – Test group 05 maximum power data set values

Property	Var. x	Baseline		Test Group 05		Diff. [%]	Unit
		Value	Std. $\pm u_x$	Value	Std. u_x		
Shaft Power	p_s	5.61	0.10	4.85	0.08	-13.6	W
Shaft Work	W_s	4.61	0.09	5.25	0.09	13.9	J
Indicated Work	W_{ind}	10.03	0.25	12.36	0.26	23.1	J
Forced Work	W_{FW}	3.39	0.18	2.89	0.18	-14.7	J
Mech. Effectiveness	E	0.70	0.02	0.64	0.02	-8.9	-
Thermal Efficiency	η_T	1.1	0.2	1.3	0.3	16.3	%

Table 6.15 – Test group 09 maximum power data set values

Property	Var. x	Baseline		Test Group 09		Diff. [%]	Unit
		Value	Std. $\pm u_x$	Value	Std. u_x		
Shaft Power	p_s	5.61	0.10	3.57	0.06	-36.4	W
Shaft Work	W_s	4.61	0.09	4.95	0.09	7.3	J
Indicated Work	W_{ind}	10.03	0.25	11.20	0.27	11.6	J
Forced Work	W_{FW}	3.39	0.18	3.20	0.19	-5.7	J
Mech. Effectiveness	E	0.70	0.02	0.67	0.02	-4.2	-
Thermal Efficiency	η_T	1.1	0.2	0.8	0.1	-27.6	%

6.5.3 Indicator Diagram Trends Over Trials of the Combined Dwelling Test Groups

The plots of the trial indicator diagram trends for test group 05 and test group 09 are shown in Figure 6.24 and Figure 6.25 respectively. The results from test group 05 using the $e = 1/5$ gears has data sets that exceed 100% engine loading. This is due to the fact that engine load is recorded as the engine torque normalized by the maximum calibrated torque measurement value of 1 Nm, and so the excessive maximum torque is calculated as a load greater than 100%. The indicated work of both trials shown display consistent work segments, and values of mechanism effectiveness between the values seen in the displacer dwelling test groups and the low values seen in the piston dwelling groups.

Both trials produced maximum power at engine loads higher than the average value of 70% from previous tests. For test group 05 maximum power was recorded at ~80% engine load, and for test group 09 it was at ~75% engine load. The double dwelled test group 09 also stalled at lower maximum engine loads than most other trials.

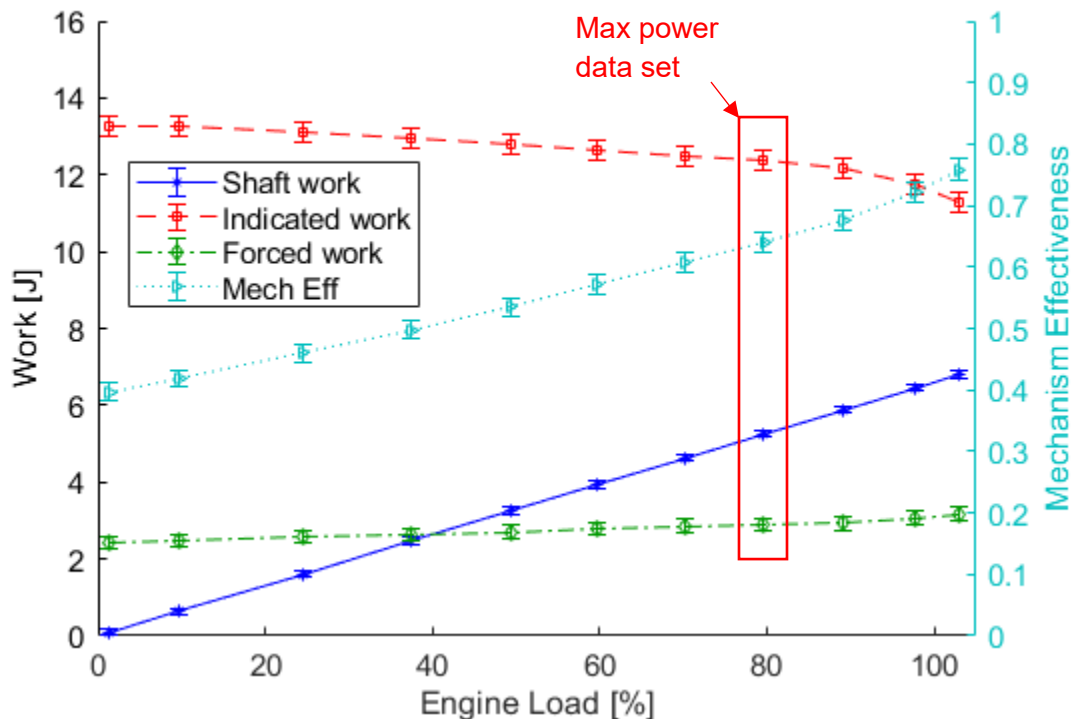


Figure 6.24 – Test group 05 trends for indicator diagram work components and mechanism effectiveness

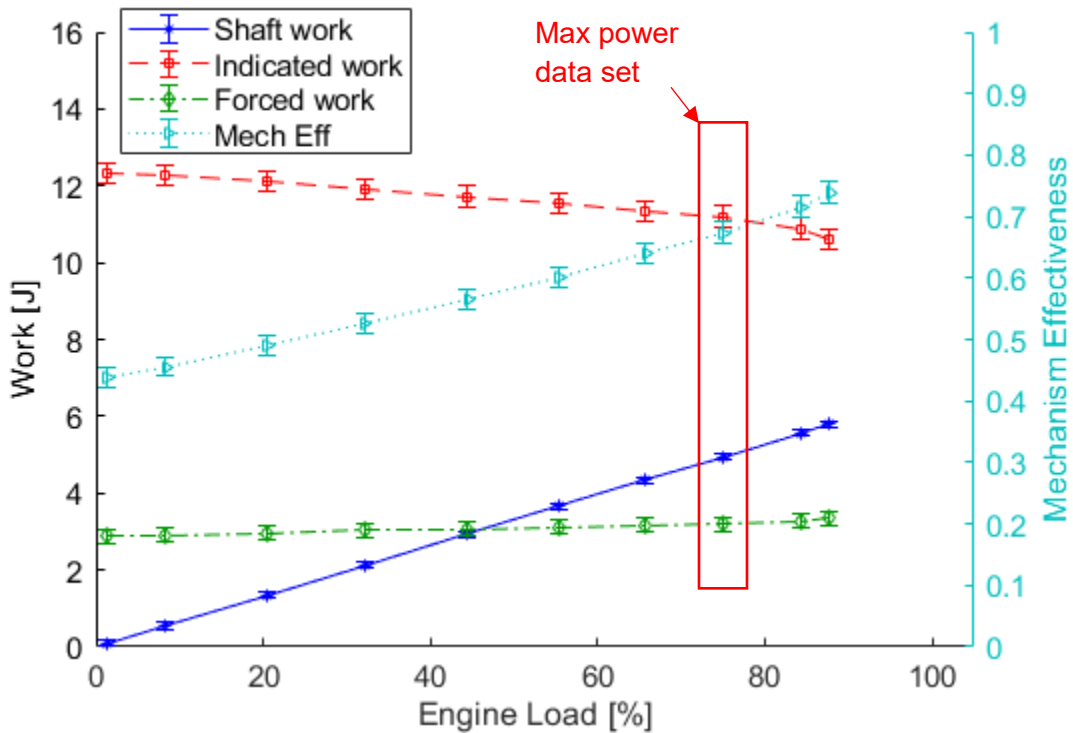


Figure 6.25 – Test group 09 trends for indicator diagram work components and mechanism effectiveness

6.5.4 Combined Dwelling Conclusions

The combined dwelling of the displacer and piston provided results that were simultaneously expected and unexpected. Measurements of the engine revealed that it was indeed possible to modified the displacer and piston motion in such a way as to closely replicate an ideal Stirling cycle. However, any gains in indicated work were limited by reductions in mechanism effectiveness and reduced engine running speeds. Both of these factors were discussed in the results of the individually dwelled displacer and piston test groups.

6.6 Triangle Displacer and Piston Dwelling: Test Groups 03, 04, and 08

This section presents the results from the test groups where the displacer motion was modified to produce a triangular wave displacement profile using the $e = 1/5$ gears set phase 90° apart from the configuration that produced dwelling displacer motion. In addition to the displacer motion modification the piston was dwelled in phase with the displacer, resulting in piston motion that was dwelled at TDP and BDC. Test group 03 served as control of the triangular displacer motion and used the conventional round gear set with eccentricity of $e = 0$ for the piston. Conditions of test group 03 is noted in Table 6.16. Test group 04 used the $e = 1/5$ gear sets to dwell the piston, which resulted in both the displacer and piston crankshafts moving together. Test conditions for the test group 04 is noted in Table 6.17. Test group 08 used the $e = 1/3$ gear sets to dwell the piston and the conditions of the test group is noted in Table 6.18.

Table 6.16 – Test conditions of combined displacer and piston dwelling motion test group 03

Property	Variable	Nominal Value	Actual Value	Unit
Displacer gear set	-	$e = 1/5$ (T)	$e = 1/5$ (T)	-
Piston gear set	-	$e = 0$	$e = 0$	-
Hot source temperature	T_{Hin}	90	89.42	$^\circ\text{C}$
Cold sink temperature	T_{Cin}	5	4.75	$^\circ\text{C}$
Total trials	-	2	2	-
Maximum power trial	-	-	2	-

Table 6.17 – Test conditions of combined displacer and piston dwelling motion test group 04

Property	Variable	Nominal Value	Actual Value	Unit
Displacer gear set	-	$e = 1/5$ (T)	$e = 1/5$ (T)	-
Piston gear set	-	$e = 1/5$	$e = 1/5$	-
Hot source temperature	T_{Hin}	90	N/A	$^\circ\text{C}$
Cold sink temperature	T_{Cin}	5	4.85	$^\circ\text{C}$
Total trials	-	2	2	-
Maximum power trial	-	-	1	-

Table 6.18 – Test conditions of combined displacer and piston dwelling motion test group 08

Property	Variable	Nominal Value	Actual Value	Unit
Displacer gear set	-	$e = 1/5$ (T)	$e = 1/5$ (T)	-
Piston gear set	-	$e = 1/3$	$e = 1/3$	-
Hot source temperature	T_{Hin}	90	92.07	°C
Cold sink temperature	T_{Cin}	5	4.86	°C
Total trials	-	2	2	-
Maximum power trial	-	-	2	-

6.6.1 Triangular Displacer Motion and Dwelled Piston: Torque and Power Curves

Results in plotted Figure 6.26 reveals that the triangular motion profile of the displacer achieved the desired effect of increasing the running speed of the engine, at least for lower shaft torque measurements. These results are in contrast the reduction in engine speed witnessed in the dwelled displacer and combined dwell test groups. These results also lend support to the theory that displacer translation speed has a significant impact on engine speed. Examining the plot of the derivative function for the $e = 1/5$ oval gear shown in Figure 2.4 it can be seen that the triangular motion profile would have a displacer crankshaft speed 33% slower than the baseline conventional case at the slowest parts of the cycle that align with displacer movement.

The power curves of the triangular motion test groups are shown in Figure 6.27 and shows that the higher engine running speeds improve the power production of the engine. Particularly at higher ends of the engine speed curve, for a target engine speed the engine is capable of producing more power.

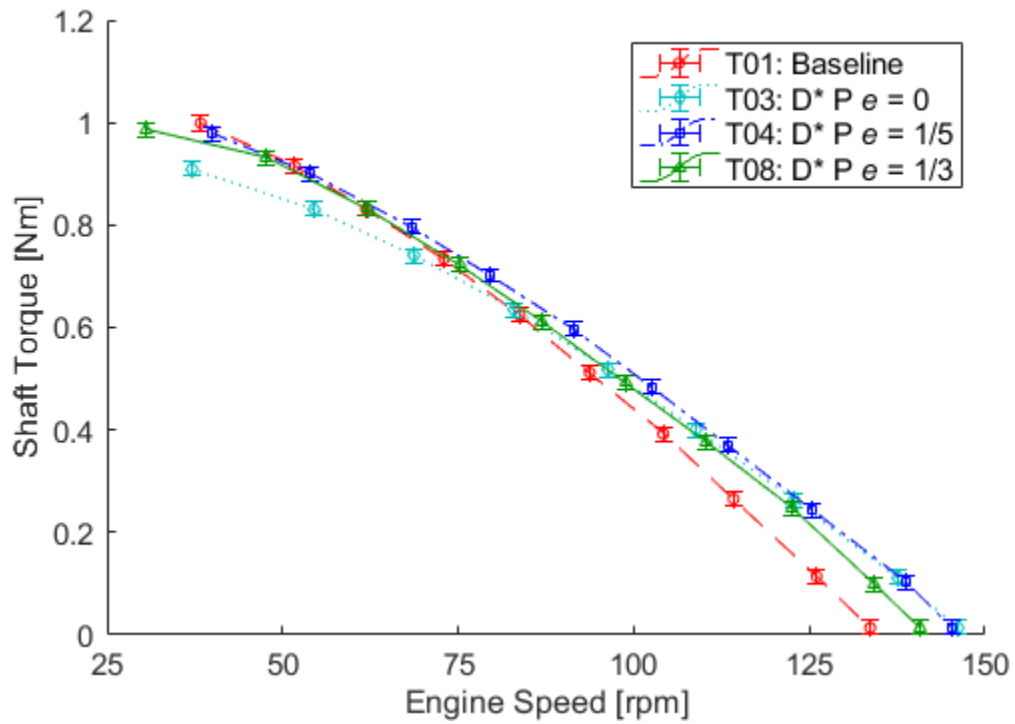


Figure 6.26 – Comparative torque curves for triangular displacer motion and piston dwelling test groups 03, 04, 08, and the baseline

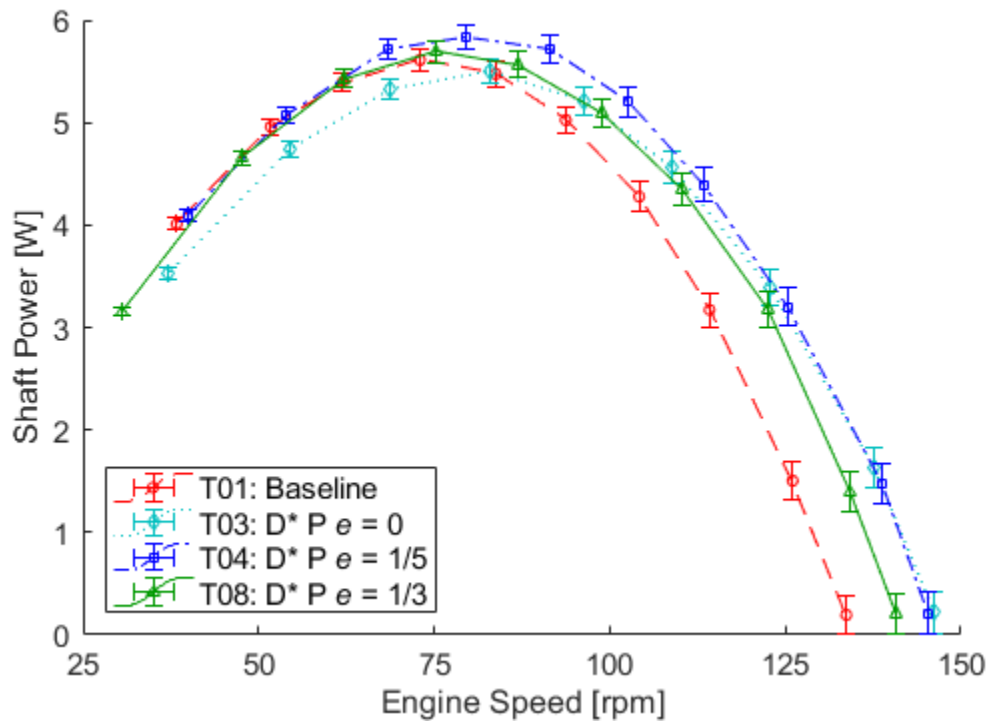


Figure 6.27 – Comparative power curves for triangular displacer motion and piston dwelling test groups 03, 04, 08, and the baseline

6.6.2 Triangular Displacer Motion and Dwelled Piston: Maximum Power Indicator Diagrams

Figure 6.28 shows a comparative plot of the indicator diagrams of the maximum power data sets for the triangular motion displacer test groups as well as the baseline case. The diagrams show favourable results in creasing the area of the indicator diagram, showing increases in the engine pressure swing in the expansion and compression strokes of the engine. The results are similar to the results for the dwelled power piston test groups, as seen in Figure 6.18. The major difference being the corners of the indicator diagram near the minimum and maximum engine volumes where the curves close to the same shape as the baseline case. The triangle displacer has a shorter duration at the TDC and BDC which results in lower peak pressures at the maximum and minimum stroke values.

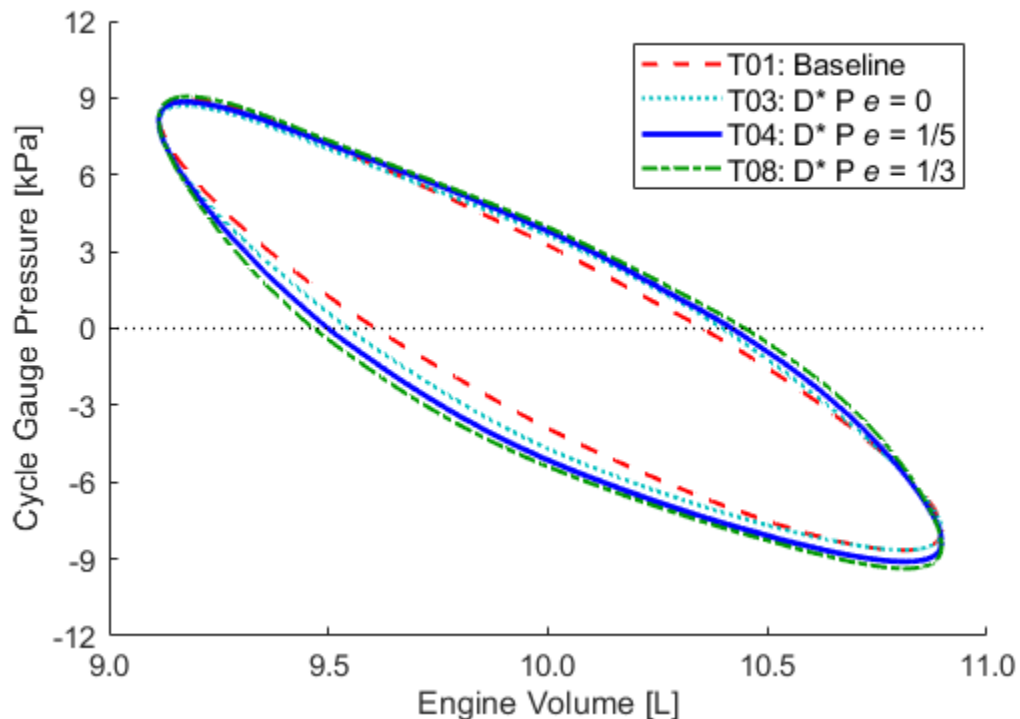


Figure 6.28 – Maximum power data set P-V indicator diagrams for test group 03, 04, and 08 compared to the baseline indicator diagram

The calculations of the work components of the indicator diagrams are presented in Table 6.19, Table 6.20, and Table 6.21. Notable observations from the results include that test group 04, with the triangular displacer and the piston dwelled with the $e = 1/5$ oval gear recorded the maximum power produced of any data set in the investigation of the modified drive mechanism. The data set recorded a maximum power measurement of 5.84 ± 0.11 W, which was a modest 4.0% improvement over the maximum data set of the baseline test group. All the test groups showed improvements to the indicated work and forced work, but like in the dwelled piston test groups, those improvements did not translate into improvements to shaft work, which decreased modestly in all trials.

Like for the piston dwelling test groups the calculated mechanism effectiveness for the triangular motion test groups dropped with increasing piston dwelling. The lowest calculated mechanism effectiveness of the maximum power data sets was in test group 08, with $E = 0.58 \pm 0.02$, a drop of 18.1% when compared to the base case.

Also of note was during recording of data for test groups 03 and 04 the inlet RTD1 experienced an error, recording temperatures that were lower than possible thermodynamically. Measurements of thermal efficiency for those test groups was consequently unavailable. The error was identified and corrected by test group 05.

Table 6.19 – Test group 03 maximum power data set values

Property	Var. x	Baseline		Test Group 03		Diff. [%]	Unit
		Value	Std. $\pm u_x$	Value	Std. u_x		
Shaft Power	p_s	5.61	0.10	5.50	0.12	-1.9	W
Shaft Work	W_s	4.61	0.09	3.98	0.09	-13.8	J
Indicated Work	W_{ind}	10.03	0.25	11.10	0.25	10.5	J
Forced Work	W_{FW}	3.39	0.18	3.07	0.18	-9.4	J
Mech. Effectiveness	E	0.70	0.02	0.63	0.02	-10.8	-
Thermal Efficiency	η_T	1.1	0.2	N/A	N/A	N/A	%

Table 6.20 – Test group 04 maximum power data set values

Property	Var. x	Baseline		Test Group 04		Diff. [%]	Unit
		Value	Std. $\pm u_x$	Value	Std. u_x		
Shaft Power	p_s	5.61	0.10	5.84	0.11	4.0	W
Shaft Work	W_s	4.61	0.09	4.41	0.09	-4.4	J
Indicated Work	W_{ind}	10.03	0.25	12.21	0.26	21.6	J
Forced Work	W_{FW}	3.39	0.18	2.83	0.19	-16.4	J
Mech. Effectiveness	E	0.70	0.02	0.6	0.02	-14.0	-
Thermal Efficiency	η_T	1.1	0.2	N/A	N/A	N/A	%

Table 6.21 – Test group 08 maximum power data set values

Property	Var. x	Baseline		Test Group 08		Diff. [%]	Unit
		Value	Std. $\pm u_x$	Value	Std. u_x		
Shaft Power	p_s	5.61	0.10	5.69	0.11	1.4	W
Shaft Work	W_s	4.61	0.09	4.54	0.09	-1.6	J
Indicated Work	W_{ind}	10.03	0.25	13.08	0.26	30.3	J
Forced Work	W_{FW}	3.39	0.18	2.56	0.19	-24.3	J
Mech. Effectiveness	E	0.70	0.02	0.58	0.02	-18.1	-
Thermal Efficiency	η_T	1.1	0.2	1.3	0.2	22.9	%

6.6.3 Indicator Diagram Trends over Trials of the Triangular Displacer Motion and Dwelled Piston Test Groups

The plots of the trial indicator diagram trends for test group 03, 04, and 08 are shown in Figure 6.29, Figure 6.30, and Figure 6.31 respectively. The indicator diagrams show trends of decreasing indicated work and increasing forced work as load on the engine increases. The indicated work at low engine loads is high when comparing the work segment diagrams of the baseline and dwelled displacer test groups, but decreases as the engine is loaded. As observed in the piston dwelling test groups, the calculation of mechanism effectiveness reconciles this discrepancy by determining a mechanism effectiveness for the engine that is below that of dwelled displacer and baseline test group results. Also noteworthy observation of the triangular displacer test groups is that engine consistently stalled at lower engine loads than previous test groups, despite having the dwelled piston that showed advantageous torque.

Examining the difference between the control test group 03 for displacer dwelling, and the trials with dwelled piston shows an improvement of mechanism of ~5%, indicating that the non-circular gearing may have a non-negligible impact on the drive mechanism efficiency. This was also true of the results for the dwelled power piston test groups 06 and 07.

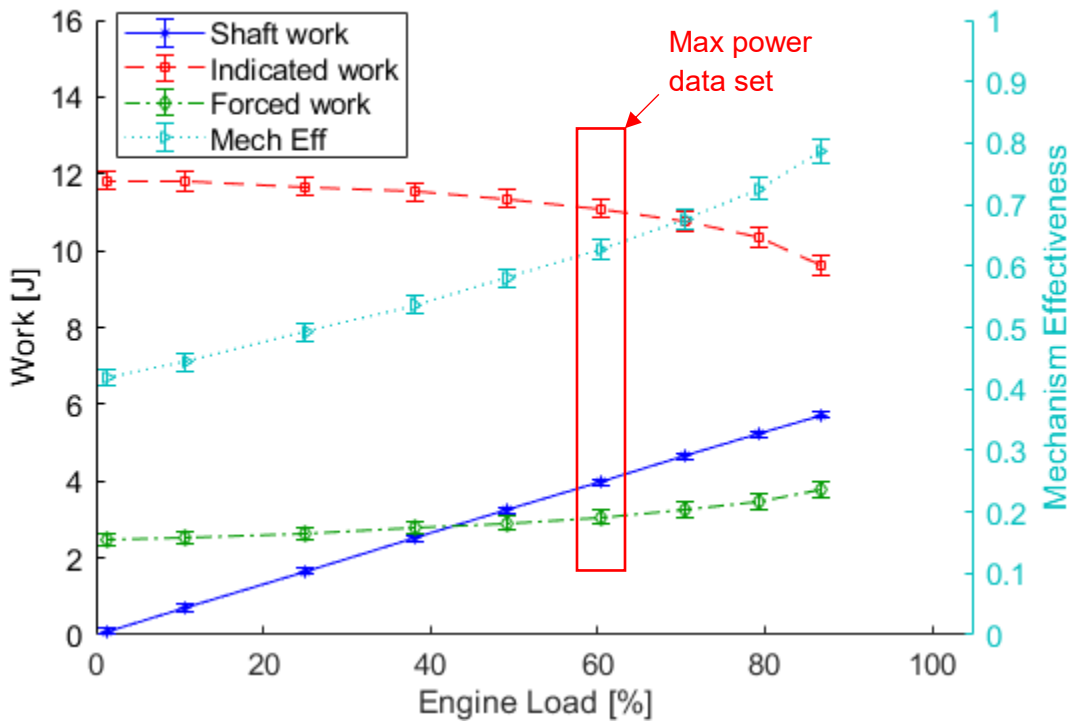


Figure 6.29 – Test group 03 trends for indicator diagram work components and mechanism effectiveness

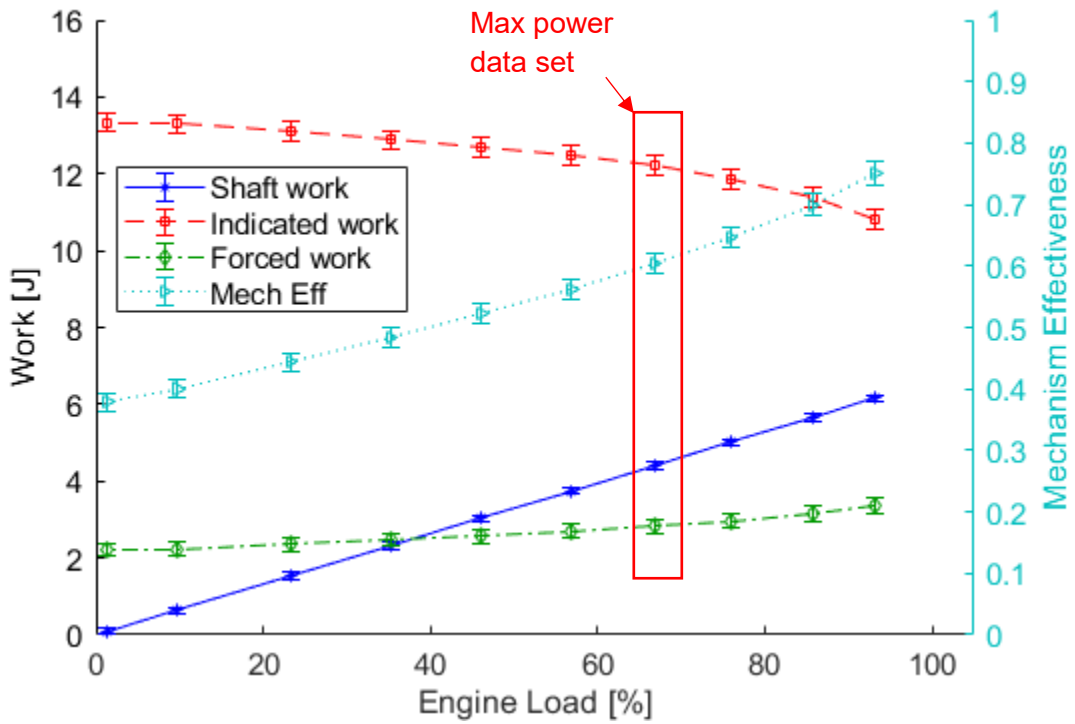


Figure 6.30 – Test group 04 trends for indicator diagram work components and mechanism effectiveness

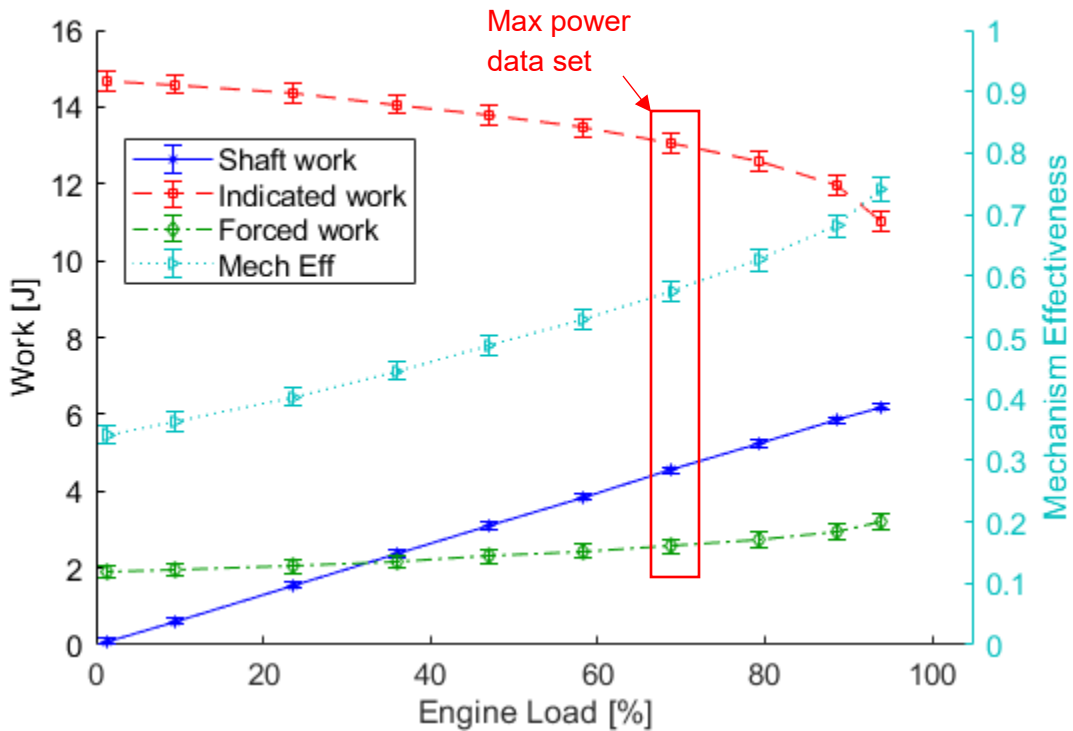


Figure 6.31 – Test group 08 trends for indicator diagram work components and mechanism effectiveness

To further examine the reason for the decreasing indicated work of the cycle comparative plots for the test group minimum shaft power data sets and the maximum shaft work data sets were plotted. Figure 6.32 shows the P-V indicator diagrams for the minimum shaft work data sets and shows a significant pressure difference between the mid points of the expansion and compression strokes. This is in contrast to Figure 6.33 that shows the maximum shaft work data sets. At maximum shaft work the large pressure swing reduces substantially, nearly completely reducing to the baseline case.

A possible explanation for this is leaks of working fluid under the low speed, high load trials. There were no significant changes in average working fluid temperatures in the expansion and compression space over course of the trials ($< \Delta 3\text{ }^{\circ}\text{C}$), that might account for pressure swing variation. Despite changes in indicated work, the shaft work of the cycles still increased under load, and any loses to the indicator diagram area did not substantially impact the shaft work of the engine.

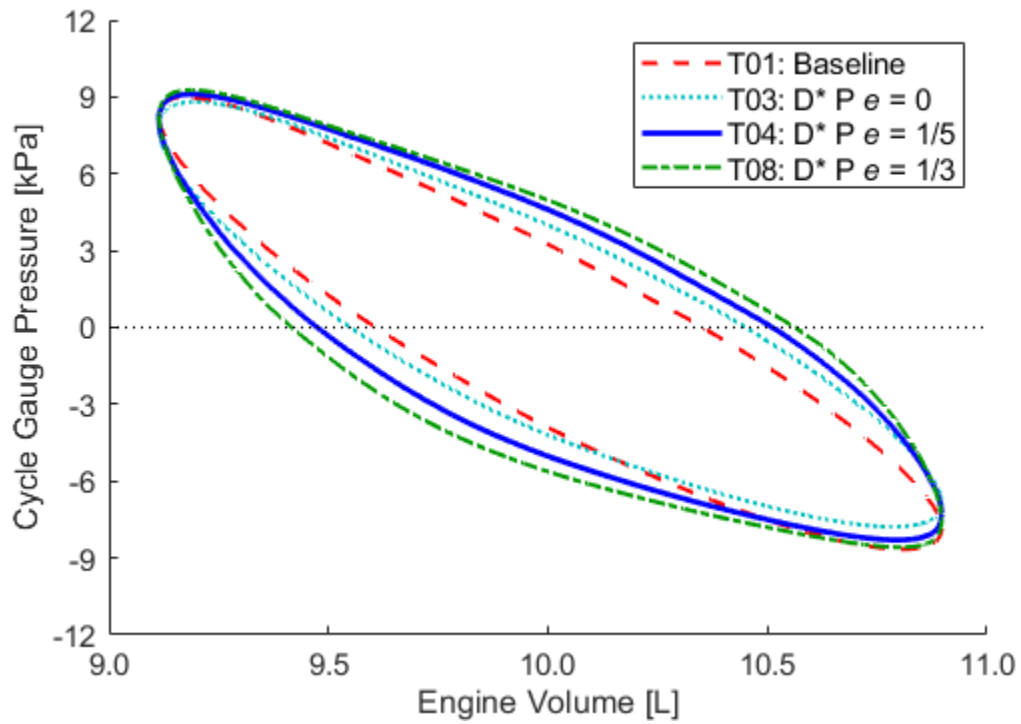


Figure 6.32 – Minimum shaft work data set P-V indicator diagrams for test group 03, 04, and 08 compared to the baseline indicator diagram

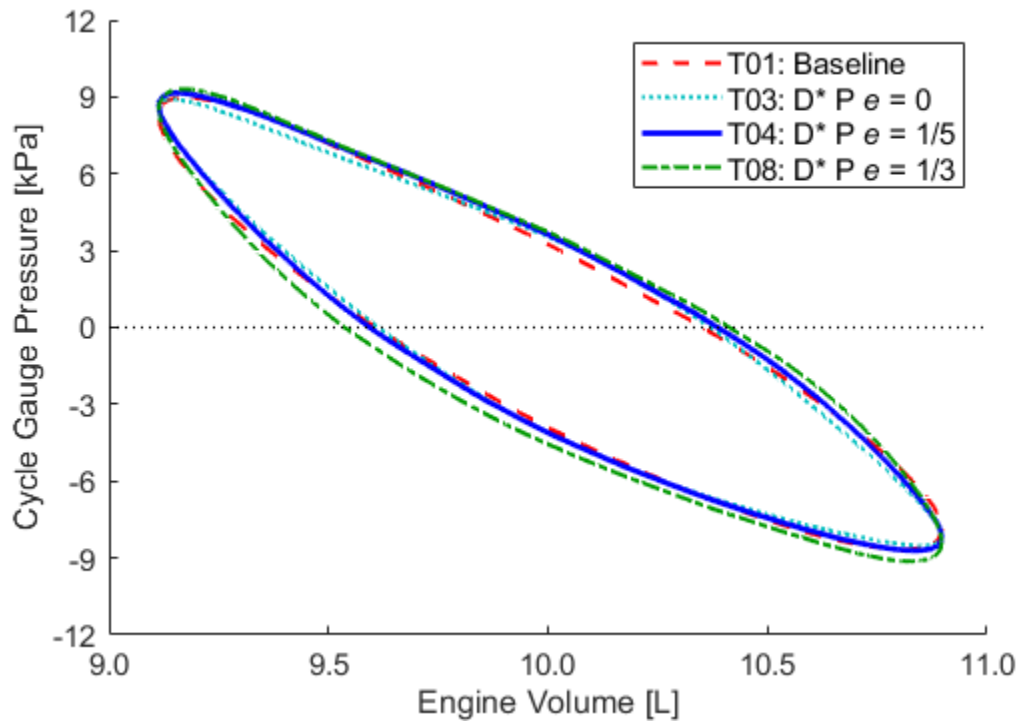


Figure 6.33 – Maximum shaft work data set P-V indicator diagrams for test group 03, 04, and 08 compared to the baseline indicator diagram

6.6.4 Triangular Displacer Motion and Dwelled Piston Conclusions

From the results of the triangular motion of the displacer test group insights into previous conclusions about the dwelling of the displacer piston were validated. Results showed that phasing the displacer crankshaft speed to have slower peak displacer translation speeds did allow the engine to run faster, and produce slightly more power when compared the baseline trials. Conversely, having the displacer piston move quickly from TDC to BDC resulted in slower engine speeds and the loss of power.

Generally, the trends observed during the piston dwelling trials were repeated when piston dwelling was paired with the triangular motion displacer. The indicator diagram was expanded substantially, but the anticipated gains in shaft power were not realized.

7 EVALUATION OF THE ISOTHERMAL MODEL

This section examines the results of the recalculated isothermal model results and how well it aligns with the empirical results for the EP1-M engine for the maximum power data set conditions. As was noted in section 5.3.7 the isothermal model was rerun with the impute variable matched to the observed conditions of the engine trials. Figures are provided that overlay the empirical and the model results, along with tabulated comparisons of the calculated indicated work, forced work, and shaft work of the cycle.

It was observed that the recalculated results of the isothermal model provided results that were very similar to the empirical results. As such only a few particularly interesting comparisons between the model and the empirical results are presented.

7.1 Baseline Test Group 01

The parameters used for the updated model calculations is noted in Table 7.1. The initial model overestimated the expansion and heater temperature by a substantial amount. The mechanism effectiveness was also overestimated for the maximum power case, but mechanism effectiveness values of $E = 0.80$ were observed during test group 01 as shown in Figure 6.9.

Table 7.1 – Changed isothermal model variables from results of test group 01

Property	Variable	Original Model No. 1	Updated Empirical Value	Unit
Displacer gear set	-	$e = 0$	$e = 0$	-
Piston gear set	-	$e = 0$	$e = 0$	-
Expansion space and heater temperature	T_e, T_h	70	60.9	°C
Compression space and cooler temperature	T_c, T_k	20	19.2	°C
Buffer Pressure	P_b	92.5	92.2	kPa
Mechanism Effectiveness	E	0.8	0.7	-

The comparison between the empirical indicator diagram and the isothermal model diagram is shown in Figure 7.1. The shapes of the two diagrams are very close, nearly within standard uncertainty of the empirical results. For easier comparisons of the two diagrams the pressure and volume curves of both results are plotted against the position of the engine output shaft in Figure 7.2.

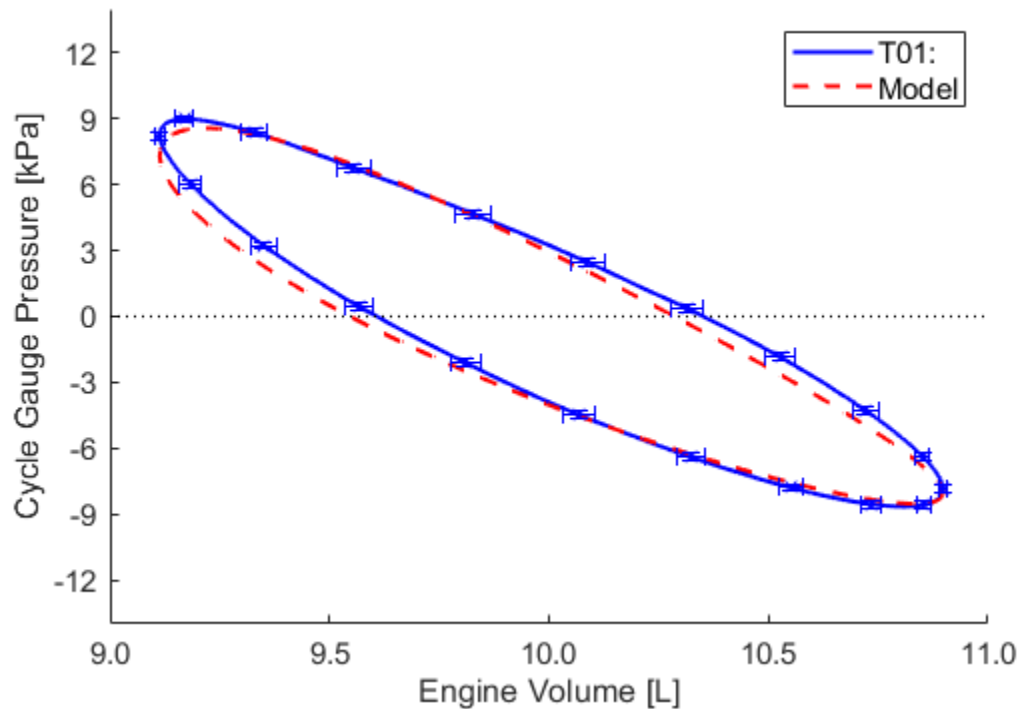


Figure 7.1 – Maximum power data set P-V indicator diagrams of experimental results and updated model for test group 01

Observing the volume curves in Figure 7.2., it is immediately clear that the volume variation of the elastomer bellow is not perfectly analogous to a piston cylinder as modeled by the isothermal mode equations. The compression stroke from maximum volume to minimum volume has volume values that are delayed by a few degrees of the output shaft when compared to equivalent volumes of the modeled piston cylinder. This may be due to the elastomer stretching radially under compression, particularly during forced compression portions of the cycle where the pressure differential is against compressing the volume. Likewise, the volume of the bellow is higher during the expansion portion of the cycle for possibly the same reasons.

The empirical pressure curve attains peak cycle pressures similar to those predicted by the isothermal model. The only significant deviations from the model in areas where the volume is higher empirically than the equivalent position for the model. These higher volumes would explain the slightly lower empirical pressures in those areas.

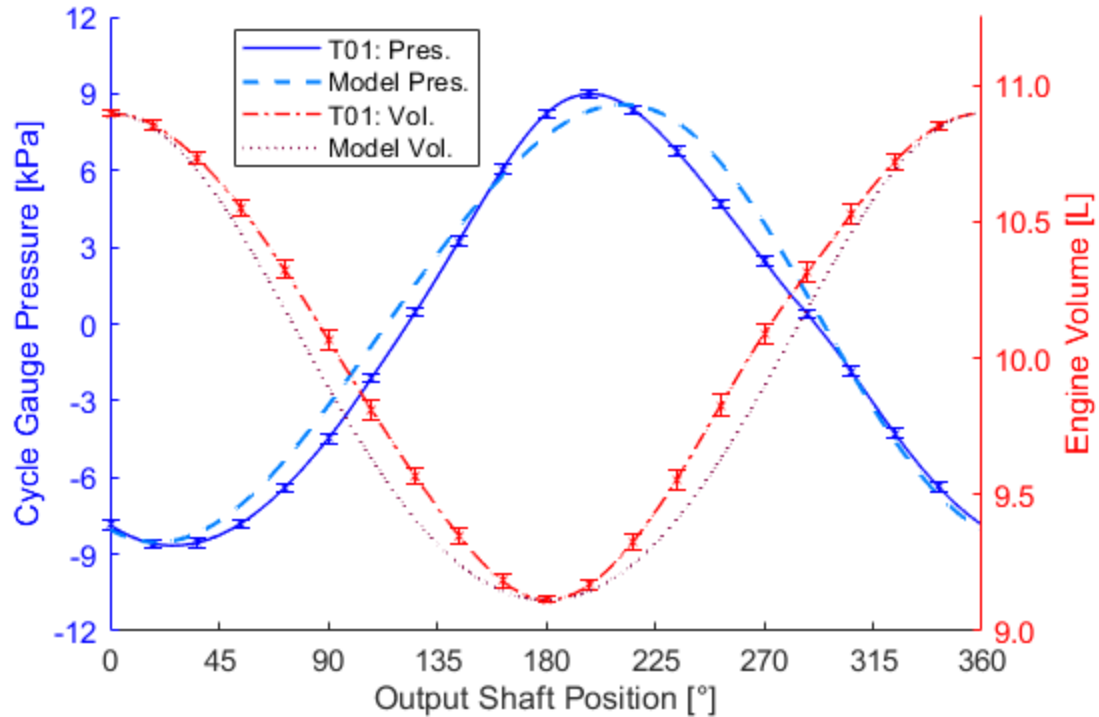


Figure 7.2 – Maximum power data set P-V indicator diagrams of experimental results and updated model for test group 01

Table 7.2 shows the results of the calculation of indicated work, forced work, and shaft work from the isothermal model. The model results are compared to the same calculated values from the empirical trials. Overall there is a less than $\pm 2\%$ difference between the recalculated results compared against the empirical results.

Table 7.2 – Test group 01 maximum power data set and updated model results

Property	Var. x	Test group 01		Updated Model	Diff. [%]	Unit
		Value	Std. $\pm u_x$	Value		
Indicated Work	W_{ind}	10.03	0.25	9.89	-1.4	J
Forced Work	W_{FW}	3.39	0.18	3.36	-0.9	J
Shaft Work	W_s	4.61	0.09	4.53	-1.7	J

In an effort to evaluate the isothermal condition assumption the average instantaneous compression and expansion space temperatures for the baseline test group was plotted and shown in Figure 7.3. As can be observed the working space temperatures do not seem to fluctuate substantially based on the measurements of the thermocouples. This was true of the temperature plots examined for the other test groups. However, it is worth noting that the thermocouples used and their locations present limitations on the instantaneous temperature measurement. These limitations are discussed in section 3.5.2. However, the temperature results, along with the relatively high accuracy of the isothermal model at predicting work segments, support the conclusion that for low temperature, unpressurized engines the isothermal assumption is applicable.

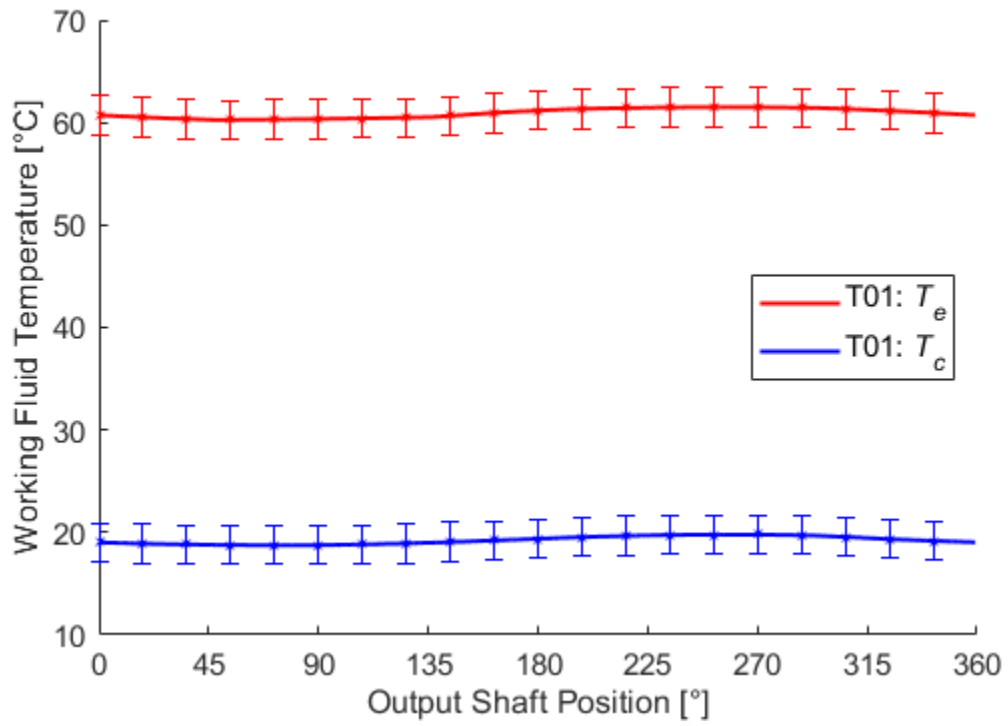


Figure 7.3 – Average instantaneous working space temperatures of the maximum power data set of test group 01

7.2 Piston Dwelling Test Group 07

It was observed that the isothermal generally underestimated the indicator diagram of the dwelled piston motion. As an example of the results of test group 07 are presented in comparison to the recalculated model. The parameters used for the updated model calculations is noted in Table 7.3. The initial model overestimated the expansion and heater temperature by a substantial amount. The mechanism effectiveness was also overestimated for the maximum power case by 0.2, as the empirical maximum power data set mechanisms effectiveness was calculated at $E = 0.61$.

Table 7.3 – Changed isothermal model variables from results of test group 07

Property	Variable	Original Model No. 5	Updated Empirical Value	Unit
Displacer gear set	-	$e = 0$	$e = 0$	-
Piston gear set	-	$e = 1/3$	$e = 1/3$	-
Expansion space and heater temperature	T_e, T_h	70	63.2	°C
Compression space and cooler temperature	T_c, T_k	20	22.3	°C
Buffer Pressure	P_b	92.5	92.7	kPa
Mechanism Effectiveness	E	0.8	0.61	-

The comparison between the empirical indicator diagram and the isothermal model diagram is shown in Figure 7.4. The shapes of the two diagrams are close, however the isothermal model did not accurately predict the pressure swing between the expansion and compression portions of the cycle.

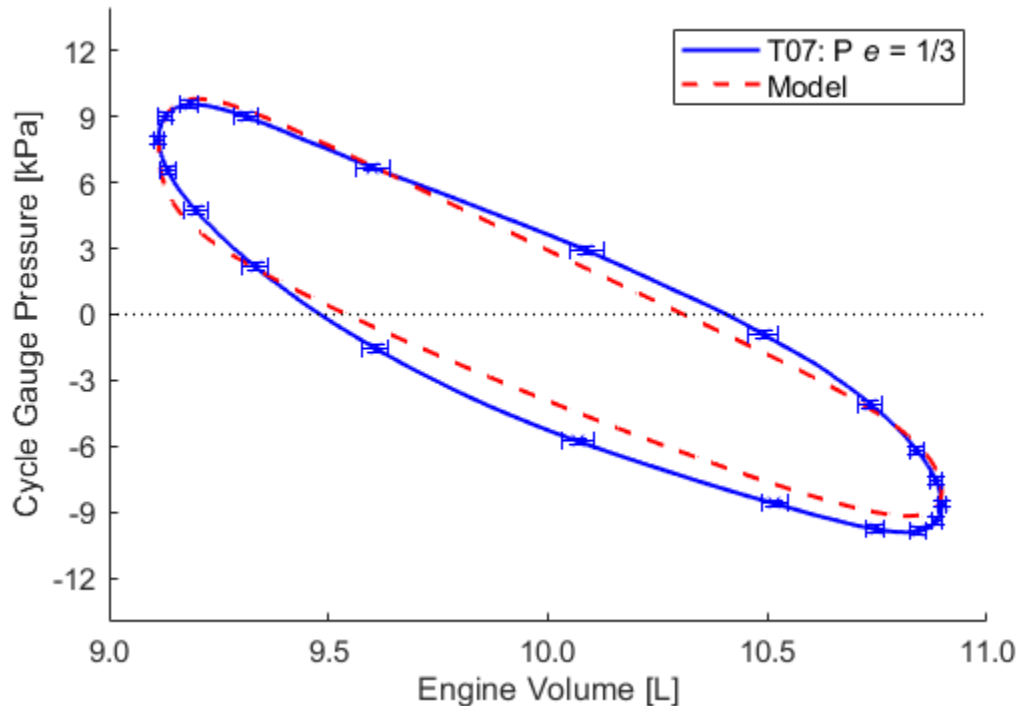


Figure 7.4 – Maximum power data set P-V indicator diagrams of experimental results and updated model for test group 07

Observing the volume curves in Figure 7.5, the same deviation between the elastomer bellow and conventional a piston cylinder as modeled by the isothermal model equations is still present. The reason of the greater area of the empirical indicator diagram and the model results can be seen in the difference between the model and experimental pressure curves. The empirical pressure during compression is lower than for the model resulting in a greater indicated area. The explanation for why the model under predicts the low-pressure peak of the cycle is unclear, but the case may be that the working fluid temperature during the tests was lower than measured by thermocouple T1. As was noted in section 3.5.2, the compression space thermocouple needed to be recessed in the bottom flange to avoid contacting the displacer. Its temperature reading may thus be higher than the actual gas temperature.

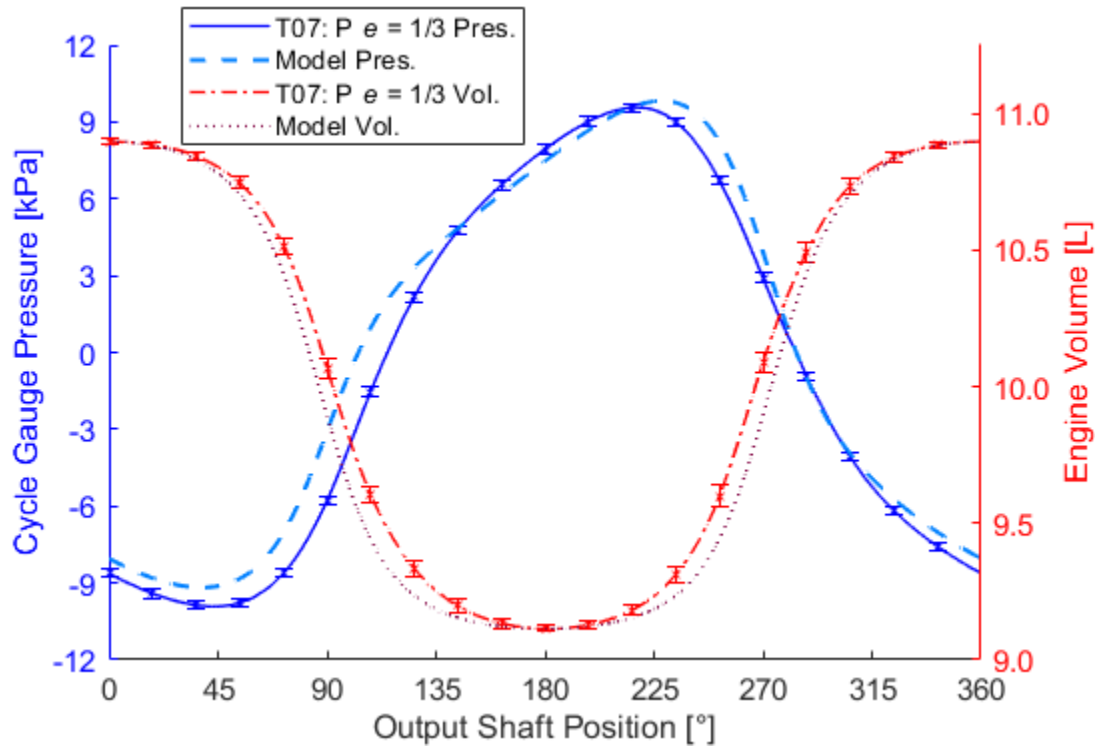


Figure 7.5 – Maximum power data set P-V indicator diagrams of experimental results and updated model for test group 07

Table 7.4 shows the results of the calculation of indicated work, forced work, and shaft work from the isothermal model. The model results are compared to the same calculated values from the empirical maximum power data set. The isothermal model under predicted the indicated work by 14.9% when compared to the experimental results, and under estimated the shaft work by 25.6%.

Table 7.4 – Test group 07 maximum power data set and updated model results

Property	Var. x	Test group 07		Updated Model	Diff. [%]	Unit
		Value	Std. $\pm u_x$	Value		
Indicated Work	W_{ind}	12.99	0.26	11.05	-14.9	J
Forced Work	W_{FW}	2.67	0.18	2.82	5.8	J
Shaft Work	W_s	5.24	0.09	3.90	-25.6	J

7.3 Combined Dwelling Test Group 09

The isothermal model's predictions for the combined dwell test groups were remarkably accurate and the results of test group 09 are presented here to demonstrate that. Parameters used for the updated model calculations is noted in Table 7.5. The initial model overestimated the expansion and heater temperature consistently across the test groups by 10 °C. As was noted previously the mechanism effectiveness was also overestimated.

Table 7.5 – Changed isothermal model variables from results of test group 09

Property	Variable	Original Model No. 7	Updated Empirical Value	Unit
Displacer gear set	-	$e = 0$	$e = 0$	-
Piston gear set	-	$e = 1/3$	$e = 1/3$	-
Expansion space and heater temperature	T_e, T_h	70	60.50	°C
Compression space and cooler temperature	T_c, T_k	20	20.8	°C
Buffer Pressure	P_b	92.5	94.4	kPa
Mechanism Effectiveness	E	0.8	0.67	-

The comparison between the empirical indicator diagram and the isothermal model diagram is shown in Figure 7.6. The shapes of the two diagrams are very close, and both curves are clearly squared off in the manner anticipated by the ideal cycle.

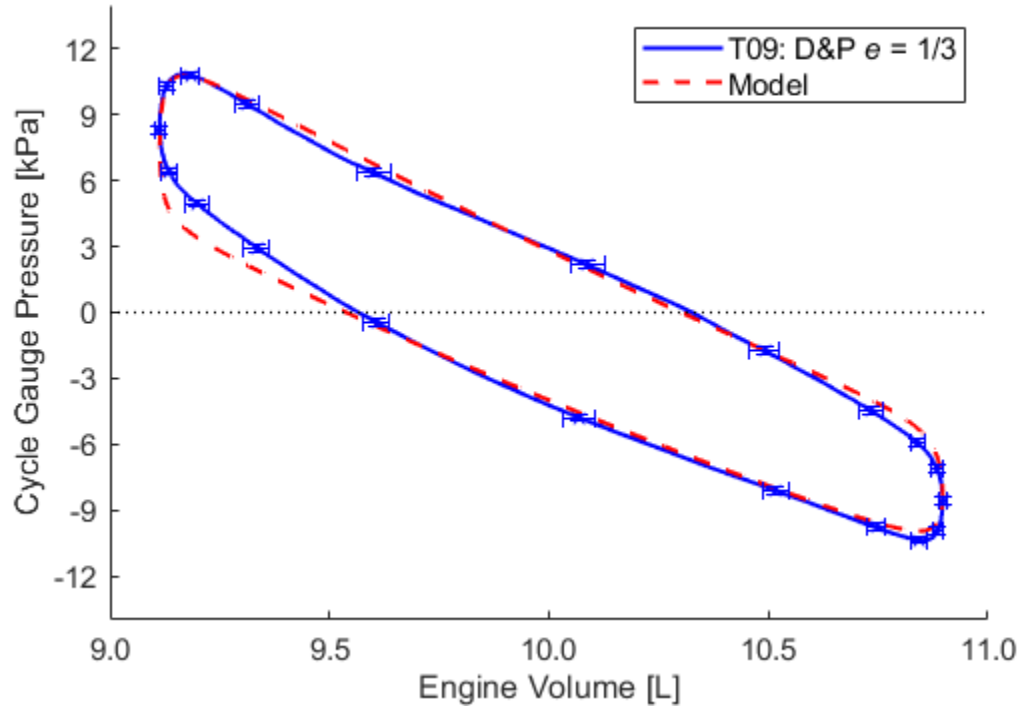


Figure 7.6 – Maximum power data set P-V indicator diagrams of experimental results and updated model for test group 09

Observing the pressure and volume curves over the complete engine cycle as shown in Figure 7.7 it can be seen that the model and the empirical results align closely. The impacts of the considerable dwelling introduced by the oval elliptical non-circular gearing on the displacer and piston were accurately predicted by the isothermal model once the inputs were adjusted to reflect conditions of the engine.

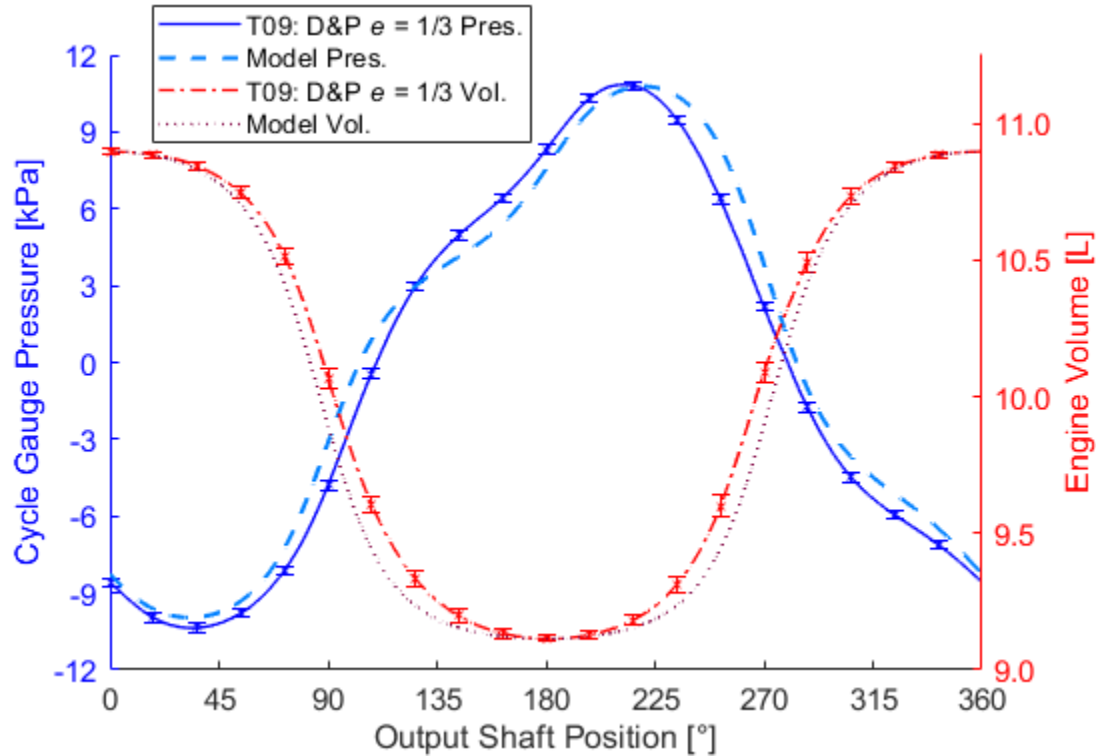


Figure 7.7 – Maximum power data set P-V indicator diagrams of experimental results and updated model for test group 09

Table 7.6 shows the results of the calculation of indicator diagram work segments and the estimation of shaft work compared against the empirical results of test group 09. The model underestimated forced work, resulting in an overestimation of shaft work.

Table 7.6 – Test group 09 maximum power data set and updated model results

Property	Var. x	Test group 09		Updated Model	Diff. [%]	Unit
		Value	Std. $\pm u_x$	Value		
Indicated Work	W_{ind}	11.20	0.27	11.71	4.5	J
Forced Work	W_{FW}	3.20	0.19	2.60	-18.5	J
Shaft Work	W_s	4.95	0.09	5.77	16.6	J

7.4 Discussion of the Utility of the Isothermal Model

Through the course of this investigation it was observed that the isothermal model could be adapted to evaluate drive mechanisms that deviated away from the closed for sinusoidal motion assumption made by Schmidt [49]. From the empirical evidence of the performance of the EP1-M engine, the assumption regarding the isothermal nature of the expansion and compression space appear to hold true. LTD engines, with their inherently low compression ratios are already unlikely to experience significant adiabatic behaviour, and thus taking the isothermal modeling approach appears valid.

The limitations of the model lie in accurately determining the multitude of assumed parameters and getting them sufficiently correct to predict performance. For example in the model of the baseline case the impact of reducing the assume temperatures from $T_e, T_h = 70\text{ °C}$ to 60.9 °C and $T_c, T_k = 20\text{ °C}$ to 19.2 °C between the original model to the updated model reduced the prediction of indicated work from 12.06J to just 9.89J. It is very difficult to make an accurate assumption of mechanism effectiveness and working fluid temperatures without results form similar engines. However in early design stages this may give indications as to where design efforts and improvements should be focused, or evaluating trade-offs of improvements that may negatively impact another parameter. When considering retrofits to existing engines as was the case with this investigation having available data does allow for reasonably accurate modeling.

8 CONCLUSIONS

This investigation had as its stated goal, to evaluate whether it was possible to improve the the thermodynamic power produced by a low temperature differential gamma Stirling engine by modifying the engine drive mechanism to better replicate the Stirling thermodynamic cycle. In pursuit of that goal there were numerous undertakings that were documented in this work: Design of a drive mechanism that enabled modified motion of the engine pistons, validation of the mechanism using an isothermal thermodynamic model, retrofit of an existing LTD engine, experimentation of multiple combinations of motion modification of the displacer and piston examining their effect on engine performance, and finally an evaluation of the initial thermodynamic model. Concluding remarks on these undertakings are summarized here along with comments regarding potential future work.

The conceptual mechanism with interchangeable gear sets was successfully designed to be implemented on the existing LTD gamma type Stirling engine, the EP1. The kinematics of the oval elliptical non-circular centrodes achieved the desired motion profiles of the displacer piston and power piston that better emulated the ideal Stirling cycle. The mechanism was also able to emulate the motion from a conventional kinematic engine in order to provide a baseline from which to evaluate the relative improvement of the modified motion. The kinematics of the mechanism were successfully implemented into the isothermal thermodynamic model which provided validation to the concept. This initial modeling indicated that motion modifications would expand the engine indicator diagrams to produce more indicated work per cycle, and would produce increased shaft power based on the model assumptions. These assumptions were taken from previous engine performance results with a conventional mechanism.

Retrofit of the EP1 to the EP1-M with the new drive mechanism was also successful and the EP1-M was able to run under its own power with the non-circular gears. This conclusively demonstrated that the new drive mechanism mechanism effectiveness was sufficient. Three sizes of Oval elliptical non-circular gears were designed featuring

eccentricities of $e = 0$, $e = 1/5$, and $e = 1/3$. Two pairs of each size were manufactured using 3D printing technology and the gears were proven to be sufficiently well built for use in the mechanism. Preliminary testing of the engine was used to refine empirical trial testing conditions and procedures for the steady state investigation of the modified displacer and piston motion. Steady state trials were run between a nominal source temperature of 90 °C and a sink temperature of 5 °C.

For the the displacer dwelling test groups slight improvements to the indicated work and shaft work of the engine cycle were observed at the maximum power data sets. The $e = 1/5$ gears improved shaft work by 1.5%, while the $e = 1/3$ gear improved the shaft work by 9.5% when compared to the baseline case. However, these gains to cycle work did not result in increases to engine power as both of the modified displacer motion test groups ran at slower engine speeds than the baseline motion configured. The maximum power point comparison for the $e = 1/5$ gear showed a reduction of 15.6% to maximum power, while the $e = 1/3$ gear showed a reduction of 27.4%.

Results from the combined displacer and piston dwell test reinforced the findings from the dwelled displacer group. Shaft work at the maximum power data set increased for the $e = 1/5$ gear sets by 13.9% over the baseline case, and the $e = 1/3$ gear sets improved shaft work by 7.3%. But both trials saw significant reductions in maximum power produced when compared to the baseline case: -13.6% for the $e = 1/5$ gears, and -36.4% for the $e = 1/3$ gears. It was observed that dwelling the displacer motion at the displacer top dead center and bottom dead center was capable of replicating a more ideal Stirling cycle indicator diagram and improving the shaft work of the engine, but the motion modification also incurred penalties to engine speed that negated work gains, and resulted in substantially lower maximum power performance when compared to the baseline conventional displacer motion trials. The losses to engine speed were seen to be proportional to the duration of the dwell, and consequently the maximum displacer speed when translating between the TDC and BDC positions. The faster displacer translations were theorized to incur additional flow losses in the engine that reduced the engine speed.

The trials of the triangular motion profile for the displacer reinforced conclusions about the importance of maximum displacer translation speed on engine speed. The

slower maximum displacer speeds of the triangular motion trials resulted in faster engine speeds for every configuration tested in comparison to the baseline case. The data set with the highest measured power was achieved with the mechanism configured with triangular displacer motion in combination with piston dwelling using the $e = 1/5$ gear set. The maximum power of the data set was 5.86 ± 0.11 W, which was a modest 4.0% improvement over the maximum power of the baseline trials of 5.61 ± 0.10 W

The empirical results showed that indicated work increased substantially for the dwelled piston gearing configurations as anticipated by the isothermal modeling. However, measurements of the cycle shaft work did not show proportional gains. To reconcile the differences between indicated work and shaft work the calculated constant mechanism effectiveness was observed to reduce by ~ 0.1 for dwelled piston trials when compared to the conventional motion baseline. Overall the maximum power produced by piston dwelling configurations, or triangular displacer motion with piston dwelling resulted in maximum power measurements that were all within $\pm 4.0\%$ of the maximum power measured from the conventional motion baseline trials. It was theorized that the apparent drop in mechanism effectiveness was a result of increased frictional losses in the mechanism. The non-circular gears have variable pressure angles that get very high when compared to conventional round gears. The continuously changing force transmission vectors through the gear set may increase loads on shaft bearings, or any surface slipping on gear teeth. Further investigations can be undertaken to assess if mechanism effectiveness can be improved to improve shaft power with the increased indicated work. No substantial decrease in engine speed or performance was otherwise observed for dwelled piston motion.

The empirical results highlighted the shortcoming of the simple thermodynamic model used. The model cannot predict engine speed, and so calculation of shaft power from shaft work must assume an engine cyclic rate. The reduction of engine speed observed in the displacer dwelling tests was not accounted for by the simple indicator diagram analysis of the isothermal model and Senft's fundamental efficiency theorem. Positive improvements of indicated work and shaft work, as anticipated by the model, are not indicative of improved engine speed and maximum power performance. The model,

once revised with actual engine conditions, is capable of accurately predicting the indicator diagram shapes.

Through the course of the investigation it can be concluded that a more ideal Stirling thermodynamic cycle can be achieved using a mechanism that is capable of dwelling the displacer piston, the power piston, or both pistons together. The indicated cycle work can be increased compared to the same engine, at the same conditions, running with conventional motion. However, the incurred losses to engine speed or engine mechanism effectiveness were shown to negate any potential gains to maximum power production of the LTD gamma type Stirling engine tested. This might be remedied by investigations into different dwelling mechanisms that replicate the examined motion, but with more efficient mechanical components. Further exploration of engine operating parameters may reveal under which conditions the motion modification may improve engine performance to a sufficient degree that warrants the added drive mechanism complexity necessary to achieve the motion modifications. These parameters may include changing the engine operating temperatures, instrumenting more elements of the engine or drive mechanism, or even altering the physical design of the engine components.

REFERENCES

- [1] V. Masson-Delmotte *et al.*, “IPCC, 2021: Summary for Policymakers.,” 2021.
- [2] International Energy Agency (2021), “Global Energy Review 2021,” Paris, 2021.
- [3] International Energy Agency (2019), “Global Energy & CO2 Status Report 2019,” Paris, 2019.
- [4] Canada Energy Regulator, “Provincial and Territorial Energy Profiles – Alberta,” 2021. [Online]. Available: <https://www.cer-rec.gc.ca/en/data-analysis/energy-markets/provincial-territorial-energy-profiles/provincial-territorial-energy-profiles-alberta.html>. [Accessed: 25-Aug-2021].
- [5] G. T. Reader and C. Hooper, *Stirling Engines*. London: E. & F. N. Spon, 1983.
- [6] L. G. Thieme and J. Schreiber, “Advanced Technology Development for Stirling Convertors,” Cleveland, 2004.
- [7] U. R. Singh and A. Kumar, “Review on solar Stirling engine: Development and performance,” *Therm. Sci. Eng. Prog.*, vol. 8, no. July, pp. 244–256, 2018.
- [8] D. Mills, “Advances in solar thermal electricity technology,” *Sol. Energy*, vol. 76, no. 1–3, pp. 19–31, 2004.
- [9] T. Schneider, D. Müller, and J. Karl, “A review of thermochemical biomass conversion combined with Stirling engines for the small-scale cogeneration of heat and power,” *Renew. Sustain. Energy Rev.*, vol. 134, no. September, p. 16, 2020.
- [10] I. Kolin, S. Koscak-kolin, M. Golub, and P. Engineering, “Geothermal Electricity Production By Means Of the Low Temperature Difference Stirling Engine,” *World Geotherm. Congr. 2000*, no. January 2000, pp. 3199–3203, 2000.
- [11] K. Wang, S. R. Sanders, S. Dubey, F. H. Choo, and F. Duan, “Stirling cycle engines for recovering low and moderate temperature heat: A review,” *Renew. Sustain. Energy Rev.*, vol. 62, pp. 89–108, 2016.
- [12] I. Szczygieł, W. Stanek, and J. Szargut, “Application of the Stirling engine driven with cryogenic exergy of LNG (liquefied natural gas) for the production of electricity,” *Energy*, vol. 105, pp. 25–31, 2016.
- [13] J. Majeski, “Stirling Engine Assessment,” Bellevue, 2002.
- [14] L. Lemaire, “Miniaturized Stirling Engines For Waste Heat Recovery,” McGill University, 2012.
- [15] F. Vélez, J. J. Segovia, M. C. Martín, G. Antolín, F. Chejne, and A. Quijano, “A technical, economical and market review of organic Rankine cycles for the conversion of low-grade heat for power generation,” *Renew. Sustain. Energy*

- Rev., vol. 16, no. 6, pp. 4175–4189, 2012.
- [16] C3, CMC Research Institutes, Alberta Innovates Technology Futures, and Alberta's Industrial Heartland Association, "Community Integrated Energy Mapping Feasibility Study In Alberta's Industrial Heartland And Strathcona Industrial Area," 2014.
- [17] B. Kongtragool and S. Wongwises, "A review of solar-powered Stirling engines and low temperature differential Stirling engines," *Renew. Sustain. Energy Rev.*, vol. 7, no. 2, pp. 131–154, 2003.
- [18] J. Banks and N. B. Harris, "Geothermal potential of Foreland Basins: A case study from the Western Canadian Sedimentary Basin," *Geothermics*, vol. 76, no. September 2017, pp. 74–92, 2018.
- [19] Y. Le Nian and W. L. Cheng, "Insights into geothermal utilization of abandoned oil and gas wells," *Renew. Sustain. Energy Rev.*, vol. 87, no. February, pp. 44–60, 2018.
- [20] C. Borgnakke and R. E. Sonntag, *Fundamentals of Thermodynamics*, 7th Editio. Hoboken: John Wiley & Sons Ltd., 2009.
- [21] G. Walker, *Stirling Cycle Machines*. London: Oxford University Press, 1973.
- [22] G. Walker, *Stirling Engines*, 1st ed. Oxford: Oxford University Press, 1980.
- [23] C. D. West, *Principles and Applications of Stirling Engines*. New York: Van Nostrand Reinhold Company Inc., 1986.
- [24] J. Reid, "Stirling Stuff," no. April. p. 11, 2016.
- [25] R. Stirling, "Improvements for Diminishing the Consumption of Fuel and in Particular, an Engine Capable of Being Applied to the Moving of Machinery on a Principle Entirely New," British Patent 4081, 1817.
- [26] I. Kolin, *Stirling Motor History - Theory - Practice*. Zagreb: Zagreb University Publication, 1991.
- [27] American Stirling Company, "MM-7 Stirling Engine," 2021. [Online]. Available: <https://www.stirlingengine.com/product/mm-7-stirling-engine>. [Accessed: 25-Aug-2021].
- [28] M. B. Ibrahim and R. C. Tew, *Stirling Convertor Regenerators*. Boca Raton: CRC Press, 2012.
- [29] J. R. Senft, *Mechanical Efficiency of Heat Engines*. New York, USA: Cambridge University Press, 2009.
- [30] S. Zare and A. R. Tavakolpour-Saleh, "Free piston Stirling engines: A review," *Int. J. Energy Res.*, vol. 44, no. 7, pp. 5039–5070, 2020.
- [31] I. Urieli and D. M. Berchowitz, *Stirling Cycle Engine Analysis*. Bristol, England: Adam Hilger Ltd., 1984.

- [32] J. R. Senft, "An ultra low temperature differential Stirling engine," in *Proceedings 5th International Stirling Engine Conference*, 1991, p. Paper No. ISEC 91032.
- [33] C. D. West, *Liquid Piston Stirling Engines*. New York: Van Nostrand Reinhold Company Inc., 1983.
- [34] C. W. Stammers, "The operation of the Fluidyne heat engine at low differential temperatures," *J. Sound Vib.*, vol. 63, no. 4, pp. 507–516, 1979.
- [35] G. W. Swift, *Thermoacoustics : a unifying perspective for some engines and refrigerators*, 2nd ed. Cham, Switzerland: Springer Nature, 2017.
- [36] M. A. G. Timmer, K. de Blok, and T. H. van der Meer, "Review on the conversion of thermoacoustic power into electricity," *J. Acoust. Soc. Am.*, vol. 143, no. 2, pp. 841–857, 2018.
- [37] J. R. Senft, "Optimum Stirling engine geometry," *Int. J. Energy Res.*, vol. 26, no. 12, pp. 1087–1101, 2002.
- [38] D. W. Kirkley, "Determination of the optimum configuration for a stirling engine," *Arch. J. Mech. Eng. Sci. 1959-1982 (vols 1-23)*, vol. 4, no. 3, pp. 204–212, 1962.
- [39] J. Egas and D. M. Clucas, "Stirling Engine Configuration Selection," *Energies*, pp. 1–22, 2018.
- [40] C. Stumpf, "Parameter Optimization of a Low Temperature Difference Gamma-Type Stirling Engine to Maximize Shaft Power," University of Alberta, 2019.
- [41] N. Boutammachte and J. Knorr, "Field-Test of a Solar Low Delta-T Stirling Engine," *Sol. Energy*, vol. 86, no. 6, pp. 1849–1856, 2012.
- [42] R. J. Meijer, "The Philips Stirling Thermal Engine: Analysis of the Rhombic Drive Mechanism and Efficiency Measurements," Technische Hogeschool Delft, 1960.
- [43] F. Aksoy, H. Solmaz, H. Karabulut, C. Cinar, Y. O. Ozgoren, and S. Polat, "A thermodynamic approach to compare the performance of rhombic-drive and crank-drive mechanisms for a beta-type Stirling engine," *Appl. Therm. Eng.*, vol. 93, pp. 359–367, 2016.
- [44] H. Karabulut, F. Aksoy, and E. Öztürk, "Thermodynamic analysis of a β type Stirling engine with a displacer driving mechanism by means of a lever," *Renew. Energy*, vol. 34, no. 1, pp. 202–208, 2009.
- [45] S. Kota, "Generic Models for Designing Dwell Mechanisms : A Novel Kinematic Design of Stirling Engines as an Example," vol. 113, no. March 1988, pp. 446–450, 2018.
- [46] H. Fang, K. Herold, H. Holland, and E. H. Beach, "A Novel Stirling Engine With an Elliptic Drive," *IECEC 96. Proc. 31st Intersoc. Energy Convers. Eng. Conf.*, vol. 2, pp. 1232–1237, 1996.
- [47] T. D. McWaters, "Kinematic Stirling Engine," US005644917A, 1996.

- [48] C. J. A. Stumpf, A. J. Hunt, and D. S. Nobes, "Effect of Scaling Up Low Temperature Differential Stirling Engines," in *Proceedings of The 18th International Stirling Engine Conference*, 2018, pp. 497–515.
- [49] G. Schmidt, "Therorie der Lehmannschen Calorischen Maschine," *Zeitschrift des Vereines Dtsch. Ingenieure*, vol. 15, pp. 1-12,97-112, 1871.
- [50] R. L. Norton, *Design of Machinery: an Introduction to the Synthesis and Analysis of Mechanism and Machines*, 3rd ed. New York: McGraw Hill, 2004.
- [51] F. L. Litvin, A. Fuentes-Aznar, I. Gonzalez-Perez, and K. Hayasaka, *Noncircular Gears - Design and Generation*. Cambridge University Press, 2009.
- [52] R. C. Juvinall and K. M. Marshek, *Fundamentals of Machine Component Design*, 5th ed. Hoboken: John Wiley & Sons Ltd., 2012.
- [53] Badger Meter, "Oval Gear Industrial Oval Gear Flow Meters."
- [54] Cunningham Industries, "Stock Gears," 2010. [Online]. Available: <http://cunningham-ind.com/stock.html>. [Accessed: 19-Apr-2021].
- [55] D. Miller, "Experimental Investigation of Stirling Engine Modelling Techniques at Reduced Source Temperatures," University of Alberta, 2019.
- [56] American Gear Manufacturers Association, *AGMA 901-A92*. Alexandria, 1992.
- [57] R. Norton, "Spur Gears," in *Machine Design*, 5th ed., N. Dias, Ed. Upper Saddle River: Prentice Hall, 2014, pp. 713–773.
- [58] R. G. Budynas and K. J. Nisbett, *Shigley's Mechanical Engineering Design*, 9th ed. New York: McGraw Hill, 2011.
- [59] "Gearotic 3.0." .
- [60] A. J. Wheeler and A. R. Ganji, *Introduction to Engineering Experimentation*, Third Edit. Upper Saddle River: Prentice Hall, 2010.
- [61] A. J. Organ, *Stirling Cycle Engines : Inner Workings and Design*. Chichester: John Wiley & Sons Ltd., 2014.
- [62] J. P. Michaud, "Low Temperature Difference Alpha-Type Stirling Engine for the Experimental Determination of Optimal Parameters to Maximize Shaft Power," University of Alberta, 2020.
- [63] MathWorks, "polyval," *Help Center*, 2021. [Online]. Available: <https://www.mathworks.com/help/matlab/ref/polyval.html#d123e1047301>. [Accessed: 27-Jul-2021].
- [64] H. W. Coleman and W. G. Steele, *Experimentation, Validation, and Uncertainty Analysis for Engineers*, 4th ed. Hoboken: John Wiley & Sons Ltd., 2018.
- [65] NIST/SEMATECH, "Uncertainty for Quadratic Calibration Using Propagation of Error," in *e-Handbook of Statistical Methods*, 2012.

- [66] Ç. A. Yunus, *Heat and Mass Transfer: A practical Approach*, 3rd Editio. New York, USA: McGraw Hill, 2007.
- [67] Validyne Engineering, "Simple Manometer to Calibrate Pressure Transducers." .
- [68] Meriam ProcessTechnologies, "General Installation , Commissioning , Operation & Maintenance Instructions for Meriam Manometers," no. 022C:440–15. .
- [69] Natural Resources Canada, "Gravity (CGSN) Edmonton." 2008.

A UNCERTAINTY EQUATIONS

This section details the calculation methodologies used to calculate measurement uncertainty and well as propagation of uncertainty for calculated variables. Only general equations are presented here, while the specific uncertainty equations used for measured variables is detailed in Appendix B, and uncertainty equations used for calculated variables is detailed in Appendix C. All uncertainties were calculate using standard uncertainty methods as described by Wheeler and Ganji [60], and by Coleman and Steele [64].

A.1 Random Uncertainty

Random uncertainty, also known as precision uncertainty, accounts for the imprecision of measurements. For a mean value of x calculated from a number of measured data points n with a normal distribution is defined by equation A.1 adapted from the work of Wheeler and Ganji [60]. Precision uncertainty was considered for measured variables where sampled signals from the recording instruments were averaged to create a single data point. The level at which precision uncertainty was applied to the measurement data during data processing is laid out in the data processing section of the thesis. The equation used to estimate the confidence interval of a mean value calculated from a normally distributed set of samples is given by the following:

$$R_x = \pm t_{\frac{\alpha}{2},v} \frac{S_x}{\sqrt{n}} \quad \text{A.1}$$

- where: R_x = random uncertainty in mean value of x
- $t_{\frac{\alpha}{2},v}$ = Student's two tail t-score of a normally distributed sample with a confidence interval of $1-\alpha$ and v degrees of freedom ($v = n - 1$ if $n < 30$)
- S_x = standard deviation of the of the data used to calculate the mean value of x
- n = number of measured data points from which the mean is calculated

A.2 Systematic Uncertainty

Systematic uncertainty, also known as bias uncertainty, accounts for fixed uncertainties in measurements. In this investigation systematic uncertainty primarily comes from the imperfection in the accuracy of the measurement instruments and should not change over the course of data collection. The various systematic sources of uncertainty of each measurement instrument used in this investigation are described in detail in Appendix B. These include, among others, general accuracy, linearity, digitization, and calibration uncertainty sources. They are typically specified by the manufacturer of the instrument or were derived through calibration procedures. The calibration procedures themselves typically relied on calculation and propagation of uncertainty from the calibrating instruments. All calibration procedures and tests are documented in Appendix B for the specific instrument.

Systematic uncertainties are typically provided as either percentage values based on the full-scale measurement range of the instrument, or as intervals of the measured value in \pm value form. The percentage values were converted to interval form so as to be appropriately combined with other systematic sources of uncertainty and precision uncertainty.

Combined Standard Uncertainty for Measured Variables

The method used for combining the various systematic uncertainty sources and the precision uncertainty was to use the combined standard uncertainty using the Taylor Series Method as described by Coleman and Steele [64]. The combined uncertainty is the root-sum-square (RSS) of the elements of standard uncertainty as defined by:

$$u_x = \left(\sum B_x^2 + R_x^2 \right)^{\frac{1}{2}} \quad \text{A.2}$$

where: u_x = total uncertainty of x
 B_x = elemental systematic uncertainties of x
 R_x = precision / random uncertainty of x

The combined standard uncertainty was determined for each directly measured variable in the data processing code. The precision uncertainty was variable depending on the number of samples any data point was derived from. All elemental sources of systematic uncertainty for any measurement device accounted for in this analysis is listed in Appendix B.

A.3 Propagation of Uncertainty

Propagation of uncertainty was necessary for any calculated variables that are a function of multiple measured variables. The methods presented are adapted from Coleman and Steele [64]. The equations and methods for the calculating variable is detailed in section 5.3. For a general calculated variable y that is a function of measured variables x such that $y = y(x_1, x_2, \dots, x_n)$, the combined standard uncertainty of y is given by:

$$u_y = \left(\left(u_{x_1} \cdot \frac{\partial y}{\partial x_1} \right)^2 + \left(u_{x_2} \cdot \frac{\partial y}{\partial x_2} \right)^2 + \dots + \left(u_{x_n} \cdot \frac{\partial y}{\partial x_n} \right)^2 \right)^{\frac{1}{2}}$$

Or

A.3

$$u_y = \left(\sum_{i=1}^n \left(u_{x_i} \cdot \frac{\partial y}{\partial x_i} \right)^2 \right)^{\frac{1}{2}}$$

where: u_y = combined standard uncertainty of y
 u_{x_i} = combined standard uncertainty of element x_i
 $\frac{\partial y}{\partial x_i}$ = absolute sensitivity coefficients

There are some specific cases where propagation of uncertainty has simplified expressions. In the case where y is the difference or summation of two variables such that $y = y(x_1, x_2)$, then the combined standard uncertainty becomes:

$$u_y = \left((u_{x_1})^2 + (u_{x_2})^2 \right)^{\frac{1}{2}} \quad \text{A.4}$$

where: u_y = combined standard uncertainty of y
 u_{x_1} = combined standard uncertainty of variable x_1
 u_{x_2} = combined standard uncertainty of variable x_2

For calculations where there is a calculated difference equation A.4 was used to simplify the term in larger expressions.

If the function for the calculated variable takes the form of a straight forward multiplication or a quotient of the form $y = kx_1^a x_2^b x_3^c \dots$ where k is a constant and a, b, c, \dots are any negative or positive integers, then the combined standard uncertainty can be calculated by the following as a special expression of equation A.3:

$$u_y = y \left(a^2 \cdot \left(\frac{u_{x_1}}{x_1} \right)^2 + b^2 \cdot \left(\frac{u_{x_2}}{x_2} \right)^2 + c^2 \cdot \left(\frac{u_{x_3}}{x_3} \right)^2 + \dots \right)^{\frac{1}{2}} \quad \text{A.5}$$

where: u_y = combined standard uncertainty of y
 u_{x_i} = combined standard uncertainty of variable x_i

B UNCERTAINTIES AND CALIBRATIONS OF MEASURED VARIABLES

This Appendix presents each direct measurement instrument and documents the source of systematic uncertainty for each of them. This Appendix also details any calibration procedures or trials undertaken to calibrate measurements from these instruments.

B.1 Pump Calibration and Uncertainty

This section details the programmable peristaltic pump and includes details regarding the instrument specifications, uncertainties, and calibration.

Table B-1 – Programmable peristaltic pumps specifications

Device Model	Mfg.	Range	Mode
07551-20 (L/S 18 tubing)	MasterFlex Cole-Parmer Instrument Company	0.023 to 2.3 L/min	Continuous

Table B-2 – Programmable peristaltic pump flow rate uncertainties

Uncertainty Source	Instrument	Uncertainty Description	Uncertainty Type	Value	Notes
Meas. Inst.	07551-20 Peristaltic pump	Calibration Accuracy	Random	± 0.190 g/s (hot) ± 0.100 g/s (cold)	Random uncertainty from the calibration 16 data points at 95% confidence interval
Inst. Calibration	Scout Pro SP6001 Scale	Linearity	Systematic	± 0.014 g/s	Manufacturer specified accuracy at ± 0.1 g over calibration time (0.1g / 7.26s)
Inst. Calibration	Scout Pro SP6001 Scale	Repeatability	Systematic	± 0.028 g/s	Manufacturer specified accuracy at ± 0.2 g over calibration time (0.2g / 7.26s)

B.1.1 Calibration Details: 2020-12-10

Calibration of the multi head pump was performed using the pump calibration mode build into the 07551-20 model as per the manufacturer manual. In calibration mode, the pump runs at its set discharge rate to discharge a default nominal volume of liquid (250ml). The pump was set to a nominal discharge rate of 2.065L/min when initial

testing of the EP1-M was done. The discharge time for 250mL at this nominal rate corresponds to 7.26392 s.

The detailed calibration as described here occurred after all the trials were complete with the hot source and cold sink loops running at their set point temperatures. The default flow rate was not changed from the conditions used during trials and the calibration discharge was measured using a beaker on a digital scale (Scout Pro SP6001, Ohaus Corporation). The masses of 8 sequential calibration discharges were measured before emptying the beaker. This process was repeated twice for both the hot source loop and the cold sink loop. The average mass discharge of each loop was divided by the discharge time at the pump set point to determine the mass flow rate of each loop.

$$R_{m_x} = \pm t_{0.025,15} \frac{S_{m_x}}{\sqrt{16}} \quad \text{B.1}$$

$$u_{\dot{m}_x} = \left[(u_{m_{lin}})^2 + (u_{m_{rep}})^2 + (R_{m_x})^2 \right]^{\frac{1}{2}} \cdot \frac{1}{t_{discharge}} \quad \text{B.2}$$

Table B-3 – Combined standard uncertainty values from pump calibration

Variable	Value	Uncertainty Variable	Uncertainty Value	Unit	Notes
\dot{m}_h	32.37	$u_{\dot{m}_h}$	± 0.20	[g/s]	
\dot{m}_c	29.14	$u_{\dot{m}_h}$	± 0.10	[g/s]	

B.2 RTD

This section details the RTD measurement devices and includes details regarding the instrument specifications, uncertainties, and calibration.

Table B-4 – RTD Sensor and DAQ specifications

Device Model	Mfg.	Range	Mode
RTD-810 Sensor	Omega Engineering Inc.	-200 °C to 750 C	Trial average
NI 9217	National Instruments Corp.	4 RTDs	Trial average

Table B-5 – RTD measurement uncertainties

Uncertainty Source	Instrument	Uncertainty Description	Uncertainty Type	Value	Notes
Meas. Inst.	RTD-810 Immersion RTD	Specified Accuracy	Systematic & Random	± 0.35 °C	Deviation for Class A RTD at 100°C
Inst. Calibration	ERTCO 1005-3S thermometer	Calibration via thermometer	Systematic	± 0.05 °C	Half the smallest analogue increment of inst.
DAQ	NI-9217 DAQ	Temperature Accuracy	Systematic	± 0.20 °C	Typical accuracy in -200°C to 150°C measurement range

B.2.1 Instrument Calibration: 2020-11-03

Calibration for the RTDs was performed by bundling the thermocouples and RTDs at the bulb of an analogue lab thermometer (ERTCO 1005-3S) with a scale resolution of 0.1 °C. The bundle was placed in a water bath that was first chilled to a nominal setting of 2.0 °C, below the 5.00 °C low temperature set point used in experiments. Recordings of the instrument outputs were collected and the analogue calibration value was also recorded. The bath set point was then increased in increments of 10 °C up to a nominal final set point of 97.0 °C just prior to boiling. Data was recorded at each set point to base a complete calibration curve. The recorded voltage outputs of the RTDs was then imported into MATLAB where a first order linear fit was applied and correlated to the calibration temperatures from the lab thermometer. The calibration coefficients were incorporated into the data processing code for the trial data.

B.3 Thermocouple

This section details the thermocouple measurement devices and includes details regarding the instrument specifications, uncertainties, and calibration.

Table B-6 – Thermocouple sensor and DAQ specifications

Device Model	Mfg.	Range	Mode
TTSS-116E-6 Type-T Thermocouple	Omega Engineering Inc.	-0°C to 260°C	Cycle average
TC 9095 Rack mount adaptor	National Instruments Corp.	32 channels	Cycle average
SCIX 1102B signal conditioning module	National Instruments Corp.	32 analogue inputs	Cycle average
SCIX 1600 USB digitizer module	National Instruments Corp.	3 SCIX modules	Cycle average

Table B-7 – Thermocouple measurement uncertainties

Uncertainty Source	Instrument	Uncertainty Description	Uncertainty Type	Value	Notes
Meas. Inst.	TTSS-116E-6 T Type Thermocouple	Specified Accuracy	Systematic & Random	$\pm 1^{\circ}\text{C}$ or $\pm 0.75\%$	Manufacture Specified tolerance at $\pm 1^{\circ}\text{C}$ or $\pm 0.75\%$, which ever is higher
Inst. Calibration	ERTCO 1005-3S thermometer	Calibration via thermometer	Systematic	$\pm 0.05^{\circ}\text{C}$	Half the smallest analogue increment of inst.
DAQ adapter	TC-2095	Repeatability	Systematic	$\pm 0.35^{\circ}\text{C}$	TC-2095 Rack repeatability specification from 15°C to 35°C
DAQ adapter	TC-2095	Accuracy	Systematic & Random	$\pm 0.65^{\circ}\text{C}$	TC-2095 Rack accuracy specification from 15°C to 35°C
DAQ Signal conditioner	SCXI-1102B	Gain Error	Systematic	0.015% of reading max	Specified at 0.015% of reading (for T type, at 100°C is 4.279mV)
DAQ Digitizer	SCXI-1600 USB 16-Bit Digitizer	Absolute Accuracy	Systematic & Random	$\pm 0.061\text{mV}$	$\pm 0.05\text{V}$ Nominal Range at FS accuracy specification ($100^{\circ}\text{C}/4.279\text{mV}$)

B.3.1 Instrument Calibration: 2020-11-03

Calibration for the thermocouples was performed by bundling the thermocouples and RTDs at the bulb of an analogue lab thermometer (ERTCO 1005-3S) with a scale resolution of 0.1 °C. The bundle was placed in a water bath that was first chilled to a nominal setting of 2.0 °C, below the 5.00 °C low temperature set point of the trials. Recordings of the instrument outputs were collected and the analogue calibration value was also recorded. The bath set point was then increased in increments of 10 °C up to a nominal final set point of 97.0 °C just prior to boiling. Data was recorded at each set point to base a complete calibration curve.

The recorded voltage outputs of the thermocouples and RTDs was then imported into MATLAB where a first order linear fit was applied and correlated to the calibration temperatures from the lab thermometer. The calibration coefficients were incorporated into the data processing code for the trial data.

B.4 Piezoelectric Pressure Sensor

This section details the piezoelectric pressure sensor measurement device and includes details regarding the instrument specifications, uncertainties, and calibration.

Table B-8 – Piezoelectric pressure sensor and DAQ specifications

Device Model	Mfg.	Range	Mode
113B21 (SN: LW35042)	PCB Piezotronics Inc.	1380kPa (200psi)	Instantaneous
482C05	PCB Piezotronics Inc.	4 Channels / sensors	Instantaneous
NI-USB-6211	National Instruments Corp.	8 differential channels	Instantaneous

Table B-9 – Piezoelectric pressure sensor measurement uncertainties

Uncertainty Source	Instrument	Uncertainty Description	Uncertainty Type	Value	Notes
Meas. Inst.	113B21 (SN: LW35041)	Specified Uncertainty	Systematic & Random	$\pm 1\%$	Manufacturer Specified at $\pm 1\%$
Meas. Inst.	113B21 (SN: LW35041)	Full scale linearity	Systematic	± 0.138 kPa	Manufacturer Specified at 0.1% FS (0.1% · 485.7mV · 1kPa/3.519mV)
DAQ I/O device	NI-USB-6211	AI Absolute Accuracy	Systematic	± 0.401 kPa	NI-USB-6211 absolute accuracy at 5V full scale (1.410mV · 1kPa/3.519mV)
Time Constant	Pressure Sensor	Rise Time	Systematic	N/A	Rise time $\leq 1.0 \mu\text{s}$ less than sampling rate interval 3.3 μs

B.4.1 Instrument calibration

Calibration data for converting the piezoelectric pressure sensor voltage measurements to pressure values was provided by the manufacturer at a calibration constant of 3.519mV/kPa. The calibration certificate provided the measurement uncertainties for the full scale linearity and instrument uncertainty shown in Figure B.1.

CALIBRATION CERTIFICATE

Model: 113B21
Serial #: LW35042

Description: Pressure Sensor
Type: ICP

Sensitivity*: 24.27 mV/PSI
 3.519 mV/kPa

Linearity*: 0.1% FS
Uncertainty:** +/- 1 %

Bias: 10.2 VDC

* Zero based, least-squares straight line.

** Measurement uncertainty represented using a coverage factor of k=2 which provides a level of confidence of approximately 95 %.

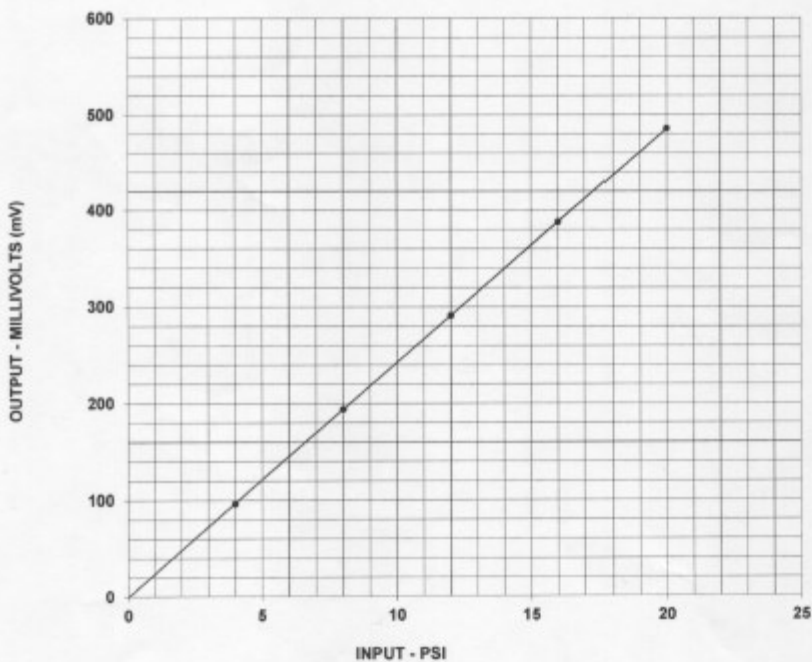
Date: 10/9/2017
By: Brad Swanson, Cal. Tech.
Station: 903 Pulse #2 (Test procedure AT601-6)

Temp: 71 deg F [22deg C]
Humidity: 64 %

Cert #: 673862

Condition of Unit:

As Found: Not applicable
As Left: In tolerance, new unit



TEST DATA

INPUT (PSI)	OUTPUT (mV)
4.00	96.6
8.00	194.0
12.0	291.1
16.0	388.0
20.0	485.7

Notes:

- 1 STATION #16
- 2 Calibration is traceable to NIST and is accredited to ISO 17025 and ANSI/NCSL Z540.3.
- 3 NIST traceability through PCB control # ME127.
- 4 This certificate may not be reproduced, except in full, without written approval from PCB Piezotronics, Inc.



CALIBRATION CERT #1862.01



Tel: 716-664-0001 Fax: 716-664-0987 Email: sales@pcb.com
 3425 Walden Avenue, Depew NY 14043

ISO 9001 CERTIFIED

Figure B.1 – Calibration certificate for piezoelectric pressure sensor 113B21 (SN: LW35042)

B.5 Diaphragm Pressure Transducer

This section details the diaphragm pressure transducer measurement device and includes details regarding the instrument specifications, uncertainties, and calibration.

Table B-10 – Diaphragm pressure transducer and DAQ specifications

Device Model	Mfg.	Range	Mode
DP15 3-36 diaphragm plate	Validyne Engineering	34.5kPag (5psig)	Instantaneous
CD280-8 carrier demodulator	Validyne Engineering	8 channels	Instantaneous
NI-USB-6211	National Instruments Corp.	8 differential channels	Instantaneous

Table B-11 – Diaphragm pressure transducer measurement uncertainties

Uncertainty Source	Instrument	Uncertainty Description	Uncertainty Type	Value	Notes
Meas. Inst.	DP15 3-36 plate	Specified Accuracy	Systematic & Random	± 0.173 kPa	Manufacturer Specified at $\pm 0.5\%$ FS (34.5 kPa \cdot 0.5%)
Inst. Calibration	Manometer Calibration	Calibration uncertainty	Systematic	± 0.009 kPa	Propagated uncertainty from monometer calibration trial
DAQ Signal demodulator	CD280-8	Linearity	Systematic	± 0.017 kPa	Manufacturer Specified $\pm 0.05\%$ FS (34.5 kPa \cdot 0.05%)
DAQ Signal demodulator	CD280-8	Temperature shift zero	Random	$\pm 0.018\%$	Manufacturer Specified $\pm 0.005\%$ per $^{\circ}$ F assume possible fluctuation of $\pm 2^{\circ}$ C or $\pm 3.6^{\circ}$ F
DAQ Signal demodulator	CD280-8	Temperature shift span	Random	$\pm 0.036\%$	Manufacturer Specified $\pm 0.01\%$ per $^{\circ}$ F assume possible fluctuation of $\pm 2^{\circ}$ C or $\pm 3.6^{\circ}$ F
I/O device	NI-USB-6211	AI Absolute Accuracy	Systematic	± 0.00928 kPa	NI-USB-6211 absolute accuracy at 10V full scale (0.002690V \cdot 34.5kPa / 10V) "

B.5.1 Calibration: 2019-10-16

To calibrate the DP15 with the 3-36 diaphragms a large scale manometer was built following recommendations from the instrument manufacturer [67]. This calibration and the processing thereof was done with great assistance from Jason Michaud. The manometer consisted of clear plastic tubing partially filled with distilled water. One end of the tube was fixed to the diaphragm pressure transducer port, and the other end of

the tube was open and the water had a free surface exposed to atmosphere. A U-bend in the tube was located prior to the pressure transducer with a pocket of air captured in the instrument to separate it from the water column. Raising and lowering the free end of the tube with the water column relative to the transducer subjected the transducer to the pressure from the raised water column. The calibration was performed in a room with a high ceiling allowing the column to be raised up to a height of 3.52m, corresponding to a water column pressure approximately equal to the maximum diaphragm pressure rating of 34.5kPa (5psi)

To calibrate the device the free end of the tube with the water column was raised and lowered in a series of height increments. At each height a tape measure was used to record the water column height, and the measurement voltage from the transducer was recorded by the DAQ at a 10kHz sample rate for 5 seconds. The pressures applied by the water column is described by the following equation:

$$P_{mano} = \rho gh \quad \text{B.3}$$

where: P_{mano} = pressure from the water column [Pa]
 ρ = density of water in column [kg/m³]
 g = gravity [m/s²]
 h = height of water column [m]

The calibration was performed at non-standard conditions so a correction needed to be applied to the measurements of the water column height. Relation B.4 describes the correction of column height, which can be substituted into B.3 with standard gravity and density [68].

$$h_s = \frac{\rho_l g_l h_l}{\rho_s g_s} \quad \text{B.4}$$

where: h_s = Corrected standard height [m]
 ρ_l = local density of water in column [kg/m³]
 g_l = local gravity [m/s²]
 h_l = local measured height of water column [m]
 ρ_s = standard density of water [kg/m³]
 g_s = standard gravity [m/s²]

The value of density was corrected using a local temperature measurement of the water column with an analogue thermometer (ERTCO 1005-3S). The water column was filled with room temperature water and assumed to be constant over the calibration. The corrected local density of the column at the measured temperature of 21.5°C was $\rho_l = 997.89$ [kg/m³] calculated from an equation described by Meriam Process Technologies [68]. The value of local gravity $g_l = 9.811586$ [m/s²] as reported by Natural Resources Canada from their Geodetic tools for Edmonton, Alberta [69].

Propagation of uncertainty for the calibration from equations B.3 and B.4 yields equations B.5 and B.6. The values used in the calibration equations are listed in Table B-12.

$$u_{h_s} = \left[\left(u_{h_l} \frac{\partial h_s}{\partial h_l} \right)^2 + \left(u_{\rho_l} \frac{\partial h_s}{\partial \rho_l} \right)^2 \right]^{\frac{1}{2}} \quad \text{B.5}$$

$$u_{P_{mano}} = \left[\left(u_{h_s} \frac{\partial u_{P_{mano}}}{\partial h_s} \right)^2 \right]^{\frac{1}{2}} \quad \text{B.6}$$

Table B-12 – Variable and uncertainty values for manometer calibration

Variable	Value	Uncertainty Variable	Uncertainty Value	Unit	Notes
ρ_l	997.86	u_{ρ_l}	± 0.22	[kg/m ³]	[68]
g_l	9.811586	u_{g_l}	Negligible	[m/s ²]	[69]
h_l	Variable	u_{h_l}	± 0.0005	[m]	Half smallest increment
ρ_s	1000	u_{ρ_s}	Negligible	[kg/m ³]	[68]
g_s	9.80665	u_{g_s}	Negligible	[m/s ²]	[68]
h_s	Variable	u_{h_s}	± 0.00093	[m]	Max value

B.6 Output Shaft and Crankshaft Rotary Position

This section details the rotary encoder measurement device and includes details regarding the instrument specifications, uncertainties, and calibration.

Table B-13 – Rotary encoder and DAQ specifications

Device Model	Mfg.	Range	Mode
15S-19M1-0500MV1ROC-F03-S1	Encoder Products Company	500 pulses/rev.	Instantaneous
NI-USB-6211	National Instruments Corp.	8 differential channels	Instantaneous

Table B-14 – Rotary encoder measurement uncertainties

Uncertainty Source	Instrument	Uncertainty Description	Uncertainty Type	Value	Notes
Meas. Inst.	15S-19M1-0500MV1ROC-F03-S1	Specified Accuracy	Systematic	$\pm 0.17^\circ$	Manufacturer Specified at $\pm 0.17^\circ$
Meas. Inst.	15S-19M1-0500MV1ROC-F03-S1	Mechanical Comm. Accuracy	Systematic	$\pm 1^\circ$	Manufacturer Specified at 1° mechanical
Gear backlash	Gear backlash calibration	Measured backlash of gears	Random	$\pm 0.914^\circ$	Measured from drive train calibration

B.6.1 Gear backlash calibration

To determine the drive train backlash impact on the position measurement of the displacer and piston crankshafts a calibration measurement was taken. The $e = 0$ round gears were installed for the displacer and piston. As all gears were manufactured and modeled by the same method it was assumed backlash for the $e = 0$ gear sets was sufficiently represented of all the gears. The output shaft was rotated to nominal positions of 90° and 270° (mid-stroke up and mid-stroke) for the displacer and piston and the rotation locks applied to the output shaft. At each position a mechanical dial indicator (model and manufacturer unknown) with a resolution of 0.001inch was then affixed to the drive mechanism frame the free movement of the piston crossheads was measured from the available free rotation of the crankshafts within the backlash

tolerance of the gears. Three measurements were take for each mid-stroke and are tabulated in

Table B-15 – Variable and uncertainty values of gear backlash calibration

Variable	Value	Uncertainty Variable	Uncertainty Value	Unit	Notes
$h_{disp\ 90^\circ}$	-	$u_{h_{disp\ 90^\circ}}$	± 0.974	[mm]	Average of 3 trials
$h_{disp\ 270^\circ}$	-	$u_{h_{disp\ 270^\circ}}$	± 0.809	[mm]	Average of 3 trials
-	-	$u_{h_{disp\ avg}}$	± 0.891	[mm]	Average displacer
$h_{pist\ 90^\circ}$	-	$u_{h_{pist\ 90^\circ}}$	± 0.809	[mm]	Average of 3 trials
$h_{pist\ 270^\circ}$	-	$u_{h_{pist\ 270^\circ}}$	± 0.673	[mm]	Average of 3 trials
-	-	$u_{h_{pist\ avg}}$	± 0.741	[mm]	Average displacer
θ_{disp}	Variable	$u_{\theta_{cranks}}$	± 0.914	[°]	Calculated from SOLIDWORKS
θ_{pist}	Variable	$u_{\theta_{cranks}}$	± 0.914	[°]	Calculated from SOLIDWORKS

The crosshead free rotation was applied into a SOLIDWORKS sketch that factored in the measured lengths of the connecting rods and the crankpin radiuses to convert the average crosshead movement into an angular uncertainty value for the gearing backlash. The connecting rod lengths and crank pin radiuses were never changed throughout the trials and any uncertainty in their lengths was assumed to be negligible.

B.7 Torque Transducer

This section details the torque measurement device and includes details regarding the instrument specifications, uncertainties, and calibration.

Table B-16 – Torque sensor specifications

Device Model	Mfg.	Range	Mode
TRS600 FSH01994	FUTEK Advanced Sensor Technology, Inc	1 Nm	Instantaneous
NI-USB-6211	National Instruments Corp.	8 differential channels	Instantaneous

Table B-17 – Torque sensor measurement uncertainties

Uncertainty Source	Instrument	Uncertainty Description	Uncertainty Type	Value	Notes
Meas. Inst.	TRS600 FSH01994	Non-linearity error	Systematic	± 0.00052 Nm	Maximum value from calibration data $\pm 0.052\%$ FS (1 Nm \cdot 0.052%)
Meas. Inst.	TRS600 FSH01994	Hysteresis	Systematic	± 0.001 Nm	Maximum value from calibration data $\pm 0.1\%$ FS (1 Nm \cdot 0.1%)
Meas. Inst.	TRS600 FSH01994	Non-repeatability	Systematic	± 0.002 Nm	Maximum value from calibration data $\pm 0.2\%$ FS (1 Nm \cdot 0.2%)
I/O device	NI-USB-6211	AI Absolute Accuracy	Systematic	± 0.00028 Nm	NI-USB-6211 absolute accuracy at 5V full scale (0.001410V \cdot 1Nm / 5V) "

B.7.1 Calibration Details

Calibration data for the torque sensor was provided by the instrument manufacturer. The calibration points were loaded into MATLAB and linear fit was applied to determine the calibration coefficients. The calibration coefficients were incorporated into the data

processing code for the trial data. The manufacturer calibration report is shown in Figure B.2.

Certificate Number: 1804130015

Single Channel Item

CALIBRATION DATA

Test Temp 70 °F (21 °C)

Relative Humidity 51 %

Excitation 20.01 Vdc

TorqueCW

Load (N-m)	Output (Vdc)	Non-Lin. Error (% R.O.)
0.0000	0.000	0.000
0.1412	0.703	-0.052
0.2825	1.410	-0.033
0.4237	2.116	-0.025
0.5649	2.821	-0.036
1.0010	5.002	0.000
0.0000	0.001	



TorqueCCW

Load (N-m)	Output (Vdc)	Non-Lin. Error (% R.O.)
0.0000	0.000	0.000
0.1412	-0.706	-0.006
0.2825	-1.411	-0.041
0.4237	-2.117	-0.047
0.5649	-2.824	-0.033
1.0010	-5.007	0.000
0.0000	-0.008	



Figure B.2 – Torque sensor calibration data

B.8 Atmospheric Pressure

This section details the diaphragm pressure transducer measurement device and includes details regarding the instrument specifications, uncertainties, and calibration. Of note, there is no published information regarding specifications and uncertainty of the SM-A520W's pressure sensor.

Table B-18 – Atmospheric pressure sensor specifications

Device Model	Mfg.	Range	Mode
SM-A520W	Samsung	Unknown	Trial average

Table B-19 – Atmospheric pressure sensor measurement uncertainties

Uncertainty Source	Instrument	Uncertainty Description	Uncertainty Type	Value	Notes
Inst. Calibration	Mercury barometer	Calibration via barometer	Systematic	±0.08 kPa	Mercury barometer calibration uncertainty

B.8.1 Calibration: 2020-08-17

To calibrate the readings from SM-A520W the pressure reading from the device was compared to a mercury barometer. The mercury barometer included calibration instructions, shown in Figure B.3, which corrected the observed reading for gravity and temperature via a series of calibration tables. The calibration factors are applied to the column height via the following equation.

$$P_{baro} = h_l + h_{cor\ g} + h_{cor\ T} \quad B.7$$

where: P_{baro} = atmospheric pressure [mmHg]
 h_l = mercury column height [mmHg]
 $h_{cor\ g}$ = gravity correction factor [mmHg]
 $h_{cor\ T}$ = temperature correction factor [mmHg]

The column height was measured using a Vernier scale rule with a resolution of 0.1mm and an uncertainty of ±0.05mm. The correction factor for gravity is based on latitude corresponding to a lookup table shown in Figure B.4. The latitude of the lab is

53.5° with negligible uncertainty effects on the correction factor. The correction factor for temperature based on the temperature of the mercury in the column. An analogue thermometer with a resolution of 1 °C and an uncertainty of ± 0.5 °C fixed to the barometer provided the temperature measurement necessary for the correction. Figure B.5 shows the temperature correction factor table used. The corrected atmospheric pressure of the mercury barometer was converted to kPa using standard unit conversion values and the $P_{baro} = 93.64\text{kPa}$. The SM-A520W's pressure sensor read $P_{atm} = 93.43$ and so a correction factor of +0.21kPa was applied to the measurements.

Propagation of uncertainty for the calibration from equation A.4 yields the calibration uncertainty equation B.8. The values used in the calibration equations are listed in Table B-20

$$u_{P_{baro}} = \left[(u_{h_l})^2 + (u_{h_{corT}})^2 \right]^{\frac{1}{2}} \quad \text{B.8}$$

Table B-20 – Variable and uncertainty values for manometer calibration calculation

Variable	Value	Uncertainty Variable	Uncertainty Value	Unit	Notes
h_l	704.50	u_{h_l}	± 0.05	[mmHg]	Convert o kPa with standard ratio
$h_{cor g}$	0.412	-	-	Negligible	Gravity correction changes minimally for small changes in latitude
$h_{cor T}$	-2.53	$u_{h_{cor T}}$	± 0.06	[mmHg]	±0.5 °C uncertainty converted to mmHg with tables

READING THE BAROMETER

Before reading the barometer be sure it is mounted securely in a vertical position. The reliable readings are obtained when the temperature has not changed greatly over the past hours. When reading the barometer the reader's eye should be in the same horizontal plane as the top of the mercury meniscus and the lower edge of the vernier plate. This position can be checked by getting the eye in line with the bottom of the vernier plate and the bottom of the metal guide in front of the mercury column directly in back of the vernier plate.

Readjustment to zero should be made whenever necessary in reading the barometer; i.e. the adjusting screw at the bottom of the reservoir casing should be manipulated until the surface of the mercury exactly coincides with the tip of the ivory zero point which is visible inside the reservoir.

The height of the meniscus will be greater for a rising mercury column than for a falling column. In order to bring the meniscus to its approximate, average height, tap the barometer lightly with your fingers before taking a reading.

The reading then observed should be corrected by use of the correction tables. For explanation of the tables, refer to the following section.

COMPARISON WITH REPORTED BAROMETRIC PRESSURE

The weather services always report barometric pressure adjusted to sea level. When reconciling your barometer with reported sea level barometric pressure, allowance must be made for the substantial decrease of pressure from sea level to your elevation (approximately 0.027 millimetres or 0.001 inches per foot of elevation). Your barometer reads more accurately than the pressure that can be obtained by this method. The scales of your barometer were adjusted at the factory for the life of the instrument and should not be tampered with.

Figure B.3 – Mercury barometer measurement instructions

Table 3. GRAVITY CORRECTION

To reduce the reading of the barometer to standard gravity

Latitude N or S	Height of the mercury column														
	Inches					Millimetres					Millibars				
	26	27	28	29	30	680	700	720	740	760	780	900	950	1000	1050
	LATITUDE 0° TO 45° THE CORRECTION IS TO BE SUBTRACTED														
	LATITUDE 46° TO 90° THE CORRECTION IS TO BE ADDED														
90°	+0.67	+0.70	+0.73	+0.75	+0.78	+1.76	+1.82	+1.87	+1.92	+1.97	+2.02	+2.33	+2.46	+2.59	+2.72
88	.067	.070	.072	.075	.078	1.76	1.81	1.86	1.91	1.97	2.02	2.33	2.46	2.59	2.72
86	.067	.069	.072	.074	.077	1.75	1.80	1.85	1.90	1.95	2.00	2.31	2.44	2.57	2.70
84	.066	.068	.071	.074	.076	1.72	1.77	1.83	1.88	1.93	1.98	2.28	2.41	2.54	2.66
82	.065	.067	.070	.072	.075	1.69	1.74	1.79	1.84	1.89	1.94	2.24	2.37	2.49	2.62
80	+0.63	+0.66	+0.68	+0.71	+0.73	+1.65	+1.70	+1.75	+1.80	+1.85	+1.90	+2.19	+2.31	+2.43	+2.56
78	.061	.064	.066	.069	.071	1.61	1.65	1.70	1.75	1.80	1.84	2.13	2.25	2.36	2.48
76	.059	.062	.064	.066	.068	1.55	1.60	1.64	1.69	1.74	1.78	2.05	2.17	2.28	2.40
74	.057	.059	.061	.064	.066	1.49	1.53	1.58	1.62	1.66	1.71	1.97	2.08	2.19	2.30
72	.054	.056	.058	.061	.063	1.42	1.46	1.50	1.54	1.59	1.63	1.88	1.98	2.09	2.19
70	+0.51	+0.53	+0.55	+0.57	+0.59	+1.34	+1.38	+1.42	+1.46	+1.50	+1.54	+1.78	+1.87	+1.97	+2.07
68	.048	.050	.052	.054	.056	1.26	1.30	1.33	1.37	1.41	1.44	1.67	1.76	1.85	1.94
66	.045	.046	.048	.050	.052	1.17	1.20	1.24	1.27	1.31	1.34	1.55	1.63	1.72	1.80
64	.041	.043	.044	.046	.047	1.07	1.10	1.13	1.17	1.20	1.23	1.42	1.50	1.58	1.65
62	.037	.039	.040	.041	.043	0.97	1.00	1.03	1.06	1.08	1.11	1.28	1.36	1.43	1.50
60	+0.33	+0.34	+0.36	+0.37	+0.38	+0.86	+0.89	+0.91	+0.94	+0.97	+0.99	+1.14	+1.21	+1.27	+1.33
58	.029	.030	.031	.032	.033	0.75	0.78	0.80	0.82	0.84	0.86	1.00	1.05	1.11	1.16
56	.024	.025	.026	.027	.028	0.64	0.66	0.68	0.69	0.71	0.73	0.84	0.89	0.94	0.99
54	.020	.021	.021	.022	.023	0.52	0.54	0.55	0.57	0.58	0.60	0.69	0.73	0.77	0.80
52	.015	.016	.016	.017	.018	0.40	0.41	0.42	0.44	0.45	0.46	0.53	0.56	0.59	0.62
50	+0.11	+0.11	+0.11	+0.12	+0.12	+0.28	+0.29	+0.29	+0.30	+0.31	+0.32	+0.37	+0.39	+0.41	+0.43
48	.006	.006	.006	.007	.007	0.15	0.16	0.16	0.17	0.17	0.18	0.20	0.21	0.23	0.24
46	+0.01	+0.01	+0.01	+0.01	+0.01	+0.03	+0.03	+0.03	+0.03	+0.03	+0.03	+0.04	+0.04	+0.04	+0.04
45	-.001	-.001	-.001	-.001	-.001	-0.03	-0.03	-0.04	-0.04	-0.04	-0.04	-0.04	-0.05	-0.05	-0.05
44	.004	.004	.004	.004	.004	0.10	0.10	0.10	0.11	0.11	0.11	0.13	0.13	0.14	0.15
42	.008	.009	.009	.009	.010	0.22	0.23	0.23	0.24	0.25	0.25	0.29	0.31	0.33	0.34
40	-.013	-.014	-.014	-.015	-.015	-0.35	-0.36	-0.37	-0.38	-0.39	-0.40	-0.46	-0.48	-0.51	-0.53
38	.018	.019	.019	.020	.021	0.47	0.48	0.50	0.51	0.52	0.54	0.62	0.65	0.69	0.72
36	.022	.023	.024	.025	.026	0.59	0.61	0.62	0.64	0.66	0.67	0.78	0.82	0.86	0.91
34	.027	.028	.029	.030	.031	0.71	0.73	0.75	0.77	0.79	0.81	0.93	0.99	1.04	1.09
32	.031	.033	.034	.035	.036	0.82	0.84	0.87	0.89	0.92	0.94	1.08	1.14	1.20	1.27
30	-.036	-.037	-.038	-.040	-.041	-0.93	-0.96	-0.98	-1.01	-1.04	-1.07	-1.23	-1.30	-1.37	-1.44
28	.040	.041	.043	.044	.046	-1.04	1.07	1.10	1.13	1.16	1.19	1.37	1.45	1.52	1.60
26	.043	.045	.047	.048	.050	1.14	1.17	1.20	1.24	1.27	1.30	1.50	1.59	1.67	1.75
24	.047	.049	.051	.053	.054	1.23	1.27	1.30	1.34	1.38	1.41	1.63	1.72	1.81	1.90
22	.051	.052	.054	.056	.058	1.32	1.36	1.40	1.44	1.48	1.52	1.75	1.85	1.94	2.04
20	-.054	-.056	-.058	-.060	-.062	-1.41	-1.45	-1.49	-1.53	-1.57	-1.61	-1.86	-1.96	-2.07	-2.17
18	.057	.059	.061	.063	.065	1.48	1.53	1.57	1.61	1.66	1.70	1.96	2.07	2.18	2.29
16	.059	.062	.064	.066	.068	1.55	1.60	1.64	1.69	1.73	1.78	2.05	2.17	2.28	2.40
14	.062	.064	.066	.069	.071	1.61	1.66	1.71	1.76	1.80	1.85	2.14	2.26	2.37	2.49
12	.064	.066	.069	.071	.074	1.67	1.72	1.77	1.82	1.87	1.91	2.21	2.33	2.45	2.58
10	-.066	-.068	-.071	-.073	-.076	-1.72	-1.77	-1.82	-1.87	-1.92	-1.97	-2.27	-2.40	-2.52	-2.65
8	.067	.070	.072	.075	.077	1.75	1.81	1.86	1.91	1.96	2.01	2.32	2.45	2.58	2.71
6	.068	.071	.073	.076	.079	1.78	1.84	1.89	1.94	1.99	2.05	2.36	2.49	2.62	2.76
4	.069	.072	.074	.077	.080	1.81	1.86	1.91	1.97	2.02	2.07	2.39	2.52	2.66	2.79
2	.070	.072	.075	.078	.080	1.82	1.87	1.93	1.98	2.03	2.09	2.41	2.54	2.67	2.81
0	-.070	-.072	-.075	-.078	-.080	-1.82	-1.88	-1.93	-1.98	-2.04	-2.09	-2.41	-2.55	-2.68	-2.82

Tables 1 thru 3 are condensed from the "Smithsonian Meteorological Tables", Sixth Revised Edition 1949, Fifth Reprint 1971; and are corrected for consistency with the recommendations contained in the "International Meteorological Tables", World Meteorological Organization, 1966, with amendments thru July 1973.

Figure B.4 – Temperature correction factors for the mercury barometer

Table 2. TEMPERATURE CORRECTION, Metric Units

To reduce the reading of the barometer to standard temperature

Temperature C	Observed Reading of the Barometer in Millimetres or Millibars												
	540	560	580	600	620	640	660	680	700	720	740	760	780
	ALL CORRECTIONS SUBTRACTIVE												
0	0.00	0.00	0.00	0.00	0.00	0.00	0.00	0.00	0.00	0.00	0.00	0.00	0.00
1	.09	.09	.09	.10	.10	.10	.11	.11	.11	.12	.12	.12	0.00
2	.18	.18	.19	.20	.20	.21	.22	.22	.23	.24	.24	.25	.13
3	.26	.27	.28	.29	.30	.31	.32	.33	.34	.35	.36	.37	.25
4	.35	.37	.38	.39	.40	.42	.43	.44	.46	.47	.48	.50	.38
5	0.44	0.46	0.47	0.49	0.51	0.52	0.54	0.56	0.57	0.59	0.60	0.62	0.51
6	.53	.55	.57	.59	.61	.63	.65	.67	.69	.71	.72	.74	.64
7	.62	.64	.66	.69	.71	.73	.75	.78	.80	.82	.85	.87	.76
8	.70	.73	.76	.78	.81	.84	.86	.89	.91	.94	.97	.99	.89
9	.79	.82	.85	.88	.91	.94	.97	1.00	1.03	1.06	1.09	1.12	1.02
10	0.88	0.91	0.95	0.98	1.01	1.04	1.08	1.11	1.14	1.17	1.21	1.24	1.15
11	.97	1.00	1.04	1.08	1.11	1.15	1.18	1.22	1.26	1.29	1.33	1.36	1.27
12	1.06	1.10	1.13	1.17	1.21	1.25	1.29	1.33	1.37	1.41	1.45	1.49	1.40
13	1.14	1.19	1.23	1.27	1.31	1.36	1.40	1.44	1.48	1.53	1.57	1.61	1.53
14	1.23	1.28	1.32	1.37	1.41	1.46	1.51	1.55	1.60	1.64	1.69	1.73	1.65
15	1.32	1.37	1.42	1.47	1.52	1.56	1.61	1.66	1.71	1.76	1.81	1.86	1.78
16	1.41	1.46	1.51	1.56	1.62	1.67	1.72	1.77	1.82	1.88	1.93	1.98	1.91
17	1.50	1.55	1.61	1.66	1.72	1.77	1.83	1.88	1.94	1.99	2.05	2.10	2.03
18	1.58	1.64	1.70	1.76	1.82	1.88	1.93	1.99	2.05	2.11	2.17	2.23	2.16
19	1.67	1.73	1.79	1.86	1.92	1.98	2.04	2.10	2.17	2.23	2.29	2.35	2.29
20	1.76	1.82	1.89	1.95	2.02	2.08	2.15	2.21	2.28	2.34	2.41	2.47	2.41
21	1.85	1.91	1.98	2.05	2.12	2.19	2.26	2.32	2.39	2.46	2.53	2.60	2.54
22	1.93	2.01	2.08	2.15	2.22	2.29	2.36	2.43	2.51	2.58	2.65	2.72	2.67
23	2.02	2.10	2.17	2.25	2.32	2.40	2.47	2.54	2.62	2.69	2.77	2.84	2.79
24	2.11	2.19	2.26	2.34	2.42	2.50	2.58	2.66	2.73	2.81	2.89	2.97	2.92
25	2.20	2.28	2.36	2.44	2.52	2.60	2.68	2.77	2.85	2.93	3.01	3.09	3.04
26	2.28	2.37	2.45	2.54	2.62	2.71	2.79	2.88	2.96	3.04	3.13	3.21	3.16
27	2.37	2.46	2.55	2.63	2.72	2.81	2.90	2.99	3.07	3.16	3.25	3.34	3.29
28	2.46	2.55	2.64	2.73	2.82	2.91	3.00	3.10	3.19	3.28	3.37	3.46	3.41
29	2.55	2.64	2.73	2.83	2.92	3.02	3.11	3.21	3.30	3.39	3.49	3.58	3.53
30	2.63	2.73	2.83	2.93	3.02	3.12	3.22	3.32	3.41	3.51	3.61	3.71	3.66
31	2.72	2.82	2.92	3.02	3.12	3.22	3.32	3.43	3.53	3.63	3.73	3.83	3.78
32	2.81	2.91	3.02	3.12	3.22	3.33	3.43	3.54	3.64	3.74	3.85	3.95	3.90
33	2.89	3.00	3.11	3.22	3.32	3.43	3.54	3.64	3.75	3.86	3.97	4.07	4.02
34	2.98	3.09	3.20	3.31	3.42	3.53	3.64	3.75	3.87	3.98	4.09	4.20	4.15

Figure B.5 – Gravitational correction factors for the mercury barometer

C UNCERTAINTIES OF CALCULATED VARIABLES

This Appendix details the propagation of uncertainty for calculated variable of the data processing.

C.1 Engine Speed

The average angular velocity of the engine output shaft was determined via the following approach:

$$\omega = \frac{n_{cycles} \cdot 2\pi}{\Delta t} = \frac{n_{cycles} \cdot 2\pi}{(t_{zn} - t_{z1})} \quad C.1$$

where: $\omega =$ Shaft angular velocity [rad/s]
 $n_{cycles} =$ Count of complete engine cycles per data set
 $\Delta t =$ duration of the data cropped set from beginning cycle to end cycle $(t_{zn} - t_{z1})$ [s]

The number of engine cycles was Z-pulses captured in a data set after the data set propping procedure of the captured data sets. The uncertainty for this count in the number of pulses stems from the systematic uncertainty of the rotary encoder measurement of the first and last Z-pulses as described by the following where n is the final encoder position as captured by the cropped data set.

$$u_{n_{cycles}} = \left((u_{\theta,n})^2 + (u_{\theta,1})^2 \right)^{\frac{1}{2}} \quad C.2$$

The uncertainty in time is straightforwardly the propagation of the subtraction of the first time stamp of angular position 1 and time stamp of angular position n in the cropped data set.

$$u_{\Delta t} = \left((u_{t,n})^2 + (u_{t,1})^2 \right)^{\frac{1}{2}} \quad C.3$$

With the intermediary uncertainties determined propagating uncertainty through the quotient of equation C.1 yields:

$$u_{\omega} = \omega \left(\left(\frac{u_{n_{cycles}}}{n_{cycles}} \right)^2 + \left(\frac{u_{\Delta t}}{\Delta t} \right)^2 \right)^{\frac{1}{2}} \quad C.4$$

C.2 Shaft work and Shaft Power

Shaft work was calculated from the measurement of output shaft torque via the following equation:

$$W_s = \tau_s \cdot 2\pi \quad \text{C.5}$$

where: $W_s =$ Shaft work [J]
 $\tau_s =$ Torque of output shaft [Nm]

The propagation of uncertainty is simply a conversion of the uncertainty in torque.

$$u_{W_s} = u_{\tau_s} \cdot 2\pi \quad \text{C.6}$$

Engine shaft power was calculated as the product of the output shaft torque and the engine speed as defined by the following:

$$p_s = \tau_s \cdot \omega \quad \text{C.7}$$

where: $p_s =$ Shaft power [W]
 $\tau_s =$ Torque of shaft [Nm]
 $\omega =$ Angular frequency [rads/s]

The error propagation for shaft power is an application of the multiplicative case propagation and results in the following:

$$u_{p_s} = p_s \left(\left(\frac{u_{\tau_s}}{\tau_s} \right)^2 + \left(\frac{u_{\omega}}{\omega} \right)^2 \right)^{\frac{1}{2}} \quad \text{C.8}$$

C.3 Indicated work

Indicated works was calculated using a trapezoidal approximation of the integral as described by:

$$W_x = \int_{V_{min}}^{V_{max}} P_{avg} \cdot dV_{avg} \cong \sum_{i=1}^{500} \left(P_{avg,i} \cdot \frac{(V_{avg,i+1} + V_{avg,i-1})}{2} \right) \quad C.9$$

where: W_x = Work of segment x [J]
 V_{max} = Maximum engine volume [m³]
 V_{min} = Minimum engine volume [m³]
 P_{avg} = Trial average gauge pressure [Pa]
 V_{avg} = Trial average volume [m³]
 i = Rotary encoder index

Propagation of uncertainty through the approximation yields

$$u_{W_i} = \left(\left(u_{P_{avg,i}} \frac{\partial W_i}{\partial P_{avg,i}} \right)^2 + \left(u_{dV_{avg,i}} \frac{\partial W_i}{\partial dV_{avg,i}} \right)^2 \right)^{\frac{1}{2}} \quad C.10$$

$$u_{W_i} = \left(\left(u_{P_{avg,i}} dV_{avg,i} \right)^2 + \left(u_{dV_{avg,i}} P_{avg,i} \right)^2 \right)^{\frac{1}{2}} \quad C.11$$

where: u_{W_i} = Uncertainty in engine work at position i [J]
 $u_{P_{avg,i}}$ = Uncertainty in engine pressure at position i [Pa]
 $u_{dV_{avg,i}}$ = Uncertainty in engine volume at position i [m³]
 $dV_{avg,i}$ = Change in volume from position $i - 1$ to $i + 1$ divided by 2 [m³]
 $P_{avg,i}$ = Engine gauge pressure at position i [Pa]

The vector of the work uncertainties is then averaged to determine the uncertainty of the calculated work segment for a trial.

$$u_{dV_{avg,i}} = \left(\left(u_{V_{avg,i+1}} \right)^2 + \left(u_{V_{avg,i-1}} \right)^2 \right)^{\frac{1}{2}} \quad C.12$$

C.4 Mechanism Effectiveness Uncertainty

Mechanism effectiveness is calculated using the quadratic equation in the data processing. Substituting the component elements into the equation allows for an easier interpretation of the partial derivative of the equation to be performed.

$$E = \frac{-c_2 + \sqrt{c_2^2 - 4c_1c_3}}{2c_1} \quad \text{C.13}$$

$$\begin{aligned} \text{where: } c_1 &= W_i + W_{FW} \\ c_2 &= -W_s \\ c_3 &= -W_{FW} \end{aligned}$$

The indicated work and forced work components are correlated as indicated work was calculated from the same data that calculated forced work. However as a worst case scenario the two elements will be treated as uncorrelated to simplify the error propagation and provide a conservative estimate of uncertainty. The uncertainty terms of the coefficients presented in the conventional form of the quadratic equation are thus:

$$u_{c_1} = \left((u_{W_i})^2 + (u_{W_{FW}})^2 \right)^{\frac{1}{2}} \quad \text{C.14}$$

$$u_{c_2} = u_{W_s} \quad \text{C.15}$$

$$u_{c_3} = u_{W_{FW}} \quad \text{C.16}$$

To propagate the partial derivative of equation C.13 with respect to the component coefficient must be determined. Formulation of the propagation of error through the quadratic equation was informed by the NIST/SEMATECH e-Handbook of Statistical Methods [65].

$$\frac{\partial E}{\partial c_1} = \frac{-c_3}{c_1 \sqrt{c_2^2 - 4c_1c_3}} - \frac{-c_2 + \sqrt{c_2^2 - 4c_1c_3}}{2c_1^2} \quad \text{C.17}$$

$$\frac{\partial E}{\partial c_2} = \frac{c_2 - \sqrt{c_2^2 - 4c_1c_3}}{2c_1 \sqrt{c_2^2 - 4c_1c_3}} \quad \text{C.18}$$

$$\frac{\partial E}{\partial c_3} = \frac{-1}{\sqrt{c_2^2 - 4c_1c_3}} \quad \text{C.19}$$

With the partial derivatives calculated the propagation of error equation becomes:

$$u_E = \left(\left(u_{c_1} \frac{\partial E}{\partial c_1} \right)^2 + \left(u_{c_2} \frac{\partial E}{\partial c_2} \right)^2 + \left(u_{c_3} \frac{\partial E}{\partial c_3} \right)^2 \right)^{\frac{1}{2}} \quad \text{C.20}$$

Table C-1 – Variable and uncertainty elements for mechanism effectiveness calculation

Variable	Value	Uncertainty Variable	Uncertainty Value	Unit	Notes
E	Calculated Variable	u_E	Calculated Variable	-	
$c_1 = W_i + W_{FW}$	Variable per trial	u_{c_1}	Variable per trial	[J]	
$c_2 = -W_s$	Variable per trial	$u_{c_2} = u_{w_s}$	Variable per trial	[J]	
$c_3 = -W_{FW}$	Variable per trial	$u_{c_3} = u_{w_{FW}}$	Variable per trial	[J]	

C.5 Heat Transfer Rates

Heat transfer rates from the thermal fluid source and sink loops is calculated using a steady state heat transfer equation.

$$\dot{Q} = \dot{m} c_p \Delta T = \dot{m} c_p (T_{in} - T_{out}) \quad \text{C.21}$$

where: \dot{Q} = Heat transfer rate [J/s]
 \dot{m} = Mass flow rate of thermal fluid [kg/s]
 c_p = Specific heat capacity [J/kg·K]
 T_{in} = Temperature of fluid entering the engine exchanger [K]
 T_{out} = Temperature of fluid leaving the engine exchanger [K]

Carrying out the propagation of uncertainty

$$u_{\dot{Q}} = \left(\left(u_{\dot{m}} \frac{\partial \dot{Q}}{\partial \dot{m}} \right)^2 + \left(u_{\Delta T} \frac{\partial \dot{Q}}{\partial \Delta T} \right)^2 \right)^{\frac{1}{2}} \quad \text{C.22}$$

$$u_{\dot{Q}} = \left((u_{\dot{m}} c_p \Delta T)^2 + (u_{\Delta T} \dot{m} c_p)^2 \right)^{\frac{1}{2}} \quad \text{C.23}$$

where

$$u_{\Delta T} = \left((u_{T_{in}})^2 + (u_{T_{out}})^2 \right)^{\frac{1}{2}} \quad \text{C.24}$$

Table C-2 – Heat transfer variables and uncertainties

Variable	Value	Uncertainty Variable	Uncertainty Value	Unit	Notes
\dot{Q}	Calculated Variable	$u_{\dot{Q}}$	Calculated Variable	[J/s]	
\dot{m}_h	3.237×10^{-2}	$u_{\dot{m}_h}$	$\pm 1.9 \times 10^{-4}$	kg/s	See Appendix B.1
\dot{m}_c	2.914×10^{-2}	$u_{\dot{m}_c}$	$\pm 1.0 \times 10^{-4}$	kg/s	See Appendix B.1
c_{p_h}	4206	$u_{c_{p_h}}$	Negligible	[J/kg·K]	Taken from [66]
c_{p_c}	4205	$u_{c_{p_c}}$	Negligible	[J/kg·K]	Taken from [66]
$T_{h\ in}$	Variable per trial	$u_{T_{h\ in}}$	Variable per trial	[°C]	Converted to [K] for calculation
$T_{h\ out}$	Variable per trial	$u_{T_{h\ out}}$	Variable per trial	[°C]	Converted to [K] for calculation
$T_{c\ in}$	Variable per trial	$u_{T_{c\ in}}$	Variable per trial	[°C]	Converted to [K] for calculation
$T_{c\ out}$	Variable per trial	$u_{T_{c\ out}}$	Variable per trial	[°C]	Converted to [K] for calculation

C.6 Engine Efficiency and Global Losses Uncertainty

Engine efficiency is calculated via the following.

$$\eta_T = \frac{p_s}{\dot{Q}_{in}} \quad \text{C.25}$$

where: η_T = Thermal efficiency of the engine
 p_s = Shaft power out of the engine
 \dot{Q}_{in} = Thermal energy delivered to the engine

Propagating uncertainty through for quotient yields the following

$$u_{\eta_T} = \eta_T \left(\left(\frac{u_{p_s}}{p_s} \right)^2 + \left(\frac{u_{\dot{Q}_{in}}}{\dot{Q}_{in}} \right)^2 \right)^{\frac{1}{2}} \quad \text{C.26}$$

Table C-3 – Variable and uncertainty elements of engine efficiency calculation

Variable	Value	Uncertainty Variable	Uncertainty Value	Unit	Notes
η_T	Calculated Variable	u_{η_T}	Calculated Variable	-	
p_s	Variable per trial	u_{p_s}	Variable per trial	[W]	See Appendix C.2 for uncertainty
\dot{Q}_{in}	Variable per trial	$u_{\dot{Q}_{in}}$	Variable per trial	[J/s]	See Appendix C.5 for uncertainty

The determination of supplementary engine losses is calculated by:

$$\dot{Q}_{Lost} = \dot{Q}_{in} - p_s - \dot{Q}_{out} \quad \text{0.1}$$

where: \dot{Q}_{Lost} = Thermal efficiency of the engine
 \dot{Q}_{in} = Thermal energy delivered to the engine
 p_s = Shaft power out of the engine
 \dot{Q}_{out} = Thermal energy taken by the cold sink loop

Propagating uncertainty from the additive terms yield the following:

$$u_{\dot{Q}_{Lost}} = \left((u_{\dot{Q}_{in}})^2 + (u_{p_s})^2 + (u_{\dot{Q}_{out}})^2 \right)^{\frac{1}{2}} \quad \text{C.27}$$

Table C-4 – Variable and uncertainty elements of engine global loss calculation

Variable	Value	Uncertainty Variable	Uncertainty Value	Unit	Notes
\dot{Q}_{Lost}	Calculated Variable	$u_{\dot{Q}_{Lost}}$	Calculated Variable	-	
\dot{Q}_{in}	Variable per trial	$u_{\dot{Q}_{in}}$	Variable per trial	[J/s]	See Appendix C.5 for uncertainty
\dot{Q}_{out}	Variable per trial	$u_{\dot{Q}_{out}}$	Variable per trial	[J/s]	See Appendix C.5 for uncertainty
p_s	Variable per trial	u_{p_s}	Variable per trial	[W]	See Appendix C.2 for uncertainty

D DATA COLLECTION PLAN AND LOG

This Appendix presents a replication of the data collection plan and log. A modified version of the summary data collection plan and log is presented in Table D-1. The original plan and log was maintained in Microsoft Excel. Summaries of the individual test trials are shown in Table D-2 to Table D-24

Table D-1– Trials collection plan summary and log

Test Set	Displacer Gear set	Config.	Piston Gear Set	Date(s)	Trial 1	Trial 2	Trial 3
1	$e = 0$	Base.	$e = 0$	2020-11-10 (2020-11-12)	x	x	(x)
2	$e = 1/5$	Dwell	$e = 0$	2020-11-12 (2020-11-13)	x	(x)	N/A
3	$e = 1/5$	Saw	$e = 0$	2020-11-13 (2020-11-25)	x	(x)	N/A
4	$e = 1/5$	Saw	$e = 1/5$	2020-11-25	x	x	N/A
5	$e = 1/5$	Dwell	$e = 1/5$	2020-11-26	x	x	N/A
6	$e = 0$	Dwell	$e = 1/5$	2020-11-27	x	x	N/A
7	$e = 0$	Dwell	$e = 1/3$	2020-11-27	x	x	N/A
8	$e = 1/5$	Saw	$e = 1/3$	2020-11-30	x	x	N/A
9	$e = 1/3$	Dwell	$e = 1/3$	2020-12-01	x	x	N/A
10	$e = 1/3$	Dwell	$e = 0$	2020-12-01	x	x	N/A
11	$e = 0$	Base.	$e = 0$	2020-12-10	x	x	N/A

Table D-2– Displacer $e = 0$, piston $e = 0$, test 1, trial 1, 2020-11-10

Data Set	Trial High T [°C]	Trial low T [°C]	Load Code	Loads Units	Complete	Comment
1	90	5	000F	0	x	
2	90	5	000L	0	x	
3	90	5	071L	2	x	
4	90	5	142L	4	x	
5	90	5	213L	6	x	
6	90	5	284L	8	x	
7	90	5	355L	10	x	
8	90	5	426L	12	x	
9	90	5	497L	14	x	
10	90	5	568L	16	x	
11	90	5	639L	18	x	
12	90	5	568D	16	x	
13	90	5	497D	14	x	
14	90	5	426D	12	x	
15	90	5	355D	10	x	
16	90	5	284D	8	x	
17	90	5	213D	6	x	
18	90	5	142D	4	x	
19	90	5	071D	2	x	
20	90	5	000D	0	x	

Table D-3– Displacer $e = 0$, piston $e = 0$, test 1, trial 2, 2020-11-10

Data Set	Trial High T [°C]	Trial low T [°C]	Load Code	Loads Units	Complete	Comment
1	90	5	000F	0	x	
2	90	5	000L	0	x	
3	90	5	071L	2	x	
4	90	5	142L	4	x	
5	90	5	213L	6	x	
6	90	5	284L	8	x	
7	90	5	355L	10	x	
8	90	5	426L	12	x	
9	90	5	497L	14	x	
10	90	5	568L	16	x	
11	90	5	639L	18		Stalled out
12	90	5	568D	16	x	
13	90	5	497D	14	x	
14	90	5	426D	12	x	
15	90	5	355D	10	x	
16	90	5	284D	8	x	
17	90	5	213D	6	x	
18	90	5	142D	4	x	
19	90	5	071D	2	x	
20	90	5	000D	0	x	
21	90	5	000f	0	x	

Table D-4– Displacer $e = 0$, piston $e = 0$, test 1, trial 3, 2020-11-12

Data Set	Trial High T [°C]	Trial low T [°C]	Load Code	Loads Units	Complete	Comment
1	90	5	000F	0	x	
2	90	5	000L	0	x	
3	90	5	071L	2	x	
4	90	5	142L	4	x	
5	90	5	213L	6	x	
6	90	5	284L	8	x	
7	90	5	355L	10	x	
8	90	5	426L	12	x	
9	90	5	497L	14	x	
10	90	5	568L	16	x	
11	90	5	639L	18	x	
12	90	5	568D	16	x	
13	90	5	497D	14	x	
14	90	5	426D	12	x	
15	90	5	355D	10	x	
16	90	5	284D	8	x	
17	90	5	213D	6	x	
18	90	5	142D	4	x	
19	90	5	071D	2	x	
20	90	5	000D	0	x	
21	90	5	000f	0	x	

Table D-5– Displacer $e = 1/5$ dwell, piston $e = 0$, test 2, trial 1, 2020-11-12

Data Set	Trial High T [°C]	Trial low T [°C]	Load Code	Loads Units	Complete	Comment
1	90	5	000F	0	x	
2	90	5	000L	0	x	
3	90	5	071L	2	x	
4	90	5	142L	4	x	
5	90	5	213L	6	x	
6	90	5	284L	8	x	
7	90	5	355L	10	x	
8	90	5	426L	12	x	
9	90	5	497L	14	x	
10	90	5	568L	16	x	
11	90	5	639L	18	x	
12	90	5	568D	16	x	
13	90	5	497D	14	x	
14	90	5	426D	12	x	
15	90	5	355D	10	x	
16	90	5	284D	8	x	
17	90	5	213D	6	x	
18	90	5	142D	4	x	
19	90	5	071D	2	x	
20	90	5	000D	0	x	
21	90	5	000f	0	x	

Table D-6– Displacer $e = 1/5$ dwell, piston $e = 0$, test 2, trial 2, 2020-11-13

Data Set	Trial High T [°C]	Trial low T [°C]	Load Code	Loads Units	Complete	Comment
1	90	5	000F	0	x	
2	90	5	000L	0	x	
3	90	5	071L	2	x	
4	90	5	142L	4	x	
5	90	5	213L	6	x	
6	90	5	284L	8	x	
7	90	5	355L	10	x	
8	90	5	426L	12	x	
9	90	5	497L	14	x	
10	90	5	568L	16	x	
11	90	5	639L	18		stalled
12	90	5	568D	16	x	
13	90	5	497D	14	x	
14	90	5	426D	12	x	
15	90	5	355D	10	x	
16	90	5	284D	8	x	
17	90	5	213D	6	x	
18	90	5	142D	4	x	
19	90	5	071D	2	x	
20	90	5	000D	0	x	
21	90	5	000f	0	x	

Table D-7– Displacer $e = 1/5$ triangular, piston $e = 0$, test 3, trial 1, 2020-11-13

Data Set	Trial High T [°C]	Trial low T [°C]	Load Code	Loads Units	Complete	Comment
1	90	5	000F	0	x	
2	90	5	000L	0	x	
3	90	5	071L	2	x	
4	90	5	142L	4	x	
5	90	5	213L	6	x	
6	90	5	284L	8	x	
7	90	5	355L	10	x	
8	90	5	426L	12	x	
9	90	5	462L	15	x	
10	90	5	568L	16		stalled
11	90	5	639L	18		stalled
12	90	5	568D	16		stalled
13	90	5	462L	14	x	
14	90	5	426D	12	x	
15	90	5	355D	10	x	
16	90	5	284D	8	x	
17	90	5	213D	6	x	
18	90	5	142D	4	x	
19	90	5	071D	2	x	
20	90	5	000D	0	x	
21	90	5	000f	0	x	

Table D-8– Displacer $e = 1/5$ triangular, piston $e = 0$, test 3, trial 2, 2020-11-25

Data Set	Trial High T [°C]	Trial low T [°C]	Load Code	Loads Units	Complete	Comment
1	90	5	000F	0	x	
2	90	5	000L	0	x	
3	90	5	071L	2	x	
4	90	5	142L	4	x	
5	90	5	213L	6	x	
6	90	5	284L	8	x	
7	90	5	355L	10	x	
8	90	5	426L	12	x	
9	90	5	497L	15	x	
10	90	5	568L	16		Stalled
11	90	5	639L	18		Stalled
12	90	5	568D	16		Stalled
13	90	5	497D	14	x	
14	90	5	426D	12	x	
15	90	5	355D	10	x	
16	90	5	284D	8	x	
17	90	5	213D	6	x	
18	90	5	142D	4	x	
19	90	5	071D	2	x	
20	90	5	000D	0	x	
21	90	5	000f	0	x	

Table D-9– Displacer $e = 1/5$ triangular, piston $e = 1/5$ dwell, test 4, trial 1, 2020-11-25

Data Set	Trial High T [°C]	Trial low T [°C]	Load Code	Loads Units	Complete	Comment
1	90	5	000F	0	x	
2	90	5	000L	0	x	
3	90	5	071L	2	x	
4	90	5	142L	4	x	
5	90	5	213L	6	x	
6	90	5	284L	8	x	
7	90	5	355L	10	x	
8	90	5	426L	12	x	
9	90	5	497L	15	x	
10	90	5	568L	16	x	603.5
11	90	5	604L	18	x	
12	90	5	568D	16	x	
13	90	5	497D	14	x	
14	90	5	426D	12	x	
15	90	5	355D	10	x	
16	90	5	284D	8	x	
17	90	5	213D	6	x	
18	90	5	142D	4	x	
19	90	5	071D	2	x	
20	90	5	000D	0	x	
21	90	5	000f	0	x	

Table D-10– Displacer $e = 1/5$ triangular, piston $e = 1/5$ dwell, test 4, trial 2, 2020-11-25

Data Set	Trial High T [°C]	Trial low T [°C]	Load Code	Loads Units	Complete	Comment
1	90	5	000F	0	x	
2	90	5	000L	0	x	
3	90	5	071L	2	x	
4	90	5	142L	4	x	
5	90	5	213L	6	x	
6	90	5	284L	8	x	
7	90	5	355L	10	x	
8	90	5	426L	12	x	
9	90	5	497L	15	x	
10	90	5	568L	16	x	603.5
11	90	5	604L	18		stalled
12	90	5	568D	16	x	
13	90	5	497D	14	x	
14	90	5	426D	12	x	
15	90	5	355D	10	x	
16	90	5	284D	8	x	
17	90	5	213D	6	x	
18	90	5	142D	4	x	
19	90	5	071D	2	x	
20	90	5	000D	0	x	
21	90	5	000f	0	x	

Table D-11– Displacer $e = 1/5$ dwell, piston $e = 1/5$ dwell, test 5, trial 1, 2020-11-26

Data Set	Trial High T [°C]	Trial low T [°C]	Load Code	Loads Units	Complete	Comment
1	90	5	000F	0	x	
2	90	5	000L	0	x	
3	90	5	071L	2	x	
4	90	5	142L	4	x	
5	90	5	213L	6	x	
6	90	5	284L	8	x	
7	90	5	355L	10	x	
8	90	5	426L	12	x	
9	90	5	497L	15	x	
10	90	5	568L	16	x	
11	90	5	639L	18	x	
12	90	5	639D	18	x	
13	90	5	568D	16	x	
14	90	5	497D	14	x	
15	90	5	426D	12	x	
16	90	5	355D	10	x	
17	90	5	284D	8	x	
18	90	5	213D	6	x	
19	90	5	142D	4	x	
20	90	5	071D	2	x	
21	90	5	000D	0	x	
22	90	5	000f	0	x	

Table D-12– Displacer $e = 1/5$ dwell, piston $e = 1/5$ dwell, test 5, trial 2, 2020-11-26

Data Set	Trial High T [°C]	Trial low T [°C]	Load Code	Loads Units	Complete	Comment
1	90	5	000F	0	x	
2	90	5	000L	0	x	
3	90	5	071L	2	x	
4	90	5	142L	4	x	
5	90	5	213L	6	x	
6	90	5	284L	8	x	
7	90	5	355L	10	x	
8	90	5	426L	12	x	
9	90	5	497L	15	x	
10	90	5	568L	16	x	
11	90	5	639L	18	x	
12	90	5	639D	18	x	
13	90	5	568D	16	x	
14	90	5	497D	14	x	
15	90	5	426D	12	x	
16	90	5	355D	10	x	
17	90	5	284D	8	x	
18	90	5	213D	6	x	
19	90	5	142D	4	x	
20	90	5	071D	2	x	
21	90	5	000D	0	x	
22	90	5	000f	0	x	

Table D-13– Displacer $e = 0$ dwell, piston $e = 1/5$ dwell, test 6, trial 1, 2020-11-27

Data Set	Trial High T [°C]	Trial low T [°C]	Load Code	Loads Units	Complete	Comment
1	90	5	000F	0	x	noticed tear in bellow, will snoop observe after each trial
2	90	5	000L	0	x	
3	90	5	071L	2	x	
4	90	5	142L	4	x	
5	90	5	213L	6	x	
6	90	5	284L	8	x	
7	90	5	355L	10	x	
8	90	5	426L	12	x	
9	90	5	497L	15	x	
10	90	5	568L	16	x	
11	90	5	639L	18	x	
12	90	5	639D	18	x	
13	90	5	568D	16	x	
14	90	5	497D	14	x	
15	90	5	426D	12	x	
16	90	5	355D	10	x	
17	90	5	284D	8	x	
18	90	5	213D	6	x	
19	90	5	142D	4	x	
20	90	5	071D	2	x	
21	90	5	000D	0	x	
22	90	5	000f	0	x	

Table D-14– Displacer $e = 0$ dwell, piston $e = 1/5$ dwell, test 6, trial 2, 2020-11-27

Data Set	Trial High T [°C]	Trial low T [°C]	Load Code	Loads Units	Complete	Comment
1	90	5	000F	0	x	no leak
2	90	5	000L	0	x	
3	90	5	071L	2	x	
4	90	5	142L	4	x	
5	90	5	213L	6	x	
6	90	5	284L	8	x	
7	90	5	355L	10	x	
8	90	5	426L	12	x	
9	90	5	497L	15	x	
10	90	5	568L	16	x	
11	90	5	639L	18	x	
12	90	5	639D	18	x	
13	90	5	568D	16	x	
14	90	5	497D	14	x	
15	90	5	426D	12	x	
16	90	5	355D	10	x	
17	90	5	284D	8	x	
18	90	5	213D	6	x	
19	90	5	142D	4	x	
20	90	5	071D	2	x	
21	90	5	000D	0	x	
22	90	5	000f	0	x	

Table D-15– Displacer $e = 0$ dwell, piston $e = 1/3$ dwell, test 7, trial 1, 2020-11-27

Data Set	Trial High T [°C]	Trial low T [°C]	Load Code	Loads Units	Complete	Comment
1	90	5	000F	0	x	no leak
2	90	5	000L	0	x	
3	90	5	071L	2	x	
4	90	5	142L	4	x	
5	90	5	213L	6	x	
6	90	5	284L	8	x	
7	90	5	355L	10	x	
8	90	5	426L	12	x	
9	90	5	497L	15	x	
10	90	5	568L	16	x	
11	90	5	639L	18	x	stalled after trial
12	90	5	604D	17	x	Inspected for leaks and loose fasteners, non
13	90	5	568D	16	x	
14	90	5	497D	14	x	
15	90	5	426D	12	x	
16	90	5	355D	10	x	
17	90	5	284D	8	x	
18	90	5	213D	6	x	
19	90	5	142D	4	x	
20	90	5	071D	2	x	
21	90	5	000D	0	x	
22	90	5	000F	0	x	

Table D-16– Displacer $e = 0$ dwell, piston $e = 1/3$ dwell, test 7, trial 2, 2020-11-27

Data Set	Trial High T [°C]	Trial low T [°C]	Load Code	Loads Units	Complete	Comment
1	90	5	000F	0	x	no leaks found
2	90	5	000L	0	x	
3	90	5	071L	2	x	
4	90	5	142L	4	x	
5	90	5	213L	6	x	
6	90	5	284L	8	x	
7	90	5	355L	10	x	
8	90	5	426L	12	x	
9	90	5	497L	15	x	
10	90	5	568L	16	x	
11	90	5	604L	17	x	
12	90	5	604D	17		Inspected for leaks – none- stalled
13	90	5	568D	16	x	
14	90	5	497D	14	x	
15	90	5	426D	12	x	
16	90	5	355D	10	x	
17	90	5	284D	8	x	
18	90	5	213D	6	x	
19	90	5	142D	4	x	
20	90	5	071D	2	x	
21	90	5	000D	0	x	
22	90	5	000F	0	x	

Table D-17– Displacer $e = 1/5$ triangular, piston $e = 1/3$ dwell, test 8, trial 1, 2020-11-30

Data Set	Trial High T [°C]	Trial low T [°C]	Load Code	Loads Units	Complete	Comment
1	90	5	000F	0	x	No leak in bellow yet
2	90	5	000L	0	x	
3	90	5	071L	2	x	
4	90	5	142L	4	x	
5	90	5	213L	6	x	
6	90	5	284L	8	x	
7	90	5	355L	10	x	
8	90	5	426L	12	x	
9	90	5	497L	15	x	
10	90	5	568L	16	x	
11	90	5	639L	18		stalled, checked for leaks, none
12	90	5	639D	18		
13	90	5	533D	15	x	
14	90	5	497D	14	x	
15	90	5	426D	12	x	
16	90	5	355D	10	x	
17	90	5	284D	8	x	
18	90	5	213D	6	x	
19	90	5	142D	4	x	
20	90	5	071D	2	x	
21	90	5	000D	0	x	
22	90	5	000f	0	x	inspected bellow, no tear

Table D-18– Displacer $e = 1/5$ triangular, piston $e = 1/3$ dwell, test 8, trial 2, 2020-11-30

Data Set	Trial High T [°C]	Trial low T [°C]	Load Code	Loads Units	Complete	Comment
1	90	5	000F	0	x	No leak in bellow yet
2	90	5	000L	0	x	
3	90	5	071L	2	x	
4	90	5	142L	4	x	
5	90	5	213L	6	x	
6	90	5	284L	8	x	
7	90	5	355L	10	x	
8	90	5	426L	12	x	
9	90	5	497L	15	x	
10	90	5	568L	16	x	
11	90	5	639L	18		stalled, checked for leaks, none
12	90	5	639D	18		
13	90	5	568D	16	x	
14	90	5	497D	14	x	
15	90	5	426D	12	x	
16	90	5	355D	10	x	
17	90	5	284D	8	x	
18	90	5	213D	6	x	
19	90	5	142D	4	x	
20	90	5	071D	2	x	
21	90	5	000D	0	x	
22	90	5	000F	0	x	inspected bellow, no tear

Table D-19– Test 9, displacer $e = 1/3$ dwell, piston $e = 1/3$ dwell, trial 1, 2020-12-01

Data Set	Trial High T [°C]	Trial low T [°C]	Load Code	Loads Units	Complete	Comment
1	90	5	000F	0	x	Small leak in bellow. Detected leak in top of can, placed acrylic patches over and CA glued in place Replaced bellow with a broken in one Leak tested and aligned tested in morning
2	90	5	000L	0	x	
3	90	5	071L	2	x	
4	90	5	142L	4	x	
5	90	5	213L	6	x	
6	90	5	284L	8	x	
7	90	5	355L	10	x	
8	90	5	426L	12	x	
9	90	5	497L	14	x	
10	90	5	533L	15	x	stalled
11	90	5	639L	18		
12	90	5	639D	18		
13	90	5	533D	15	x	
14	90	5	497D	14	x	
15	90	5	426D	12	x	
16	90	5	355D	10	x	
17	90	5	284D	8	x	
18	90	5	213D	6	x	
19	90	5	142D	4	x	
20	90	5	071D	2	x	
21	90	5	000D	0	x	
22	90	5	000F	0	x	patched small leak in top plate

Table D-20– Test 9, displacer $e = 1/3$ dwell, piston $e = 1/3$ dwell, trial 2, 2020-12-01

Data Set	Trial High T [°C]	Trial low T [°C]	Load Code	Load Units	Complete	Comment
1	90	5	000F	0	x	Checked leak fixes and tdc
2	90	5	000L	0	x	
3	90	5	071L	2	x	fixed loose nut on gear
4	90	5	142L	4	x	
5	90	5	213L	6	x	
6	90	5	284L	8	x	
7	90	5	355L	10	x	
8	90	5	426L	12	x	
9	90	5	497L	14	x	
10	90	5	533L	15	x	
11	90	5	639L	18		
12	90	5	639D	18		
13	90	5	533D	15	x	
14	90	5	497D	14	x	
15	90	5	426D	12	x	
16	90	5	355D	10	x	
17	90	5	284D	8	x	
18	90	5	213D	6	x	
19	90	5	142D	4	x	
20	90	5	071D	2	x	
21	90	5	000D	0	x	
22	90	5	000F	0	x	

Table D-21– Test 10, displacer $e = 1/3$ dwell, piston $e = 0$, trial 1, 2020-12-01

Data Set	Trial High T [°C]	Trial low T [°C]	Load Code	Load Units	Complete	Comment
1	90	5	000F	0	x	Checked leak fixes and adjusted TDC, broke shank off PCB sensor adaptor, replaced adaptor with spare and re leak tested
2	90	5	000L	0	x	
3	90	5	071L	2	x	
4	90	5	142L	4	x	
5	90	5	213L	6	x	
6	90	5	284L	8	x	
7	90	5	355L	10	x	
8	90	5	426L	12	x	
9	90	5	497L	14	x	
10	90	5	568L	16	x	
11	90	5	639L	18	x	very slow, const. speed assumption invalid
12	90	5	639D	18	x	
13	90	5	568D	16	x	
14	90	5	497D	14	x	
15	90	5	426D	12	x	
16	90	5	355D	10	x	
17	90	5	284D	8	x	
18	90	5	213D	6	x	
19	90	5	142D	4	x	
20	90	5	071D	2	x	
21	90	5	000D	0	x	
22	90	5	000F	0	x	

Table D-22– Test 10, displacer $e = 1/3$ dwell, piston $e = 0$, trial 2, 2020-12-01

Data Set	Trial High T [°C]	Trial low T [°C]	Load Code	Load Units	Complete	Comment
1	90	5	000F	0	x	Checked leak fixes, adjusted TDC, checked drive train. All good
2	90	5	000L	0	x	
3	90	5	071L	2	x	
4	90	5	142L	4	x	
5	90	5	213L	6	x	
6	90	5	284L	8	x	
7	90	5	355L	10	x	
8	90	5	426L	12	x	
9	90	5	497L	14	x	
10	90	5	568L	16	x	
11	90	5	639L	18	x	very slow, const. speed assumption invalid
12	90	5	639D	18	x	
13	90	5	568D	16	x	
14	90	5	497D	14	x	
15	90	5	426D	12	x	
16	90	5	355D	10	x	
17	90	5	284D	8	x	
18	90	5	213D	6	x	
19	90	5	142D	4	x	
20	90	5	071D	2	x	
21	90	5	000D	0	x	
22	90	5	000F	0	x	

Table D-23– Test 11, displacer $e = 0$, piston $e = 0$, trial 1, 2020-12-10

Data Set	Trial High T [°C]	Trial low T [°C]	Load Code	Load Units	Complete	Comment
1	90	5	000F	0	x	
2	90	5	000L	0	x	
3	90	5	071L	2	x	
4	90	5	142L	4	x	
5	90	5	213L	6	x	
6	90	5	284L	8	x	
7	90	5	355L	10	x	
8	90	5	426L	12	x	
9	90	5	497L	14	x	
10	90	5	568L	16	x	
11	90	5	639L	18	x	
12	90	5	639D	18	x	
13	90	5	568D	16	x	
14	90	5	497D	14	x	
15	90	5	426D	12	x	
16	90	5	355D	10	x	
17	90	5	284D	8	x	
18	90	5	213D	6	x	
19	90	5	142D	4	x	
20	90	5	071D	2	x	
21	90	5	000D	0	x	
22	90	5	000F	0	x	

Table D-24– Test 11, displacer $e = 0$, piston $e = 0$, trial 2, 2020-12-10

Data Set	Trial High T [°C]	Trial low T [°C]	Load Code	Load Units	Complete	Comment
1	90	5	000F	0	x	checked for leaks (none), inspected drive train
2	90	5	000L	0	x	
3	90	5	071L	2	x	
4	90	5	142L	4	x	
5	90	5	213L	6	x	
6	90	5	284L	8	x	
7	90	5	355L	10	x	
8	90	5	426L	12	x	
9	90	5	497L	14	x	
10	90	5	568L	16	x	
11	90	5	639L	18	x	
12	90	5	639D	18	x	
13	90	5	568D	16	x	
14	90	5	497D	14	x	
15	90	5	426D	12	x	
16	90	5	355D	10	x	
17	90	5	284D	8	x	
18	90	5	213D	6	x	
19	90	5	142D	4	x	
20	90	5	071D	2	x	
21	90	5	000D	0	x	
22	90	5	000F	0	x	

E DATA PROCESSING CODE

This Appendix documents some of the various data processing codes used in this investigation. The code presented is to provide insight into the implementation of the modeling and data processing in the MATLAB environment. Certain data processing sub functions and the scripts used to consolidate trial data and plot results is not included.

E.1 Isothermal Model Script

The isothermal model was written as a function script to be integrated into other scripts. The script takes the following inputs as variable for the function: displacer gear eccentricity, piston gear eccentricity, expansion/heater space working fluid temperature, compression/cooler spacer working fluid temperature, cycle buffer pressure, and mechanism effectiveness. Other input parameters of the model are coded into the script. The script outputs vectors of the instantaneous total volume and gauge pressure of the modeled engine over a complete rotation. The engine also outputs a calculation of indicated work, forced work, and shaft work of the engine.

```
function [V_t,P_t,WI,WF,WS] = Isotherm(DP_Gear,PP_Gear,Th_gas,Tc_gas,Vsp,P_buff,E)

%% Thesis 2021 Isothermal model. Adapted from earlier scripts. Written 2021-08

% creates isothermal model data for loading and comparing with the
% experimental results

% Set Figure Config
% set(groot, 'defaultFigureUnits', 'centimeters', 'defaultFigurePosition', [0 0 15 10]);
% set(groot, 'DefaultAxesFontName','Arial','DefaultTextFontName','Arial')
% set(groot, 'DefaultAxesFontSize',11)
Font = 11;

%% Engine crank properties
% set nominal PP phasing relative to DP
PP_Phase = 0 ; %[rad] Phased by 90° ahead (+125 encoder ticks)
PP_Pattern = 1 ; % Set 1 for 90° offset to lobe (dwelling)
                % Set 2 for inline with lobes (sawtooth)

% DP phasing
% set the nominal DP phasing relative to main encoder shaft (Z pulse)
DP_Phase = pi/2 ; % [rad] DP BDC is set for encoder Z pulse

Theta = linspace(0,2*pi,500); % Main crank angle array [rad]
```

```

switch PP_Gear %determine the gear pair eccentricity of the power piston
    case 1
        e_PP = 0;
    case 2
        e_PP = 1/5;
    case 3
        e_PP = 1/3;
    case 4
        Theta_PP = zeros(1,500)*2*pi;
        Theta_PP(1:63) = (0);
        Theta_PP(64:188) = linspace(0,pi,125);
        Theta_PP(189:313) = pi;
        Theta_PP(314:438) = linspace(pi,2*pi,125);
        Theta_PP(439:500) = 2*pi;
    otherwise
        disp('PP Gear code invalid')
        pause ;
end

switch DP_Gear %determine the gear pair eccentricity of the displacer piston
    case 1
        e_DP = 0;
        DP_Pattern = 1;
        % Calculate the shaft positions
        [m21_PP,m21_DP,Theta_PP,Theta_DP] =
Ellipse_Trans_Func(Theta,e_PP,e_DP,PP_Phase,DP_Phase,PP_Pattern,DP_Pattern);

    case 2
        e_DP = 1/5;
        DP_Pattern = 1;
        % Calculate the shaft positions
        [m21_PP,m21_DP,Theta_PP,Theta_DP] =
Ellipse_Trans_Func(Theta,e_PP,e_DP,PP_Phase,DP_Phase,PP_Pattern,DP_Pattern);

    case 3
        e_DP = 1/3;
        DP_Pattern = 1;
        % Calculate the shaft positions

```

```

        [m21_PP,m21_DP,Theta_PP,Theta_DP] =
Ellipse_Trans_Func(Theta,e_PP,e_DP,PP_Phase,DP_Phase,PP_Pattern,DP_Pattern);

    case 4
        e_DP = 1/5;
        DP_Pattern = 2;
        % Calculate the shaft positions
        [m21_PP,m21_DP,Theta_PP,Theta_DP] =
Ellipse_Trans_Func(Theta,e_PP,e_DP,PP_Phase,DP_Phase,PP_Pattern,DP_Pattern);

    case 5
        Theta_DP = zeros(1,500)*2*pi;
        Theta_DP(1:62) = linspace(pi/2,pi,62);
        Theta_DP(63:187) = pi;
        Theta_DP(188:312) = linspace(pi,2*pi,125);
        Theta_DP(313:437) = 2*pi;
        Theta_DP(438:500) = linspace(2*pi,5*pi/2,63);

    otherwise
        disp('DP Gear code invalid')
        pause ;
end

%% Drive Mech details
r_d = 0.058; % disp crank radius [m]
r_p = 0.045; % pist crank radius [m]

L_d = 0.385; % disp con rod lenght [m]
L_p = 0.185; % pist con rod lenght [m]

% piston height with respect to BDC, theta(1) = TDC
[h_d] = Slider_Crank(Theta_DP,L_d,r_d) ;
[h_p] = Slider_Crank(Theta_PP,L_p,r_p) ;

%% Working Fluid and Temperature details
R = 287; % Specific gas constant of dry air [J/kg K]

```

```

% Temperatures of various components of the engine
Th_gas = Th_gas + 273.15; % Hot side gas temperature in [K].
Tc_gas = Tc_gas + 273.15; % Cold side gas temperature in [K].

tau = Th_gas/Tc_gas; % Temperature ratio
delta_T = Th_gas-Tc_gas; % Temperature difference
Tr = delta_T/log(tau); % Log mean temp of regenerator [K]

% P_buff = 92.5e3; % Engine fill pressure (atmo) [Pa]

%% Engine Volumes
% Displacer Volume
Dd = 0.250; % Displacer diameter in [m].
Sd = 0.116; % Displacer stroke in [m].
Vsd = (pi)*((Dd/2)^2)*(Sd); % Displacer swept volume in [m^3].

% Dead Volume Components (assumed proportions of in each)
Vh = 1.934743666/1000 ; % Heater Volume[m^3]
Vk = 1.374017796/1000 ; % Cooler Volume[m^3]
Vr = 0.110619989/1000 ; % Regenerator Volume[m^3]

%% Calculation of volumes
% DP volumes
disp_d = h_d/(2*r_d) ; % [%] ratio of full stroke from TDC
Ve_d = Vsd*disp_d; % [m^3] displacer expansion space volume
Vc_d = Vsd-Ve_d; % [m^3] displacer compression space volume

% PP volumes
disp_p = h_p/(2*r_p) ; % [%] ratio of full stroke from BDC
Ve_p = Vsp*disp_p; % [m^3]

%% Calculation of Engine Pressure
% calculation of engine pressure incorporates iteration to adjust mass of gas to match means cycle
% pressure to buffer pressure

P_mean_calc = P_buff;
P_mean_diff = 0.0001; % Define acceptable % difference in Pmean
diff = 1; % Arbitrary

```

```

% Initial guess of engine mass
M = (P_buff/R).*((mean(Ve_d)+Vh)/Th_gas + mean(Ve_p)/Th_gas + ...
    (mean(Vc_d)+Vk)/Tc_gas + Vr/Tr); % [kg]

% Loop to correct mass of fluid based on calculated mean pressure
while abs(diff) > P_mean_diff
% Initial guess of engine mass

% Ideal gas law Isothermal pressure calculation [Pa]
P = M*R./(Vk/Tc_gas + Vh/Th_gas + Vr/Tr + Vc_d/Tc_gas + Ve_d/Th_gas + Ve_p/Th_gas);

P_mean_calc = mean(P); %calculated mean cycle pressure [Pa]
diff = (P_mean_calc - P_buff)/P_buff;

M = M - M*diff; % Adjust mass by percent difference

end

P_g = P-P_buff; % guage pressure[Pa]

% Make output and vectors
V_t = (Ve_p + Ve_d + Vh + Vr + Vk + Vc_d)*1000; % [m^3]
P_t = P_g/1000 ; % [kPa]

%% Calculation of Indicated, Forced work, and efficatious work

%Indicated Work
WI = polyarea(V_t,P_t); % [J]

% Forced Work - Riemann Summ Midpoint
% create the volume differential [m^3]
Len = length(V_t);
dV = zeros(Len:1);
dV(1) = (V_t(2)-V_t(Len))/2;
dV(2:(Len-1))=(V_t(3:Len)-V_t(1:(Len-2)))/2;
dV(Len) = (V_t(1)-V_t(Len-1))/2;

% Calculation of forced work via deffinition (sign Dp ~= sign Dv)
Forced_Work = 0; % [J]

```



```

index_FW = 0; % index count of ticks making up each area
for i = 1:length(P_t)
    if sign(dV(i))~= sign(P_t(i))
        Forced_Work = Forced_Work + abs(P_t(i)*dV(i)); %[J]
        index_FW = index_FW + 1;
    end
end

% Calculation of efficacious work via deffinition (sign Dp == sign Dv)
Eff_Work = 0; % [J]

index_EffW = 0; % index count of ticks making up each area
for i = 1:length(P_t)
    if sign(dV(i))== sign(P_t(i))
        Eff_Work = Eff_Work + abs(P_t(i)*dV(i)); %[J]
        index_EffW = index_EffW + 1;
    end
end

WF = Forced_Work; %[J]
Weff = Eff_Work; %[J]
WI_2 = Weff-WF;

% estimate of shaft work using E assumption
WS = E*WI - ((1/E)-E)*WF ;

% Sub function that calculates the hight of a piston using the slider-crank equations
function [h] = Slider_Crank(theta,L,r)

    h = (r*cos(theta)+sqrt((L^2)-(r^2)*(sin(theta).^2)))-L+r ;

end

end

```

E.2 Oval Elliptical Gear Transmission and Derivative Function Script

This script is a sub function that is integrated into the data processing script and the isothermal modelling script to calculate the angular position of the displacer crankshaft and piston crankshaft based on inputs from the output shaft position. The sub function uses the kinematics of the oval non-circular gearing as described in section 2.2. The script takes as input: angular position vector of the output shaft, displacer gear eccentricity, piston gear eccentricity, phase of the displacer gear relative to output shaft, phase of the piston gear relative to output shaft (dwelling or triangular motion), displacer motion pattern (dwelling or triangular motion), and piston motion pattern (dwelling or triangular motion). The function outputs the derivative ratios of the displacer and piston crankshafts, as well the angular positions of the displacer and piston crankshafts.

```
function [m21_PP,m21_DP,Theta_PP,Theta_DP] =  
Ellipse_Trans_Func(Theta,e_PP,e_DP,PP_Phase,DP_Phase,PP_Pattern,DP_Pattern)  
% Elliptical Gear transfer function  
% Written by Michael Nicol-Seto 2020-05  
  
% Theory from Litvin, F.L, Noncircular Gears: Design and Generation, 2009  
% Ch. 4  
  
% For bi-lobed oval gear pair transmission function  
  
% Inputs:  
% Theta : Angular position of main shaft  
% e : eccentricity of the gear model  
% PP_Phase : Phase of PP crank relative to Theta  
% DP_Phase : Phase of DP crank relative to Theta  
% PP_Pattern : Determines the PP crank phase offset (dwell or saw)  
% DP_Pattern : Determines the DP crank phase offset (dwell or saw)  
  
% Outputs:  
% m21(theta_1) : derivative (angular velocity) function d(theta_2) / d(theta_1)
```

```

% Theta_PP : Angular position of the power piston crank arm
% Theta_DP : Angular position of the displacer piston crank arm

% Establish crank arm shifting
switch PP_Pattern
    case 1
        PP_Shift = (pi)/2 ; % Crank arm is 90° out of phase with gear lobe
    case 2
        PP_Shift = 0 ; % Crank arm is in line with the gear lobe
    otherwise
        disp('PP shift invalid')
        pause ;
end

switch DP_Pattern
    case 1
        DP_Shift = (pi)/2 ; % Crank arm is 90° out of phase with gear lobes
    case 2
        DP_Shift = 0 ; % Crank arm is in line with the gear lobe
    otherwise
        disp('DP shift invalid')
        pause ;
end

% Theta arrays
% PP_In = shiftVector(Theta,PP_Shift) + PP_Phase ;
PP_In = Theta + PP_Phase + PP_Shift ;
% DP_In = shiftVector(Theta,DP_Shift) + DP_Phase ;
DP_In = Theta + DP_Phase + DP_Shift;

% Ellipse properties
a = 1; % assume unit circle
p_PP = a*(1-(e_PP)^2);
p_DP = a*(1-(e_DP)^2);
% center to center distance
E_PP = a*(1+(1+(1^2-1)*(1-(e_PP)))^0.5);
E_DP = a*(1+(1+(1^2-1)*(1-(e_DP)))^0.5);

% Derivative (Speed Ratio) function (p.58)
m21_PP = (p_PP./(E_PP - p_PP - E_PP.*(e_PP).*cos(2.*PP_In))); %

```

```

m21_DP = (p_PP./(E_DP - p_DP - E_DP.*(e_DP).*cos(2.*DP_In))); %

% radius of gear (not needed)
%r_pinion= p./(1-e*cos(2.*theta));

% angular position function
Theta_PP = atanSmooth(((1+(e_PP))/(1-(e_PP)))*tan(PP_In)); % [rads]
Theta_DP = atanSmooth(((1+(e_DP))/(1-(e_DP)))*tan(DP_In)); % [rads]

% Adjust to zero at initial point (account for oddness in atan)
Theta_PP = Theta_PP - Theta_PP(1);
Theta_DP = Theta_DP - Theta_DP(1);

% Add phase and theta(1) so modified function starts at corect values
Theta_PP = Theta_PP + PP_Phase + Theta(1);
Theta_DP = Theta_DP + DP_Phase + Theta(1);

[...]

end

```

E.3 Data Processing Script

The data processing script processed the raw measurement *.log files for a data set and process them to create a *.mat structure of all measured variable values and calculated variable values of a data set. This includes calculated combined standard uncertainty intervals. Certain sub functions called by the script are not included in this Appendix as they are either administrative for managing files, discussed in sufficient details in section or appendices of the thesis to understand their implementation, or were not used in the final presentation of data for the thesis.

Special acknowledgements to the following members of team Stirling for contributing to parts of this data processing code: Connor Speer, Steven Middleton, Calynn Stumpf, David Miller, and Jason Michaud

```
%% Data Importing and Processing
%
% By Micahel Nicol-Seto
% 2019-09
%
% This code imports ,log data files form EP1-M experiments
% Creates a raw data structure

% Volt samples taken at 30kHz for 20s
% Thermocouple samples taken at 5kHz for 20s
% RTD samples taken at 0.1kHz for 20s

clear, clc, close all

%% Global Engine Properties
% adjust these based on trial parameters / engine set-up
% These values are used by the Ellipse_Trans_Func to calculate the angular
% postion of the half crank shafts

% Power Piston Phasing
% set nominal PP phasing relative to DP
PP_Phase = 0 ; %[rad] Phased by 90° ahead (+125 encoder ticks)
```

```

PP_Pattern = 1 ; % Set 1 for 90° offset to lobe (dwelling)
                % Set 2 for inline with lobes (sawtooth)

% DP phasing
% set the nominal DP phasing relative to main encoder shaft (Z pulse)
DP_Phase = pi/2 ; % [rad] DP BDC is set for encoder Z pulse

DP_Pattern = 1 ; % Set 1 for 90° offset to lobe (dwelling)
                % Set 2 for inline with lobe (sawtooth)

% Calibration regime
% Volume lookup calibrated to Z = PP TDC. Circshift must be applied to
% match if it TDC or BDC calibration

Vol_Lookup_Shift = 0 ;
Table_Shift_Case = 1;
% Table shift case uses the original (2) or aligned vol lookup table (1)

% Gain of signal conditioner set at 100x for trials after 2020-11-09,
% 2x for trials before 2020-11-09, FS = 5V
P_PCB_Gain = 100;

%% File Location and Names

%Current folder directory where .log files are
% (set current folder)
log_File_Loc = pwd;

% Collects log files from the current folder
log_Files_Info = dir(fullfile(log_File_Loc, '*.log'));

%% Create Waitbar and Display how many log files are found in the folder and ETA
% % Taken from Data_Import_and_Process.m by Calynn Stumpf
% str=num2str(length(log_Files_Info)) + " Data files files found" + newline + "Time remaining:
Calculating";
% str=splitlines(str);
% Waitbar=waitbar(0, 'Loading', 'Name','Loading Experimental Data');
% waitbar(0,Waitbar, str , 'Name','Loading Experimental Data');

```

```

% pause(3);
%
% %For loop preamble - Time remaning calculator
% trc=1;
%
% %Structure Index Value
% SIV=1;

%% Imports the all log files into matlab structures
% Largely taken from NDGDataSetProcessorFx.m by David Miller

% uses increments of 3 for the three .log files per sample

for File_Num = 1:3:length(log_Files_Info)

    % Generate generic file name to (corrects for sorting order)
    File_Name = erase(log_Files_Info(File_Num).name, '_RTD.log');
    File_Name = erase(File_Name, '_Temp.log');
    File_Name = erase(File_Name, '_Volt.log');

    % Creates individual file names to process of the group
    DATA.Vfilename = strcat(log_File_Loc, '\', File_Name, '_Volt.log'); % voltage file name
    DATA.Tfilename = strcat(log_File_Loc, '\', File_Name, '_Temp.log'); % thermocouple file name
    DATA.RTDfilename = strcat(log_File_Loc, '\', File_Name, '_RTD.log'); % RTD file name

    % Extract trial data from file name format:
    % 'MMDDYYYY_HHMMSS_000_00_0000_00000_XYZ_L.log'
    DATA.Date = str2double(File_Name(1:8));
    DATA.Time = str2double(File_Name(10:15));
    DATA.TH = str2double(File_Name(17:19));
    DATA.TC = str2double(File_Name(21:22));
    DATA.Load_Mass = str2double(File_Name(24:27));
    DATA.Atm_Pres = str2double(File_Name(29:33)); % [Pa]
    DATA.U_Atm_Pres = 0.080277252*1000; %[Pa]
    DATA.PP_Gear = str2double(File_Name(35));
    DATA.DP_Gear = str2double(File_Name(36));
    DATA.Crank_L = File_Name(37);
    DATA.LoadCond = File_Name(39);
    % Assign numeric code to loading condition
    switch DATA.LoadCond

```

```

    case 'F' % Free running case
        DATA.LoadCond_Num = 1;
    case 'L' % Loaded - Loading ramp up
        DATA.LoadCond_Num = 2;
    case 'D' % Driven - Down Loading ramp down
        DATA.LoadCond_Num = 3;
    case 'G' % Driven - Down Loading ramp down
        DATA.LoadCond_Num = 4;
    otherwise
        disp('Load Cond invalid')
        pause ;
end

% Import voltage data from file using Volt_Import.m
[DATA.V_Time,DATA.A,DATA.Z,DATA.TOR,DATA.P_Val,DATA.P_PCB] ...
= Volt_Import(DATA.Vfilename);
% VTime -> Time for voltage data [s] (Time0 at aquire start)
% A      -> Rotarty encoder A pulse [V] (500 PPR)
% Z      -> Rotarty encoder Z pulse [V] (1 PPR)
% TOR    -> Torque transducer output [V]
% P1     -> Validyne Body [V]
% P2     -> PCB Body [V]

% Import thermocouple data from file using Therm_Import.m
[DATA.T_Time,DATA.T0,DATA.T1] ...
= Therm_Import(DATA.Tfilename);
% TTime -> Time for thermocouple data [s] (Time0 at aquire start)
% T0    -> Expansion space gas temperature [deg. C]
% T1    -> HH-regen gas temperature [deg. C]

% Import RTD data from file using RTD_Import.m
[DATA.RTD_Time,DATA.RTD1,DATA.RTD2,DATA.RTD3,DATA.RTD4] ...
= RTD_Import(DATA.RTDfilename);
% RTDTime -> Time for RTD data [s] (Time0 at aquire start)
% RTD1    -> Cooler inlet water temperature [deg. C]
% RTD2    -> Cooler outlet water temperature [deg. C]
% RTD3    -> Power cylinder inlet water temperature [deg. C]
% RTD4    -> Power cylinder outlet water temperature [deg. C]

%     DATA.ENGINE_DATA = ENGINE_DATA;

```



```

% Save raw data structure as .mat file with same base name as log files
RAW_File_Name = strcat(File_Name, '_RAW');
evalc([matlab.lang.makeValidName(RAW_File_Name), ' = DATA']);
save(strcat(log_File_Loc, '/', RAW_File_Name, '.mat'));
clear(RAW_File_Name);

%% Atmospheric pressure correction - 2021-06-22
% applying the calibration correction factor
DATA.Atm_Pres_Corr = DATA.Atm_Pres + 211; % [Pa]

%% Establish Rotary Encoder Positions

% Calculate main crankshaft position
% Sufunction creates a linear vector of the crank angles and a vector
% of the voltage index of the unique encoder positions
[DATA.Theta, DATA.A_Unique] = Encoder_2_Angle_Spline(DATA.A, DATA.Z);

%% Average Voltage Data at Each Rotary Encoder Step

index = 1 ; %Temp value index
uniquecount = length(unique(DATA.A_Unique)); % total number of unique encoder steps
ticks = find(DATA.A_Unique, uniquecount); % finds voltage index of the unique encoder steps
init_tick = ticks(1); last_tick = ticks(end);
set_length = length(ticks)-2; %length of the averaged data set taking off the beginning and end point

Temp_Theta_Tick = zeros(set_length,1); % counted A pulse index
Temp_Theta = zeros(set_length,1); % Temporary crankshaft position [rad]
Temp_TOR = zeros(set_length,1); % Temporary torque [V]
Temp_P_Val = zeros(set_length,1); % Temporary validyne pressure [V]
Temp_P_PCB = zeros(set_length,1); % Temporary PCB pressure [V]
Temp_V_Time = zeros(set_length,1); % Temporary Voltage DAQ Time [s]
Temp_T0_Corr = zeros(set_length,1); % Temporary correlated T0 voltages [V]
Temp_T1_Corr = zeros(set_length,1); % Temporary correlated T1 voltages [V]
Temp_RTD1_Corr = zeros(set_length,1); % Temporary correlated RTD1 voltages [V]
Temp_RTD2_Corr = zeros(set_length,1); % Temporary correlated RTD2 voltages [V]
Temp_RTD3_Corr = zeros(set_length,1); % Temporary correlated RTD3 voltages [V]
Temp_RTD4_Corr = zeros(set_length,1); % Temporary correlated RTD4 voltages [V]

```

```

% Systematic theta uncertainty
Us_Theta = zeros(set_length,1); % Theta uncertainty (from encoder)

% Random uncertainty arrays
Ur_TOR = zeros(set_length,1); % torque random uncertainty [V]
Ur_P_Val = zeros(uniquecount,1); % validyne pressure random uncertainty [V]
Ur_P_PCB = zeros(uniquecount,1); % PCB pressure random uncertainty [V]
U_V_Time = zeros(uniquecount,1); % Voltage DAQ Time Random Uncertainty [s]

Ur_T0_Corr = zeros(uniquecount,1); % Correlated T_0 temperature random uncertainty [V]
Ur_T1_Corr = zeros(uniquecount,1); % Correlated T_1 temperature random uncertainty [V]

Ur_RTD1_Corr = zeros(uniquecount,1); % Correlated RTD_1 temperature random uncertainty [V]
Ur_RTD2_Corr = zeros(uniquecount,1); % Correlated RTD_2 temperature random uncertainty [V]
Ur_RTD3_Corr = zeros(uniquecount,1); % Correlated RTD_3 temperature random uncertainty [V]
Ur_RTD4_Corr = zeros(uniquecount,1); % Correlated RTD_4 temperature random uncertainty [V]

%Current average scheme is basic mean of points grouped about individual ticks
for n = 2:1:(set_length+1) % for encoder tick after the first

    V_ind_up = floor((ticks(n+1)+ticks(n))/2); %upper midpoint between tick(n) and tick(n+1)
    V_ind_low = ceil((ticks(n-1)+ticks(n))/2); %lower midpoint between tick(n) and tick(n-1)
    count = V_ind_up - V_ind_low + 1; % count of number of data points taken for the tick

    Temp_Theta_Tick(index) = DATA.A_Unique(ticks(n)) ; %unique encoder count of point
    Temp_Theta(index) = DATA.Theta(ticks(n)); % Crankshaft position at tick [rad]
    Temp_TOR(index) = sum(DATA.TOR(V_ind_low:V_ind_up))/count; % average torque [V]
    Temp_P_Val(index) = sum(DATA.P_Val(V_ind_low:V_ind_up))/count; % average validyne pressure [V]
    Temp_P_PCB(index) = sum(DATA.P_PCB(V_ind_low:V_ind_up))/count; % average PCB pressure [V]
    Temp_V_Time(index) = DATA.V_Time(ticks(n)); % time value at tick Voltage DAQ Time [s]
    %Test_time(index) = sum(DATA.V_Time(V_ind_low:V_ind_up))/count; %
    %should match above value

    % theta systematic uncertainty
    Us_Theta(index) = sqrt(((0.17*pi/180)^2)+(1*pi/180)^2); % [rad]
    % Encoder accuracy & encoder comm. accuracy

    % sample random uncertainties
    t_0025 = tinv(0.975,count-1); % inverse 2 tail t-test with 95% confidence interval

```

```

Ur_TOR(index) = t_0025*(std(DATA.TOR(V_ind_low:V_ind_up))./sqrt(count));
Ur_P_Val(index) = t_0025*(std(DATA.P_Val(V_ind_low:V_ind_up))./sqrt(count));
Ur_P_PCB(index) = t_0025*(std(DATA.P_PCB(V_ind_low:V_ind_up))./sqrt(count));

U_V_Time(index) = (DATA.V_Time(V_ind_up)-DATA.V_Time(V_ind_low))./(2*count);

index = index + 1;

end

% Move temporary data to data structure
DATA.Theta_Tick = Temp_Theta_Tick;
DATA.Theta = Temp_Theta;
DATA.TOR = Temp_TOR;
DATA.P_Val = Temp_P_Val;
DATA.P_PCB = Temp_P_PCB;
DATA.V_Time = Temp_V_Time;

DATA.Us_Theta = Us_Theta;
DATA.U_V_Time = U_V_Time;

%% Calculation of instantaneous Velocity

% Currently first order linear derivative based on a moving fit of 5%
% of the angular increment
[DATA.Vel_Inst] = Inst_Angular_Velocity(DATA.Theta,DATA.V_Time);

%% Group Thermocouple data and average to Volt index
% assign nearest average V_index to each thermcouple data point

set_length = length(DATA.T_Time);
% Corrilation index for each point to the associated encoder position
Temp_T_V_Corr = zeros(set_length,1);

% for each therm time, compare to closest voltage time
for n = 1:1:set_length
    [temp,V_index] = min(abs(DATA.V_Time - DATA.T_Time(n)));
    Temp_T_V_Corr(n) = V_index;

```

```

end

% Each value of temp set assigned a matched voltage series index
DATA.T_V_Corr = Temp_T_V_Corr;

% average the thermocouple data for each tick
for n = DATA.T_V_Corr(1):1:length(DATA.V_Time)
    Match_Ind = find(DATA.T_V_Corr == n); % finds indicies of matching therm data
    Match_Ind_I = Match_Ind(1); % finds initial index of matching therm data
    Match_Ind_End = Match_Ind(end); % finds last index of matching therm data
    Match_Ind_L = length(Match_Ind); % finds length matching therm data
    % Basic average of thermocouple data
    Temp_T0_Corr(n) = sum(DATA.T0(Match_Ind_I:Match_Ind_End))/Match_Ind_L;
    Temp_T1_Corr(n) = sum(DATA.T1(Match_Ind_I:Match_Ind_End))/Match_Ind_L;

    % Random Uncertainty for the data averaged for this tick
    t_0025 = tinverse(0.975,Match_Ind_L-1); % inverse 2 tail t-test with 95% confidence interval

    Ur_T0_Corr(n) = t_0025.*std(DATA.T0(Match_Ind_I:Match_Ind_End))./sqrt(Match_Ind_L);
    Ur_T1_Corr(n) = t_0025.*std(DATA.T1(Match_Ind_I:Match_Ind_End))./sqrt(Match_Ind_L);

end

DATA.T0_Corr = Temp_T0_Corr;
DATA.T1_Corr = Temp_T1_Corr;

%% Calibrate Thermocouple data and uncertainty

% Loading calibration coefficients
load Therm_RTD_Calibration.mat

% Apply fit coefficients to data
DATA.T0_Corr = Temp_T0_Corr.*Temps_Fit.T_0(1)+Temps_Fit.T_0(2);
DATA.T1_Corr = Temp_T1_Corr.*Temps_Fit.T_1(1)+Temps_Fit.T_1(2);

% Systematic Thermocouple uncertainty [ +/- °C]

```

```

Us_T_Corr = sqrt((1.0^2)+(0.05^2)+(0.35^2)+(0.65^2)+((0.00015*100)^2)+((0.061*(100/4.279))^2)) ;
% +/-1.0°C inst accuracy, +/-0.05°C Calibration inst, +/- 0.35°C Rack
% Repeatability, +/-0.65°C Rack Accuracy, +/-0.015°C Therm Signal
% Conditioner, +/-0.061mV (100°C/4.279mV) Digitizer accuracy

% Combine systematic and random uncertainty [ +/-°C]
DATA.U_T0_Corr = sqrt(((Ur_T0_Corr.*Temps_Fit.T_0(1)).^2)+((Us_T_Corr).^2)) ;
DATA.U_T1_Corr = sqrt(((Ur_T1_Corr.*Temps_Fit.T_1(1)).^2)+((Us_T_Corr).^2)) ;

%% Group RTD data and average to to Volt index
% assign nearest average V_index to each RTD data point
set_length = length(DATA.RTD_Time);
% Corrilation index for each point to the associated encoder position
Temp_RTD_V_Corr = zeros(set_length,1);

% for each RTD time, compare to closest voltage time
for n = 1:1:set_length
    [temp,V_index] = min(abs(DATA.V_Time - DATA.RTD_Time(n)));
    Temp_RTD_V_Corr(n) = V_index;
end

DATA.RTD_V_Corr = Temp_RTD_V_Corr;

% Group RTD data and average to a single cycle (increment of 500)
Cycles = ceil((length(DATA.Theta_Tick)/500));

% Set up the temporary averaged vectors
Temp_RTD1_Corr_Cycle = zeros(Cycles,1);
Temp_RTD2_Corr_Cycle = zeros(Cycles,1);
Temp_RTD3_Corr_Cycle = zeros(Cycles,1);
Temp_RTD4_Corr_Cycle = zeros(Cycles,1);

Temp_Ur_RTD1_Corr_Cycle = zeros(Cycles,1);
Temp_Ur_RTD2_Corr_Cycle = zeros(Cycles,1);
Temp_Ur_RTD3_Corr_Cycle = zeros(Cycles,1);
Temp_Ur_RTD4_Corr_Cycle = zeros(Cycles,1);

for n = 1:1:length(DATA.RTD_V_Corr) %Cycle through all the RTD data

```

```

for i = 1:1:Cycles % Check what cycle the correlation falls into
    if (DATA.RTD_V_Corr(n)/(500*i)) < 1
        Temp_RTD_V_Corr(n) = 500*i; % Assign rotation cycle to correlation

        break
    end
end

end
end

DATA.RTD_V_Corr = Temp_RTD_V_Corr;

% average the RTD data for each cycle and assign it to a cycle
index = 1;

for n = DATA.RTD_V_Corr(1):500:DATA.RTD_V_Corr(end) % Check each cycle of 500 points
    Match_Ind = find(DATA.RTD_V_Corr == n); % finds index of matching therms data
    Match_Ind_I = Match_Ind(1); % finds initial index of matching therm data
    Match_Ind_End = Match_Ind(end); % finds last index of matching therm data
    Match_Ind_L = length(Match_Ind); % finds length matching therm data
    % Basic average of RTD data
    Temp_RTD1_Corr_Cycle(index) = sum(DATA.RTD1(Match_Ind_I:Match_Ind_End))/Match_Ind_L;
    Temp_RTD2_Corr_Cycle(index) = sum(DATA.RTD2(Match_Ind_I:Match_Ind_End))/Match_Ind_L;
    Temp_RTD3_Corr_Cycle(index) = sum(DATA.RTD3(Match_Ind_I:Match_Ind_End))/Match_Ind_L;
    Temp_RTD4_Corr_Cycle(index) = sum(DATA.RTD4(Match_Ind_I:Match_Ind_End))/Match_Ind_L;

    % Random Uncertainty for the data averaged for this cycle
    t_0025 = tinv(0.975,Match_Ind_L-1); % inverse 2 tail t-test with 95% confidence interval

    Temp_Ur_RTD1_Corr_Cycle(index) =
t_0025.*std(DATA.RTD1(Match_Ind_I:Match_Ind_End))./sqrt(Match_Ind_L);
    Temp_Ur_RTD2_Corr_Cycle(index) =
t_0025.*std(DATA.RTD2(Match_Ind_I:Match_Ind_End))./sqrt(Match_Ind_L);
    Temp_Ur_RTD3_Corr_Cycle(index) =
t_0025.*std(DATA.RTD3(Match_Ind_I:Match_Ind_End))./sqrt(Match_Ind_L);
    Temp_Ur_RTD4_Corr_Cycle(index) =
t_0025.*std(DATA.RTD4(Match_Ind_I:Match_Ind_End))./sqrt(Match_Ind_L);

    % Update the cycle index

```

```

    index = index + 1;
end

% Expand averaged data and uncertainty to each encoder index
for n = 1:length(DATA.Theta_Tick) % go through each encoder point
    for i = 1:Cycles % Check which cycle the encoder point belongs to
        if (DATA.Theta_Tick(n)/(500*i)) < 1
            Temp_RTD1_Corr(n) = Temp_RTD1_Corr_Cycle(i);
            Temp_RTD2_Corr(n) = Temp_RTD2_Corr_Cycle(i);
            Temp_RTD3_Corr(n) = Temp_RTD3_Corr_Cycle(i);
            Temp_RTD4_Corr(n) = Temp_RTD4_Corr_Cycle(i);

            Ur_RTD1_Corr(n) = Temp_Ur_RTD1_Corr_Cycle(i);
            Ur_RTD2_Corr(n) = Temp_Ur_RTD2_Corr_Cycle(i);
            Ur_RTD3_Corr(n) = Temp_Ur_RTD3_Corr_Cycle(i);
            Ur_RTD4_Corr(n) = Temp_Ur_RTD4_Corr_Cycle(i);

            break
        end
    end
end

DATA.RTD1_Corr = Temp_RTD1_Corr;
DATA.RTD2_Corr = Temp_RTD2_Corr;
DATA.RTD3_Corr = Temp_RTD3_Corr;
DATA.RTD4_Corr = Temp_RTD4_Corr;

%% Calibrate RTD data and uncertainty

% Apply fit coefficients to data
DATA.RTD1_Corr = Temp_RTD1_Corr.*Temps_Fit.RTD_1(1)+Temps_Fit.RTD_1(2);
DATA.RTD2_Corr = Temp_RTD2_Corr.*Temps_Fit.RTD_2(1)+Temps_Fit.RTD_2(2);
DATA.RTD3_Corr = Temp_RTD3_Corr.*Temps_Fit.RTD_3(1)+Temps_Fit.RTD_3(2);
DATA.RTD4_Corr = Temp_RTD4_Corr.*Temps_Fit.RTD_4(1)+Temps_Fit.RTD_4(2);

% Systematic Thermocouple uncertainty [ +/- °C]
Us_RTD_Corr = sqrt((0.35^2)+(0.05^2)+(0.2^2)) ;

```

```

% 0.35°C inst deviation, 0.05°C Calibration inst accuracy, 0.20°C RTD
% DAQ accuracy

% Combine systematic and random uncertainty [ +/-°C]
DATA.U_RTD1_Corr = sqrt(((Ur_RTD1_Corr.*Temps_Fit.RTD_1(1)).^2)+(Us_RTD_Corr.^2));
DATA.U_RTD2_Corr = sqrt(((Ur_RTD2_Corr.*Temps_Fit.RTD_2(1)).^2)+(Us_RTD_Corr.^2));
DATA.U_RTD3_Corr = sqrt(((Ur_RTD3_Corr.*Temps_Fit.RTD_3(1)).^2)+(Us_RTD_Corr.^2));
DATA.U_RTD4_Corr = sqrt(((Ur_RTD4_Corr.*Temps_Fit.RTD_4(1)).^2)+(Us_RTD_Corr.^2));

%% Crop data to start time and 1st Z-pulse

% find start time of recorded data across sets
Start_t_data = max([DATA.RTD_Time(1) DATA.T_Time(1) DATA.V_Time(1)]);

% Find the index of the first Z pulse in the averaged data sets
Z_pulse_1 = find(DATA.Theta_Tick == 500);

% Check to see if data start time is after the first Z-pulse
[Time_V_1,V_start_I] = min(abs(DATA.V_Time-Start_t_data)); % Volt minimum start time index

while Z_pulse_1 < V_start_I % Compare index of Z pulses and volt time
    Z_pulse_1 = Z_pulse_1+500; % Add 1 rotation (500 ticks) to the Z Pulse index
end

Start_time = DATA.V_Time(Z_pulse_1); % Start time of the starting Z pulse

% Find the start indexes for the Volt, Thermocouple and RTD sets
V_start_I = Z_pulse_1; % Volt start index

% [Time_T_1,T_start_I] = min(abs(DATA.T_Time-Start_time)); % Thermocouple start index
% [Time_RTD_1,RTD_start_I] = min(abs(DATA.RTD_Time-Start_time)); % RTD start index

% Find the number of complete cycles and last A pulse (Z pulse -1) to crop end of
set_length = length(DATA.V_Time);

Cycles = floor((set_length-V_start_I)/500);
V_end_I = V_start_I+(500*Cycles)-1; %index of the last data point

```



```

End_time = DATA.V_Time(V_end_I); % end time of the last A pulse

% [Time_T_1,T_end_I] = min(abs(DATA.T_Time-End_time)); % Thermocouple start index
% [Time_RTD_1,RTD_end_I] = min(abs(DATA.RTD_Time-End_time)); % RTD start index

% Crop the data sets to the start time
% Voltage data trim
DATA.V_Time = DATA.V_Time(V_start_I:V_end_I);
DATA.Theta = DATA.Theta(V_start_I:V_end_I);
DATA.Theta_Tick = DATA.Theta_Tick(V_start_I:V_end_I);
DATA.TOR = DATA.TOR(V_start_I:V_end_I);
DATA.P_Val = DATA.P_Val(V_start_I:V_end_I);
DATA.P_PCB = DATA.P_PCB(V_start_I:V_end_I);
DATA.Vel_Inst = DATA.Vel_Inst(V_start_I:V_end_I);

Ur_TOR = Ur_TOR(V_start_I:V_end_I);
Ur_P_Val = Ur_P_Val(V_start_I:V_end_I);
Ur_P_PCB = Ur_P_PCB(V_start_I:V_end_I);

DATA.Us_Theta = DATA.Us_Theta(V_start_I:V_end_I);
DATA.U_V_Time = DATA.U_V_Time(V_start_I:V_end_I);

DATA.T0_Corr = DATA.T0_Corr(V_start_I:V_end_I);
DATA.T1_Corr = DATA.T1_Corr(V_start_I:V_end_I);

DATA.U_T0_Corr = DATA.U_T0_Corr(V_start_I:V_end_I);
DATA.U_T1_Corr = DATA.U_T1_Corr(V_start_I:V_end_I);

DATA.RTD1_Corr = DATA.RTD1_Corr(V_start_I:V_end_I);
DATA.RTD2_Corr = DATA.RTD2_Corr(V_start_I:V_end_I);
DATA.RTD3_Corr = DATA.RTD3_Corr(V_start_I:V_end_I);
DATA.RTD4_Corr = DATA.RTD4_Corr(V_start_I:V_end_I);

DATA.U_RTD1_Corr = DATA.U_RTD1_Corr(V_start_I:V_end_I);
DATA.U_RTD2_Corr = DATA.U_RTD2_Corr(V_start_I:V_end_I);
DATA.U_RTD3_Corr = DATA.U_RTD3_Corr(V_start_I:V_end_I);
DATA.U_RTD4_Corr = DATA.U_RTD4_Corr(V_start_I:V_end_I);

DATA.Cycles = Cycles;

```

```

%cycle count uncertainty
DATA.U_Cycles = sqrt((DATA.Us_Theta(1).^2)+(DATA.Us_Theta(end).^2))/(2*pi); %[rev]

%% Calculation of Piston Half Shaft Positions

% Switch case to determine engine gearings from log file names.
switch DATA.PP_Gear %determine the gear pair eccentricity of the power piston
    case 1
        e_PP = 0;
    case 2
        e_PP = 1/5;
    case 3
        e_PP = 1/3;
    otherwise
        disp('PP Gear code invalid')
        pause ;
end

switch DATA.DP_Gear %determine the gear pair eccentricity of the displacer piston
    case 1
        e_DP = 0;
    case 2
        e_DP = 1/5;
    case 3
        e_DP = 1/3;
    otherwise
        disp('DP Gear code invalid')
        pause ;
end

% Transferred theta values of piston cranks
% [currently assumes both gears sets have same eccentricity)
[m21_PP,m21_DP,Theta_PP,Theta_DP] =
Ellipse_Trans_Func(DATA.Theta,e_PP,e_DP,PP_Phase,DP_Phase,PP_Pattern,DP_Pattern) ;

DATA.Theta_PP = Theta_PP ; %[rad]
DATA.Theta_DP = Theta_DP ; %[rad]

```

```

% Half shaft position uncertainty
% is the RSS addition of the random backlash uncertainty of the
% gears. All gears are of the same specification (t=2 95% confidence)
DATA.Us_Theta_PP = sqrt((DATA.Us_Theta.^2)+(2*0.91*(pi/180))^2) ; %[rad]
DATA.Us_Theta_DP = sqrt((DATA.Us_Theta.^2)+(2*0.91*(pi/180))^2) ; %[rad]

%% Volume Calculation & Uncertainty
% use the phase adjusted theta arrays
[V_Tot,U_V_Tot,V_PP] = Volume_EPM1(DATA.Theta_PP,DATA.Us_Theta_PP,Vol_Lookup_Shift,Table_Shift_Case);

DATA.V_Tot = V_Tot; % [m^3] Total volume
DATA.V_PP = V_PP; % [m^3] Volume of power piston
DATA.U_V_Tot = U_V_Tot; % [m^3] plus minus uncertainty

%% Engine Source / Sink Flow Calculation

% data was taken using the PD pump and measuring the mass of water
% pumped at the running settings from both heads
Pump_time = 250/2065*60; %[s] dispensed volume / total flow ratio

% Thermal Source side differentials
% [g] per dose at the specified flow rate
m_hot =
[234.4,239.9,229.1,234.6,236.6,236.0,236.1,238.8,234.3,238.4,232.5,235.0,233.2,231.7,237.2,234.3];
m_dot_Hot = mean(m_hot)/Pump_time/1000 ; %[kg/s]

% Hot flow rate uncertainty
t_0025 = tinv(0.975,length(m_hot)-1);
Ur_m_Hot = t_0025*(std(m_hot)./sqrt(length(m_hot)))/Pump_time/1000 ; %[kg/s]
U_m_dot_Hot = sqrt((Ur_m_Hot.^2)+((0.1/Pump_time/1000).^2));

DATA.m_dot_Hot = m_dot_Hot;
DATA.U_m_dot_Hot = U_m_dot_Hot;

% [g] per dose at the specified flow rate
m_cold =
[214.3,211.6,212.6,210.5,210.3,211.2,210.3,213.6,214.1,211.8,211.5,211.1,210.5,211.5,211.0,210.9];
m_dot_Cold = mean(m_cold)/Pump_time/1000 ; %[kg/s]

```

```

% Cold flow uncertainty
t_0025 = tinv(0.975,length(m_cold)-1);
Ur_m_Cold = t_0025*(std(m_cold)./sqrt(length(m_cold)))/Pump_time/1000 ; %[kg/s]
U_m_dot_Cold = sqrt((Ur_m_Cold.^2)+((0.1/Pump_time/1000).^2));

DATA.m_dot_Cold = m_dot_Cold;
DATA.U_m_dot_Cold = U_m_dot_Cold;

%% Pressure Calibrations & Uncertainties

% Valydyne DP-15 pressure transducer

% Valydyne pressure uncertainty
% Determine the FS value from the calibration expt (5PSI @ 10V)
[Temp,P_Val_FS] = Calibrate_Pressure_Manometer(10); %[Pa/10V]

% Systematic uncertainty elements for Valydyn pressure sensor [Pa]
% 0.5%FS(10V) inst acc, 0.026% cal, 0.05%FS demod acc, 0.00269V abs DAQ
U_sys_P_Val =
sqrt(((0.005*P_Val_FS)^2)+((9.148380349)^2)+((0.0005*P_Val_FS)^2)+((0.00269*(P_Val_FS/10))^2));

% Random uncertainty elements for Valydyn pressure sensor [Pa]
% 0.018% demod temp zero drift, 0.036% demod temp span, averaging SD
U_rand_P_Val =
sqrt(((0.00018*DATA.P_Val*P_Val_FS/10).^2)+((0.00036*DATA.P_Val*P_Val_FS/10).^2)+((Ur_P_Val*P_Val_FS/10).^2
));

% Combined final uncertainty vector [Pa]
DATA.U_P_Val = sqrt(((U_sys_P_Val)^2)+((U_rand_P_Val).^2));

% Uses calibration function written by Jason Michaud 2019-10 convert
% voltages to Pa
[Temp_P_Val_PSI, Temp_P_Val_Pa] = Calibrate_Pressure_Manometer(DATA.P_Val);
DATA.P_Val = Temp_P_Val_Pa; % store the converted data [Pa] + Atmospheric pressure

% PCB peiziotronic transducer 113B21 SN LW35042

% Conversion Factor for PCB measurments,

```

```

% calibration certificate sensitivity 3.519 mV/kPa
P_PCB_CF = (1000/3.519)*1000; % [Pa/V]

% PCB systematic uncertainty [Pa]
% 0.1%FS Linearity,changed FS to calibration FS (5V to 0.4857mV)
% 0.00141V abs DAQ %
U_sys_P_PCB = sqrt(((0.001*0.4857*P_PCB_CF).^2)+((0.00141*P_PCB_CF).^2)); % [Pa]

% PCB random uncertainty [Pa]
% 1.0% Uncert @95% conf, averaging SD
U_rand_P_PCB =
sqrt(((0.01*(DATA.P_PCB/P_PCB_Gain).*P_PCB_CF).^2)+(((Ur_P_PCB/P_PCB_Gain).*P_PCB_CF).^2)) ;

% Combined final uncertainty vector [Pa]
DATA.U_P_PCB = sqrt(((U_sys_P_PCB)^2)+((U_rand_P_PCB).^2));

% Convert voltages to pressure as per calibration certificate sensitivity 3.519 mV/kPa
Temp_P_PCB = (DATA.P_PCB/P_PCB_Gain)*P_PCB_CF; % [Pa]

% Combine the static and dynamic pressure
DATA.P_Mean = ones(size(DATA.P_Val)).*(mean(DATA.P_Val)); % Mean engine pressure [Pa]
DATA.P_PCB = Temp_P_PCB + DATA.P_Mean; % Mean adjusted PCB pressure [Pa]

%% Speed per cycle
%uncertainty added 21-01-30

% Total cycles / time of cropped dataset
DATA.Vel_Avg = ((DATA.Cycles*(2*pi))/(DATA.V_Time(end)-DATA.V_Time(1))); % [rad/s]

% Cycle speed uncertainty
U_Cycle_Time = sqrt((DATA.U_V_Time(1).^2)+(DATA.U_V_Time(end).^2)); %[s]
U_Vel_Avg = DATA.Vel_Avg*sqrt(((DATA.U_Cycles/DATA.Cycles).^2)+((U_Cycle_Time/(DATA.V_Time(end)-
DATA.V_Time(1))).^2)); % +/-[rad/s]
DATA.U_Vel_Avg = U_Vel_Avg;

DATA.f_Avg = (DATA.V_Time(end)-DATA.V_Time(1))/DATA.Cycles; %[Hz]
DATA.U_f_Avg = (2*pi)/DATA.U_Vel_Avg ;

```

```

DATA.Vel_Avg_RPM = ((DATA.Cycles)/(DATA.V_Time(end)-DATA.V_Time(1)))*60; % [RPM]
DATA.U_Vel_Avg_RPM = DATA.U_Vel_Avg*60/(2*pi);
%% Torque Calibration and Uncertainty

% Test data from the calibration certificate, Futek 1Nm sensor:
Cal_Input_Nm = [0.000; 0.1412; 0.2825; 0.4237; 0.5649; 1.0010; 0.0000; 0.0000; -0.1412; -0.2825; -
0.2437; -0.5649; -1.0010; 0.0000];
Cal_Output_V = [0.000; 0.703; 1.410; 2.116; 2.821; 5.002; 0.001; 0.000; -0.706; -1.411; -2.117; -2.824;
-5.007; -0.008];

% Fit a linear polynomial to the calibration data.
Tor_Data_Fit = fit(Cal_Output_V,Cal_Input_Nm,'poly1');
Torque_Coeffs = coeffvalues(Tor_Data_Fit);
%Torque_Coeffs = polyfit(Cal_Output_V,Cal_Input_Nm,1); % Alternative

% Apply equation of fitted polynomial to calculate torque in [Nm]
DATA.TOR_Cal = DATA.TOR.*Torque_Coeffs(1) + Torque_Coeffs(2); % [Nm]
%Torque_Nm2 = polyval(Torque_Coeffs,DATA.TOR); %(Nm) % Alternative

% Average of torque values over all cycles
DATA.TOR_Avg_Tot = mean(DATA.TOR_Cal);

% Uncertainty
Tor_RO = 1; % Rated Output for transducer @ 5 V [+/- Nm]

% Random uncertainty [Nm]
U_r_TOR = Ur_TOR*Torque_Coeffs(1) + Torque_Coeffs(2); % [Nm]

% Systematic uncertainty [Nm]
% 0.052%RO non-linearity error (max from calib docs)
% 0.1%RO hysteresis from spec sheet
% 0.2%RO nonrepeatability from spec sheet
% 0.00141V DAQ uncertainty
U_sys_TOR = sqrt((0.00052*Tor_RO)^2 + (0.001*Tor_RO)^2 + (0.002*Tor_RO)^2 + (0.00141*Tor_RO/5)^2);

DATA.U_TOR_Cal = sqrt(((U_sys_TOR)^2)+(U_r_TOR).^2);

% Average of torque values over all cycles

```

```

DATA.U_TOR_Avg_Tot = mean(DATA.U_TOR_Cal);

%% Power Calculation

DATA.Power = DATA.TOR_Avg_Tot*DATA.Vel_Avg ; % dW[W] = T[Nm]*omega[rad/sec]

% Power uncertainty
U_Power =
DATA.Power*sqrt(((DATA.U_TOR_Avg_Tot/DATA.TOR_Avg_Tot).^2)+((DATA.U_Vel_Avg/DATA.Vel_Avg).^2)); % +/- [Nm]
DATA.U_Power = U_Power;

%% Organize data into matrix [encoder position x revolutions]%%
% to be put at end once all values are calculated in arrays

n_Row = 500; % number of rows equivalent to rotatry encoder pos (0 = TDC)
n_Col = DATA.Cycles; % Number of columns equivalent to number of cycles

% Initialize matrices
Temp_Theta_Tick = zeros(n_Row,n_Col);
Temp_Theta = zeros(n_Row,n_Col);
Temp_Us_Theta = zeros(n_Row,n_Col);
Temp_Theta_PP = zeros(n_Row,n_Col);
Temp_Us_Theta_PP = zeros(n_Row,n_Col);
Temp_Theta_DP = zeros(n_Row,n_Col);
Temp_Us_Theta_DP = zeros(n_Row,n_Col);

Temp_V_Time = zeros(n_Row,n_Col);
Temp_U_V_Time = zeros(n_Row,n_Col);

Temp_TOR = zeros(n_Row,n_Col);
Temp_U_TOR = zeros(n_Row,n_Col);

Temp_P_Val = zeros(n_Row,n_Col);
Temp_U_P_Val = zeros(n_Row,n_Col);
Temp_P_PCB = zeros(n_Row,n_Col);
Temp_U_P_PCB = zeros(n_Row,n_Col);

```

```

Temp_Vel_Inst = zeros(n_Row,n_Col);

Temp_V_Tot = zeros(n_Row,n_Col);
Temp_U_V_Tot = zeros(n_Row,n_Col);

Temp_T0_Corr = zeros(n_Row,n_Col);
Temp_U_T0_Corr = zeros(n_Row,n_Col);
Temp_T1_Corr = zeros(n_Row,n_Col);
Temp_U_T1_Corr = zeros(n_Row,n_Col);

Temp_RTD1_Corr = zeros(n_Row,n_Col);
Temp_U_RTD1_Corr = zeros(n_Row,n_Col);
Temp_RTD2_Corr = zeros(n_Row,n_Col);
Temp_U_RTD2_Corr = zeros(n_Row,n_Col);
Temp_RTD3_Corr = zeros(n_Row,n_Col);
Temp_U_RTD3_Corr = zeros(n_Row,n_Col);
Temp_RTD4_Corr = zeros(n_Row,n_Col);
Temp_U_RTD4_Corr = zeros(n_Row,n_Col);

% Sort data into rows and columns
for Z = 1:1:n_Col

    for A = 1:1:n_Row

        index = (Z-1)*500 + (A);

        Temp_Theta_Tick(A,Z) = DATA.Theta_Tick(index);
        Temp_Theta(A,Z) = DATA.Theta(index);
        Temp_Us_Theta(A,Z) = DATA.Us_Theta(index);
        Temp_Theta_PP(A,Z) = DATA.Theta_PP(index);
        Temp_Us_Theta_PP(A,Z) = DATA.Us_Theta_PP(index);
        Temp_Theta_DP(A,Z) = DATA.Theta_DP(index);
        Temp_Us_Theta_DP(A,Z) = DATA.Us_Theta_DP(index);

        Temp_V_Time(A,Z) = DATA.V_Time(index);
        Temp_U_V_Time(A,Z) = DATA.U_V_Time(index);

        Temp_TOR(A,Z) = DATA.TOR_Cal(index);

```



```

Temp_U_TOR(A,Z) = DATA.U_TOR_Cal(index);

Temp_P_Val(A,Z) = DATA.P_Val(index);
Temp_U_P_Val(A,Z) = DATA.U_P_Val(index);
Temp_P_PCB(A,Z) = DATA.P_PCB(index);
Temp_U_P_PCB(A,Z) = DATA.U_P_PCB(index);

Temp_Vel_Inst(A,Z) = DATA.Vel_Inst(index);

Temp_V_Tot(A,Z) = DATA.V_Tot(index);
Temp_U_V_Tot(A,Z) = DATA.U_V_Tot(index);

Temp_T0_Corr(A,Z) = DATA.T0_Corr(index);
Temp_U_T0_Corr(A,Z) = DATA.U_T0_Corr(index);
Temp_T1_Corr(A,Z) = DATA.T1_Corr(index);
Temp_U_T1_Corr(A,Z) = DATA.U_T1_Corr(index);

Temp_RTD1_Corr(A,Z) = DATA.RTD1_Corr(index);
Temp_U_RTD1_Corr(A,Z) = DATA.U_RTD1_Corr(index);
Temp_RTD2_Corr(A,Z) = DATA.RTD2_Corr(index);
Temp_U_RTD2_Corr(A,Z) = DATA.U_RTD2_Corr(index);
Temp_RTD3_Corr(A,Z) = DATA.RTD3_Corr(index);
Temp_U_RTD3_Corr(A,Z) = DATA.U_RTD3_Corr(index);
Temp_RTD4_Corr(A,Z) = DATA.RTD4_Corr(index);
Temp_U_RTD4_Corr(A,Z) = DATA.U_RTD4_Corr(index);

end
end

% Store new sorted data in a matrix variable
DATA.Theta_Tick_M = Temp_Theta_Tick;
DATA.Theta_M = Temp_Theta;
DATA.Us_Theta = Temp_Us_Theta;
DATA.Theta_PP_M = Temp_Theta_PP;
DATA.Us_Theta_PP = Temp_Us_Theta_PP;
DATA.Theta_DP_M = Temp_Theta_DP;
DATA.Us_Theta_DP = Temp_Us_Theta_DP;

DATA.V_Time_M = Temp_V_Time;

```

```

DATA.U_V_Time_M = Temp_U_V_Time;

DATA.TOR_M = Temp_TOR;
DATA.U_TOR_M = Temp_U_TOR;

DATA.P_Val_M = Temp_P_Val;
DATA.U_P_Val_M = Temp_U_P_Val;
DATA.P_PCB_M = Temp_P_PCB;
DATA.U_P_PCB_M = Temp_U_P_PCB;

DATA.Vel_Inst_M = Temp_Vel_Inst;

DATA.V_Tot_M = Temp_V_Tot;
DATA.U_V_Tot_M = Temp_U_V_Tot;

DATA.T0_Corr_M = Temp_T0_Corr;
DATA.U_T0_Corr_M = Temp_U_T0_Corr;
DATA.T1_Corr_M = Temp_T1_Corr;
DATA.U_T1_Corr_M = Temp_U_T1_Corr;

DATA.RTD1_Corr_M = Temp_RTD1_Corr;
DATA.U_RTD1_Corr_M = Temp_U_RTD1_Corr;
DATA.RTD2_Corr_M = Temp_RTD2_Corr;
DATA.U_RTD2_Corr_M = Temp_U_RTD2_Corr;
DATA.RTD3_Corr_M = Temp_RTD3_Corr;
DATA.U_RTD3_Corr_M = Temp_U_RTD3_Corr;
DATA.RTD4_Corr_M = Temp_RTD4_Corr;
DATA.U_RTD4_Corr_M = Temp_U_RTD4_Corr;

%% Matrix Row Averaging %%

% Theta & Ticks
DATA.Avg_Theta_Tick = mod(DATA.Theta_Tick_M(:,1),500); %[encoder pos]
DATA.Theta_M = mod(DATA.Theta_M(:,1),(2*pi)); %[rad]

% Pressures
DATA.Avg_P_Val = mean(DATA.P_Val_M,2); % [Pa]
DATA.Avg_U_P_Val = mean(DATA.U_P_Val_M,2); % [+/-Pa]
DATA.Avg_P_PCB = mean(DATA.P_PCB_M,2); % [Pa]

```

```

DATA.Avg_U_P_PCB = mean(DATA.U_P_PCB_M,2); % [+/-Pa]

% Torque
DATA.Avg_TOR = mean(DATA.TOR_M,2); % [Nm]
DATA.Avg_U_TOR = mean(DATA.U_TOR_M,2); % [+/- Nm]

% Volumes
DATA.Avg_V_Tot = mean(DATA.V_Tot_M,2); % [m^3]
DATA.Avg_U_V_Tot = mean(DATA.U_V_Tot_M,2); % [+/-m^3]

%% Calculation of Indicated, Forced work, and efficacious work

%Indicated Work
DATA.Ind_Work = polyarea(DATA.Avg_V_Tot,DATA.Avg_P_Val); % [J]

% Forced Work - Riemann Summ Midpoint
% create the volume differential [m^3]
Len = length(DATA.Avg_V_Tot);
dV = zeros(Len:1);
dV(1) = (DATA.Avg_V_Tot(2)-DATA.Avg_V_Tot(Len))/2;
dV(2:(Len-1))=(DATA.Avg_V_Tot(3:Len)-DATA.Avg_V_Tot(1:(Len-2)))/2;
dV(Len) = (DATA.Avg_V_Tot(1)-DATA.Avg_V_Tot(Len-1))/2;
% uncertainty in dVol [m^3]
U_dV = zeros(Len:1);
U_dV(1) = sqrt((DATA.Avg_U_V_Tot(2)^2)+(DATA.Avg_U_V_Tot(Len)^2));
for i = 2:Len-1
    U_dV(i) = sqrt((DATA.Avg_U_V_Tot(i+1)^2)+(DATA.Avg_U_V_Tot(i-1)^2));
end
U_dV(Len) = sqrt((DATA.Avg_U_V_Tot(i)^2)+(DATA.Avg_U_V_Tot(Len-1)^2));

% Calculation of forced work via deffinition (sign Dp ~= sign Dv)
Forced_Work = 0; % [J]
U_FW_sum = 0; % sum of uncertainty in FW [J]
index_FW = 0; % index count of ticks making up each area
for i = 1:length(DATA.Avg_P_Val)
    if sign(dV(i))~= sign(DATA.Avg_P_Val(i))
        Forced_Work = Forced_Work + abs(DATA.Avg_P_Val(i)*dV(i)); %[J]
        U_FW_sum = U_FW_sum + sqrt(((DATA.Avg_U_P_Val(i).*dV(i)).^2)+2*(U_dV(i).*DATA.Avg_P_Val(i))^2); %
uncertainty in FW [J]
        index_FW = index_FW + 1;
    end
end

```

```

    end
end
DATA.U_FW = U_FW_sum/index_FW ; % uncertainty in FW [J]

% Calculation of efficacious work via definition (sign Dp == sign Dv)
Eff_Work = 0; % [J]
U_EffW_Sum = 0; % sum of uncertainty in Eff Work [J]
index_EffW = 0; % index count of ticks making up each area
for i = 1:length(DATA.Avg_P_Val)
    if sign(dV(i))== sign(DATA.Avg_P_Val(i))
        Eff_Work = Eff_Work + abs(DATA.Avg_P_Val(i)*dV(i)); %[J]
        U_EffW_Sum = U_EffW_Sum + sqrt(((DATA.Avg_U_P_Val(i).*dV(i)).^2)+2*(U_dV(i).*DATA.Avg_P_Val(i))^2);
% [J]
        index_EffW = index_EffW + 1;
    end
end
DATA.U_Eff_W = U_EffW_Sum/index_EffW ; % uncertainty in FW [J]

DATA.FW = Forced_Work; %[J]
DATA.Eff_W = Eff_Work; %[J]

%Uncertainty in indicated work
DATA.U_Ind_Work = (DATA.U_Eff_W+DATA.U_FW)/2 ; % [J]

% Calculation of shaft work (torque * 2pi)
DATA.Shaft_Work = mean(DATA.Avg_TOR.*(2*pi)); %[J]
DATA.U_Shaft_Work = mean(DATA.Avg_U_TOR.*(2*pi)); %[J]

% Estimation of Mechansim Effectiveness
% isolated from the fundamental efficiency theorem
Mech_Eff = zeros(2,1);
% Solve using quadratic formula
a = (DATA.Ind_Work+DATA.FW); %[J]
b = -(DATA.Power*DATA.f_Avg); %[J]
c = -DATA.FW; %[J]

u_a = sqrt((DATA.U_Ind_Work^2)+(DATA.U_FW^2)); % uncertainty of "a" term [J]
u_b = DATA.U_Shaft_Work; % uncertainty of "b" term [J]
u_c = DATA.U_FW; % uncertainty of "c" term [J]

```

```

% calcualte mechanism effectiveness
Mech_Eff(1) = (-b+sqrt(b^2-4*a*c))/(2*a);
Mech_Eff(2) = (-b-sqrt(b^2-4*a*c))/(2*a);

% Caculation of ucnertainty in E
% Partial derivatives of uncertainty terms
dEda = ((-c)/(a*sqrt((b^2)-4*a*c)))-(((b)+sqrt((b^2)-4*a*c))/(2*a^2)) ;
dEdb = ((b)-sqrt((b^2)-4*a*c))/(2*a*sqrt((b^2)-4*a*c)) ;
dEdc = (-1)/(sqrt((b^2)-4*a*c)) ;

U_Mech_Eff = sqrt(((u_a*dEda)^2)+((u_b*dEdb)^2)+((u_c*dEdc)^2)) ;

DATA.Mech_Eff = Mech_Eff(1);
DATA.U_Mech_Eff = U_Mech_Eff;

%% Heat transfer, efficiency, and global losses
cp_90 = 4206; %[J/(kg K)] taken from Cengel A-9
cp_05 = 4205; %[J/(kg K)] taken from Cengel A-9
CtoK = 273.15 ; % [°C] to [K]
% heat transfer calcualtions
dTh = (mean(mean(DATA.RTD1_Corr_M))-mean(mean(DATA.RTD2_Corr_M))); % [K]
dTc = (mean(mean(DATA.RTD4_Corr_M))-mean(mean(DATA.RTD3_Corr_M))); % [K]
u_dTh = sqrt((mean(mean(DATA.U_RTD1_Corr_M))^2 + (mean(mean(DATA.U_RTD2_Corr_M))^2)); % +/-[°C]
u_dTc = sqrt((mean(mean(DATA.U_RTD4_Corr_M))^2 + (mean(mean(DATA.U_RTD3_Corr_M))^2)); % +/-[°C]

Q_h = DATA.m_dot_Hot.*cp_90.*dTh; %[J/s]
Q_c = DATA.m_dot_Cold.*cp_05.*dTc; %[J/s]
U_Q_h = sqrt(((DATA.U_m_dot_Hot.*cp_90.*dTh)^2)+((u_dTh.*DATA.m_dot_Hot.*cp_90)^2)) ; %+/-[J/s]
U_Q_c = sqrt(((DATA.U_m_dot_Cold.*cp_05.*dTc)^2)+((u_dTc.*DATA.m_dot_Cold.*cp_05)^2)) ; %+/-[J/s]

DATA.Q_h = Q_h ;
DATA.Q_c = Q_c ;
DATA.U_Q_h = U_Q_h ;
DATA.U_Q_c = U_Q_c ;

% Efficiency Calculation
n_T = DATA.Power./DATA.Q_h;
u_n_T = n_T*sqrt(((DATA.U_Power./DATA.Power)^2)+((U_Q_h./Q_h)^2)) ;

```

```

DATA.n_T = n_T ;
DATA.U_n_T = u_n_T ;

% Global loss calculation
Q_l = Q_h - DATA.Power - Q_c ; %[W]
u_Q_l = sqrt((U_Q_h^2)+(DATA.U_Power^2)+(U_Q_c^2)) ; %[W]

DATA.Q_l = Q_l ;
DATA.U_Q_l = u_Q_l;

%% Save the processed and calibrated data

% Save processed data structure as .mat file with same base name as log files
Pro_File_Name = strcat(File_Name, '_PRO_V2');
evalc([matlab.lang.makeValidName(Pro_File_Name), ' = DATA']);
save(strcat(log_File_Loc, '/', Pro_File_Name, '.mat'), 'DATA');
clear(Pro_File_Name);

[...]

close all

clearvars DATA;
end

```

E.4 Engine Volume Table Lookup Script

This script is called by the main data processing script to determine the total volume of the EP1-M. As inputs it take the angular position of the piston crankshaft (with position uncertainty), and any correction to the top dead center correlation for the piston crankshaft position that may be necessary (If any data set was not calibrated to piston TDC as specified in the procedures of section 4.5). As output the script determines the total engine volume (with combined volume uncertainty), as well as the volume of the piston specifically.

```
function [V_tot,U_V_Tot,V_PP] = Volume_EPM1(Theta_PP,Us_Theta,Vol_Lookup_Shift,Table_Shift_Case)

% Written by Michael Nicol-Seto, 2020-01

% Determines the volumes of EPM-1 at a given crank angle depending on the
% configuration

% Inputs
% Theta: Crank position of the PP [rad]

% Outputs (to be added to)
% V_tot: total volume of the engine space [m^3]

%% Fixed volumes and dimensions of the EPM-1

% presently taken from: (updated 2020-11-22)
% X:\01_Current_Students\Michael Nicol-Seto\THESIS\Engine Properties
% Taken from Volume Tables 2.xlsx

V_min = 0.008937594071; % [m^3] minimum engine volume EPM-1 up to PP cuff

% Internal volume of the PP moving Structures as calculated from the solid model
V_PP_int = 0.0005465282900 ; % [m^3]
% this must be subtracted from the calculated volume of the bellow
```

```

%% the volume variation call out function
% Load the volume lookup table (shifted)
switch Table_Shift_Case
    case 1
        Vol_Table_Loc = 'X:\01_Current_Students\Michael Nicol-Seto\02-DATA_COLLECTION\02-PROCESSING_CODE\02-
02_Data_Processing_Functions\Vol_Lookup_Table.mat' ;
        Vol_Data = open(Vol_Table_Loc);

        case 2
            Vol_Table_Loc = 'X:\01_Current_Students\Michael Nicol-Seto\02-DATA_COLLECTION\02-PROCESSING_CODE\02-
02_Data_Processing_Functions\Vol_Lookup_Table_Alt.mat' ;
            Vol_Data = open(Vol_Table_Loc);

        otherwise
            disp('Table_Shift_Case invalid')
            pause ;
end

Vol_Table = Vol_Data.Vol.Vol_Var_T ;
% Vol_Table_U = Vol_Data.Vol.U_Vol_Var_T ;
Vol_Table_U = 2.*Vol_Data.Vol.U_Vol_Var_T ;
%FIX (x2)for 95% confidence interval for U-vol

%% Run the lookup table interpolation

% circshift of the vector to align lookup with calibration
[Vol_Table_Shift] = shiftVector(Vol_Table,Vol_Lookup_Shift) ;
[Vol_Table_U_Shift] = shiftVector(Vol_Table_U,Vol_Lookup_Shift) ;

% look up the values using 1-D interpolation
X_Sample = linspace(0, (2*pi),length(Vol_Table_Shift)) ;

Theta_PP_Look = mod(Theta_PP,2*pi) ; % Use mod for look up query

method = 'linear' ;

V_PP = interp1(X_Sample, (Vol_Table_Shift.'),Theta_PP_Look,method) ;

```



```

% Volume lookup uncertainty using max min uncertainty in theta
V_PP_max = interp1(X_Sample, (Vol_Table_Shift.'), (Theta_PP_Look+Us_Theta),method) ;
V_PP_min = interp1(X_Sample, (Vol_Table_Shift.'), (Theta_PP_Look-Us_Theta),method) ;

% Generate the array of the maximum uncertainties from theta conversion to
% volume
U_V_Theta = max(abs(V_PP_max-V_PP),abs(V_PP_min-V_PP));

% Look up uncertainty for theta from volume variation uncertainty
U_V_VVar = interp1(X_Sample, (Vol_Table_U_Shift.'),Theta_PP_Look,method) ;

% Combine conversion uncertainty with vol var uncertainty using RSS
U_V_Tot = sqrt((U_V_Theta.^2)+(U_V_VVar.^2));

% Subtract the internal volumes of the bellow (calculated from SW)
V_PP = V_PP - V_PP_int ;

%% Determining Engine Volume

V_tot = V_min + V_PP ;

end

```

E.5 Encoder Position Array Generation Sub Function

This sub function is used by the data processing code to determine the position of the rotary encoder tick values and their positions in the raw data arrays from the loaded *.log files. The script implements the data organization scheme as described in 5.2.1. It takes as input the raw position data arrays of the A-channel and Z-channel of the rotary encoder. The script outputs two array of the same size as the *.log raw arrays, one with incremental values of the encoder positions at the correct array indices, and one of the angular positions of this ticks in rads.

The original version of this script was written by Connor Speer, modified by Calynn Stumpf, and finally modified by the author.

```
function [Theta_Deg,A_Unique] = Encoder_2_Angle_Spline(A,Z)

% Written by Connor Speer, October 2017. Subfunction to convert rotary
% encoder voltage data into crank angles.

% Edited and Updated by Calynn Stumpf, March 2018.
% Change Log:
% - Updated count to go from 0 -> 500 to 1 - > 500 (360° = 0°)
% - Added more comments to describe codes functions

%% Inputs:
% A --> column vector of A-output voltages from the rotary encoder (500 Ticks / Rev)
% Z --> column vector of Z-output voltages from the rotary encoder (1 Tick / Rev)
% *** A and Z must be the same length

%% Outputs
% theta_deg --> column vector of angles corresponding to rotary encoder outputs in (deg)

%% Find reference pulse in Z output
threshold = 2.5; % Threshold voltage value
ref_pulse = find(Z > threshold, 1); % Find index of FIRST instance in Z vector to be larger than threshold
value
```

```

if A(ref_pulse) < threshold % check if the A rise is aligned with the Z rise
    while A(ref_pulse) < threshold % if it is after, add to ref_pulse until rise
        ref_pulse = ref_pulse + 1;
    end

else A(ref_pulse) >= threshold; % check if the A rise is aligned with the Z rise
    while A(ref_pulse-1) >= threshold % if it is before, subtract from ref_pulse
        ref_pulse = ref_pulse - 1;
    end
end

%*****
pulse_flag = (A(ref_pulse-1) > threshold); % should be zero
%*****

A_count = zeros(size(A)); % setup ocunter index

bwd_counter = 499; % starting backwards is the 499 tick (500 - 1)
row = ref_pulse - 1; % move backwards through the A vector

while row ~= 0 % cycle backwards until at the begining of the array
    if pulse_flag == 1 % if on pulse check to see if it drops bellow threshold
        if A(row) < threshold
            bwd_counter = bwd_counter - 1; % pulse drops tick down the counter

            pulse_flag = 0; % pulse drops pulse flag is off
        end
    elseif A(row) > threshold % pulse raises pulse flag is on
        pulse_flag = 1;
    end

    % while pulse is on, record the counter in the A_count vector
    if pulse_flag == 1
        A_count(row) = bwd_counter;
    end

    row = row - 1;
end

```

```

%% Work forwards from reference pulse to find pulse counts

% CODE NOT REQUIRED:
% Reason: A(5V) and Z(5V) tick occur at the same time so they should follow
% the same on off format
%*****
pulse_flag = (A(ref_pulse) > threshold); % should be 1
%*****

fwd_counter = 500;

% Go forward until end of A pulses and assign incremented counter postions
for row = ref_pulse:length(A)
    if pulse_flag == 0 % if pulse flag is off check to see if pulse rises
        if A(row) > threshold
            fwd_counter = fwd_counter + 1; % add increment to counter

            pulse_flag = 1; % switch pulse flag on
        end
    elseif A(row) < threshold % check to see if pulse drops
        pulse_flag = 0; % turns flag off
    end

    % while pulse is on, record the counter in the A_count vector
    if pulse_flag == 1
        A_count(row) = fwd_counter;
    end

end

% A_count = [0 0 0 2 2 2 2 0 0 0 3 3 3 3 3 0 0 4 4 4 4 4 0 0 ...]
% Scan through and for each time the angle changes, find the middle of that
% section, mark it and set the others between this and the previously
cur_count = A_count(find(A_count > 0, 1)); % find the array index of the first count
pulse_flag = 1 if on counts, pulse_flag = 0 if on zeros
pulse_flag = 0; % initialize variables
start = 0;
finish = 0;
for row = 1:length(A)

```

```

if pulse_flag == 0 % check if count goes on
    if A_count(row) > 0
        start = row; % index first count
        pulse_flag = 1;
    end
else
    if A_count(row) == 0 % check if count goes off
        finish = row - 1; % index last count (row -1)
        pulse_flag = 0;
        mid = start+floor((finish-start)/2); % finds middle of counts (rounding down)
        for rowi = start:finish % zero the the other values around the mid count of a specific count
            if rowi ~= mid
                A_count(rowi) = 0;
            end
        end
    end
end
end
end
end
end
% A_count = [0 0 0 2 2 2 2 0 0 0 3 3 3 3 3 0 0 4 4 4 4 4 0 0 ...]
% is now
% A_count = [0 0 0 0 2 0 0 0 0 0 0 0 3 0 0 0 0 0 4 0 0 0 0 ...]

% Establish output array of A_count with unique counter values
A_Unique = A_count;

% replace zeros with NaN
A_count(A_count == 0) = NaN;

% A_count = fillmissing(A_count,'spline');

% fill in th NaN voids with a linear fill
A_count = fillmissing(A_count,'linear');

%% Use pulse count to calculate crank angles in radians
Theta_Deg = A_count*(2*pi/500); % [rad] (2 pi is TDC)

```

E.6 Volume Variation Image Processing Script

This script processes the raw images of the volume variation calibration trial of the EP1-M as described in thesis section 4.3.3. The script takes as input the file name of the image to be processed and the index of the image given by the processing script. The script outputs a vector of the radii of the pixel width disks from the top of the processed camera frame to the bottom (in pixel counts). This script is called by a modified version of the processing script detailed in Appendix E.3 used to determine the engine properties for the volume variation trials and to create the volume variation lookup tables.

This script was written by Linda Hasanovich and implemented into the modified processing script by the author.

```
function radii = bellowArea(filenameImg, file_name, ind)

% Written by Linda Hasanovich
% 2020-03

close all ;

% row_num is the row you select to average about (less than number of rows)
% col_num is the column to average about (less than number of columns)
% x_avg and y_avg is +/- the row you select to average about - selected based on image
row_num = 228;
col_num = 0; %placeholder value
x_avg = 24;
y_avg = 6;

% set figure number
i = 3;
%% load in image and get basic properties
rawImg = imread(filenameImg);
no_cols = 1:size(rawImg,2);
no_rows = 1:size(rawImg,1);
% crop right edge of image to get rid of secondary peak in edge detection
```

```

rawcImg = rawImg(1:no_rows(end),1:no_cols(end)-30);
no_cols = 1:size(rawcImg,2);
% show image

% figure(2);
% imshow(rawcImg);
figure(1);
imshow(rawcImg);

%% cleanup in order to crop accurately

% high pass filtering
fourImg = fft2(rawcImg);
fourMagImg = fftshift(log(fourImg));
fourPhaImg = angle(fourMagImg);
% show magnitude freq spectrum

% figure(i);
% i = i+1;
% imshow(fourMagImg,[])

filtTW = 0.17; %TW 0.01 of nyquist freq % let more low pass through to keep background bright (is the
effect of high tw and low cutoff)
filtLPB = 0.03; % LPB freq 0.01 of nyquist freq
filtLength = roundUpOdd(3.32*2/filtTW);
% creative 1d filter
filt1D = fir1(filtLength-1,filtLPB,'high',hann(filtLength));

% figure(i);
% i = i+1;
% freqz(filt1D);

% convert filter to 2D
filt2D=ftrans2(filt1D);
% apply designed filter to cropped image
filtImg = filter2(filt2D,rawcImg);
filtImg = uint8(filtImg); % convert back to 8bit image

% check effect of filtering on fft

```

```

fouraImg = fft2(filtImg);
fouraMagImg = fftshift(log(fouraImg));
% show magnitude freq spectrum

% figure(i);
% i = i+1;
% imshow(fouraMagImg, [])
%
figure(i); % highpass filtered image (leaves only high frequencies)
i = i+1;
imshow(filtImg);

% get the gray pixels to go to white
adjImg = imadjust(filtImg, [0.01 0.5]);

figure(i); % post imadjust - pushes grayscale to either full black or full white
i = i+1;
imshow(adjImg);

%% edge detection to crop

% show image

figure(1);
hold on
refline(0, row_num-x_avg);
refline(0, row_num+x_avg);
hold off

% get Iavg
Ixsum = zeros(1, no_cols(end)); % empty container of entire row of intensities
for j = -x_avg:x_avg % j is just a counter for the number of rows being averaged
    Iadd = double(adjImg((row_num + j), :)); %row of intensities at a given spot
    Ixsum = Ixsum + Iadd; % summing a bunch of rows to get an average intensity
end
Ix = Ixsum./(x_avg*2 + 1); % averaging by dividing by number of row intensities summed
% plot I vs x

% figure(i);

```



```

% i = i+1;
% plot(no_cols,Ix);
% axis([0 no_cols(end) 0 255]);
% xlabel('x (pixel)');
% ylabel('I (intensity)');

% generate plot of dI vs x at selected row and frame
dIx = Ix(2:no_cols(end)) - Ix(1:no_cols(end-1)); % difference between pixels next to each other

% figure(i);
% i = i+1;
% plot(no_cols(1:end-1),dIx);
% hold on

% peak detection - find minimum
dIx_inv = -dIx;
[~,locx1] = findpeaks(dIx, 'NPeaks',1, 'SortStr', 'descend'); %find end of arm/beginning of bellow
[~,locx2] = findpeaks(flip(dIx_inv), 'NPeaks',1, 'SortStr', 'none', 'MinPeakHeight',20);
locx2 = length(no_cols)-locx2;

% continuing with plotting
% plot(locx1,dIx(locx1), 'rs',locx2,dIx(locx2), 'gs');
% hold off
% axis([0 no_cols(end) -255 255]);
% xlabel('x (pixel)');
% ylabel('dI/dx (slope of intensity)');
% need to get locations of the two peaks to crop horizontally
% vertical crop will depend on edge finding the outside arm, then adding a
% fixed pixel amount that michael can convert into actual space

col_num = locx1 - 15; %place col_num behind the location of the edge to find the edges
% show image

figure(1);
hold on
line([col_num-y_avg col_num-y_avg],[0 no_rows(end)]);
line([col_num+y_avg col_num+y_avg],[0 no_rows(end)]);
hold off
% get Iavg
Iysum = zeros(1,no_rows(end)); % empty container of entire row of intensities

```

```

for j = -y_avg:y_avg % j is just a counter for the number of rows being averaged
    Iadd = double(adjImg(:,(col_num + j))'); %row of intensities at a given spot
    Iysum = Iysum + Iadd; % summing a bunch of rows to get an average intensity
end
Iy = Iysum./(y_avg*2 + 1); % averaging by dividing by number of row intensities summed
% plot I vs y

% figure(i);
% i = i+1;
% plot(no_rows,Iy);
% axis([0 no_rows(end) 0 255]);
% xlabel('y (pixel)');
% ylabel('I (intensity)');
% generate plot of dI vs x at selected row and frame
dIy = Iy(2:no_rows(end)) - Iy(1:no_rows(end-1)); % difference between pixels next to each other

% figure(i);
% i = i+1;
% plot(no_rows(1:end-1),dIy);
% hold on
% peak detection - find minimum
dIy_inv = -dIy;
[~,locy1] = findpeaks(dIy_inv,'NPeaks',1,'SortStr','none','MinPeakHeight',50); %find end of arm/beginning
of bellow
% continuing with plotting
% plot(locy1,dIy(locy1),'rs');
% hold off
% axis([0 no_rows(end) -255 255]);
% xlabel('y (pixel)');
% ylabel('dI/dy (slope of intensity)');

% figure(i);
% i = i+1;
% imhist(adjImg);

%% crop image

% locx1 = bottom edge of target arm
% locx2 = frame rails (fixed frame edge)
% locy1 = inner edge of target arm

```

```

% 250 = fixed amount from target arm from lock y1(does not exist)

% x offset on locx1
xoff1 = 20;
% x offset on locx2
xoff2 = 0;
% y offset on locy1
yoff1 = 50;
% required image thickness from locy1 (number of pixels)
yoff2 = round(105*(63/10)); % 105mm distance from centerline to crop line

figure(1);
hold on
hline1 = reffline(0,locy1); %horizontal line
hline1.Color = 'r';
hline2 = reffline(0,locy1+yoff1); %horizontal line
hline2.Color = 'g';
hline3 = reffline(0,locy1+yoff2); % line for centre of bellow
hline3.Color = 'g';
line([locx1 locx1],[0 no_rows(end)],'Color','r'); %vertical line
line([locx1+xoff1 locx1+xoff1],[0 no_rows(end)],'Color','g');
line([locx2+xoff2 locx2+xoff2],[0 no_rows(end)],'Color','r'); %vertical line
hold off

% cropping raw image for comparison
rawcropImg = imcrop(rawcImg,[locx1+xoff1 locy1+yoff1 (locx2+xoff2-(locx1+xoff1)) no_rows(end)]); %[xmin
ymin width height]
% figure(i);
% i = i+1;
% imshow(rawcropImg);

% crop filtered image for use
cropImg = imcrop(adjImg,[locx1+xoff1 locy1+yoff1 (locx2+xoff2-(locx1+xoff1)) no_rows(end)]); %[xmin ymin
width height]

% add rows to bottom to be as large as set length
no_rows = 1:size(cropImg,1); %reset no_rows to be the actual number of rows now present in the image
cropImg((no_rows(end)+1):(yoff2-yoff1),:) = 0; % need to add yoff1 to the centreline at bottom since the
image is shorter by yoff1 to begin with
% cropping was done first to make the image x [locx1+xoff1 locx2+xoff2] and

```

```

% image y [locy1+yoff1 yoff2]

figure(i);
i = i+1;
imshow(cropImg);

%% binarization
binImg = imbinarize(cropImg,0.5);

% figure(i);
% i = i+1;
% imshow(binImg);

%% output
compImg = imcomplement(binImg); %swap black and white pixels

figure(i);
i = i+1;
imshow(compImg);

% count of white pixels per column of image (ie disk of bellow / radius)
% top to bottom
radii = sum(compImg,1)'; % 1 is white and 0 is black

% % xtra close up fig to compare
% figure(i);
% i = i+1;
% imshow(cropImg(90:191,528:608));
% figure(i);
% i = i+1;
% imshow(compImg(90:191,528:608));

%% save final processed image as jpeg for final assesments
save_name = erase(file_name, '.tiff');
save_name_post = strcat(save_name, '_post.jpeg');
imwrite(compImg,save_name_post);

ind = num2str(ind);

```

```
save_name_post_index = strcat(ind, '_', save_name, '_post.jpeg');  
saveas(figure(1), save_name_post_index);
```

```
close all ;
```

```
end
```

```
% rounding function to nearest HIGH odd number
```

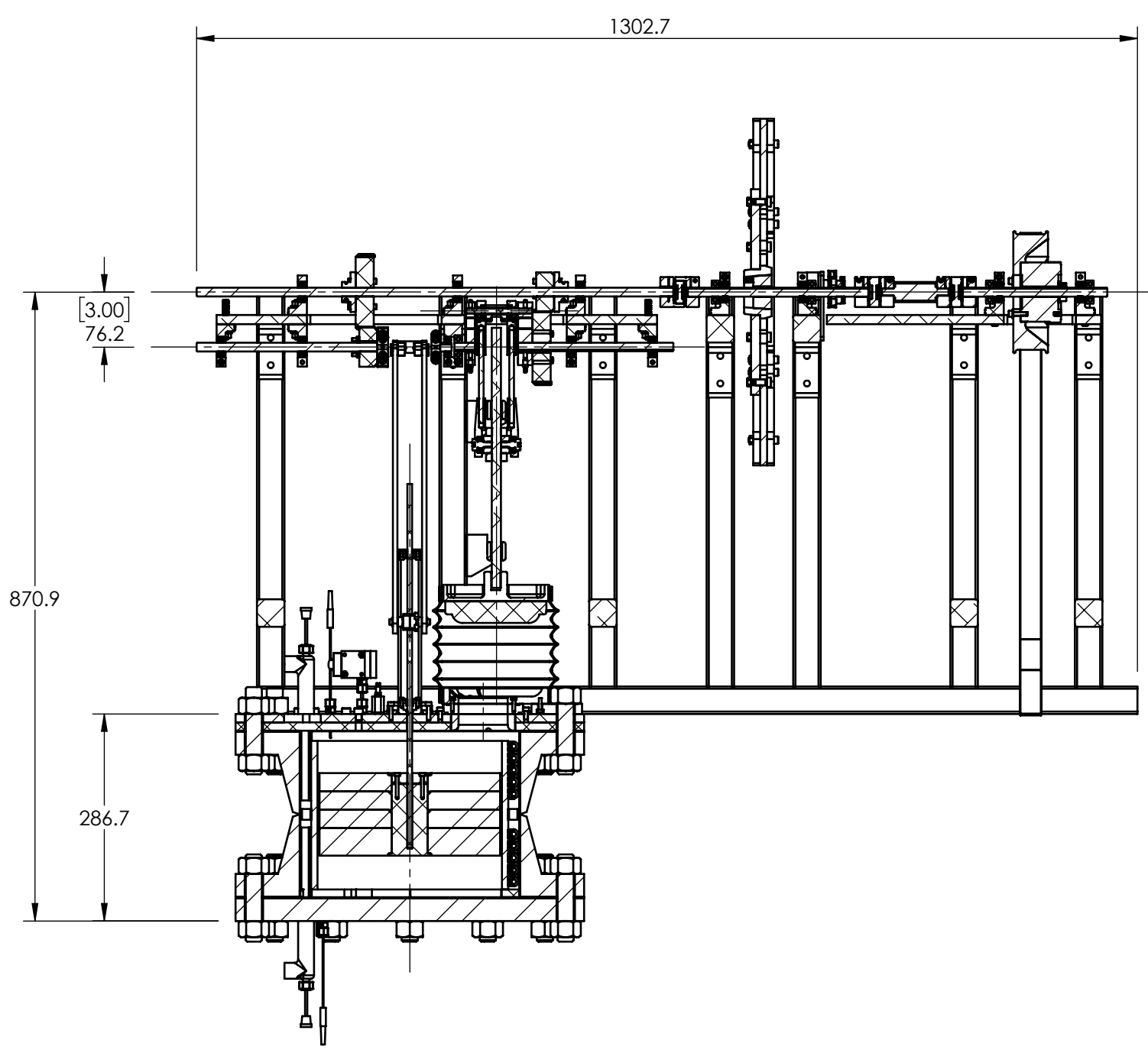
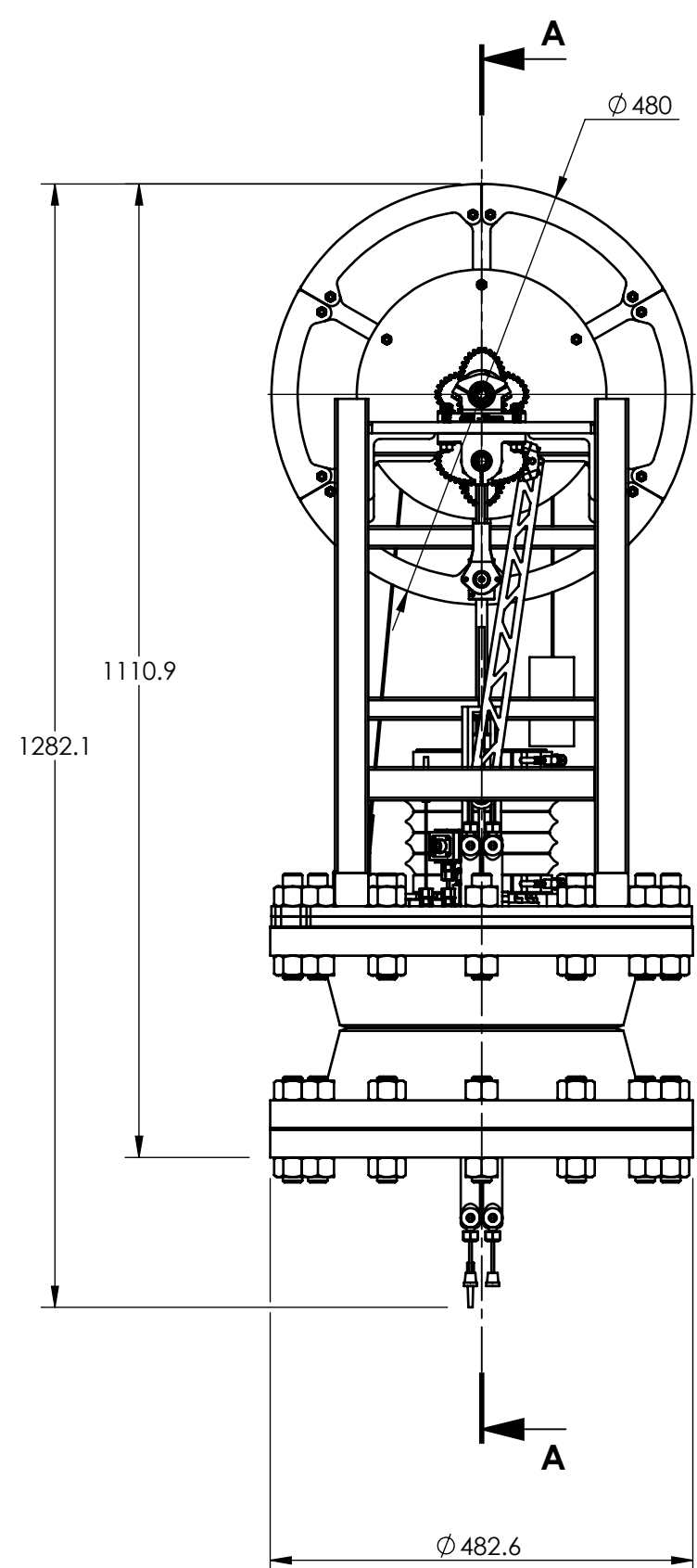
```
function y=roundUpOdd(x)
```

```
y = 2*round(x/2)+1;
```

```
end
```



F DRAWING PACKAGE

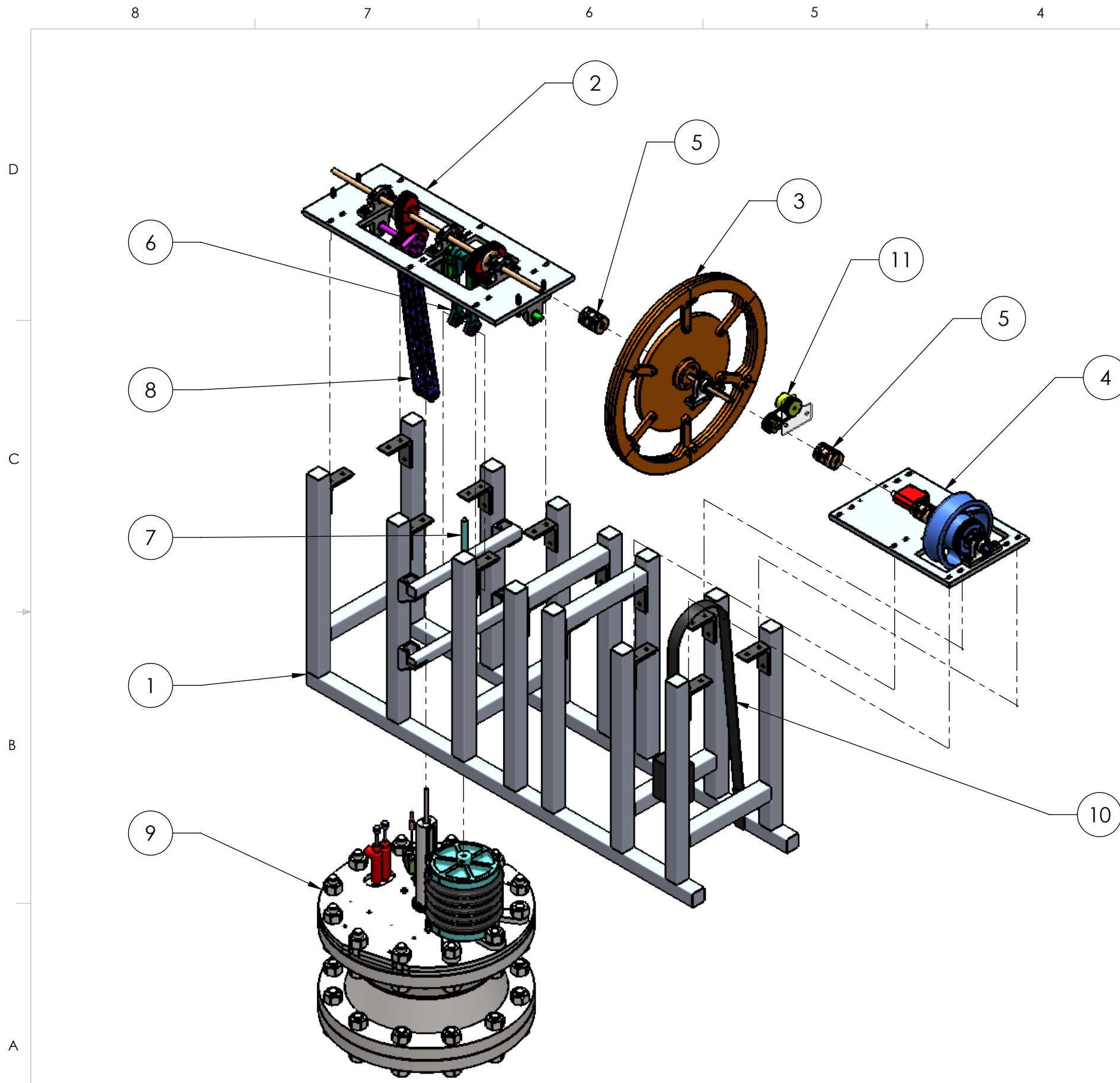
This Appendix contains a drawing package of certain high level assemblies of the the EP1-M Stirling Engine used in this investigation. The drawing are presented to provide dimensions and detailed orthogonal view of the overall and lower assembly of the EP1-M. Additional orthogonal drawings of the all three designed gear pairs is also documented.



SECTION A-A

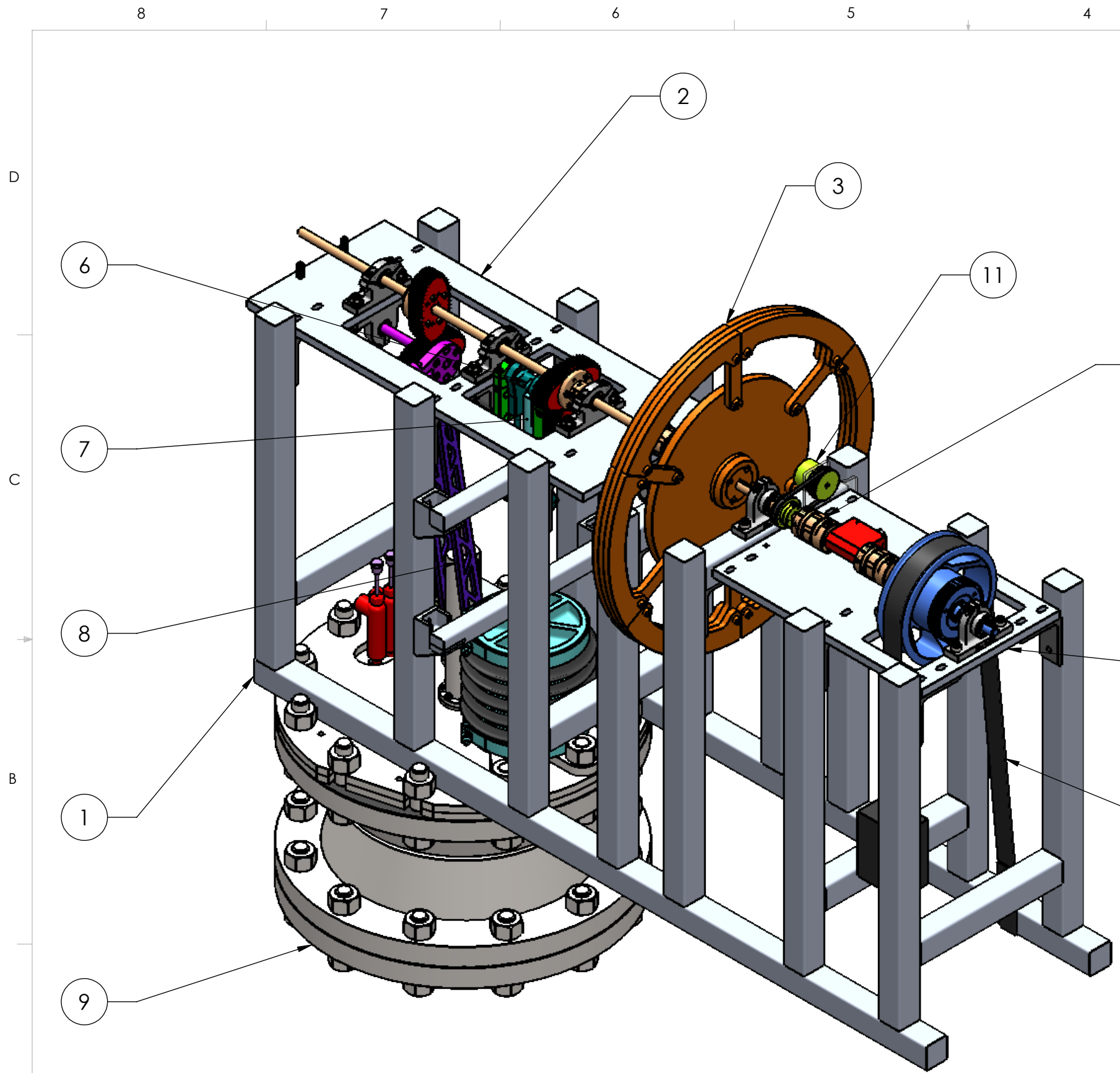
NOTE: DISPLACER CRANKARMS AND CONNECTING RODS NOT SECTIONED

UNLESS OTHERWISE SPECIFIED: Dimensions are in mm Tolerances: Angular: ± 0.5° Linear: X = ± 0.5 X.X = ± 0.1 X.XX = ± 0.025 SURFACE FINISH μm 0.6		Comments:	 Department of Mechanical Engineering UNIVERSITY OF ALBERTA	
		DRW By: MICHAEL NICOL-SETO	TITLE: OVERALL ASSEMBLY: ORTHOGONAL SECTION	
MATERIAL:		SM By: MICHAEL NICOL-SETO	Size: B	Project: EPM-1
FILE NAME: 00_OVERALL_UPPER_ASSEMBLY_Google_Drive_BACKUP		CHK By: nicolset June 2, 2019 August 30, 2021	Rev.: A	Mass:
		SCALE: 1:8	SHEET 1 OF 11	



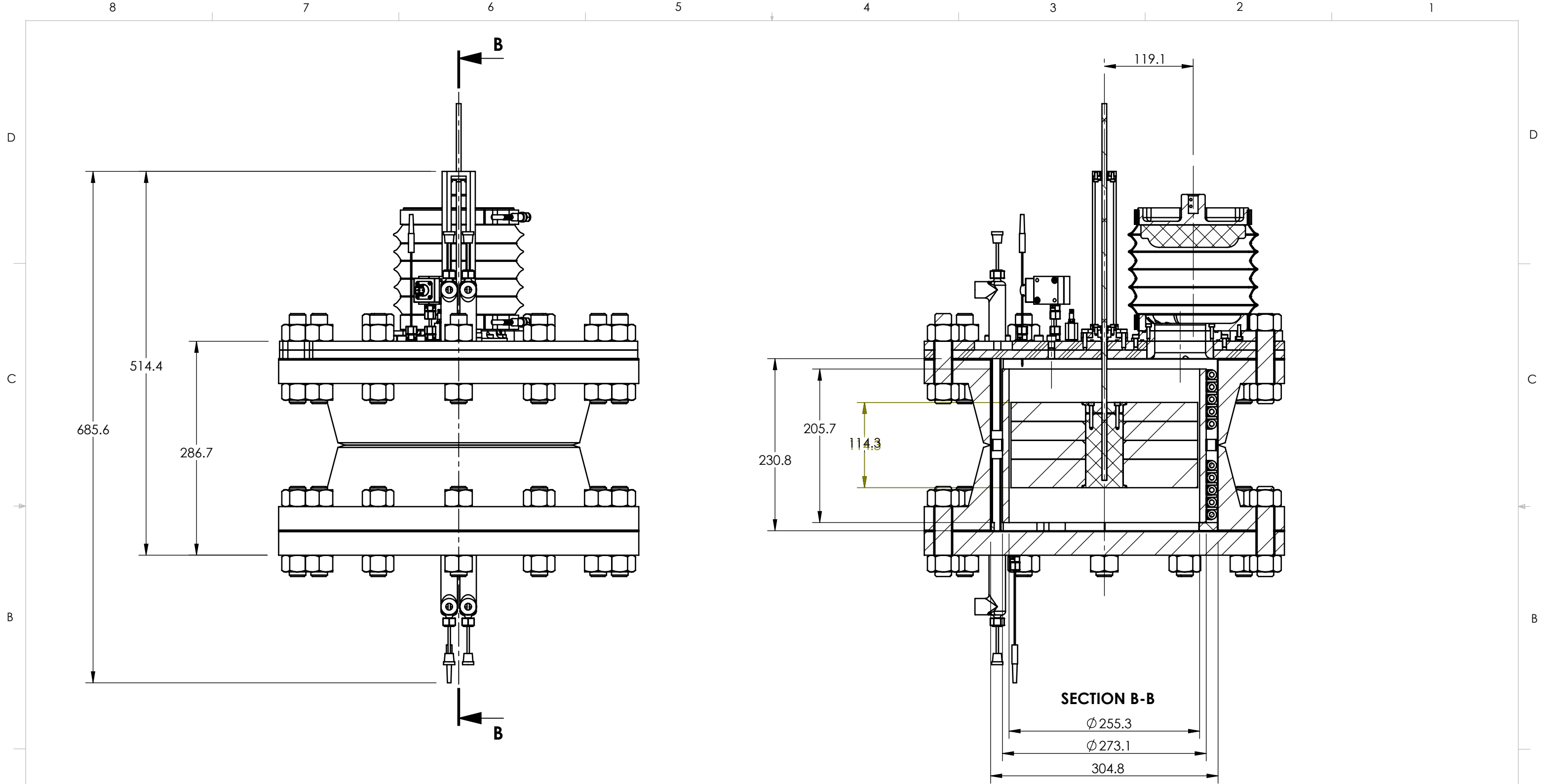
ITEM NO.	PART NUMBER	QTY.
1	09-MAIN_FRAME_ASSEM	1
2	05-CRANK_PLATE_ASSEM	1
3	06-FLYWHEEL_ASSEM	1
4	05-INSTRUMENT_PLATE	1
5	08-03-COUPLER_ASSEM	2
6	04-03-PP_CONNECTING_ROD_ASSEM	1
7	04-01-POWER_PISTON_UPPER_ASSEM	1
8	03-02_CONNECTING_ROD_ASSEM	1
9	01-01_MAIN_LOWER_ASSEM	1
10	07-04-BELT_ASSEM	1
11	10-06-MOUNTED_ENCODER_ASSEM	1

UNLESS OTHERWISE SPECIFIED: Dimensions are in mm Tolerances: Angular: $\pm 0.5^\circ$ Linear: X = ± 0.5 X.X = ± 0.1 X.XX = ± 0.025 SURFACE FINISH μm 0.6		Comments:		Department of Mechanical Engineering UNIVERSITY OF ALBERTA	
DRW By: MICHAEL NICOL-SETO SM By: MICHAEL NICOL-SETO CHK By:		TITLE: OVERALL ASSEMBLY: DRIVE-MECH. EXPLODE		Size: B Project: EPM-1 Rev.: A	
FILE NAME: 00_OVERALL_UPPER_ASSEMBLY_Google_Drive_BACKUP		SCALE: 1:10 Mass:		SHEET 2 OF 11	



ITEM NO.	PART NUMBER	QTY.
1	09-MAIN_FRAME_ASSEM	1
2	05-CRANK_PLATE_ASSEM	1
3	06-FLYWHEEL_ASSEM	1
4	05-INSTRUMENT_PLATE	1
5	08-03-COUPLER_ASSEM	2
6	04-03-PP_CONNECTING_ROD_ASSEM	1
7	04-01-POWER_PISTON_UPPER_ASSEM	1
8	03-02_CONNECTING_ROD_ASSEM	1
9	01-01_MAIN_LOWER_ASSEM	1
10	07-04-BELT_ASSEM	1
11	10-06-MOUNTED_ENCODER_ASSEM	1


UNLESS OTHERWISE SPECIFIED: Dimensions are in mm Tolerances: Angular: ± 0.5° Linear: X = ± 0.5 X.X = ± 0.1 X.XX = ± 0.025 SURFACE FINISH μm 0.6		Comments:		Department of Mechanical Engineering UNIVERSITY OF ALBERTA	
DRW By: MICHAEL NICOL-SETO SM By: MICHAEL NICOL-SETO CHK By:		TITLE: OVERALL ASSEMBLY: ASSEMBLY VIEW		Size: B Project: EPM-1 Rev.: A	
FILE NAME: 00_OVERALL_UPPER_ASSEMBLY_Google_Drive_BACKUP		nicolset June 2, 2019 August 30, 2021		SCALE: 1:6 Mass: SHEET 3 OF 11	

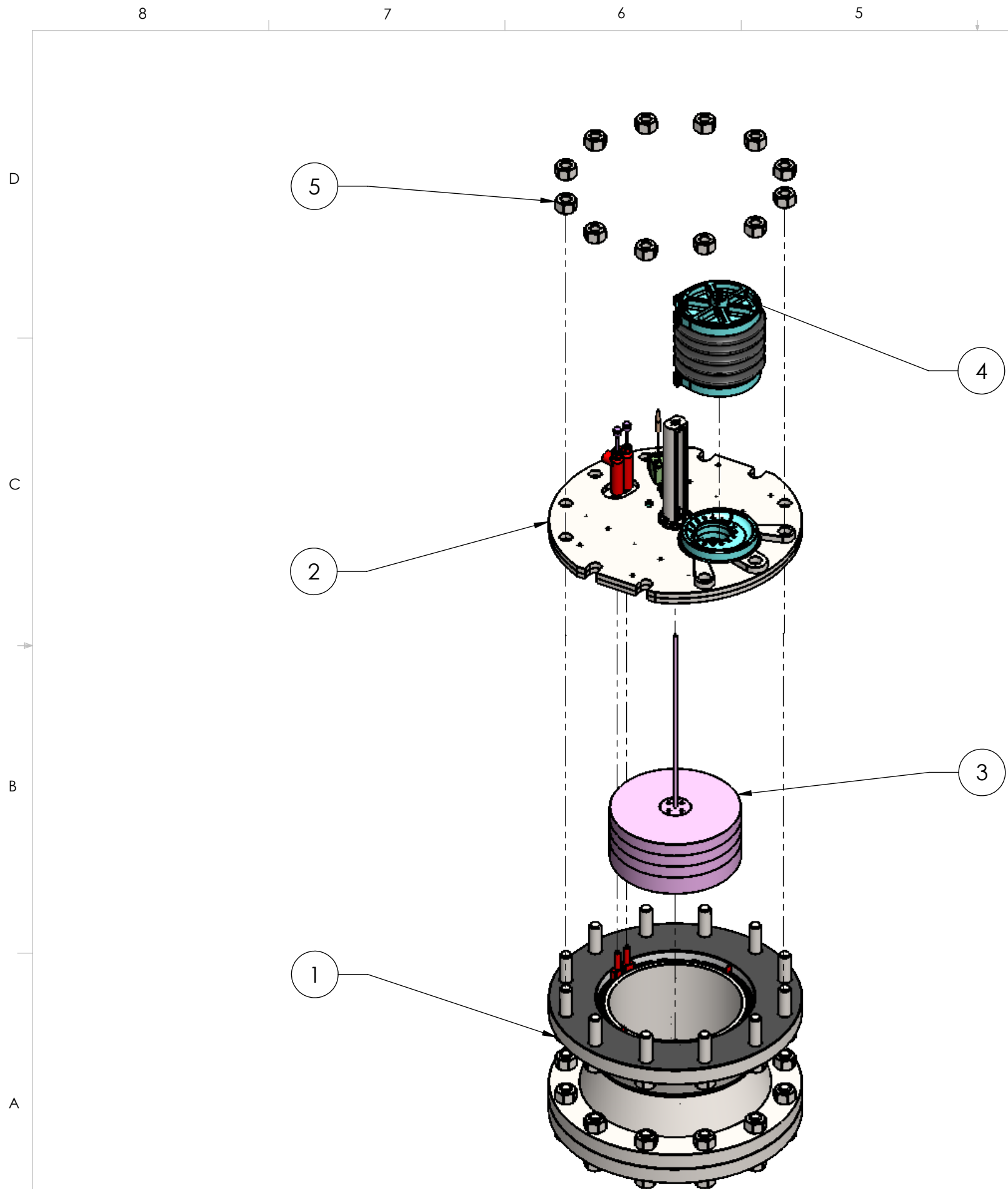


UNLESS OTHERWISE SPECIFIED:
 Dimensions are in mm
 Tolerances:
 Angular: $\pm 0.5^\circ$
 Linear: X = ± 0.5
 X.X = ± 0.1
 X.XX = ± 0.025
 SURFACE FINISH μm 0.6

Comments:
 DRW By: **MICHAEL NICOL-SETO**
 SM By: **MICHAEL NICOL-SETO**
 CHK By:
 nicolset
 July 29, 2020
 August 29, 2021

MATERIAL:
 FILE NAME:
 01-01_MAIN_LOWER_ASSEM

 Department of Mechanical Engineering UNIVERSITY OF ALBERTA		
TITLE: LOWER ENGINE ASSEMBLY: ORTHOGONAL SECTION		
Size	Project	Rev.
B	EPM-1	A
SCALE: 1:5	Mass:	SHEET 4 OF 11



ITEM NO.	PART NUMBER	QTY.
1	01-01_MAIN_LOWER_ASSEM (DISASSEMBLE)	1
2	02-01-TOP_FLANGE_ASSEM	1
3	03-03_DISP_PISTON_BODY	1
4	04-01-POWER_PISTON_UPPER_ASSEM_2	1
5	01-00-02-0.875in_HEAVY_NUT	12

UNLESS OTHERWISE SPECIFIED: Dimensions are in mm Tolerances: Angular: $\pm 0.5^\circ$ Linear: X = ± 0.5 X.X = ± 0.1 X.XX = ± 0.025		Comments:		Department of Mechanical Engineering UNIVERSITY OF ALBERTA	
SURFACE FINISH μm 0.6 ✓		DRW By: MICHAEL NICOL-SETO	TITLE: LOWER ENGINE ASSEMBLY: DISASSEMBLY EXPLODE		
		SM By: MICHAEL NICOL-SETO	Size: B	Project: EPM-1	Rev.: A
MATERIAL:		CHK By: nicolset July 29, 2020 August 29, 2021	SCALE: 1:9	Mass:	SHEET 5 OF 11
FILE NAME: 01-01_MAIN_LOWER_ASSEM					

8

7

6

5

4

3

2

1

D

C

B

A

12X ϕ 4.5 THRU
0.5 X 45° CHAM
EVENLY SPACED

ϕ 12

15°

4X 45°

D

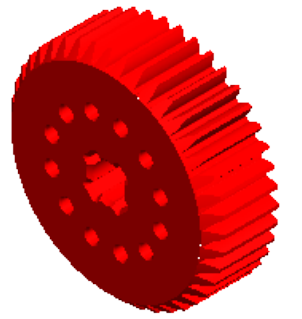
ϕ 42 BHC

4X 4.1

4X 16.2

D

PITCH CIRCLE DIAMETER: 3 IN

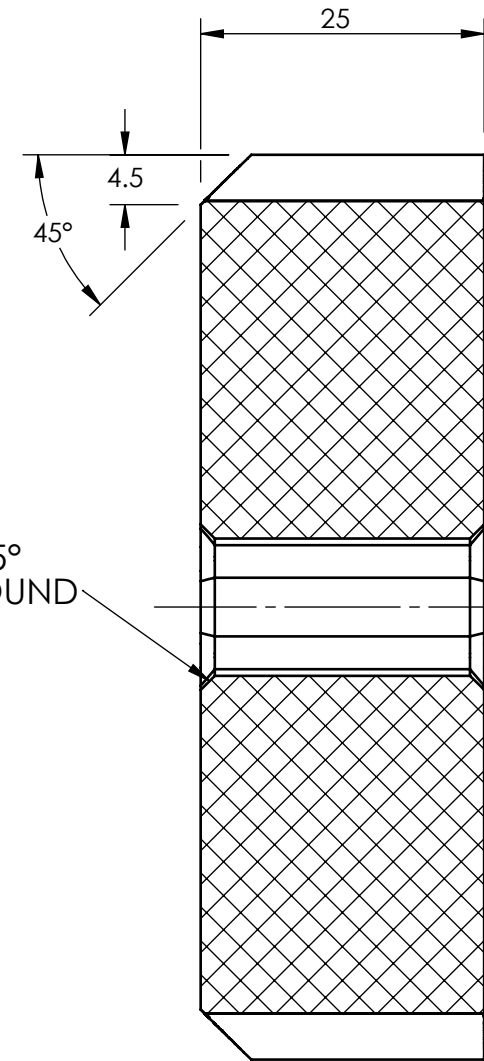


D

C

B

A



2X 1 X 45°
ALL AROUND

SECTION D-D

UNLESS OTHERWISE SPECIFIED:

Dimensions are in mm

Tolerances:

Angular: \pm 0.5°

Linear: X = \pm 0.5

X.X = \pm 0.1

X.XX = \pm 0.025

SURFACE FINISH μ m 0.6



MATERIAL:

FILE NAME:
05-05-01-01_ROUND_42T_CD3_PINION_V3

Comments:

DRW By: MICHAEL NICOL-SETO

SM By: MICHAEL NICOL-SETO

CHK By:

nicolset
May 22, 2019
August 30, 2021



Department of Mechanical Engineering
UNIVERSITY OF ALBERTA

TITLE:

$e = 0$ GEAR 1 (SHAFT)

42T, $p_d 14$, $\phi_C 20^\circ$

Size

B

Project

EPM-1

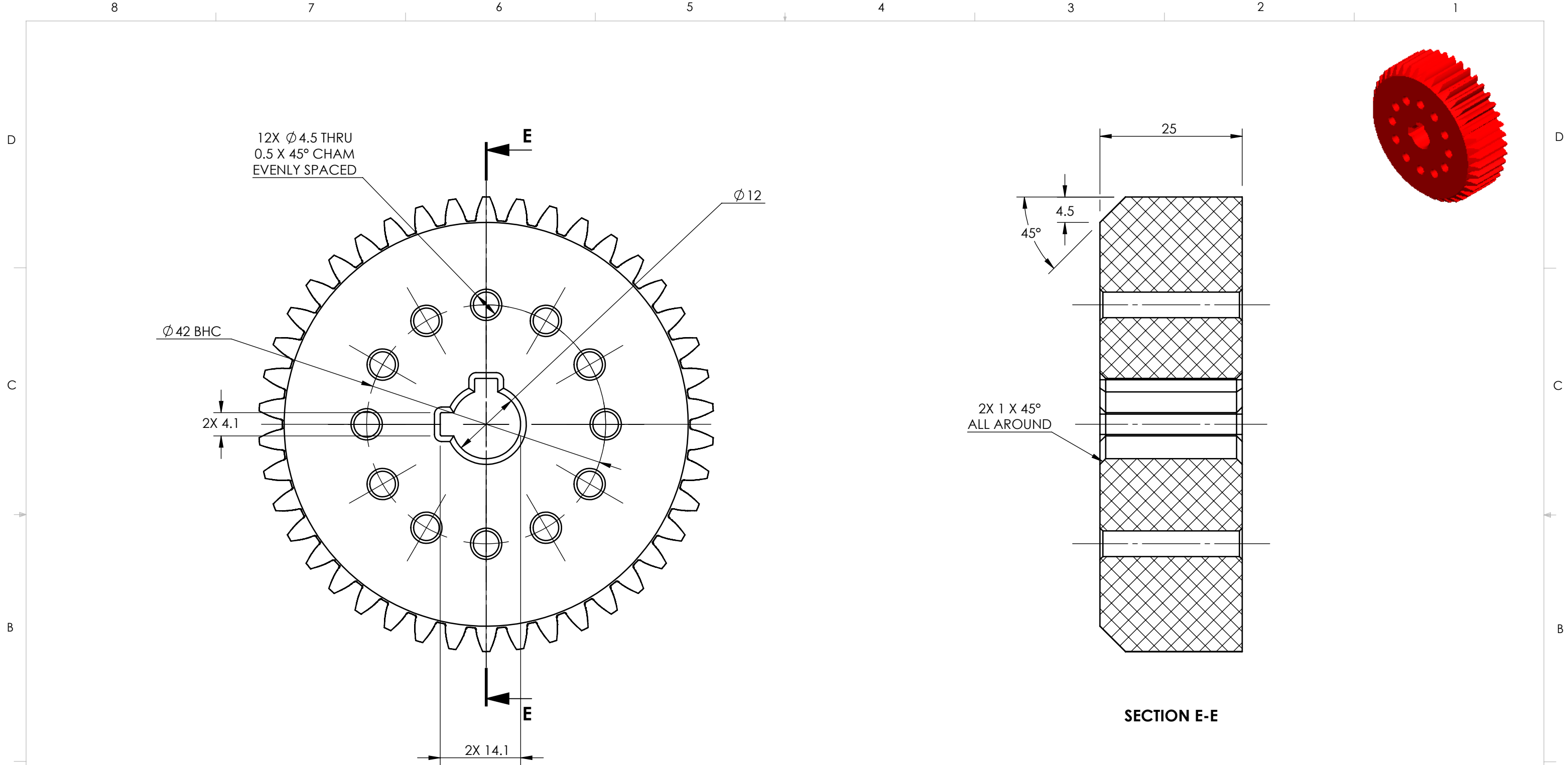
Rev.

A

SCALE: 3:2

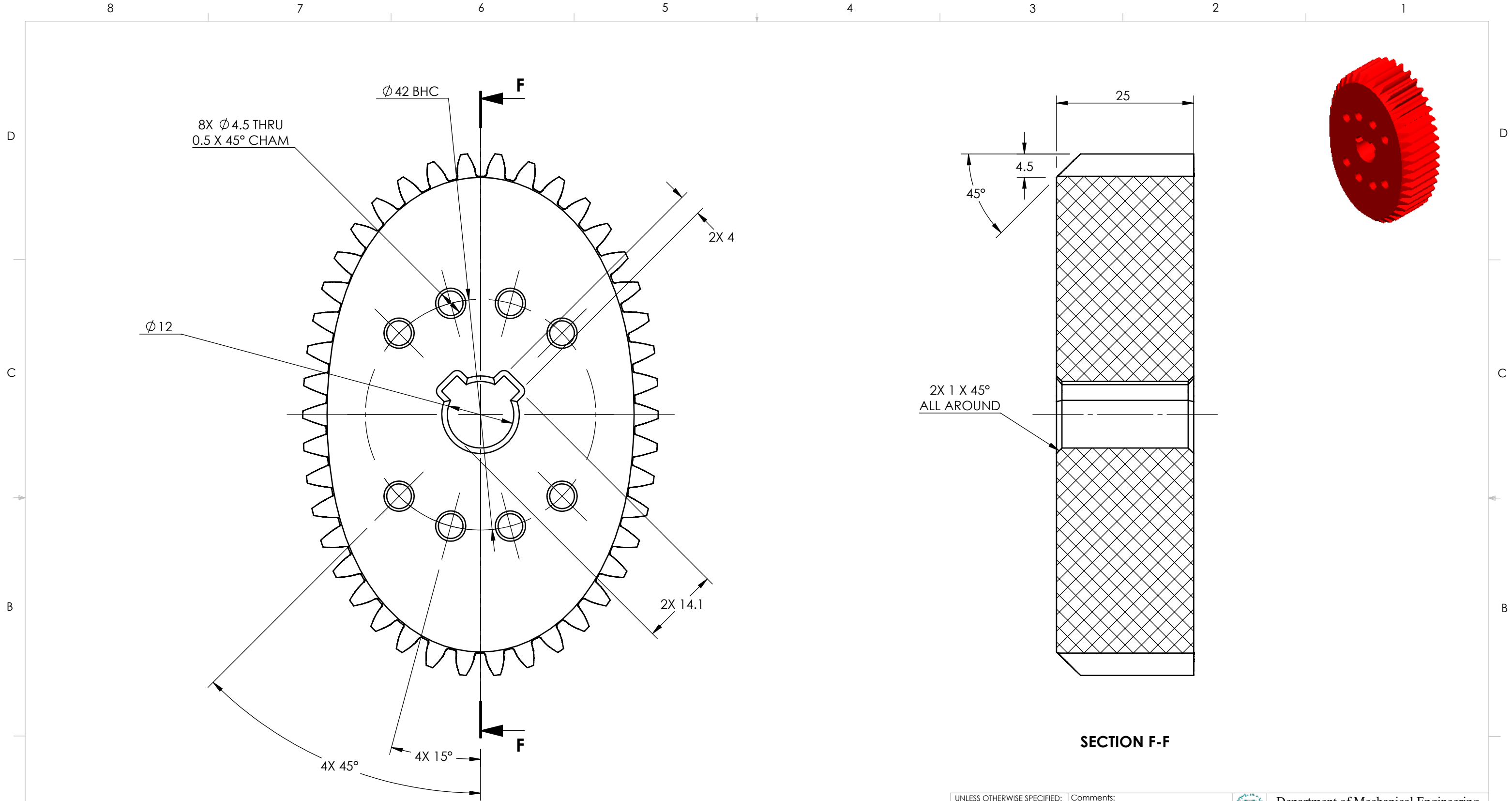
Mass:

SHEET 6 OF 11





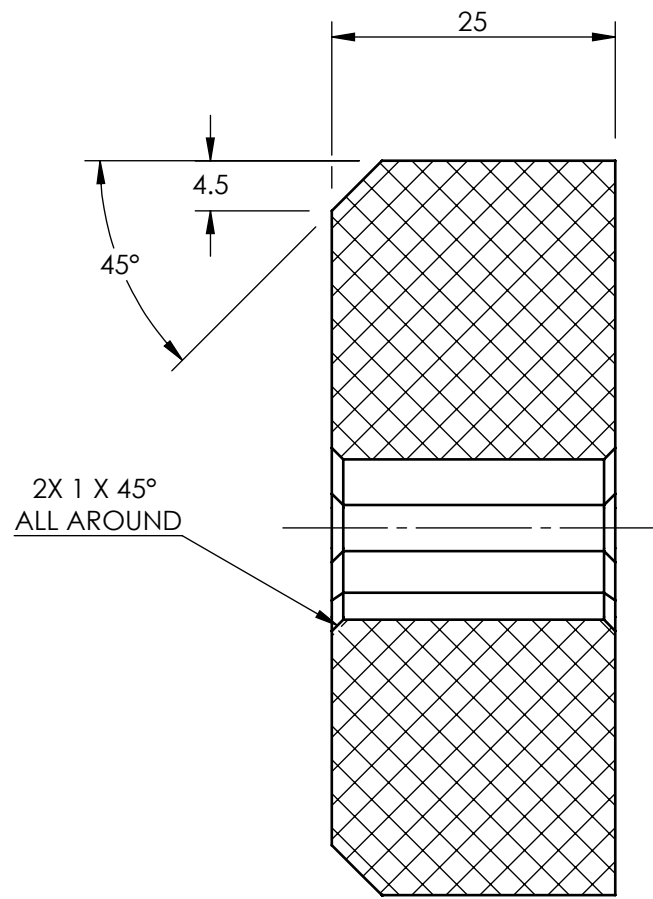
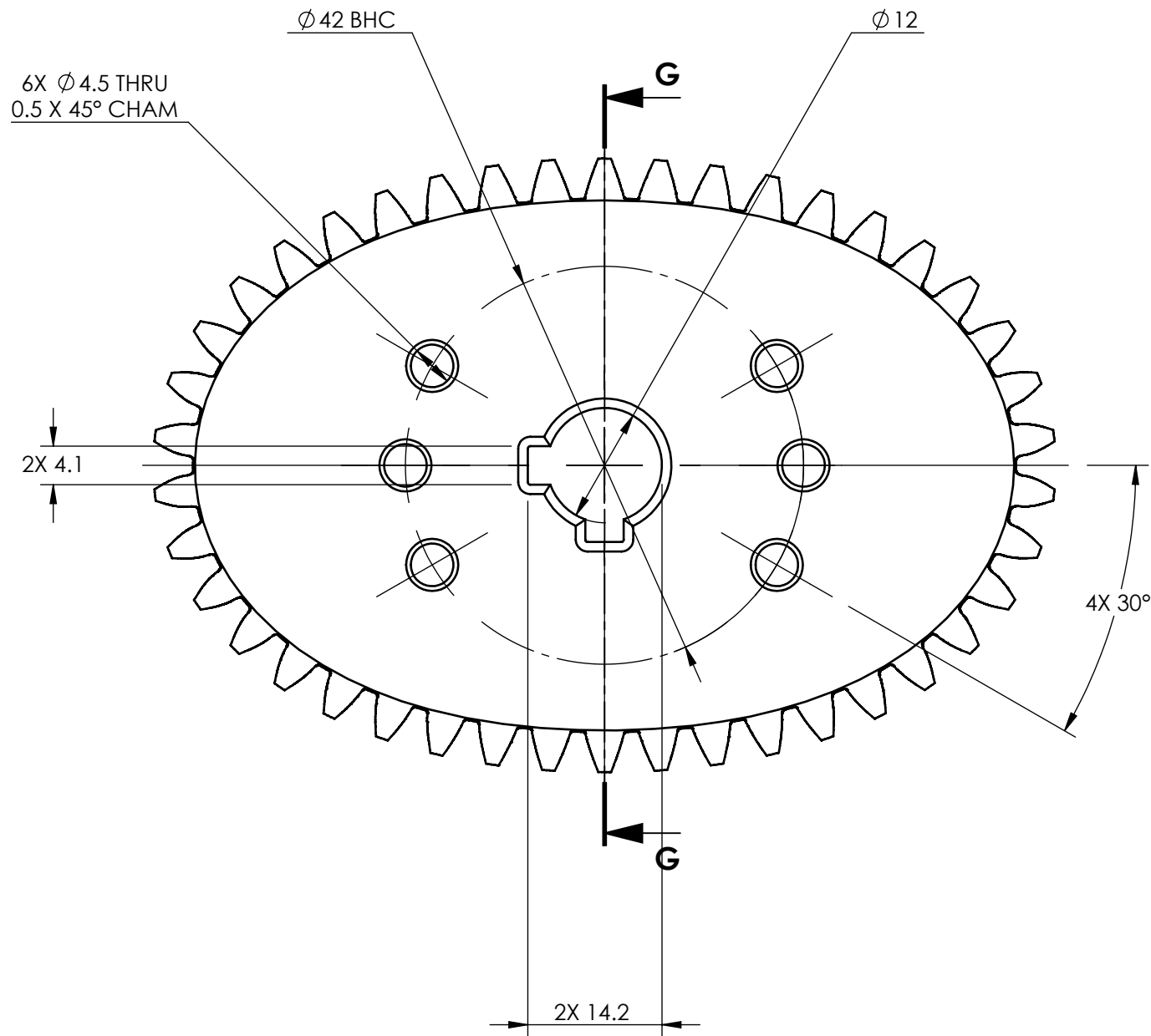
PITCH CIRCLE / CENTRODE DIAMETER: 3 IN

UNLESS OTHERWISE SPECIFIED: Dimensions are in mm Tolerances: Angular: $\pm 0.5^\circ$ Linear: X = ± 0.5 X.X = ± 0.1 X.XX = ± 0.025 SURFACE FINISH μm 0.6	Comments:		Department of Mechanical Engineering UNIVERSITY OF ALBERTA
	DRW By: MICHAEL NICOL-SETO	TITLE: $e = 0$ GEAR 2 (CRANK)	
	SM By: MICHAEL NICOL-SETO	42T, $p_d 14$, $\phi_C 20^\circ$	
	CHK By:	Size	Project
	nicolset May 22, 2019 August 30, 2021	B	EPM-1
MATERIAL:		Rev.	A
FILE NAME: 05-05-01-02_ROUND_42T_CD3_WHEEL_V3	SCALE: 3:2	Mass:	SHEET 7 OF 11

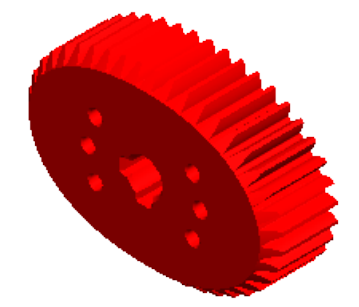


CENTRODE: $e=1/5$

UNLESS OTHERWISE SPECIFIED: Dimensions are in mm Tolerances: Angular: $\pm 0.5^\circ$ Linear: X = ± 0.5 X.X = ± 0.1 X.XX = ± 0.025 SURFACE FINISH μm 0.6		Comments:		 Department of Mechanical Engineering UNIVERSITY OF ALBERTA	
		DRW By: MICHAEL NICOL-SETO	TITLE: $e = 1/5$ GEAR 1 (SHAFT)		
MATERIAL:		SM By: MICHAEL NICOL-SETO	42T, $p_d 14$, $\phi_c 20^\circ$		
FILE NAME: 05-05-02-01_OVAL_e1-5_42T_CD3_PINION		CHK By: nicolset May 22, 2019 August 30, 2021	Size: B	Project: EPM-1	Rev.: A
			SCALE: 3:2	Mass:	SHEET 8 OF 11

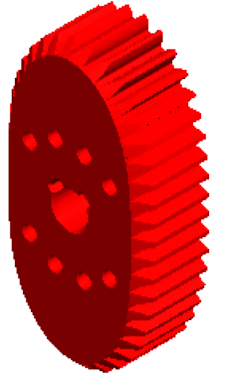
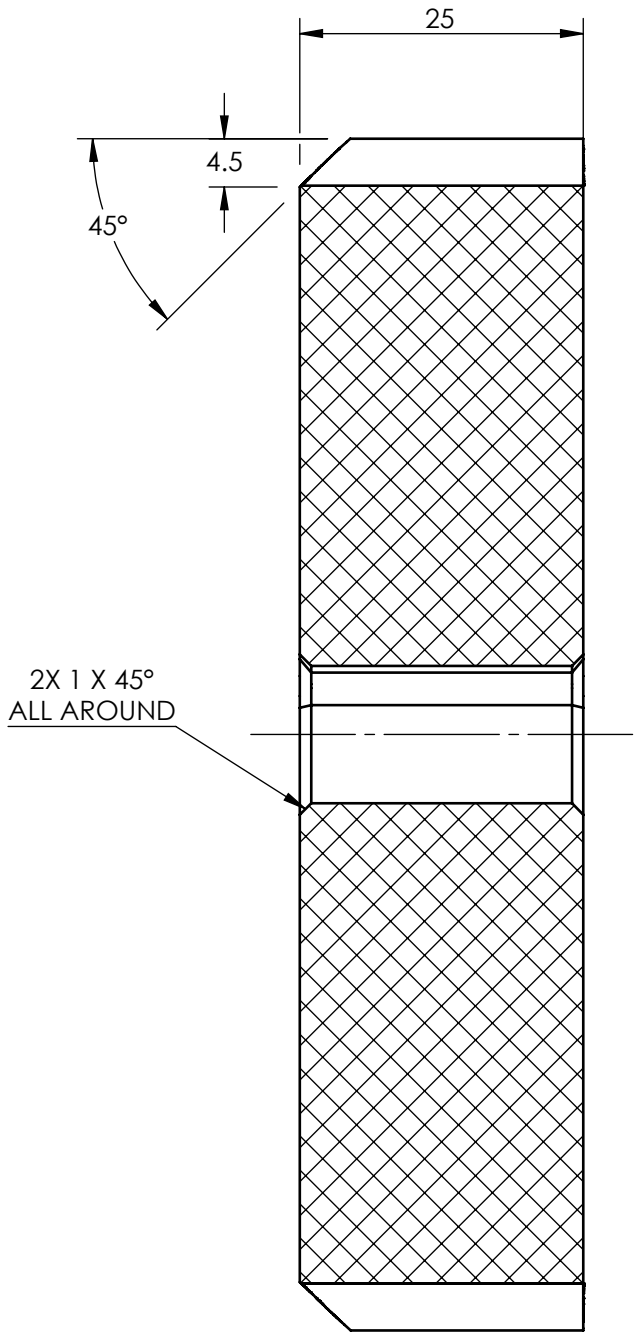
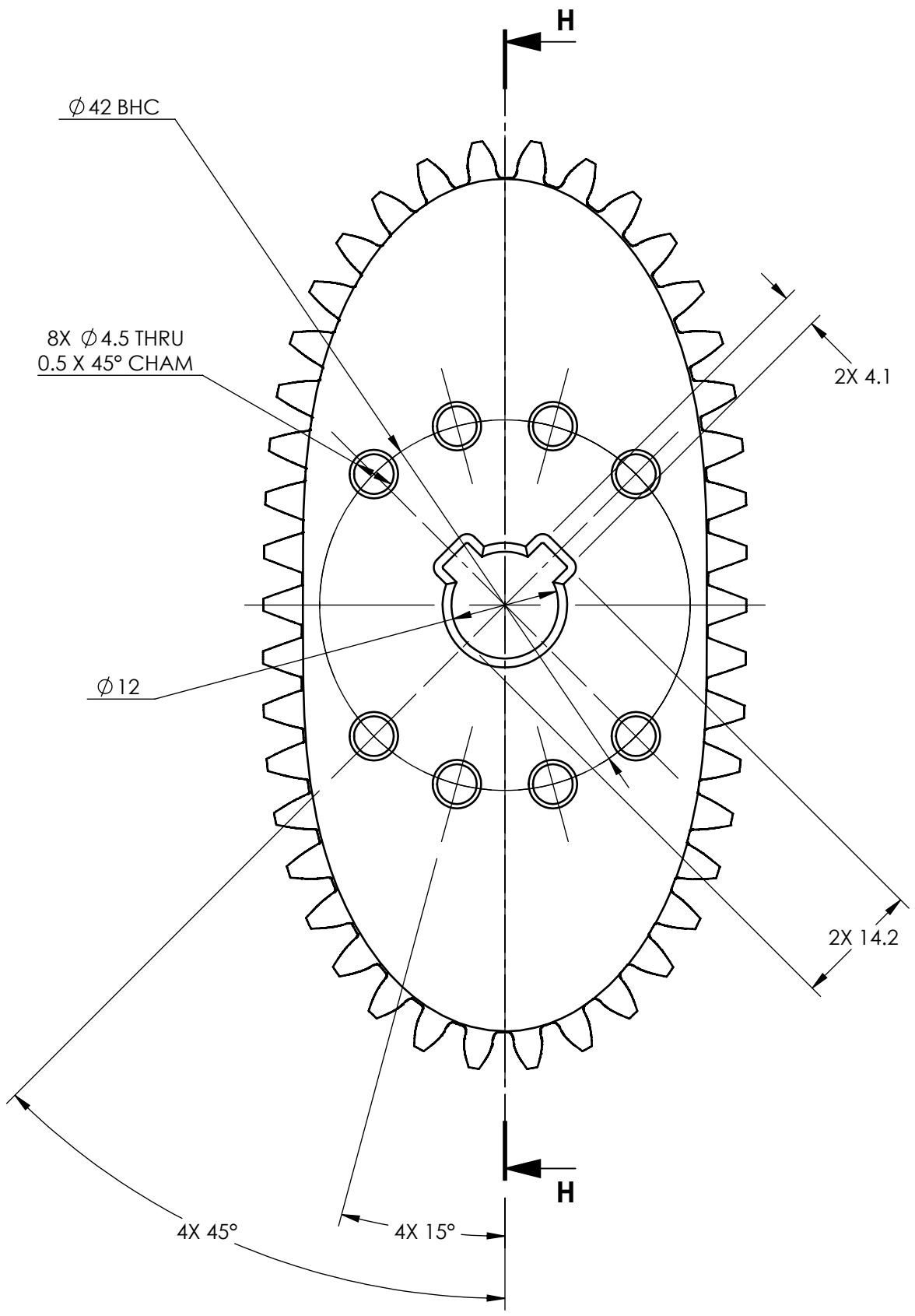


SECTION G-G



CENTRODE: $e=1/5$

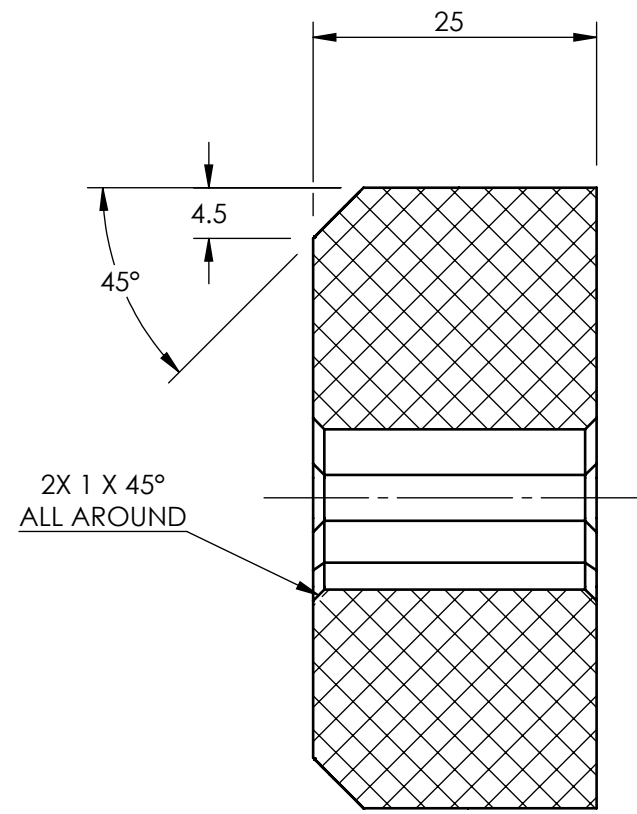
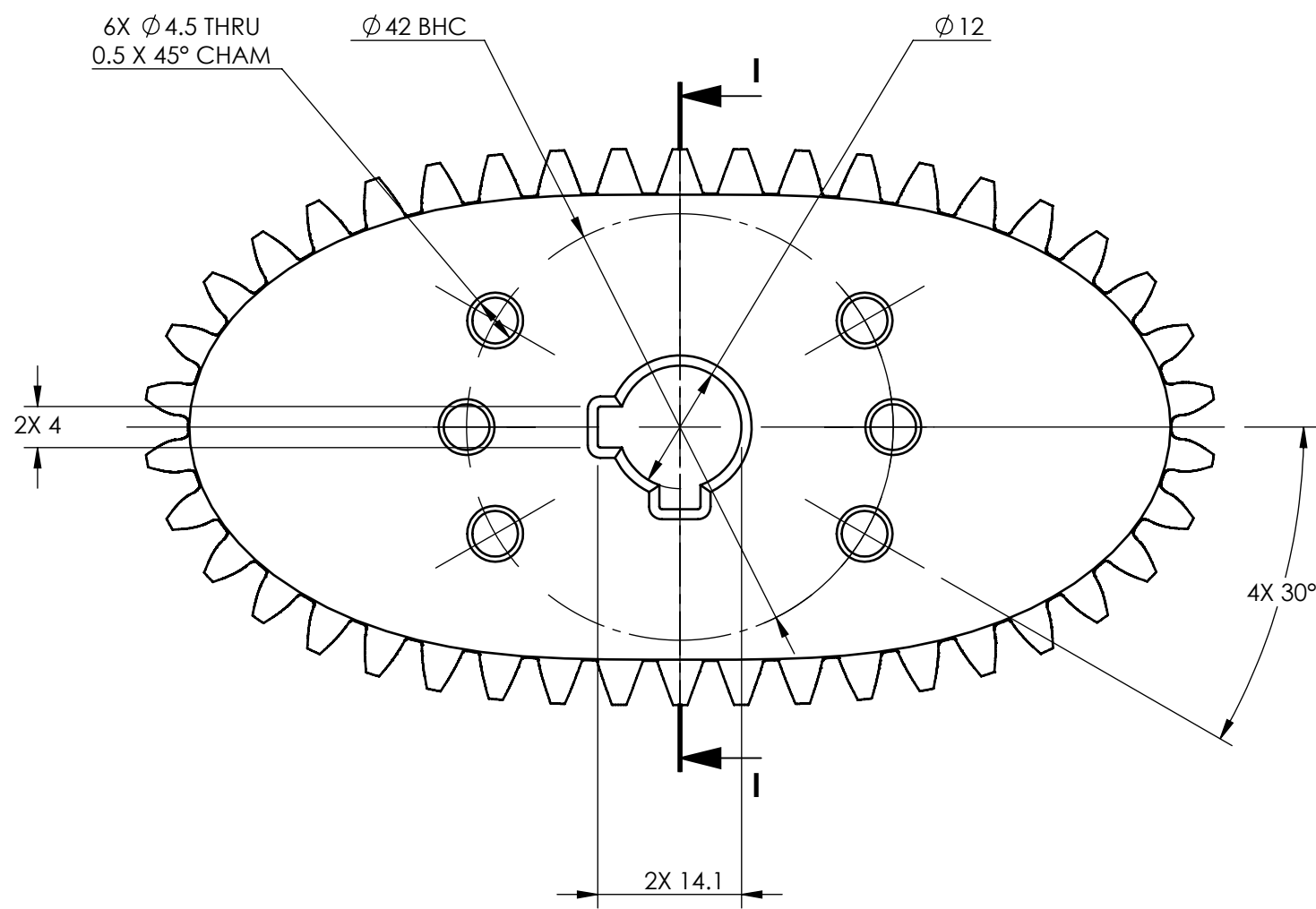
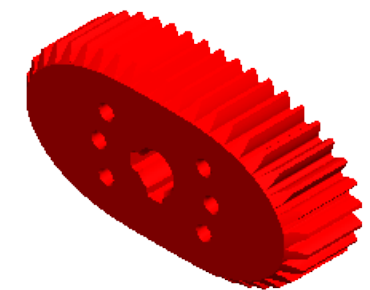
UNLESS OTHERWISE SPECIFIED: Dimensions are in mm Tolerances: Angular: $\pm 0.5^\circ$ Linear: X = ± 0.5 X.X = ± 0.1 X.XX = ± 0.025 SURFACE FINISH μm 0.6		Comments:		Department of Mechanical Engineering UNIVERSITY OF ALBERTA	
		DRW By: MICHAEL NICOL-SETO	TITLE: $e = 1/5$ GEAR 2 (CRANK)		
MATERIAL:		SM By: MICHAEL NICOL-SETO	$42T, p_d 14, \phi_C 20^\circ$		
FILE NAME: 05-05-02-02_OVAL_e1-5_42T_CD3_WHEEL		CHK By:	Size: B	Project: EPM-1	Rev.: A
		nicolset May 22, 2019 August 30, 2021	SCALE: 3:2	Mass:	SHEET 9 OF 11



SECTION H-H

UNLESS OTHERWISE SPECIFIED: Dimensions are in mm Tolerances: Angular: $\pm 0.5^\circ$ Linear: X = ± 0.5 X.X = ± 0.1 X.XX = ± 0.025		Comments:		Department of Mechanical Engineering UNIVERSITY OF ALBERTA	
SURFACE FINISH μm 0.6		DRW By: MICHAEL NICOL-SETO	TITLE: $e = 1/3$ GEAR 1 (SHAFT)		
		SM By: MICHAEL NICOL-SETO	42T, $p_d 14$, $\phi_C 20^\circ$		
MATERIAL:		CHK By:	Size	Project	Rev.
		nicolset May 22, 2019 August 30, 2021	B	EPM-1	A
FILE NAME: 05-05-03-01_OVAL_e1-3_42T_CD3_PINION		SCALE: 3:2	Mass:	SHEET 10 OF 11	

CENTRODE: $e=1/3$



SECTION I-I

CENTRODE: $e=1/3$

UNLESS OTHERWISE SPECIFIED: Dimensions are in mm Tolerances: Angular: $\pm 0.5^\circ$ Linear: X = ± 0.5 X.X = ± 0.1 X.XX = ± 0.025 SURFACE FINISH μm 0.6	Comments:		Department of Mechanical Engineering UNIVERSITY OF ALBERTA	
	DRW By:	MICHAEL NICOL-SETO		TITLE:
	SM By:	MICHAEL NICOL-SETO	$e = 1/3$ GEAR 2 (CRANK) $42T, p_d 14, \phi_c 20^\circ$	
	CHK By:	nicolset May 22, 2019 August 30, 2021	Size	Project
MATERIAL:		B	EPM-1	
FILE NAME: 05-05-03-02_OVAL_e1-3_42T_CD3_WHEEL	SCALE: 3:2	Mass:	SHEET 11 OF 11	